Dissertation

submitted to the

Combined Faculties of the Natural Sciences and Mathematics

of the Ruperto-Carola-University of Heidelberg, Germany,

for the degree of

Doctor of Natural Sciences

Put forward by

Asmita Bhandare

born in Pune, Maharashtra, India

Oral examination: June 19th, 2020

Numerical simulations of star and disc formation

ASMITA BHANDARE

Referees: Prof. Dr. Thomas Henning
Prof. Dr. Cornelis P. Dullemond

Zusammenfassung

Kalte, dichte Molekülwolkenkerne bilden die Geburtsumgebung für Sterne, Scheiben und Planeten. Das Szenario der massearmen Sternentstehung erfolgt durch die Bildung zweier quasi-hydrostatischer Kerne. Darüber hinaus kann die Drehimpulserhaltung zur Bildung einer Scheibe um den zweiten Kern (d.h. den sich bildenden Protostern) führen. Während dieser frühen Phasen der Sternentstehung können magnetisch getriebene Ausflüsse und Jets vom ersten bzw. zweiten Kern aus gestartet werden. Die Stern-, Scheiben- und Ausflussbildung umfasst komplexe physikalische Prozesse, die eine robuste, selbstkonsistente numerische Behandlung erfordern.

In dieser Studie verwenden wir numerische Simulationen, um den Übergang von einem isolierten molekularen Wolkenkern zu einem hydrostatischen Kern mit einer umgebenden Scheibe zu untersuchen. Wir verwenden den *PLUTO*-Code, um strahlungs (magneto-)hydrodynamische (MHD) Kollapssimulationen mit ein- und zweidimensionalen (2D) Gittern durchzuführen. Wir berücksichtigen die Effekte der Eigengravitation und des Strahlungstransports. Zusätzlich verwenden wir eine Gas-Zustandsgleichung inklusive dichte- und temperaturabhängiger thermodynamischer Größen, um die Dissoziation, Ionisierung, sowie Molekülschwingungen und -rotationen zu berücksichtigen.

Unsere kugelsymmetrischen Simulationen erstrecken sich über räumliche Skalen von sieben Größenordnungen. Wir untersuchen eine große Spannbreite anfänglicher Wolkenkerne mit niedriger bis hoher Masse ($0.5 - 100\,M_\odot$), was den bislang größten Parameter-Scan darstellt. Diese Simulationen weisen darauf hin, dass aufgrund hoher Akkretionsraten im Regime hoher Massen nicht genügend Zeit für die Entstehung des ersten hydrostatischen Kerns vorhanden ist.

Im nächsten Schritt führen wir 2D-Simulationen für nicht-rotierende molekulare Wolkenkerne mit Massen von $1\,M_\odot$, $5\,M_\odot$, $10\,M_\odot$, und $20\,M_\odot$ durch. Für jeden dieser Fälle verwenden wir eine bislang nicht erreichte Auflösung, um die Entwicklung des zweiten Kerns für ≥ 100 Jahre nach dessen Entstehung zu modellieren. In diesen Modellen wird zum ersten Mal gezeigt, dass in den äußeren Schichten des zweiten Kerns Konvektion erzeugt wird. Dies bedeutet, dass dynamo-getriebene Magnetfelder in den frühesten Phasen der Sternentstehung erzeugt werden können. Anschließend analysieren wir die Auswirkungen von Rotation auf die Eigenschaften der hydrostatischen Kerne und der Scheibenbildung für das Modell mit $1\,M_\odot$. In dieser Simulation entwickelt sich der erste hydrostatische Kern in eine eher abgeplattete, pseudoscheibenartige Struktur und nach der Entstehung des zweiten Kerns bildet sich eine kleine (sub-au) Scheibe. Schließlich untersuchen wir die Auswirkungen der idealen und nicht-idealen MHD (einschließlich der Effekte des ohmschen Widerstandes). Wir untersuchen die Abhängigkeit der molekularen Ausflüsse und der Scheibenbildung von der anfänglichen Wolkenkernmasse, der Rotation, dem spezifischen Widerstand und der magnetischen Feldstärke. In den Modellen die spezifischen Widerstand berücksichtigen finden wir magnetisch angetriebene Ausflüsse, die sowohl vom ersten als auch vom zweiten Kern ausgehen.

Zusammenfassend verwenden wir detaillierte thermodynamische Modelle, um die Eigenschaften der hydrostatischen Kerne, Ausflüsse und Scheiben für Kollapsszenarien mit einer großen Spannbreite an Anfangsbedingungen zu quantifizieren. Die hier vorgestellten Modelle dienen als Grundlage für Folgestudien, die diese theoretischen Erkenntnisse mit Beobachtungssignaturen vergleichen werden.

Abstract

Magnetized, cold, dense molecular cloud cores provide the birth environment for stars, discs, and planets. The multi-scale scenario of low-mass star formation occurs via the formation of two quasi-hydrostatic cores. Furthermore, the conservation of angular momentum can lead to the formation of a disc around the second core (i.e. the forming protostar). During these early stages of star formation, magnetically driven outflows and jets can be launched from the first and second cores, respectively. Star, disc, and outflow formation involve complex physical processes, which require a robust, self-consistent numerical treatment.

In this thesis, we use numerical simulations to probe the gravitational collapse scenario that involves the transition of an isolated molecular cloud core to a hydrostatic core with a surrounding disc. We use the *PLUTO* code to perform radiation (magneto-)hydrodynamic (MHD) collapse simulations, using one- and two-dimensional (2D) grids. We include the effects of self-gravity and a grey flux-limited diffusion approximation for the radiative transfer. Additionally, we use for the gas equation of state density- and temperature-dependent thermodynamic quantities to account for the dissociation, ionisation, and molecular vibrations and rotations.

Our spherically symmetric simulations span seven orders of magnitude in spatial scale. We survey a wide range of initial low- to high-mass ($0.5 - 100 \, M_\odot$) molecular cloud cores, yielding the largest parameter scan so far. Our results highlight the dependence of the first and second hydrostatic core properties on the initial cloud core properties. These simulations indicate that in the high-mass regime, the first hydrostatic cores do not have enough time to form due to large accretion rates.

We further expand our studies to three different sets of 2D simulations using axial and midplane symmetry. First, we perform 2D simulations for non-rotating molecular cloud cores with masses of $1 \, M_\odot$, $5 \, M_\odot$, $10 \, M_\odot$, and $20 \, M_\odot$. For each of these cases, we use an unprecedented resolution to model the evolution of the second core for ≥ 100 years after its formation. For the first time, we demonstrate that convection is generated in the outer layers of the second core. This supports the intriguing possibility that dynamo-driven magnetic fields may be generated during the earliest phases of star formation. Following which, for the $1 \, M_\odot$ case, we analyse the effects of solid-body rotation on the properties of the hydrostatic cores and disc formation. In this model, the first hydrostatic core evolves into a more oblate, pseudo-disc like structure and a sub-au disc starts forming after the formation of the second core. Finally, we explore the effects of ideal and non-ideal (including Ohmic resistivity) MHD during the collapse of rotating molecular cloud cores. We investigate the dependence of molecular outflows and disc formation on the initial cloud core mass, rotation, resistivity, and magnetic field strength. We find the presence of magnetically driven outflows launched from both first and second cores in the resistive models. We also reveal ongoing disc formation in some of our resistive simulations.

In conclusion, we use detailed thermodynamical modelling to quantify the properties of the hydrostatic cores, outflows, and discs for collapse scenarios with a wide range of initial cloud core properties. The models presented herein will serve as the foundation for follow-up studies that link these theoretical insights with observational signatures.

For my parents & sister.

Contents

List of Figures

List of Tables

List of Abbreviations

1D   One-**D**imensional
2D   Two-**D**imensional
2T   Two-**T**emperature
3D   Three-**D**imensional
ALMA   **A**tacama **L**arge **M**illimetre/submillimetre **A**rray
CFL   **C**ourant–**F**riedrichs–**L**ewy
EOS   **E**quation **O**f **S**tate
FLD   **F**lux **L**imited **D**iffusion
GMCs   **G**iant **M**olecular **C**loud**s**
LTE   **L**ocal **T**hermodynamic **E**quilibrium
MHD   **M**agneto-**H**ydro**D**ynamics
PMS   **P**re-**M**ain-**S**equence
RHD   **R**adiation **H**ydro**D**ynamics
RMHD   **R**adiation **M**agneto-**H**ydro**D**ynamics
RK2   second order **R**unge–**K**utta method
SASI   **S**tanding **A**ccretion **S**hock **I**nstability
SED   **S**pectral **E**nergy **D**istribution
SPH   **S**moothed **P**article **H**ydrodynamics
YSOs   **Y**oung **S**tellar **O**bject**s**

Introduction

The recent wealth of high-resolution infrared and (sub-)millimetre observations have helped to trace the dawn of stellar birth and have provided unprecedented views of discs surrounding these stars. However, observing young embedded protostars and discs still pose several challenges due to the obscuration from dust in the surrounding envelope. Theoretical and numerical studies help elucidate and quantify the physical picture of the star-disc systems, which provide the building blocks for planets to form. A detailed understanding of the star-disc connection plays a pivotal role in bringing us a step closer to deciphering planet formation. In this thesis, I use numerical simulations to gain insights into the early stages of low-mass star and disc formation, including the origins of molecular outflows.

1.1 Zooming in on star and disc formation

Star formation is a multi-scale, multi-physics process that involves a chain of events occurring within giant molecular clouds at larger scales (≥ 10 parsec) down to the smaller scales of individual stars and discs ($\sim 10 - 200$ au). Each of these evolutionary stages involve complex physical processes resulting from the effects of gravity,
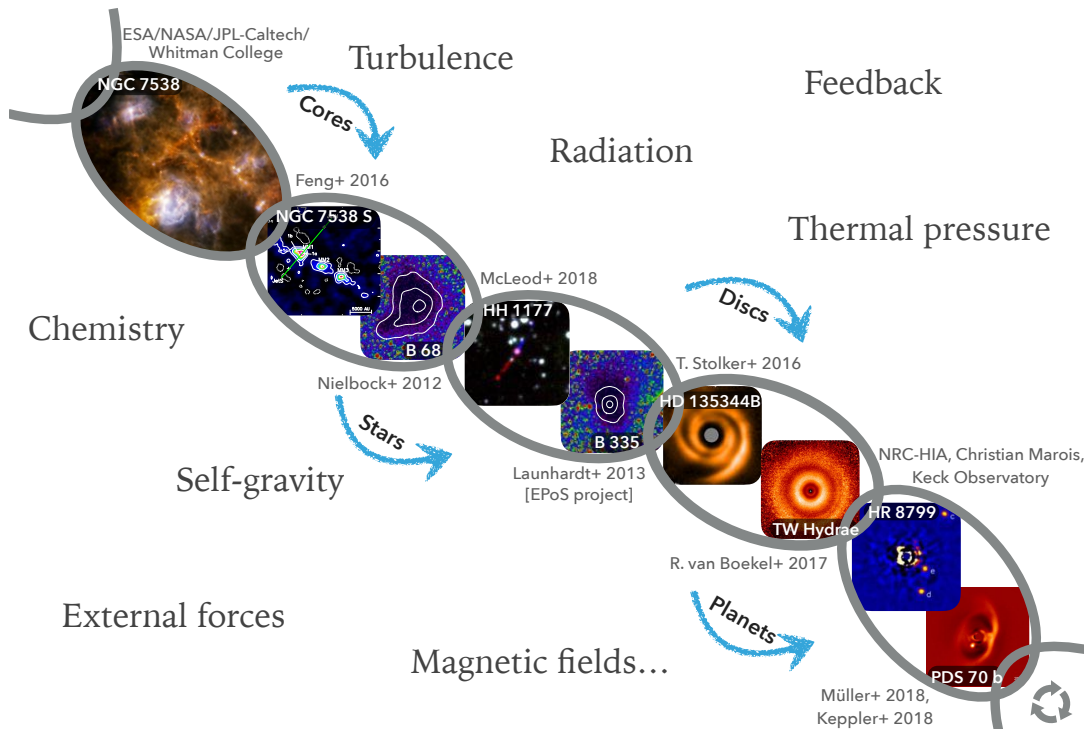
Figure 1.1: Schematic showing the chain of events and the key dynamical processes that lead to the formation of stars, discs, and planets.

Cloud ($\gtrsim$10 pc)

Clump ($\sim$1 pc)

Filament ($\sim$0.1 pc wide)

Core ($\sim$0.05 - 0.1 pc)

Envelope ($\sim$300 – 3000 AU)

Disk and star ($\sim$10 - 200 AU)
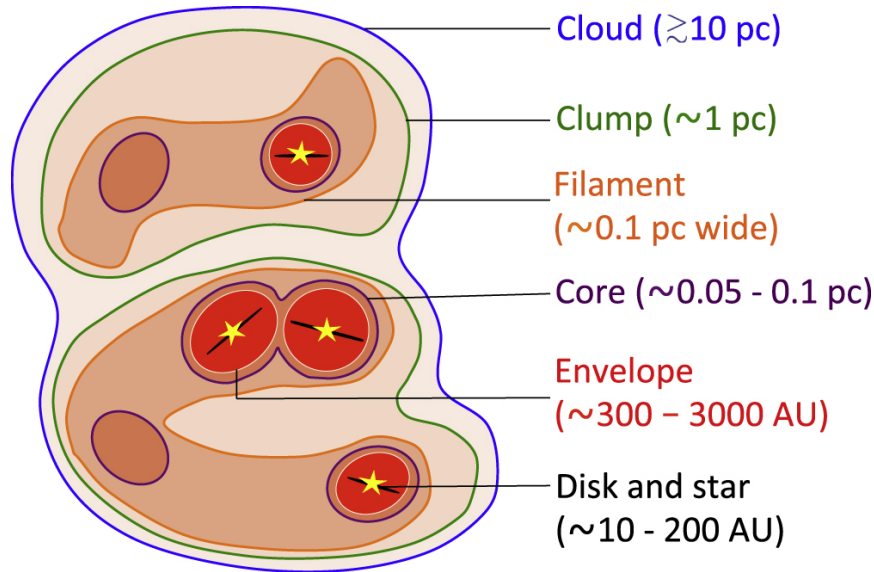
Figure 1.2: Schematic showing the hierarchical structure within a molecular cloud, which serves as the cradle for star and disc formation. Figure taken from Pokhrel et al. (2018).

pressure, radiation, chemistry, turbulence, and magnetic fields, to name a few. The schematic shown in Fig. 1.1 displays the order of these events ultimately leading to the formation of stars as well as the byproducts of the star formation process, namely, outflows, discs, and planets.

Giant molecular clouds (GMCs), mostly found in the spiral arms of galaxies, have an extent of tens of parsecs, are cold (10 – 30 K), dense (n $\geq 10^2$ cm^{-3}), with masses in the range $10^4 - 10^6$ $M_\odot$ or more, and lifetimes of the order of 10^6 years (McKee & Ostriker, 2007). GMCs, composed mainly of molecular hydrogen (H$_2$) with $\sim 1\%$ dust (Lilley, 1955; Tielens, 2005), are highly structured, consisting of numerous clumps, filaments, and dense cores (see reviews by André et al., 2014; Dobbs et al., 2014; Heyer & Dame, 2015, and references therein). The schematic in Fig. 1.2 shows the hierarchical structure within GMCs, as per definitions of these substructures in Pokhrel et al. (2018). GMCs fragment into (generally) gravitationally bound "clumps" that are roughly a few parsec in size. These over-dense regions provide the birth environment for clusters of stars to form (Williams et al., 2000; Bergin & Tafalla, 2007; Schneider et al., 2012). Massive dense clumps with typical masses between 10s - 10^4 $M_\odot$ serve as the locations for high-mass (≥ 8 $M_\odot$) star formation (e.g. Beuther et al., 2007; Urquhart et al., 2018, and references therein).

Filaments were first described as vacant lanes by Barnard (1907) and are now commonly-observed, elongated structures with a width of ~ 0.1 pc (e.g. Arzoumanian et al., 2011, 2019). The presence of ubiquitous filamentary structures within GMCs has been highlighted by *Herschel* images (Hennebelle & Falgarone, 2012; André et al., 2014). On scales of ~ 0.1 pc along these filaments or within isolated clouds (called Bok globules; Bok & Reilly, 1947), dense ($10^5 - 10^7$ cm^{-3}) "cores", with masses of a few $M_\odot$, act as the progenitors of individual or multiple stars (Larson, 2003; di Francesco et al., 2007). These gravitationally bound cores are initially supported against gravity by a combination of thermal, turbulent, and magnetic pressure forces. Considering a simplified case of thermal pressure force balancing gravity, an infinite uniform density medium can collapse beyond a wavelength where density perturbations can grow, thus leading to an instability. The corresponding wavelength, known as the

Jeans length (Jeans, 1902, 1928) is

$$\lambda_J = \sqrt{\frac{\pi c_s^2}{G\rho}}.$$

(1.1)

In the above equation G is the gravitational constant, ρ is the mass density, and c_s is the isothermal sound speed given as $\sqrt{k_B T/\mu m_H}$, where μ is the mean molecular weight and m_H is the mass of atomic hydrogen. This gravitationally unstable region can collapse when its mass exceeds the Jeans mass

$$M_J = \left(\frac{\pi k_B T}{\mu m_H G}\right)^{1.5} \rho^{-0.5} = 0.5 \left(\frac{T}{10 \text{ K}}\right)^{1.5} \left(\frac{n}{10^4 \text{ cm}^{-3}}\right)^{-0.5} M_\odot,$$

(1.2)

where k_B is the Boltzmann constant, T is the gas temperature, and n is the number density. The characteristic time scale required for a uniform sphere of gas to collapse under its own gravity, in a medium with negligible pressure support, called the free-fall time, is given by

$$t_{\text{ff}} = \sqrt{\frac{3\pi}{32G\rho}}.$$

(1.3)

Gravitational collapse is a natural outcome in optically thin, isothermal molecular cloud cores (i.e. pre-stellar cores), wherein thermal emission from the dust grains is highly efficient. Several processes can trigger such a collapse, namely, the effects of non-ideal magneto-hydrodynamics (MHD; e.g. Shu et al., 1987; Mouschovias, 1991), contraction of marginally stable Bonnor–Ebert spheres (Ebert, 1955; Bonnor, 1956), external shock waves (Masunaga & Inutsuka, 2000), or a reduction of the effective sound speed in pre-stellar cores due to the dissipation of turbulence (e.g. Nakano, 1998).

As the pre-stellar core becomes denser during the initial isothermal collapse phase, the optical depth becomes greater than unity. The temperature in this dense central region increases from the initial low values of $10 – 30$ K, as the compressional heating dominates over radiative cooling. The collapse almost halts as the gas pressure provides sufficient support against gravity, leading to the formation of the *first quasi-hydrostatic core*. The first core can be identified by an accretion shock at its surface, caused due to deceleration of the infalling velocity as a response to the enhanced pressure. The first core radius in spherically symmetric calculations is found to be roughly a few au and may vary in two- and three-dimensional numerical simulations. The formation timescale of the first core is $10^3 – 10^4$ years. At this stage, the gas acts as monatomic, since the rotational degrees of freedom of molecular hydrogen are not excited ($E_{J=2\rightarrow0}/k_B = 512$ K). The first core gradually evolves through a phase of adiabatic contraction. A further rise in temperature excites the rotational degrees of freedom and the core transitions from being effectively monatomic to diatomic.

The process of H_2 dissociation is triggered once temperatures within the first core reach ~ 2000 K. During this strongly endothermic dissociation process, gravity dominates over thermal pressure. Thus, the first core becomes unstable, which initiates the second collapse phase. Once most of the H_2 is dissociated, a *second quasi-hydrostatic core* is formed almost instantaneously within the first core at typical central densities of 10^{-8} g cm^{-3}. The first and second cores are famously known as the Larson

cores, named after the first numerical study by Larson (1969) of the non-homologous[1] collapse of an isolated pre-stellar core. As the second core (i.e. the forming protostar) undergoes a phase of adiabatic contraction, the balance between thermal pressure and gravity eventually halts the collapse. During this initial embedded phase, known as the main accretion phase, material from the surrounding envelope continues to accrete onto the central protostar as it reaches stellar densities $\rho \approx 1 \, \mathrm{g \, cm^{-3}}$. The protostar transforms into a star once it reaches ignition temperatures for nuclear fusion, with deuterium burning initiating at $T \sim 10^6 \, \mathrm{K}$, followed by hydrogen burning at $T \sim 10^7 \, \mathrm{K}$. The newly-formed star continues its journey in the pre-main-sequence phase before further evolving along the main sequence. The collapse of a pre-stellar core, proceeding through the formation stage of the first core and until the second core evolves into a protostar, has been widely discussed in the literature (e.g. see textbook by Stahler & Palla, 2005).

In the main accretion phase, material continues to accrete onto the central protostar via its surrounding disc. This centrifugally-supported protostellar disc is formed during the early collapse stages of a rotating and/or turbulent pre-stellar core due to the conservation of angular momentum. This disc can eventually either become marginally stable or unstable. The generation of spiral density fluctuations in a marginally stable disc produces gravitational torques that play a role in the redistribution of angular momentum. On the other hand, unstable discs can fragment to form binary or multiple stellar systems. The formation of discs or multiple stars contribute towards the outward transport of angular momentum that would otherwise spin up the central star, resulting in a much faster rotation rate than that observed (referred to as the angular momentum problem). The rotation rate is typically inferred from measuring velocity gradients. The rotational energy of the core is observed to be a few percent of the gravitational energy (Arquilla & Goldsmith, 1986; Goodman et al., 1993; Caselli et al., 2002).

Star-forming pre-stellar cores are observed to be strongly magnetized, with their magnetic energy being comparable to or less than the gravitational energy (Crutcher, 1999; Bourke et al., 2001; Troland & Crutcher, 2008). In the presence of rotation and magnetic fields, contributions from the Lorentz force via magnetic tension can generate torques, which can hinder or delay the formation of discs. In an idealised case, that means assuming that the bulk neutral gas is well coupled to the magnetic field, disc formation can be prevented due to an extremely efficient removal of angular momentum via magnetic fields, known as magnetic braking (Mestel & Spitzer, 1956). It is important to note that this so-called magnetic braking catastrophe is most effective when the magnetic fields are aligned with the rotation axis and can be dampened for non-axisymmetric perturbations such as magnetic misalignment and turbulence (discussed in the recent review by Wurster & Li, 2018). Observationally, dense pre-stellar cores are only weakly ionised, which results in the decoupling of the magnetic fields from the bulk neutral gas (Bergin & Tafalla, 2007). This decoupling enables redistribution of the magnetic flux that would have otherwise been dragged into the central object, as is the case in the ideal limit. Therefore, it is important to account for the interactions between the charged and neutral species via the non-ideal dissipative, diffusive, and dispersive terms (for more details see Sect. 2.2). The inclusion of Ohmic resistivity, ambipolar diffusion and/or the Hall effect enable discs to form during the early stages of star formation, in some cases even before the second core formation,

---

[1] In this context, the term non-homologous refers to a faster increase of the density in the centre such that it can reach stellar densities and stop collapsing before most of the remaining cloud can collapse.
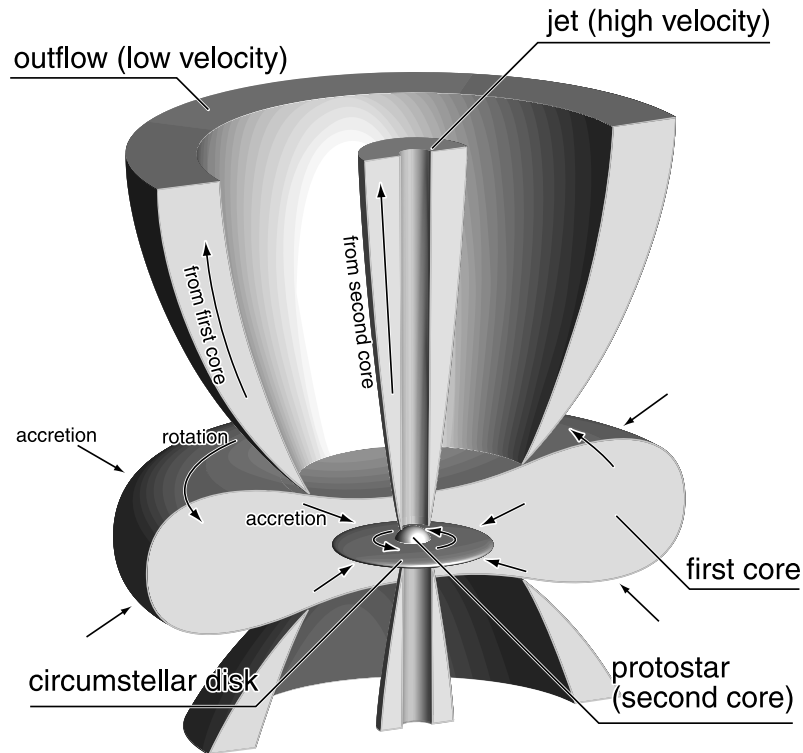
Figure 1.3: Schematic showing the disc, outflow, and jet configuration around a protostar. Figure is taken from Machida et al. (2008).

as seen in the various numerical studies listed in Table 1.1. These discs further evolve into the birthsites for planets.

Magnetic fields also play an important role in the launching of molecular outflows and collimated jets from the first and second cores, respectively. Magnetic field lines threading the rotating hydrostatic cores (and eventually the star) can drag the surrounding gas, thus enforcing it to co-rotate up to the Alfvén surface where the poloidal[2] flow velocity equals the poloidal Alfvén velocity. Thus, the outflows, jets, and disc winds act as another mechanism for the outward transport of angular momentum from the accreting material (see recent review by Pudritz & Ray, 2019, and references therein).

The outflows and jets that often accompany the forming discs, prove to be a vital part of star formation because they can limit the accretion onto the central protostar and remove excess energy and angular momentum, while creating cavities in the surrounding envelope. The main driving mechanisms are the magnetic pressure (Lynden-Bell, 2003) and magneto-centrifugal forces (Blandford & Payne, 1982; Pudritz & Norman, 1983; Pelletier & Pudritz, 1992; Shu et al., 1994). The magnetic pressure launching mechanism operates when the magnetic pressure above the rotor (such as a rapidly spinning protostar, first core, or an accretion disc) is enhanced due to the toroidal magnetic field component generated by the rotor. This increased magnetic pressure can then launch an outflow. The magneto-centrifugal launching mechanism operates such that the magnetic fields anchored to an underlying rotor can lift off material from the rotor, which allows angular momentum to be carried away. This material is accelerated due to centrifugal forces until it reaches the Alfvén radius,

---

[2]In spherical coordinates, the toroidal term is defined using the ϕ components, whereas the poloidal term is defined using the combination of r and θ components.

where the magnetic force balances the inertial force. A simple analogy for this process is to imagine it as the flow of beads on a wire. The outflow or jet can be collimated beyond the Alfvén radius as the inertial forces bend the field lines, yielding a hoop stress toward the rotation axis.

Ever since the first few detections of outflows and jets from young protostars (Schwartz, 1977; Snell et al., 1980), they have been a commonly-observed phenomenon. Similar outflows and jets have been observed across the spectrum from brown dwarfs (e.g. Whelan et al., 2005) to O stars (e.g. Caratti o Garatti et al., 2017) as well as from extragalactic sources (McLeod et al., 2018). Several numerical studies have shown that outflows and/or jets launched from the first and second hydrostatic cores are a natural outcome of magnetized pre-stellar core collapse. One such example from Machida et al. (2008) is shown in Fig. 1.3 using a schematic of the disc, low-velocity outflow, and high-velocity jet configuration around a protostar during the early formation stages. In this thesis, we discuss the presence of magnetically driven outflows from the first and second hydrostatic cores in Chapter 5.

The system of the central protostar, its surrounding disc, and the outflows evolves further as material continues to accrete from the surrounding envelope. The young stellar objects (YSOs), as first termed by Strom (1972), are objects at different evolutionary stages of star formation. YSOs can be classified based on their emission in the infrared and sub-millimetre parts of the spectral energy distribution (SED), as first proposed by Lada (1987). The standard observational technique for categorisation of these objects is to measure the spectral index of the SED, i.e. the slope of the SED in the infrared, which changes from positive (Class I) to negative (Class II) to strongly negative (Class III). Figure 1.4 shows the four different classes of YSOs according to these observational diagnostics and their corresponding geometry. The earliest stage of star formation corresponding to the least evolved phase of YSOs, with no signs of excess infrared emission, is known as the Class 0 phase. The outer envelope appears as a modified black-body with the cold dust contributing towards the thermal emission. During this phase, there may be a presence of an outflow that provides an indication of the central compact object. In this thesis, we mainly focus on the very early stages of star formation, that means phases even before this Class 0 stage.

The distinction between Class 0 and Class I sources is the non-trivial infrared emission seen as the star begins to heat the dust around it. Class I sources also exhibit signatures of an early disc around the central star. Both these sources belong to the protostellar phase and are still embedded in the surrounding infalling envelope of gas and dust. By the pre-main-sequence (PMS) phase, enough material accretes onto the central protostar via its disc or is blown away due to feedback processes (e.g. Arce & Sargent, 2006; Koyamatsu et al., 2014). As the surrounding envelope depletes, the star-disc system becomes visible in the optical and near infrared. In the flat-shaped SED for Class II sources, the central PMS star can be identified from the black-body emission and its surrounding disc is visible as the emission at near- or mid-infrared wavelengths. Class II is the last stage for the presence of a disc with substantial mass and hence, also the phase where planet formation should occur (Isella et al., 2018; Tobin et al., 2020). The final stage is Class III, where the SED predominantly shows the stellar black body emission in the optical and mid-infrared, with a tiny contribution (if at all) in the far-infrared from the debris disc[3] or transition disc[4]. The

---

[3]Debris discs are gas poor discs where the opacity is dominated by second-generation dust produced by collisions between larger bodies rather than dust from the interstellar medium.

[4]A transition disc is suggested to be a disc with a hole in its centre that is mostly devoid of dust. In some transition discs, gas is visible in these gaps. These discs show a strong mid- to far-infrared emission in observations.
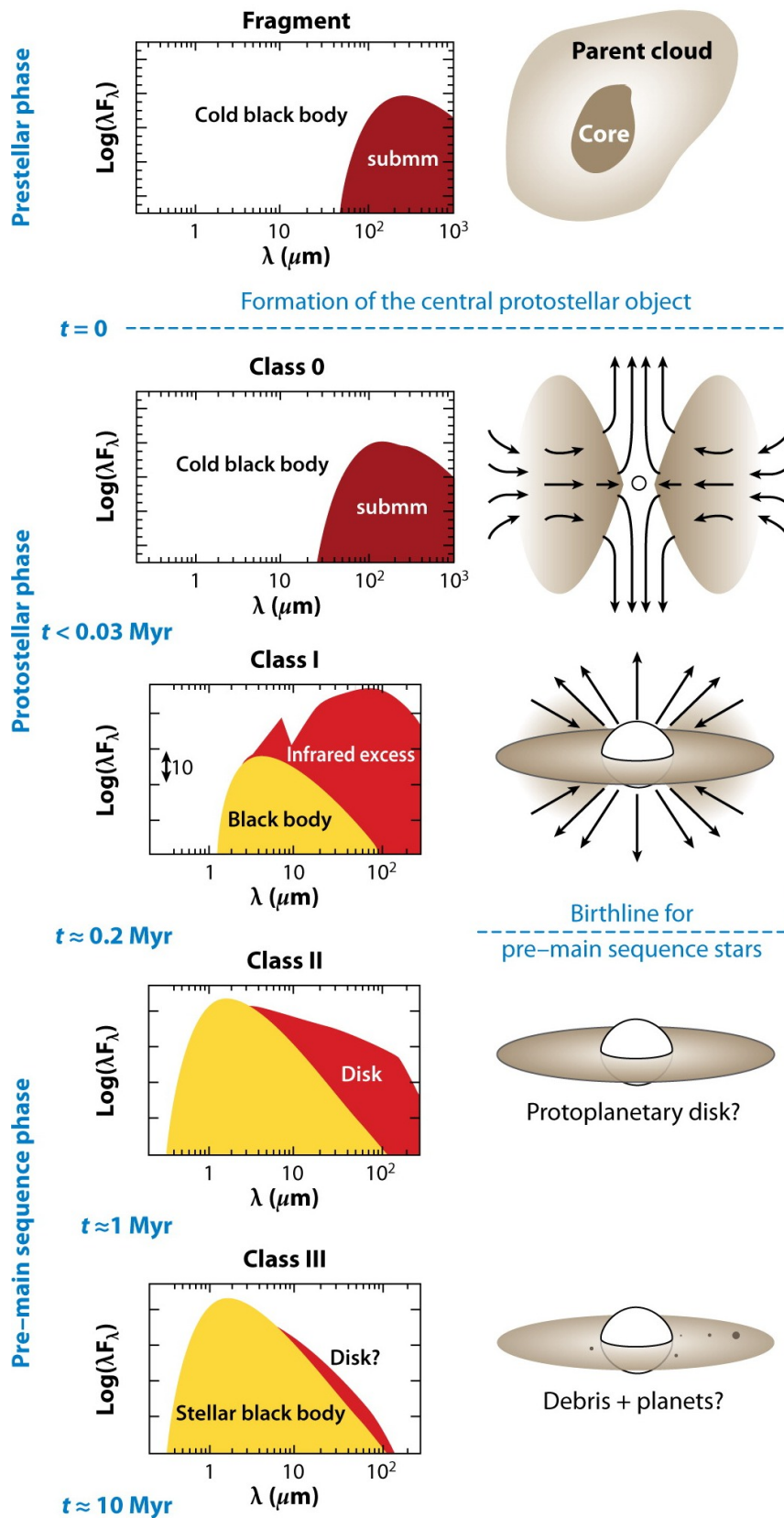
Figure 1.4: Schematic showing the classification scheme for the spectral energy distributions of young stellar objects as first proposed by Lada (1987) as well as the corresponding geometry. This figure is adapted from André (2002).

advent of more sensitive infrared detectors have made the transition between the different stages less clear. Thus, a bolometric luminosity or temperature cut-off also serve as a useful distinction between the different classes. In the PMS phase, young stars with masses below $\sim 2\ M_\odot$ are known as T Tauri stars, while the more massive ones in the range between $\sim 2-10\ M_\odot$ are known as Herbig Ae/Be stars (Herbig, 1960).

1.2   Theoretical developments in collapse studies

The earliest epochs of star formation involve several complex physical processes such as hydrodynamics, radiative transfer, phase transition (in particular hydrogen dissociation), magnetic fields, turbulence, and chemistry. Ever since the first numerical collapse study by Richard Larson (Larson, 1969), there have been a plethora of theoretical, numerical, and observational efforts to answer the most fundamental questions involved in the early processes of star formation. Among the various open questions that still remain unanswered are the values of initial magnetic field strength and orientation, angular momenta as well as turbulence within pre-stellar cores, which act as the birthplace for stars, discs, and planets (as highlighted in reviews by Larson, 2003; McKee & Ostriker, 2007; Inutsuka, 2012; Wurster & Li, 2018; Hull & Zhang, 2019; Teyssier & Commerçon, 2019; Pudritz & Ray, 2019). Various robust, detailed, and self-consistent numerical studies have been performed to better understand the isolated collapse scenario of low-mass star formation, using both grid-based (Bodenheimer & Sweigart, 1968; Winkler & Newman, 1980a,b; Stahler et al., 1980a,b, 1981; Masunaga et al., 1998; Masunaga & Inutsuka, 2000; Tomida et al., 2010b; Commerçon et al., 2011a; Vaytet et al., 2012; Tomida et al., 2013; Vaytet et al., 2013; Vaytet & Haugbølle, 2017; Bhandare et al., 2018; Vaytet et al., 2018, and references therein) and smoothed particle hydrodynamics (SPH) methods (Bate, 1998; Whitehouse & Bate, 2006; Stamatellos et al., 2007; Bate et al., 2014; Wurster et al., 2018b). The recent review by Teyssier & Commerçon (2019) details the most commonly used numerical techniques.

The numerical study by Larson (1969) indicated the presence of two quasi-hydrostatic cores formed during a non-homologous collapse of the molecular cloud core. They performed one-dimensional (1D) hydrodynamic simulations with a modified Eulerian scheme, using the diffusion approximation for radiative transfer. Stahler et al. (1980a,b) and Winkler & Newman (1980a,b) were among the first studies to confirm this non-homologous behaviour, which is now a well established picture of the formation of low-mass stars. The biggest challenge for long-term collapse simulations since these historical works, has been due to computational time limitations. Thus, the non-homologous collapse of isolated pre-stellar cores has been extensively investigated using simplifications, such as the 1D analysis.

The main focus of modern numerical collapse studies has been on the microphysics of these hydrostatic cores. The microphysics is described by including a realistic gas equation of state (to account for the effects of H_2 dissociation, ionisation of atomic hydrogen and helium, and molecular rotations and vibrations), dust and gas opacities, an accurate treatment of the radiation transport as well as different chemical networks. The two most commonly used gas equation of state (EOS) are the ones from D'Angelo & Bodenheimer (2013) and Saumon et al. (1995). A proper treatment of radiative transfer is required to accurately investigate the thermal evolution of the collapsing pre-stellar core. The importance of multi-group (i.e. frequency

dependent) radiative transfer schemes at later stages during the long-term evolution of the second core has been suggested in the studies by Vaytet et al. (2012, 2013).

The self-consistent 1D numerical study by Masunaga & Inutsuka (2000) used an accurate radiation transport scheme as well as a realistic gas EOS. This study has been the only one so far to evolve the second hydrostatic core until the end of the main accretion phase, using an accurate numerical treatment. Recent investigations by Vaytet & Haugbølle (2017) focused on understanding the dependence of hydro-static core properties on the initial pre-stellar core properties. They scanned a wide range of initial properties such as size, temperature, mass ($\leq 8\ M_\odot$), and uniform as well as Bonnor–Ebert (Ebert, 1955; Bonnor, 1956) density distributions. Using a similar numerical method, we extended this work to the intermediate- and high-mass regimes, covering cases of initial pre-stellar cores ranging in mass from 0.5 $M_\odot$ to 100 $M_\odot$ in Bhandare et al. (2018). The results highlight that the first hydrostatic cores are essentially non-existent in the high-mass regime due to high accretion rates, as detailed in Chapter 3 of this thesis. These 1D studies provide some useful constraints for observational efforts detecting first hydrostatic core candidates.

Although 1D studies still prove to be fruitful in terms of including more ac-curate physics and for scanning different initial properties, they miss important dynamical processes such as rotation, turbulence, and magnetic fields. Two- and three-dimensional simulations have indicated differences in the first core properties, for example, longer first core lifetimes result due to the rotational, turbulent (i.e. ki-netic), and magnetic support (Tomida et al. 2013 and Chapter 5 of this thesis). The early stages of star formation including an initial cloud rotation were first investigated by Bate (1998), using three-dimensional (3D) hydrodynamic simulations with SPH methods. In order to reduce the CPU time, a piecewise polytropic EOS was used instead of accounting for the radiative transfer. The first set of SPH simulations by Whitehouse & Bate (2006), Stamatellos et al. (2007), and Bate (2010) captured the full process of molecular cloud collapse through the first and second core stages until formation of the stellar core, using a 3D radiation hydrodynamic (RHD) treatment. The radiative transfer was accounted for by using either a flux limited diffusion (FLD) approximation (Whitehouse & Bate, 2006; Bate, 2010) or a local radiative cooling approximation (Stamatellos et al., 2007). There have been no grid-based 3D RHD calculations (without magnetic fields) of the second core formation so far. Some purely hydrodynamical calculations suggested that large discs ($\gtrsim 30$ au) can form due to angular momentum conservation as early as the first core stage and definitely by the main accretion phase (Bate, 1998, 2010; Machida et al., 2010; Tomida, 2014; Wurster et al., 2018a).

Multi-dimensional numerical efforts, which account for the presence of rotation and magnetic fields via radiation magneto-hydrodynamic (RMHD) simulations, have proven to be valuable to trace the formation and evolution of protostellar discs with sizes that are comparable to observations. A proper treatment of magnetic fields entails several challenges, which may prevent or delay the formation of a disc due to the efficient transport of angular momentum, known as the magnetic braking catastrophe (Allen et al., 2003; Galli et al., 2006). Earlier 3D disc formation simulations treated the magnetic fields in the ideal MHD limit, i.e. coupled with the bulk neutral gas that is sufficiently ionised (Tomida, 2014; Tomida et al., 2015; Tsukamoto et al., 2015; Wurster et al., 2018b; Vaytet et al., 2018). In these investigations, for realistic values of the magnetic field strength the discs either do not form at all or form at a much later stage after the formation of the second hydrostatic core. In the former case, an initial pseudo-disc never evolves into a Keplerian disc, at least

until the formation stage of the second hydrostatic core (Bate et al., 2014). Two-dimensional (2D) axisymmetric, nested grid calculations including ideal MHD effects were performed by Tomisaka (2002), using cylindrical coordinates. Although, no centrifugally-supported discs were reported, this work paved the way to examine the launching of a magnetically driven molecular bipolar outflow from the first core and a collimated jet from the second core.

Expanding these studies to account for the effects of interactions between charged and neutral species (i.e. non-ideal dissipative, diffusive, and dispersive terms) helped overcome the magnetic braking catastrophe (see recent review by Wurster & Li, 2018). The first 3D MHD nested grid simulations using Cartesian coordinates were performed by Machida et al. (2006a). Within 10 years after second core formation, they find an extremely small disc with a size of 0.09 au. They account for non-ideal (including Ohmic resistivity) MHD effects and use a polytropic gas EOS, which fails to account for the cooling due to adiabatic expansion. Thus, Banerjee & Pudritz (2006) performed 3D MHD adaptive mesh refinement simulations by incorporating cooling by molecular line emission. They were able to reproduce earlier results from Tomisaka (2002) and Machida et al. (2006a), while capturing the shock physics more accurately. This was followed by several 3D studies dedicated to the first hydrostatic core formation, which used a proper treatment of the cooling by using accurate radiative transfer schemes (Commerçon et al., 2010; Tomida et al., 2010b; Lee & Hennebelle, 2018). These radiative transfer models also allowed to accurately capture the fragmentation processes within young discs formed during this early collapse phase. Recently, the first two thousand years of pre- to protostellar evolution were traced using 3D resistive MHD simulations with a barotropic EOS (Machida & Basu, 2019). They find a disc of size $\sim 2 - 4$ au. In their resistive MHD calculations, Machida et al. (2011) and Wurster et al. (2016) find ~ 10 au discs during the early accretion phase. Considering only the effects of ambipolar diffusion, Mellon & Li (2009) performed 2D axisymmetric MHD simulations, using an isothermal gas EOS. They concluded that ambipolar diffusion alone is not sufficient to form discs during the early stages.

Using grid-based (Tomida et al., 2013, 2015; Vaytet et al., 2018) and SPH (Bate et al., 2014) methods, 3D MHD collapse simulations captured the effects due to self-gravity, dissociation and ionisation, radiative transfer (FLD approximation) as well as the Ohmic resistivity and ambipolar diffusion. All these studies find discs smaller than 5 au during the initial formation stages. Long-term simulations using sink particles found that these discs evolve into much bigger sizes (≥ 100 au) by Class 0/I phase (e.g. Tomida et al., 2017). The latest numerical development in 3D MHD collapse studies is the treatment of all three non-ideal terms, namely, Ohmic resistivity, ambipolar diffusion, and the Hall term, in addition to a proper treatment of the radiative transfer and a realistic gas EOS. These detailed studies are performed by using SPH methods (Tsukamoto et al., 2017; Wurster et al., 2018a,b,c). In the studies by Tsukamoto et al. (2017) and Wurster et al. (2018a), a disc (~ 25 au) is only formed for anti-aligned non-ideal MHD models. The cosmic ray ionisation rate in these models assumes the canonical value of 10^{-17} s^{-1} for the Milky Way interstellar medium (Spitzer & Tomasko, 1968; Umebayashi & Nakano, 1981). Wurster et al. (2018c) found that disc formation can be suppressed for high values of the cosmic ray ionisation rate. So far, there have been contradicting results in terms of disc formation for investigations of the effects of non-axisymmetric perturbations such as turbulence and misalignment of the magnetic fields with the rotation axis. This has resulted in uncertain conclusions about the contribution from these effects on disc formation.

Depending on the initial conditions and the included physics, some grid-based

Table 1.1: List[5] of 3D and 2D numerical collapse studies of star and disc formation.

Reference	Numerical Method	EOS	Radiative transfer	Magnetic fields	Non-ideal MHD		
					Ohmic	Ambipolar	Hall
3D							
Bate (1998)	SPH	Barotropic	No	No	No	No	No
Whitehouse & Bate (2006)	SPH	H_2+H+He	FLD	No	No	No	No
Machida et al. (2006b, 2007a, 2008)	Nested grid	Barotropic	No	Yes	Yes	No	No
Stamatellos et al. (2007)	SPH	H_2+H+He	Cooling	No	No	No	No
Saigo et al. (2008)	Nested grid	Barotropic	No	No	No	No	No
Bate (2010, 2011)	SPH	H_2+H+He	FLD	No	No	No	No
Commerçon et al. (2010)	AMR	H_2+H+He	FLD	Yes	No	No	No
Tomida et al. (2010b)	Nested grid	H_2+H+He	FLD	Yes	No	No	No
Machida & Matsumoto (2011); Machida et al. (2011)	Nested grid	Barotropic	No	Yes	Yes	No	No
Joos et al. (2012)	AMR	Barotropic	No	Yes (misaligned)	No	No	No
Tomida et al. (2013)	Nested grid	H_2+H+He	FLD	Yes	Yes	No	No
Machida et al. (2014)	Nested grid	Barotropic	No	Yes	Yes	No	No
Bate et al. (2014)	SPH	H_2+H+He	FLD	Yes	Yes	No	No
Li et al. (2014)	Static grid	Isothermal	No	Yes	No	No	No
Tomida et al. (2015)	Nested grid	H_2+H+He	FLD	Yes	Yes	Yes	No
Tsukamoto et al. (2015)	SPH	H_2+H+He	FLD	Yes	Yes	Yes	No
Wurster et al. (2016)	SPH	H_2+H+He	No	Yes	Yes	Yes	Yes
Masson et al. (2016)	AMR	Barotropic	No	Yes (misaligned)	Yes	Yes	No
Tsukamoto et al. (2017)	SPH	H_2+H+He	FLD	Yes (misaligned)	Yes	Yes	Yes
Tomida et al. (2017)	Nested grid	Barotropic	No	Yes	Yes	No	No
Tsukamoto et al. (2018)	SPH	H_2+H+He	FLD	Yes (misaligned)	Yes	Yes	No
Wurster et al. (2018b,c,a)	SPH	H_2+H+He	FLD	Yes (anti-aligned)	Yes	Yes	Yes
Vaytet et al. (2018)	AMR	H_2+H+He	FLD	Yes	Yes	Yes	No
Machida & Basu (2019)	Nested grid	Barotropic	No	Yes	Yes	No	No
Wurster & Bate (2019)	SPH	H_2+H+He	FLD	Yes	Yes	Yes	Yes
Hirano & Machida (2019)	Nested grid	Barotropic	No	Yes (misaligned)	Yes	No	No
Lam et al. (2019)	Zoom-in grid	Isothermal	No	Yes	No	Yes	No
2D							
Boss (1984)	Static grid	H_2+H+He	Eddington	No	No	No	No
Tscharnuter (1987); Tscharnuter et al. (2009)	Self-adaptive grid	H_2+H+He	No	No	No	No	No
Tomisaka (1998, 2000, 2002)	Nested grid	Barotropic	No	Yes	No	No	No
Allen et al. (2003)	Static grid	Isothermal	No	Yes	No	No	No
Tassis & Mouschovias (2005, 2007a,b)	Adaptive + Static grid	Isothermal + Adiabatic	No	Yes	Yes	Yes	No
Saigo & Tomisaka (2006)	Nested grid	Barotropic	No	No	No	No	No
Mellon & Li (2009)	Static grid	Isothermal	No	Yes	No	Yes	No
Kunz & Mouschovias (2010)	Static grid	Adiabatic	FLD	Yes	Yes	Yes	No
Dapp & Basu (2010)	Adaptive grid	Barotropic	No	Yes	Yes	No	No
Krasnopolsky et al. (2011)	Static grid	Isothermal	No	Yes	No	No	Yes
Li et al. (2011)	Static grid	Isothermal	No	Yes	Yes	Yes	Yes
Schönke & Tscharnuter (2011)	Static grid	H_2+H+He	FLD	No	No	No	No
Dapp et al. (2012)	Adaptive grid	Barotropic	No	Yes	Yes	Yes	No
This work (Chapter 5)	**Static grid**	**H_2+H+He**	**FLD**	**Yes**	**Yes**	**No**	**No**

and SPH numerical studies have found that the first hydrostatic core evolves into a disc even before the onset of the second core formation (e.g. Bate, 1998; Saigo & Tomisaka, 2006; Machida et al., 2006b, 2007a, 2008; Saigo et al., 2008; Commerçon et al., 2010; Machida et al., 2010; Tomida et al., 2010b; Bate, 2010, 2011; Machida & Matsumoto, 2011; Joos et al., 2012; Bate et al., 2014; Machida et al., 2014; Tomida et al., 2015; Masson et al., 2016; Tsukamoto et al., 2017, 2018; Wurster et al., 2018a,c). In contrast, other studies have found that the disc is formed only during or after the formation of the second hydrostatic core (e.g. Dapp & Basu, 2010; Machida et al., 2011; Dapp et al., 2012; Tomida et al., 2013; Machida et al., 2014; Tomida et al., 2015; Tsukamoto et al., 2015; Wurster et al., 2016; Tomida et al., 2017; Wurster et al., 2018b; Vaytet et al., 2018; Lam et al., 2019). Table 1.1 lists some of the grid-based and SPH simulations in 2D and 3D that investigate the formation of the first core, the second core, and its surrounding disc as well as outflows and jets launched from these two hydrostatic cores.

Significant progress has been made in numerical studies of star and disc formation over the past few years. However, the properties of the hydrostatic cores and discs are considerably affected by the initial conditions, numerics, and the included physics. In this thesis, we perform R(M)HD collapse simulations, including accurate microphysics. Using 1D and 2D grids gives us the advantage of scanning a wider parameter space for the initial properties of the pre-stellar cores. This enables us to derive better constraints for the properties of the hydrostatic cores and young discs.

The next steps in numerical investigations of low-mass star and disc formation will be to replace the second core with a sink particle or a sink cell using accurate sub-grid models (a detailed description can be found in Teyssier & Commerçon, 2019). This will serve as a possible solution for the long-term evolution of the system, which

---

[5]This list is by no means exhaustive.

is currently hindered due to computational time restrictions. Future 3D calculations tracing the collapse of pre-stellar cores to protostellar cores and discs, will include effects due to chemistry and dust grain dynamics. This will play an important role in determining the cooling efficiency and opacities and will be crucial for resistivity calculations. Additionally, effects due to turbulence and misalignment will provide further insights to better understand the physical processes involved in low-mass star and disc formation.

1.3   Observational motivation

In recent years, infrared data from the *Spitzer* Space Telescope, Wide-field Infrared Survey Explorer (WISE), and the *Herschel* Space Observatory as well as (sub-)millimetre data from the Berkeley-Illinois-Maryland Association (BIMA) millimetre array, the Combined Array for Research in Millimetre-wave Astronomy (CARMA), the Sub-Millimetre Array (SMA), and the Atacama Large Millimetre/submillimetre Array (ALMA) have revolutionised our understanding of the physical processes involved in star, disc, and planet formation (see the recent review by Hull & Zhang, 2019, and references therein).

On sub-parsec scales, observations of the Bok globule Barnard 68 (Alves et al., 2001) have demonstrated that the density profile resembles a critical Bonnor–Ebert sphere (Ebert, 1955; Bonnor, 1956). On the other hand, the mapping of pre-stellar cores, for example by Kirk et al. (2005), show flat central density profiles that steepen towards the edge, similar to super-critical Bonnor–Ebert spheres. Many observational studies find the temperature of pre-stellar cores and Bok globules to be in the range of 10 – 20 K (e.g. Kirk et al., 2005; Launhardt et al., 2013). This has been a strong motivation to use a Bonnor–Ebert sphere like density profile and temperature of ~ 10 K as initial conditions in many numerical collapse simulations, including the ones presented in this thesis.

Dust polarization observations have pointed out the existence of ordered magnetic fields on cloud scales (e.g. Planck Collaboration et al., 2015, 2016; Soler et al., 2016;
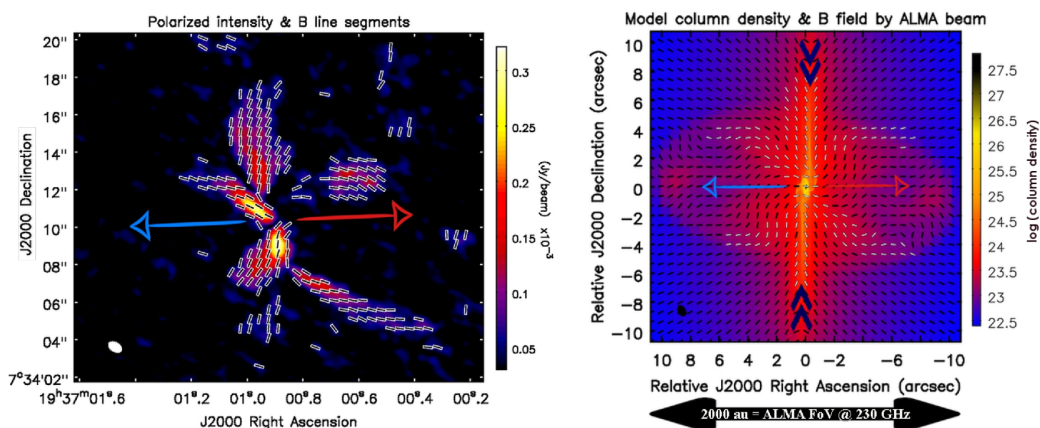
Figure 1.5: Dust polarization observations indicating the presence of magnetic fields (left) and the edge-on view of results from a numerical collapse model showing the column density (right) of the Class 0 protostar B335. The superimposed lines show the orientation of the field lines (i.e. the polarization angle is rotated by 90°). The thick blue arrows in the right panel indicate the infalling material. The red/blue arrows mark the direction of the outflows. Figure is taken from Maury et al. (2018).

Soler, 2019) as well as on individual pre-stellar core and envelope scales (e.g. Pattle et al., 2017; Maury et al., 2018; Santos et al., 2019). As an example, Fig. 1.5 shows the observational evidence of magnetic fields traced using dust polarization for the Class 0 protostar B335 (Maury et al., 2018). The pinching effect of the magnetic fields at the equator (i.e. the hourglass shape) provides a direct evidence of the magnetic field lines being dragged towards the centre by the infalling envelope material (Girart et al., 2006; Stephens et al., 2013; Maury et al., 2018; Sadavoy et al., 2019). For the case of B335, the presence of a small (< 10 au) disc is suggested due to indications of a decrease in angular momentum in the central regions, with no clear evidence of rotation at the scale of tens of au (Yen et al., 2015; Maury et al., 2018; Bjerkeli et al., 2019).

Due to the optically thick regime, obtaining reliable observational constraints during the earliest phases of star formation still remains quite challenging (Nielbock et al., 2012; Launhardt et al., 2013; Dunham et al., 2014). It is important to note that so far the presence of the first hydrostatic Larson core has only been confirmed by theoretical and numerical studies (including those discussed in this thesis). Observational studies only hint towards some candidate objects (e.g. Chen et al., 2010; Dunham et al., 2011; Pineda et al., 2011; Pezzuto et al., 2012; Gerin et al., 2015; Maureira et al., 2017; Karnath et al., 2020). Some of the sources in these studies also identify low-velocity (< 10 km s^{-1}) molecular outflows that indicate the presence of the first cores. Observations suggest that the feedback from these outflows can change the morphology of magnetic fields (Hull et al., 2014, 2017a,b). Thus, current numerical studies seek to better understand the dynamical effects of a magnetically-regulated scenario of collapsing pre-stellar cores and its implications on the properties of the hydrostatic cores and outflows as well as on the formation of discs (also investigated in Chapter 5).

The capabilities of instruments in the ALMA-era have enabled characterisation of young discs as early as in the Class 0 stage of low-mass YSOs. These observations indicate that the process of disc formation should begin in the early stages of star formation and definitely by the Class 0 phase (e.g. Tobin et al., 2012; Gerin et al., 2017; Andersen et al., 2019). Thus, the observations of young star-disc systems provide a strong motivation to quantitatively infer the onset of disc formation and evolution.

1.4 Structure of the thesis

In this thesis, we model the very early stages of star and disc formation using state-of-the-art, self-consistent, and robust numerical methods. We follow the evolution of collapsing molecular cloud cores (i.e. pre-stellar cores), which transition through the formation stages of the first and second hydrostatic cores. Additionally, we investigate the onset of disc formation around the second core as well as the launching of magnetically driven outflows from the two hydrostatic cores.

We perform several 1D and 2D R(M)HD collapse simulations using the *PLUTO* code. We use a grey FLD approximation for the radiative transfer to accurately model the thermal evolution of the collapsing pre-stellar core. We employ a realistic gas EOS that includes density- and temperature-dependent thermodynamic quantities (heat capacity, mean molecular weight, etc.) to account for the effects such as H_2 dissociation, ionisation of atomic hydrogen and helium, and molecular vibrations and rotations.

In the following chapter, we give an overview of the MHD equations and the microphysics in terms of the radiative transfer scheme, dust and gas opacity tables as

well as the gas EOS relevant for our studies. We also provide details of our numerical method, including the initial setup and computational grid. In Chapter 3, we showcase results from our spherically symmetric collapse studies that include effects of self-gravity and radiation transport. We utilise the advantage of our computationally less expensive 1D setup to scan a wide range of initial pre-stellar core properties. Our parameter space includes initial pre-stellar core masses ranging across low-, intermediate-, and high-mass regimes from 0.5 $M_\odot$ until 100 $M_\odot$, a constant initial temperature between 5 K to 100 K, and a fixed outer core radius of 3000 au and 5000 au. We follow the evolution of the pre-stellar core until the onset of the second core formation. In this chapter, we highlight the dependence of the first core properties on the initial properties of the pre-stellar core.

In the first part of Chapter 4, we exhibit findings from our 1D models that were evolved for a longer time than the ones presented in the previous chapter. Here, we focus on the properties of the second hydrostatic core (i.e. the forming protostar). Going a step beyond our 1D studies, we present the outcome from our 2D, axial and midplane symmetric, RHD simulations. We describe the physics within the second hydrostatic core, for the cases of 1 $M_\odot$, 2 $M_\odot$, 5 $M_\odot$, and 10 $M_\odot$ non-rotating pre-stellar cores. We show the presence of convection being driven in the outer layers of the second core formed from a collapsing 1 $M_\odot$ pre-stellar core.

Using 2D RMHD simulations, we analyse the effects of magnetic fields (including Ohmic resistivity) on the collapse of rotating pre-stellar cores in Chapter 5. We present the dependence of outflow properties and disc formation on the initial magnetic field strength, solid-body rotation rate, and pre-stellar core mass. In some of our models, a disc starts forming at sub-au scales, after the onset of the second core formation. The second core and its surrounding disc evolve simultaneously. We carefully list the caveats of our numerical methods in all the corresponding chapters. The results presented in this thesis are summarised in Chapter 6. Lastly, future ideas for follow-up star and disc formation research are outlined in Chapter 7.

Numerical Methods

In this thesis, we investigate different evolutionary stages during the formation of protostars and their surrounding discs via numerical simulations, using the *PLUTO* code (Mignone et al., 2007) as a tool. Therefore, I first describe the fundamental equations of (magneto-)hydrodynamics, followed by a discussion of the microphysics and numerical setup used in our simulations.

This chapter is organised as follows. Sections 2.1 and 2.2 provide a brief overview of the basic equations of RHD and MHD. Section 2.3 details the gas EOS and Sect. 2.4 describes the tabulated dust and gas opacities used in our simulations. The numerics and initial setup for the 1D and 2D simulations, including the grid setup and boundary conditions are stated in Sect. 2.5. Lastly, the conditions that define the computational time of our simulations are discussed in Sect. 2.6.

2.1 Equations of radiation hydrodynamics

In the simulations presented in this thesis, gas thermodynamics is considered under the approximation of local thermodynamic equilibrium (LTE) and a two-temperature (2T) approach, for the gas and radiation. The basic hydrodynamic equations that account for the conservation of mass, momentum, and energy, i.e. the continuity, Euler's, and energy equation, respectively, are given as

$$\partial_t \rho + \boldsymbol{\nabla} \cdot (\rho \mathbf{u}) = 0, \tag{2.1}$$

$$\partial_t (\rho \mathbf{u}) + \boldsymbol{\nabla} \cdot (\rho \mathbf{u} \otimes \mathbf{u} + P \mathbb{I}) = \rho \mathbf{a}, \tag{2.2}$$

$$\partial_t E + \boldsymbol{\nabla} \cdot ((E + P)\mathbf{u}) = \rho \mathbf{u} \cdot \mathbf{a}, \tag{2.3}$$

where ρ is the density, $\mathbf{u}$ is the dynamical velocity, and P is the thermal pressure. The importance of the pressure term in the momentum equation can be characterised by the Mach number M defined as the ratio of the flow velocity to the sound speed ($M = v_{\text{flow}}/c_{\text{s}}$). This pressure term is most effective in determining the behaviour of the fluid in sub-sonic regions where $M \ll 1$. The total energy E is the sum of internal and kinetic energies given as $E = E_{\text{int}} + E_{\text{kin}}$. The kinetic energy density $E_{\text{kin}} = \frac{1}{2}\rho u^2$, whereas the internal energy density is calculated by taking into account the contributions from various hydrogen and helium species. This is described in Sect. 2.3.

The source term **a** denotes the acceleration due to self-gravity given by

$$\mathbf{a} = -\boldsymbol{\nabla}\boldsymbol{\Phi}_{\mathrm{sg}}, \tag{2.4}$$

where $\boldsymbol{\Phi}_{\mathrm{sg}}$ is the gravitational potential determined using Poisson's equation, expressed as

$$\boldsymbol{\nabla}^2\boldsymbol{\Phi}_{\mathrm{sg}} = 4\pi G\rho, \tag{2.5}$$

where G is the gravitational constant. Apart from the force terms due to the pressure gradient and gravity, additional terms need to be accounted for when describing the effects of attraction and repulsion between neighbouring molecules in a viscous fluid. The force due to viscosity can be added as an extra source term to the momentum and energy equations as described by the Navier-Stokes equations. This viscous source term is given by $\boldsymbol{\nabla} \cdot \mathbf{T}$, where $\mathbf{T}$ is the viscous stress tensor.

Angular momentum transport during the collapse and protostellar disc formation can be achieved via mechanisms such as gravitational torques exerted from the spiral arms or bar-like structures, magneto-rotational instability, hydrodynamically driven turbulence, outflows, disc winds, and jets. In order to mimic these effects of angular momentum transport in our 2D simulations that include an initial cloud core rotation, we consider physical shear viscosity of the protostellar disc medium as detailed in Kuiper et al. (2010). The shear viscosity is described using the so-called α-parameterisation from Shakura & Sunyaev (1973) and is given as

$$\nu = \alpha \, c_s \, H \, \rho \approx \alpha \, \Omega_{\mathrm{K}}(r) \, R^2 \left(\frac{H}{R}\right)^2 \rho, \tag{2.6}$$

where H is the local pressure scale height. The local sound speed c_s is given by $c_s \approx H \, \Omega_{\mathrm{K}}(r)$, where the Keplerian angular velocity is $\Omega_{\mathrm{K}}(r) \approx \sqrt{GM(r)/r^3}$ with $M(r)$ being the mass inside radius r. The cylindrical radius R is defined as $R = r \sin(\theta)$. The dimensionless parameters $(H/R) = 0.05$ and $\alpha = 1.0$ are fixed in space and time for all the simulations presented in Chapter 5. This shear viscosity is equivalent to the β-viscosity prescription for self-gravitating discs by Duschl et al. (2000) with a β-parameter of $\beta = 2.5 \times 10^{-3}$. This temperature independent β-viscosity prescription is also used in the low-mass collapse studies by Schönke & Tscharnuter (2011) as well as in the high-mass collapse studies by Kuiper et al. (2010), Kuiper & Yorke (2013), Kuiper et al. (2015), Kuiper et al. (2016), and Kuiper & Hosokawa (2018).

The time-dependent radiation transport equation, in case of locally isotropic radiation, when neglecting small contributions due to scattering can be written as

$$\partial_t E_{\mathrm{rad}} + \boldsymbol{\nabla} \cdot \boldsymbol{F}_{\mathrm{rad}} = c \, \chi_{\mathrm{abs}} \, (B_{\mathrm{rad}} - E_{\mathrm{rad}}), \tag{2.7}$$

where E_{rad} is the radiation energy density, $\boldsymbol{F}_{\mathrm{rad}}$ is the radiation energy flux, c is the speed of light, χ_{abs} is the coefficient of absorption, and B_{rad} is the integral of the black-body Planck spectrum. The flux of radiation energy density $\boldsymbol{F}_{\mathrm{rad}}$ in the FLD approximation is determined as

$$\boldsymbol{F}_{\mathrm{rad}} = -\,D_{\mathrm{rad}} \, \boldsymbol{\nabla} E_{\mathrm{rad}} = -\,\frac{\lambda c}{\kappa_{\mathrm{R}}\rho} \, \boldsymbol{\nabla} E_{\mathrm{rad}}, \tag{2.8}$$

where D_{rad} is the radiative diffusion coefficient, κ_{R} is the Rosseland mean opacity, and the flux limiter λ is chosen following Levermore & Pomraning (1981). The flux limiter recovers the limiting cases of diffusion and free streaming, respectively.

Using Eq. (2.8) in the conservation Eq. (2.7) gives the time evolution of radiation energy density as

$$\partial_t E_{\text{rad}} - \boldsymbol{\nabla} \cdot (D_{\text{rad}} \, \boldsymbol{\nabla} E_{\text{rad}}) = c \, \chi_{\text{abs}} \, (B_{\text{rad}} - E_{\text{rad}}). \tag{2.9}$$

The two unknowns in Eq. (2.9), namely the radiation energy density E_{rad} and the local temperature of the medium $B_{\text{rad}} = aT^4$, where a is the radiation constant, are coupled to each other via heating and cooling processes. The time evolution of the local internal energy is given by

$$\partial_t E_{\text{int}} = - c \, \chi_{\text{abs}} \, (B_{\text{rad}} - E_{\text{rad}}). \tag{2.10}$$

For the 2T model, the coupled Eqns. (2.9) and (2.10) can be reduced to a single equation using a linearisation approach in which the radiation and medium temperatures evolve as two different quantities (Commerçon et al., 2011b). Additionally, the specific heat capacity is taken to be constant over the course of a single main iteration.

2.2 Equations of magneto-hydrodynamics

In the project described in Chapter 5, we simulate the collapse of a rotating magnetized molecular cloud core to investigate the formation of protostellar discs and the launching of magnetically driven outflows. Hence, this section provides extensions to the hydrodynamic equations detailed in Sect. 2.1.

The equation for the conservation of momentum including the magnetic forces can be expressed as

$$\partial_t(\rho \mathbf{u}) + \boldsymbol{\nabla} \cdot \left(\rho \mathbf{u} \otimes \mathbf{u} + P_{\text{tot}} \mathbb{I} - \frac{1}{4\pi} \, \mathbf{B} \otimes \mathbf{B} \right) = -(\boldsymbol{\nabla} \cdot \mathbf{B}) \, \mathbf{B} + \rho \mathbf{a}, \tag{2.11}$$

where $\mathbf{B}$ is the magnetic field vector and the total pressure P_{tot} is given as the sum of thermal pressure and magnetic pressure

$$P_{\text{tot}} = P + \frac{1}{8\pi} B^2. \tag{2.12}$$

The importance of the magnetic force terms can be characterised by the Alfvén Mach number M_{A}, such that the magnetic force terms dominate in flows where $M_{\text{A}} \ll 1$, i.e. sub-Alfvénic regions. The Alfvén Mach number M_{A} is defined as the ratio of flow velocity to Alfvén velocity ($M_{\text{A}} = v_{\text{flow}}/v_{\text{A}}$), where $v_{\text{A}} = B/\sqrt{4\pi\rho}$.

The total fluid energy conservation equation is given by

$$\partial_t E_{\text{tot}} + \boldsymbol{\nabla} \cdot \left((E_{\text{tot}} + P_{\text{tot}})\mathbf{u} - \frac{1}{4\pi} \, \mathbf{B}(\mathbf{B} \cdot \mathbf{u}) \right) = -(\boldsymbol{\nabla} \cdot \mathbf{B}) \, \mathbf{B} \cdot \mathbf{u} + \rho \mathbf{u} \cdot \mathbf{a}. \tag{2.13}$$

In the above equation, the total energy E_{tot} is defined as the sum of kinetic energy, internal energy, and magnetic energy

$$E_{\text{tot}} = \frac{1}{2}\rho u^2 + e + \frac{1}{8\pi} B^2. \tag{2.14}$$

All the above equations are expressed in cgs units and hence include the 4π term.

In the ideal MHD approximation the gas is assumed to be sufficiently ionised, such that the bulk neutral gas and magnetic field are well coupled. In the ideal limit,
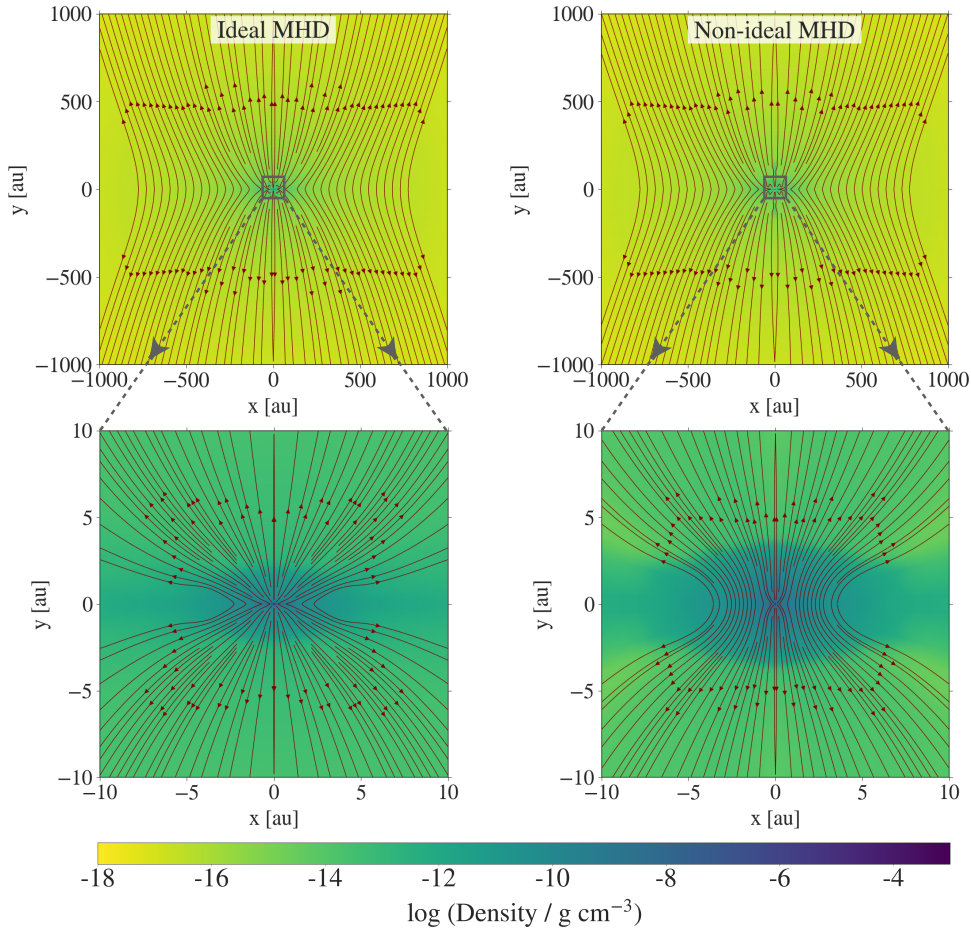
Figure 2.1: Two-dimensional density snapshots at large and small scales showing the hourglass shape of magnetic field lines in an ideal and non-ideal collapse simulation. The poloidal field lines in red indicate a stronger pinching effect in the ideal MHD simulation run compared to the non-ideal MHD simulation run. Shown here is the final simulation snapshot for the collapse of a 1 $M_\odot$ cloud core with an initial temperature of 10 K and outer radius of 3000 au. Both the ideal and non-ideal simulations use an initial mass-to-magnetic flux ratio of $\mu_0 = 5$, which corresponds to the highest magnetic field strength prescribed in our simulations. The initial rotation rate used here is $\Omega = 2.099 \times 10^{-13}$ rad s^{-1}.

the induction equation is given by

$$\partial_t \mathbf{B} - \boldsymbol{\nabla} \times (\mathbf{u} \times \mathbf{B}) = -(\boldsymbol{\nabla} \cdot \mathbf{B})\,\mathbf{u}. \qquad (2.15)$$

As the cloud core collapses in idealised numerical simulations, the magnetic field is dragged inwards with the fluid. This leads to the formation of the characteristic hourglass shape of the magnetic field lines as shown in Fig. 2.1. The extent of the pinching effect is dependent on the strength of the magnetic field. In our simulations, we prescribe the magnetic field strength characterised in terms of the mass-to-magnetic flux ratio μ_0 as detailed in Sect. 5.1 (see Eq. 5.2).

Protostellar discs can form due to the conservation of angular momentum during the collapse of molecular cloud cores. It is hence important to note that magnetic fields play a crucial role in transporting angular momentum outwards in collapsing molecular cloud cores (Mestel & Spitzer, 1956; Mouschovias & Paleologou, 1979,

1980; Basu & Mouschovias, 1994, 1995a,b; Mellon & Li, 2008). In the ideal MHD limit, this effect can be extremely efficient and may prevent or delay the formation of discs during the early collapse phases, as first shown in studies by Tomisaka (2002), Allen et al. (2003), and Galli et al. (2006). It is hence necessary to adopt methods that help overcome this "magnetic braking catastrophe" at the early stages when the magnetic braking is quite efficient. Additionally, observations (Bergin & Tafalla, 2007) as well as numerical models (e.g. Nakano et al., 2002) have indicated that star-forming molecular cloud cores have low ionisation levels, that means the magnetic field is not perfectly coupled to the bulk neutral material. In recent years, the detailed treatment of non-ideal dissipative, diffusive, and dispersive terms, which account for the interactions between charged and neutral species, has been tested to enable disc formation during the early stages of star formation (a list of these MHD collapse studies can be found in Table 1.1).

To account for different charged species, the induction equation including the three terms for Ohmic resistivity, ambipolar diffusion, and the Hall effect is given by

$$
\begin{aligned}
\partial_t \mathbf{B} &= (\partial_t \mathbf{B})_{\text{ideal}} + (\partial_t \mathbf{B})_{\text{non-ideal}} \\
&= \boldsymbol{\nabla} \times (\mathbf{u} \times \mathbf{B}) \\
&\quad - \boldsymbol{\nabla} \times \left\{ \eta_{\text{O}} \left(\boldsymbol{\nabla} \times \mathbf{B} \right) + \frac{\eta_{\text{H}}}{\|\mathbf{B}\|} (\boldsymbol{\nabla} \times \mathbf{B}) \times \mathbf{B} - \frac{\eta_{\text{AD}}}{\|\mathbf{B}\|^2} \left[(\boldsymbol{\nabla} \times \mathbf{B}) \times \mathbf{B} \right] \times \mathbf{B} \right\},
\end{aligned}
\tag{2.16}
$$

where the notation $\|\mathbf{B}\|$ is the norm of the magnetic field vector $\mathbf{B}$. The η coefficients represent all the microphysics involved in three different regimes of interaction between neutrals (i.e. molecule, atoms, and dust grains) and various charged species (i.e. electrons, atomic and molecular ions as well as charged grains):

- Dissipative term:

  1. Ohmic resistivity η_{O}: This term describes the collisions between electrons and neutrals. In this regime, the electrons, ions, and charged grains are completely decoupled from the magnetic field. Ohmic dissipation is most effective in the highest density regions, for example inner regions of the disc midplane.

- Diffusive term:

  2. Ambipolar diffusion η_{AD}: This term describes the collisions between ions and neutral species. In this regime massive charged particles (i.e. ions and charged grains) and the electrons are coupled and frozen into the magnetic field, which drifts through the neutrals. Ambipolar diffusion is most efficient in the low density regions, for example molecular cloud cores, the upper and outer regions of the disc, and throughout the surrounding envelope.

- Dispersive term:

  3. Hall effect η_{H}: This term accounts for different drift velocities between positively and negatively charged species. The massive charged particles (i.e. ions and charged grains) are decoupled from the magnetic field. On the other hand, the electrons are coupled and frozen into the magnetic field, which drifts through the ions and charged grains. Similar to ambipolar diffusion, the Hall effect dominates in the low and intermediate density regions.

The total energy conservation equation needs to further be modified to account for the heating resulting from the diffusive terms and is given by

$$\partial_t E_{\text{tot}} + \boldsymbol{\nabla} \cdot \left((E_{\text{tot}} + P_{\text{tot}})\mathbf{u} - \frac{1}{4\pi}\,\mathbf{B}(\mathbf{B}\cdot\mathbf{u}) \right) = \rho\mathbf{u}\cdot\mathbf{a} + \eta_{\text{O}}\,\|\mathbf{J}\|^2 + \eta_{\text{AD}}\frac{\|\mathbf{J}\times\mathbf{B}\|^2}{\|\mathbf{B}\|^2},$$

(2.17)

where $\mathbf{J} = \nabla \times \mathbf{B}$ is the current.

As described above, since the neutral gas can drift across the magnetic field lines due to their imperfect coupling, the hour-glass shaped pinching effect is less prominent in the innermost regions when accounting for the non-ideal MHD effects (see Fig. 2.1). This leads to a weaker magnetic field strength in the central regions, which reduces the effect of magnetic braking and thus increases the possibility of disc formation during the early stages of star formation. In the studies presented in this thesis, we focus solely on the effect of the Ohmic resistivity on disc formation and the launching of outflows from the hydrostatic cores. Further details of the numerical methods and the influence of different non-ideal MHD terms in the context of star and disc formation can be found in the recent reviews by Wurster & Li (2018) and Teyssier & Commerçon (2019).

2.3   Gas equation of state

We use the gas EOS of D'Angelo & Bodenheimer (2013) to account for effects such as H_2 dissociation, ionisation of atomic hydrogen and helium, and molecular vibrations and rotations. This is a realistic approach for modelling the second collapse phase where H_2 begins to dissociate depending on the pressure, temperature, and density. This gas EOS from D'Angelo & Bodenheimer (2013) has been implemented in the *PLUTO* code by Vaidya et al. (2015) and for our studies we have updated the radiation transport module in *PLUTO* to make use of this EOS (see details in Marleau et al., in prep.).

The adiabatic index or ratio of specific heats

$$\gamma = \frac{C_P}{C_V},$$

(2.18)

takes into account the translational, rotational, and vibrational degrees of freedom. Figure 2.2 shows the mean molecular weight μ and γ as a function of temperature and also indicates the dependence on gas density. The mean molecular weight μ has an upper limit of ~ 2.3 and lower limit of ~ 0.6. The first transition (i.e. the plateau region) indicates the dissociation of H_2 whereas the second transition shows the ionisation phase. In the plot showing γ as a function of temperature, the gas behaves as a monatomic ideal gas with $\gamma \approx 5/3$ at lower temperatures. The transition from a monatomic gas $\gamma \approx 5/3$ (where rotational degrees of freedom of H_2 are frozen) to a diatomic gas $\gamma \approx 7/5$ and further to the dissociation phase where $\gamma \approx 1.1$ is also seen as dips in γ. Following the curve to higher temperatures, the other dips occur at the ionisation of hydrogen and at the first and second ionisation of helium. Increasing the density raises the temperature at which these processes occur. Since the range in $\log T$ over which they occur widens and the γ dips become shallower, the dips gradually blend. This can be clearly seen when comparing the curves at $\rho = 10^{-19}$ g cm^{-3} and at $\rho = 10^{-3}$ g cm^{-3}.
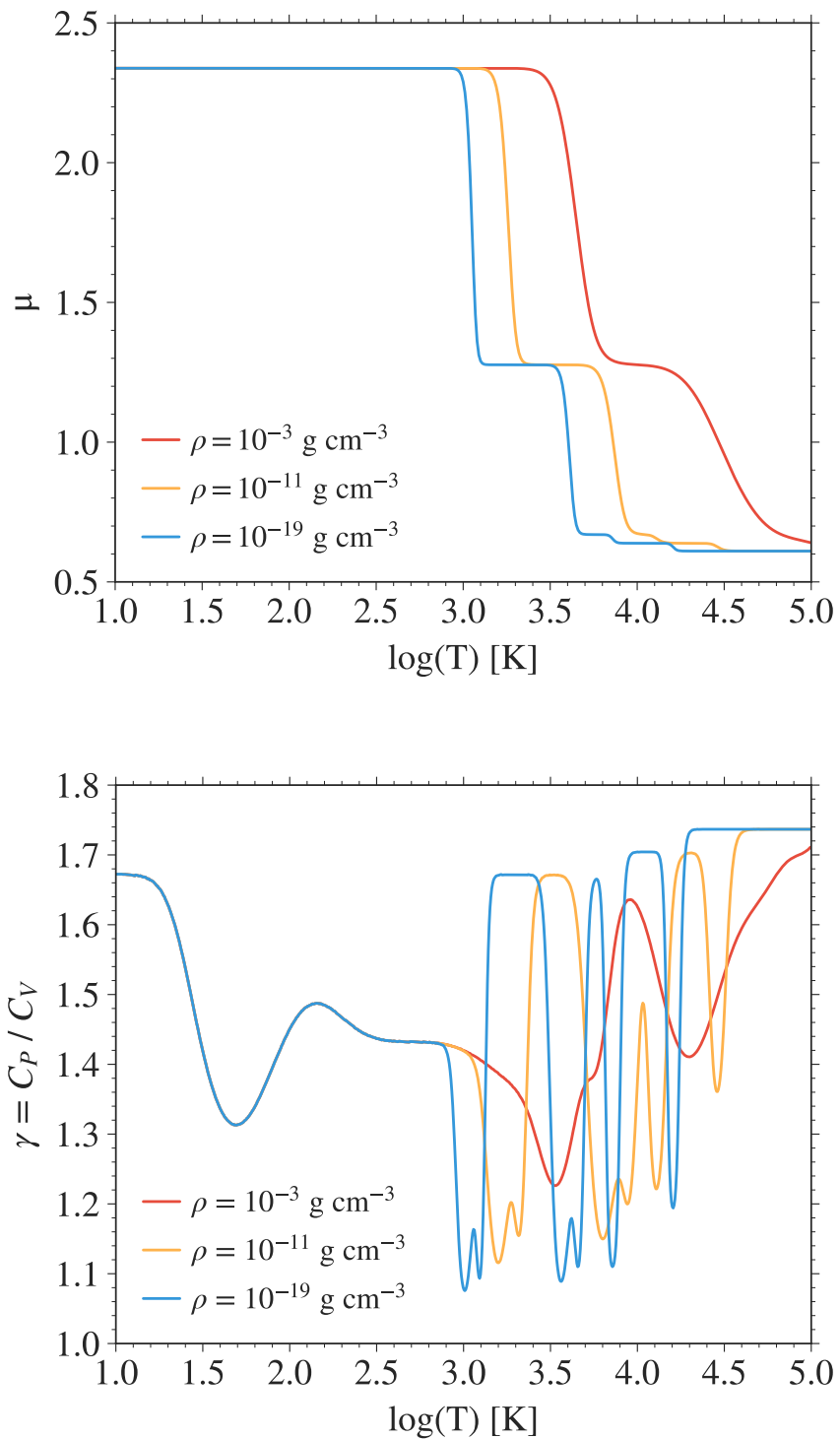
Figure 2.2: Mean molecular weight μ and adiabatic index γ as a function of temperature for three different gas densities ($\rho = 10^{-3}$, 10^{-11}, and 10^{-19} g cm^{-3}).

In our studies, we assume the ortho-to-para ratio of H_2 to be in thermal equilibrium at all temperatures. Vaytet et al. (2014) showed that the ortho-to-para ratio influences the thermal evolution of the first core but has negligible effects on the core properties. It still remains unclear which ortho-to-para ratio should be used in the initial conditions for star formation.

Considering LTE, the ionisation-recombination and dissociation processes for hydrogen are given by

$$
\begin{aligned}
H + e^- &\rightleftharpoons H^+ + 2e^- \\
H_2 &\rightleftharpoons H + H,
\end{aligned}
\tag{2.19}
$$

respectively. The degree of ionisation of atomic hydrogen x, the degree of dissociation of molecular hydrogen y, and the degrees of single z_1 and double z_2 ionisation of helium are defined from D'Angelo & Bodenheimer (2013) as

$$
x = \frac{\rho_{H^+}}{\rho_{H^+} + \rho_H},
\tag{2.20}
$$

$$
y = \frac{\rho_H}{\rho_H + \rho_{H_2}},
\tag{2.21}
$$

$$
z_1 = \frac{\rho_{He^+}}{\rho_{He^+} + \rho_{He}},
\tag{2.22}
$$

$$
z_2 = \frac{\rho_{He^{2+}}}{\rho_{He^{2+}} + \rho_{He^+}}.
\tag{2.23}
$$

Following the Boltzmann law of the energy distribution, the ionisation and dissociation degrees using Saha equations is given as (e.g. Black & Bodenheimer, 1975)

$$
\frac{x^2}{1-x} = \frac{m_H}{X\rho} \left(\frac{m_e k_B T}{2\pi\hbar^2} \right)^{3/2} e^{-13.60\ \text{eV}/(k_B T)},
\tag{2.24}
$$

$$
\frac{y^2}{1-y} = \frac{m_H}{2X\rho} \left(\frac{m_H k_B T}{4\pi\hbar^2} \right)^{3/2} e^{-4.48\ \text{eV}/(k_B T)},
\tag{2.25}
$$

$$
\frac{z_1}{1-z_1} = \frac{4 m_H}{\rho} \left(\frac{m_e k_B T}{2\pi\hbar^2} \right)^{3/2} \frac{e^{-24.59\ \text{eV}/(k_B T)}}{X + z_1 Y/4},
\tag{2.26}
$$

$$
\frac{z_2}{1-z_2} = \frac{m_H}{\rho} \left(\frac{m_e k_B T}{2\pi\hbar^2} \right)^{3/2} \frac{e^{-54.42\ \text{eV}/(k_B T)}}{X + (z_2+1)\, Y/4},
\tag{2.27}
$$

where m_e is the electron mass, m_H is the hydrogen mass, k_B is the Boltzmann constant, $\hbar$ is the Planck constant divided by 2π, and $\rho = n\mu m_u$ is the total gas density. The hydrogen and helium mass fractions are taken as $X = 0.711$ and $Y = 0.289$, respectively.

For a gas mixture mainly consisting of hydrogen (atoms, molecules, and ions), helium, and a negligible fraction of metals, the mean molecular weight μ is given by (e.g. Black & Bodenheimer 1975)

$$\frac{\mu}{4} = [2X(1 + y + 2xy) + Y(1 + z_1 + z_1 z_2)]^{-1}, \tag{2.28}$$

and the gas internal energy density $(\rho e)_{\text{gas}}$ is given by

$$(\rho e)_{\text{gas}} = (\epsilon_{\text{H}_2} + \epsilon_{\text{H}} + \epsilon_{\text{He}} + \epsilon_{\text{H+H}} + \epsilon_{\text{H}^+} + \epsilon_{\text{He}^+} + \epsilon_{\text{He}^{2+}}) \frac{\rho k_{\text{B}} T}{m_{\text{u}}}. \tag{2.29}$$

The quantity m_{u} is the atomic mass unit. Contributions from various species in the parenthesis are dimensionless and can be obtained using an appropriate partition function ζ by taking into account the translational, rotational, and vibrational degrees of freedom as detailed in D'Angelo & Bodenheimer (2013).

The stability condition needed for numerical calculations requires an estimate of the sound speed c_{s}, which relates pressure and density and is defined as

$$c_{\text{s}}^2 = \frac{\Gamma_1 P}{\rho}. \tag{2.30}$$

The parameter Γ_1 is the first adiabatic index, which has a functional dependence on temperature and density, given as

$$\Gamma_1 = \frac{1}{C_{\text{V}}(T)} \left(\frac{P}{\rho T} \right) \chi_{\text{T}}^2 + \chi_{\rho}, \tag{2.31}$$

where $C_{\text{V}}(T)$ is obtained by taking the derivative of the specific gas internal energy $e(T)$ with respect to temperature at a constant volume and the temperature χ_{T} and density χ_{ρ} exponents (see D'Angelo & Bodenheimer 2013) are defined by

$$\chi_{\text{T}} = \left(\frac{\partial \ln P}{\partial \ln T} \right)_{\rho} = 1 - \frac{\partial \ln \mu}{\partial \ln T}, \tag{2.32}$$

$$\chi_{\rho} = \left(\frac{\partial \ln P}{\partial \ln \rho} \right)_{T} = 1 - \frac{\partial \ln \mu}{\partial \ln \rho}. \tag{2.33}$$

We note that for an ideal gas where phase transitions are ignored (i.e. with constant μ and γ), Γ_1 is equal to the adiabatic index γ.

With all of the above considerations, the thermal EOS (relating pressure, temperature, and volume) and the caloric EOS (relating internal energy, volume, and temperature) can be expressed as

$$P = \frac{\rho k_{\text{B}} T}{m_{\text{u}} \mu(X)}$$

$$e = e(T, X), \tag{2.34}$$

where the mean molecular weight $\mu(X)$ depends on the gas composition. The chemical fractions are not solved independently and can be expressed as $X = X(T, \rho)$ under

equilibrium assumptions. Thus the thermal and caloric EOS can also be expressed as a function of temperature and density, $P = P(\rho, T)$ and $e = e(T, \rho)$, respectively. Owing to the explicit temperature dependence, the conversion between pressure and internal energy density and vice versa is preceded by computing temperatures using the thermal EOS and pre-computed lookup tables of pressure and internal energy density. Further details on the implementation of lookup tables can be found in Vaidya et al. (2015).

2.4 Opacities

We make use of tabulated dust opacities from Ossenkopf & Henning (1994) and tabulated gas opacities from Malygin et al. (2014). At lower temperatures the contribution from dust dominates whereas at higher temperatures this is negligible since the dust is evaporated.

Code-wise, we updated the evaporation and sublimation module to consider a time-dependent evolution of the dust. The dust is treated as being perfectly coupled to the gas, that means the dust is moving with the gas flow, but the dust content is allowed to change in time due to evaporation and sublimation of dust grains. Hence, in addition to the gas mass density, we store the local dust-to-gas mass ratio $R(t) = M_{\text{dust}} / M_{\text{gas}}$.

The evaporation temperature T_{evap} is computed based on Pollack et al. (1994) utilising the power-law formula by Isella & Natta (2005, Eq. 16)

$$T_{\text{evap}} = \beta_1 \times \left(\frac{\rho_{\text{gas}}}{1 \text{ g cm}^{-3}} \right)^{\beta_2}, \tag{2.35}$$

with $\beta_1 = 2000$ K and $\beta_2 = 1.95 \times 10^{-2}$. In the sublimation regime $T_{\text{dust}} < T_{\text{evap}}$, the temporal evolution of the dust-to-gas mass ratio $R(t)$ is described by

$$R(t + \Delta t) = R(t) + dR \times R_{\text{max}} \times \left(1 - \exp \left(-\frac{\Delta t}{t_{\text{subl}}} \times dT \times dR \right) \right), \tag{2.36}$$

with $dT = |T_{\text{evap}} - T_{\text{dust}}| / T_{\text{evap}}$ and $dR = (R_{\text{max}} - R(t)) / R_{\text{max}}$. In the evaporation regime $T_{\text{dust}} > T_{\text{evap}}$, the temporal evolution of the dust-to-gas mass ratio is described by

$$R(t + \Delta t) = R(t) \times \exp \left(-\frac{\Delta t}{t_{\text{evap}}} \times dT \times \frac{1}{dR + \omega} \right). \tag{2.37}$$

The value ω serves as a lower limit to the dR term, which prevents the dR^{-1} term from diverging.

In a nutshell, evaporation and sublimation become more efficient for higher temperature differences between dust and evaporation temperature. Furthermore, the evaporation efficiency decreases towards lower dust-to-gas mass ratios and the sublimation efficiency decreases towards the maximum allowed dust-to-gas mass ratio. For all simulations performed, we used $R_{\text{max}} = 0.01$, $t_{\text{subl}} = 10$ yr, $t_{\text{evap}} = 100$ yr, and $\omega = 0.01$.

2.5 Numerics and initial setup

This section describes the initial setup and numerical treatment used in the 1D and 2D RHD collapse simulations presented in this thesis. A detailed description of the numerical code *PLUTO* can be found in Mignone et al. (2007) and Mignone et al. (2012) for the hydrodynamics and Kuiper et al. (2010) and Kuiper et al. (2011) for the self-gravity. The details of the gas EOS, as described in Sect. 2.3, can be found in Vaidya et al. (2015) and Marleau et al. (in prep.). We make use of the grey FLD radiation transport module MAKEMAKE. The theory and numerics of the radiation transfer scheme are described and tested in Kuiper et al. (2010) and Kuiper et al. (subm.). Vaytet et al. (2012, 2013) have indicated slight differences in the core properties between the grey and multi-group methods. However, they argued that the grey method is sufficient for the 1D case and the multi-group radiative transfer may be more important in the later evolutionary stages of the protostar.

We make use of a conservative finite volume approach based on second-order Godunov-type schemes, that means the shock-capturing Riemann solver implemented in *PLUTO* to solve the equations of hydrodynamics. Our basic configuration for the flux computation consists of the Harten-Lax-Van Leer approximate Riemann solver that restores the middle contact discontinuity (hllc) and a monotonised central difference (MC) flux limiter using piecewise linear interpolation. We integrate with a Runge-Kutta second order (RK2) method. On the other hand, the FLD equation is solved in an implicit way using a standard generalised minimal residual solver with approximations to the error from previous restart cycles (LGMRES). A relative convergence tolerance value of 10^{-10} in terms of temperature is used. More details about the open-source solver library PETSc (Portable, Extensible Toolkit for Scientific Computation) can be found in Balay et al. (1997, 2019a,b).

As an initial density distribution we use a stable Bonnor–Ebert (Ebert, 1955; Bonnor, 1956) sphere like density profile. Comparisons to an initially uniform density cloud core are described in Sect. 3.3.4.

Given an initial cloud core mass M_0 and outer radius R_{cloud}, the initial sound speed c_{s0} is computed as

$$c_{\text{s0}}^2 = \frac{GM_0}{\ln(14.1)\ R_{\text{cloud}}}. \tag{2.38}$$

The initial cloud core masses range from 0.5 $M_\odot$ to 100 $M_\odot$. The temperature T_{BE} for the stable sphere is calculated as

$$T_{\text{BE}} = \frac{\mu\ c_{\text{s0}}^2}{\gamma\ \Re}, \tag{2.39}$$

where the mean molecular weight $\mu = 2.353$, $\gamma = 5/3$, and $\Re$ is the universal gas constant.

Due to the fact that the hydrostatic equilibrium condition of a Bonnor–Ebert sphere does not have an analytical solution, the density profile $\rho(r)$ has to be solved for numerically. The initial outer ρ_{o} and central ρ_{c} densities are determined by

$$\rho_{\text{o}} = \left(\frac{1.18\ c_{\text{s0}}^3}{M_0\ G^{3/2}} \right)^2 \tag{2.40}$$

$$\rho_{\text{c}} = 14.1\ \rho_{\text{o}}.$$

The density contrast between the centre and edge of the sphere corresponds to a dimensionless radius of $\xi = 6.45$, where ξ is defined as

$$\xi = \sqrt{\frac{4\pi G \rho_{\mathrm{o}}}{c_{\mathrm{s}}^2}} R_{\mathrm{cloud}}, \tag{2.41}$$

where R_{cloud} is the cloud core radius. The integrated mass of the cloud core is the same as that of a critical Bonnor–Ebert sphere. The thermal pressure is computed using Eq. (2.34) for a fixed lower temperature T_0 in comparison to the stable Bonnor–Ebert sphere set-up, which causes gravity to dominate and initiates the collapse. This temperature T_0 varies from $5 - 100$ K. The radiation temperature is set to be initially in equilibrium with the gas temperature. The dust and gas temperatures are treated as perfectly coupled throughout the simulation.

2.5.1   One-dimensional grid setup

The computational grid for the 1D simulations is comprised of 4416 cells. We use 320 uniformly spaced cells from 10^{-4} au to 10^{-2} au and 4096 logarithmically spaced cells from 10^{-2} au to 3000 au, covering a dynamical range of seven orders of magnitude. We made sure that the last uniform cell and the first logarithmic cell are identical in size. A logarithmic binning throughout the whole domain would lead to extremely small grid cells resulting in much smaller time steps. The domain was thus scaled differently in the inner dense regions to prevent the simulations from being computationally very expensive. The smallest radial cell size $\Delta x_{\mathrm{min}} = \Delta r = 3.09 \times 10^{-5}$ au. We use a minimum of 50 cells per Jeans length, which is estimated at the highest central density. Otherwise, we use $10^3 - 10^5$ cells per Jeans length. We performed convergence tests using different resolutions (see Appendix A.1.1) and different inner radii R_{in} (see Appendix A.1.2) in order to test our approach. These tests show that the applied resolution is fully sufficient and hence there is no need to use higher resolution in the inner parts.

2.5.2   Two-dimensional grid setup

We expand our 1D studies for a few cases of 1 $M_{\odot}$, 5 $M_{\odot}$, 10 $M_{\odot}$, and 20 $M_{\odot}$ cloud cores, thus accounting for cases from the low-, intermediate-, and high-mass regimes. For this, we adopt a 2D spherical Eulerian grid with axial and midplane symmetry. The grid comprises of 1445 logarithmically spaced cells in the radial direction extending from 10^{-2} au to 3000 au, thus spanning a dynamical range covering five orders of magnitude. The logarithmic spacing increases resolution in the central parts of the computational domain. In the polar direction, we use 180 uniformly spaced cells stretching from the pole ($\theta = 0°$) to the midplane ($\theta = 90°$). The number of cells is tuned in order to ensure an equal spatial extent in the radial and polar direction with the smallest cell size $\Delta x_{\mathrm{min}} = \Delta r = r\Delta\theta = 8.77 \times 10^{-5}$ au. We use a minimum of 49 cells per Jeans length, which is estimated at the highest central density. Otherwise, we use $300 - 10^4$ cells per Jeans length. Convergence tests using different resolutions for the 2D studies are described in Appendix A.2.

2.5.3   Boundary conditions

We use a reflective boundary condition at the inner radial edge R_{in} for the hydrodynamics and a zero gradient condition for the radiation energy (i.e. no radiative flux

Table 2.1: Computational run time for different simulations.

Simulation run	R_{in} (au)	N_g	Δt (years)	Δt_O (years)
1D (RHD)	10^{-4}	4416	3.7238×10^{-6}	-
2D (RHD)	10^{-2}	1445	2.2344×10^{-5}	-
2D (RMHD)	10^{-2}	120	5.5469×10^{-4}	8.7149×10^{-5}

Note: Listed above is the time $\Delta t = \Delta r / c_s$ (years) for RHD simulations and the time $\Delta t_O = \Delta r^2 / \eta_O$ (years) for the resistive RMHD simulations. The different columns also list the inner radius R_{in} (au) and the total number of radial grid cells N_g used in the respective simulations.

can cross the inner boundary interface). At the outer radial edge, we use a Dirichlet boundary condition on the radiation temperature with a constant boundary value of T_0. Additionally, we use an outflow–no-inflow condition for the hydrodynamics that includes a zero-gradient (i.e. no force) boundary condition for the thermal pressure, the polar, and the azimuthal velocity components given as

$$\frac{dP}{dr} = \frac{dv_\theta}{dr} = \frac{dv_\phi}{dr} = 0. \tag{2.42}$$

For the 2D runs, we use axisymmetric boundaries at the pole and mirror-symmetric boundaries at the equator.

2.6 Computational time

The time step Δt is limited by Courant–Friedrichs–Lewy (CFL) condition (Courant et al., 1928). The CFL stability condition restricts the time step in numerical simulations that use time integration schemes which are explicit (i.e. the next time step depends on the previous time step). The CFL condition for a 1D case is given by

$$C = \frac{u \Delta t}{\Delta r} \leq C_{\text{max}}, \tag{2.43}$$

where $C_{\text{max}} = 1$ for explicit time stepping methods, which are also used for our purposes in the *PLUTO* code. The physical interpretation of this is that the physical distance covered by a solution in one time step $u\Delta t$ should be less that the spacing between two neighbouring grid points (i.e. cell size) Δr. In other words, the CFL number (C) controls the time step length. For the RK2 time integration scheme used in this work, $C \leq 1/N_{\text{dim}}$, where N_{dim} is the number of spatial dimensions, hence, for example $C_{\text{max}} = 0.5$ for our 2D simulations. We use CFL values of 0.8 and 0.4 for the 1D and 2D simulations, respectively, thus ensuring the stability to achieve numerical convergence.

Furthermore, the purely radiation hydrodynamical time step Δt is constrained by the ratio of the radial grid cell size and the sound speed as $\Delta t = \Delta r / c_s$. On the other hand, the Ohmic diffusion time step Δt_O is defined as $\Delta t_O = \Delta r^2 / \eta_O$, where η_O is the resistivity. We fix the upper limit of η_O to a value of 10^{17} cm^2 s^{-1} in all the 2D RMHD simulations presented herein to minimise the computational expense. As an example, Table 2.1 lists the time(s) at the final snapshot of the 1 $M_\odot$ cloud core collapse simulations for the 1D and 2D RHD runs as well as the 2D RMHD

run with the mass-to-magnetic flux ratio μ_0 of 5 (which is the highest magnetic field strength that we use). The sound speed and resistivity increase with increasing temperature and for the collapse physics, the temperature increases with increasing density. Thus, the hydrodynamical and diffusion time steps become lower (i.e. high CPU time) as the cloud core collapses to higher central densities. Additionally, both the hydrodynamical and diffusion time steps become lower with a higher spatial resolution, that means for smaller Δr.

From molecular cloud cores to hydrostatic cores

Based on Bhandare et al. (2018), published in *Astronomy and Astrophysics* (618, A95).

In this chapter, I discuss results from our 1D simulations that model the gravitational collapse of isolated gas spheres with a uniform temperature and an initial Bonnor–Ebert sphere like density profile. The main goal of this work is to understand the entire collapse process through stages of the first and second hydrostatic core formation by incorporating a realistic gas EOS and appropriate opacity tables. This is done, for the first time, for a wide range of initial cloud core masses from 0.5 $M_\odot$ to 100 $M_\odot$. The initial cloud core parameters also include temperatures ranging from 5 K to 100 K and outer radii of 3000 au and 5000 au. In doing so, we quantify the dependence of the first and second core properties on the initial cloud core properties. This chapter highlights properties of the first hydrostatic core while the next chapter mainly focuses on properties of the second hydrostatic core (i.e. the forming protostar).

In this work, we focus on the properties of hydrostatic cores governed by gravity and thermal pressure and not of the environment. Because thermal pressure is isotropic, a 1D approach is a good approximation for these objects, even though the collapsing environment is not described accurately. One-dimensional studies have proven to be of importance in understanding the role of different physical processes involved, while 3D studies can still be computationally very expensive.

Thermodynamical modelling in terms of radiation transport and phase transitions is crucial to better understand the complex physical mechanisms involved in the collapse process. Hence, we use grey FLD radiative transfer (Levermore & Pomraning, 1981) coupled with hydrodynamics to simulate the molecular cloud core collapse. Different chemical species affect the gas hydrodynamics via heat capacity, line cooling, and chemical energy and affect the radiation via gas and dust opacities. In order to take into account effects such as the dissociation, ionisation, rotational, and vibrational degrees of freedom for the molecules in our studies, we use a realistic gas EOS, with a density- and temperature-dependent adiabatic index and mean molecular weight, to model the phase transitions. Using a non-constant adiabatic index is particularly important since it has a strong influence on the thermal evolution of the gas and in general also on the stability of the gas against gravitational collapse (Stamatellos & Whitworth, 2009). The specific heat and mean molecular weight are computed as a function of temperature by solving partition functions for rotational, vibrational, and translational energy levels of H_2 instead of using a constant value. Details of the microphysics, numerical scheme, and initial setup can be found in Chapter 2.

This chapter is organised as follows. The scanned parameter space is described in Sect. 3.1. The evolution of the cloud core through various stages until the formation of the second hydrostatic core is presented in Sect. 3.2. A detailed description of the

Table 3.1: Initial cloud core properties.

M_0 ($M_\odot$)	R_{cloud} (au)	T_0 (K)	T_{BE} (K)	M_{BE}/M_0	ρ_{c} (g cm^{-3})
0.5	3000	10.0	9.49	1.05e-00	1.16e-17
1.0	3000	10.0	18.98	5.27e-01	2.33e-17
2.0	3000	10.0	37.96	2.64e-01	4.66e-17
5.0	3000	10.0	94.91	1.05e-01	1.17e-16
8.0	3000	10.0	151.85	6.58e-02	1.87e-16
10.0	3000	10.0	189.81	5.27e-02	2.33e-16
12.0	3000	10.0	227.78	4.39e-02	2.80e-16
14.0	3000	10.0	265.74	3.76e-02	3.26e-16
15.0	3000	10.0	284.72	3.51e-02	3.50e-16
16.0	3000	10.0	303.70	3.29e-02	3.73e-16
18.0	3000	10.0	341.66	2.93e-02	4.20e-16
20.0	3000	10.0	379.63	2.63e-02	4.66e-16
30.0	3000	10.0	569.44	1.76e-02	6.99e-16
40.0	3000	10.0	759.25	1.32e-02	9.33e-16
60.0	3000	10.0	1138.88	8.78e-03	1.40e-15
80.0	3000	10.0	1518.50	6.58e-03	1.87e-15
100.0	3000	10.0	1898.13	5.27e-03	2.33e-15

Note: Listed above are the cloud core properties for runs with different initial cloud core mass M_0 ($M_\odot$), outer radius R_{cloud} (au), temperature T_0 (K), temperature T_{BE} (K) of a stable Bonnor-Ebert cloud core, stability parameter M_{BE}/M_0, and central density ρ_{c} (g cm^{-3}).

collapse of an initial 1 $M_\odot$ cloud core is provided in Sect. 3.2.1. This is followed by a similar description in Sect. 3.2.2, for cases with different initial cloud core masses ranging from 0.5 $M_\odot$ up to 100 $M_\odot$. The dependence of the first core properties on the initial cloud core mass, radius, temperature, and density profile are discussed in Sects. 3.3.1 – 3.3.4, respectively. Our results are in good agreement with previous work and comparisons are provided in Sect. 3.4. The limitations of our method are discussed in Sect. 3.5. Lastly, Sect. 3.6 provides a summary of the results from our 1D collapse simulations.

3.1   Parameter scan

Our 1D studies span a wide range of initial cloud core masses from 0.5 $M_\odot$ to 100 $M_\odot$. As described in Sect. 2.5.1, the spatial domain extends from 10^{-4} au up to 3000 au for all the different cases, which implies that for a constant initial temperature of 10 K, the central density of the different Bonnor-Ebert spheres scales as a function of initial cloud core mass (see Table 3.1).

We also perform the set of simulations listed in Table 3.3 with an outer radius of 5000 au and a constant initial temperature of 10 K for initial cloud core masses ranging from 1 $M_\odot$ to 100 $M_\odot$. Additionally, in order to investigate the dependence on the initial cloud core properties, we explore a range of initial conditions by performing three sets of simulations using a different constant stability parameter M_{BE}/M_0 for the low-mass (0.5 $M_\odot$ to 10 $M_\odot$), intermediate-mass (8 $M_\odot$ to 20 $M_\odot$) and high-mass

regimes (30 $M_\odot$ to 100 $M_\odot$), respectively. For these runs we fixed the outer radius to 3000 au but varied the initial cloud core temperature from 5 – 100 K. The initial cloud core properties for the selected parameter space are listed in Table 3.4.

3.2 Formation of the first and second hydrostatic cores

3.2.1 Fiducial 1 $M_\odot$ case

This section provides a general overview of the collapse evolution and its effects on various properties for an initial 1 $M_\odot$ cloud core. Figure 3.1 shows the radial profiles of the density, pressure, gas temperature, velocity, enclosed mass, optical depth, Mach number, mean molecular weight μ, and the thermal structure at a time step right after the second core formation. We consider an initial Bonnor–Ebert sphere like density profile (as described in Sect. 2.5), where the initial central density is $\rho_c \approx 10^{-17}$ g cm^{-3}. The evolution of the cloud core through its first and second collapse phase can be understood as follows:

- Initially the optically thin cloud core collapses isothermally with $\gamma_{\text{actual}} \approx 1$ under its own gravity, where γ_{actual} is the change in the slope of the temperature evolution with density (see Fig. 3.2).

- During the first collapse phase, as the density and pressure increase, the optical depth becomes greater than unity (Masunaga & Inutsuka, 1999) and the cloud core compresses adiabatically. The cloud core starts absorbing the thermal radiation and heats up leading to an adiabatic collapse phase.

- These conditions lead to the formation of the first hydrostatic core after about 10^4 years with initial values of the radius of $R_{\text{fc}} \approx 2$ au and enclosed mass of $M_{\text{fc}} \approx 10^{-3}$ $M_\odot$, which subsequently contracts adiabatically with $\gamma_{\text{actual}} \approx 5/3$.

- The strong compression leads to the first shock at the border of the first core as seen in the velocity profile (Fig. 3.1*d*). Comparing this to the temperature profile (Fig. 3.1*c*), the first shock is supercritical, that means pre- and post-shock temperatures are similar, as discussed in Commerçon et al. (2011a).

- The first core mainly consists of H_2 molecules and neutral He and has a constant mean molecular weight μ of 2.353.

- With a rise in temperature, the adiabatic index γ changes from its initial monatomic value of $\gamma = 5/3$ to the value for a diatomic gas, $\gamma = 7/5$, once the gas is warm enough to excite the rotational degrees of freedom. As Fig. 3.2 indicates, γ_{actual} undergoes the same evolution.

- Once the temperature inside the first core reaches ~ 2000 K, H_2 molecules begin to dissociate, which leads to the second collapse phase. During this phase, γ_{actual} changes roughly to 1.1, which is well below the critical value of 4/3 for stability of a self-gravitational sphere.

- As the H_2 and neutral helium concentration change and the fraction of atomic hydrogen increases during the dissociation phase, μ gradually decreases in the inner regions, as seen in Fig. 3.1*h*.

- Once most of the H_2 has been dissociated, it is followed by the formation of the second hydrostatic core with initial values for the radius and enclosed mass of $R_{\text{sc}} \approx 1.8 \times 10^{-2}$ au ≈ 3.9 $R_\odot$ and $M_{\text{sc}} \approx 4.6 \times 10^{-3}$ $M_\odot$, respectively.
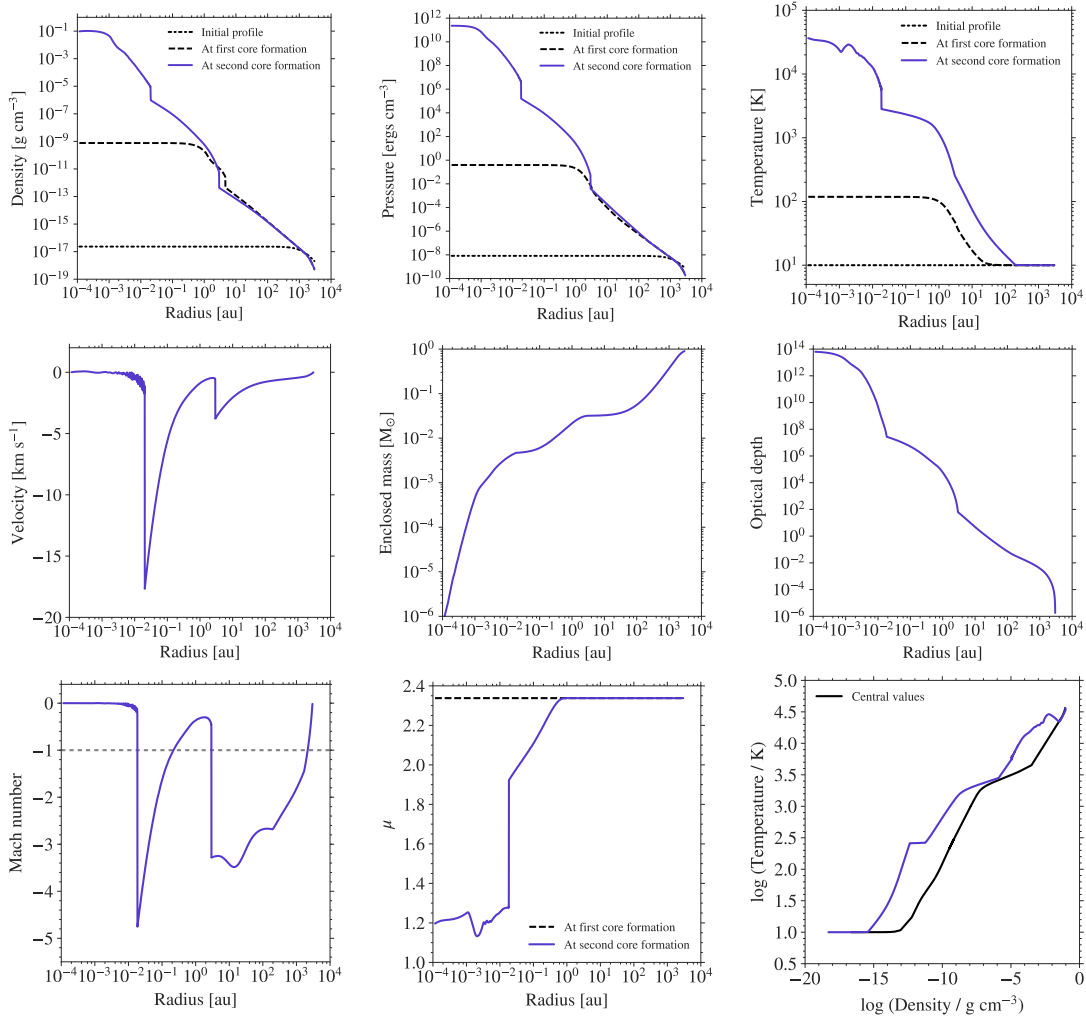
Figure 3.1: Collapse of a 1 $M_\odot$ cloud core. Radial profiles (across and down) of **a)** density, **b)** pressure, **c)** gas temperature, **d)** velocity, **e)** enclosed mass, **f)** optical depth, **g)** Mach number, **h)** mean molecular weight, and **i)** thermal structure are shown at the time snapshot after second core formation. The black line in panel *i* shows the temporal evolution of the central temperature and density. The initial profile is shown by the black dot dashed line, the first collapse phase is indicated by the black dashed line, and the bluish purple line describes the structure after formation of the second hydrostatic core.

- The second shock at the border of the second core is seen in the velocity profile (Fig. 3.1*d*). Comparing this to the temperature profile, the second shock is subcritical, that means the post-shock temperature is higher than the pre-shock temperature, suggesting that the accretion energy is transferred onto the second core and not radiated away.

- The central density rapidly rises up to $\rho_c \approx 10^{-1}$ g cm^{-3} at the end of the second collapse phase, which lasts only for a few years since the second hydrostatic core forms almost instantaneously.

- At later times when the central density is $\rho_c \approx 10^{-1}$ g cm^{-3}, the outer layers tend to have higher temperatures due to the effects of shock heating and
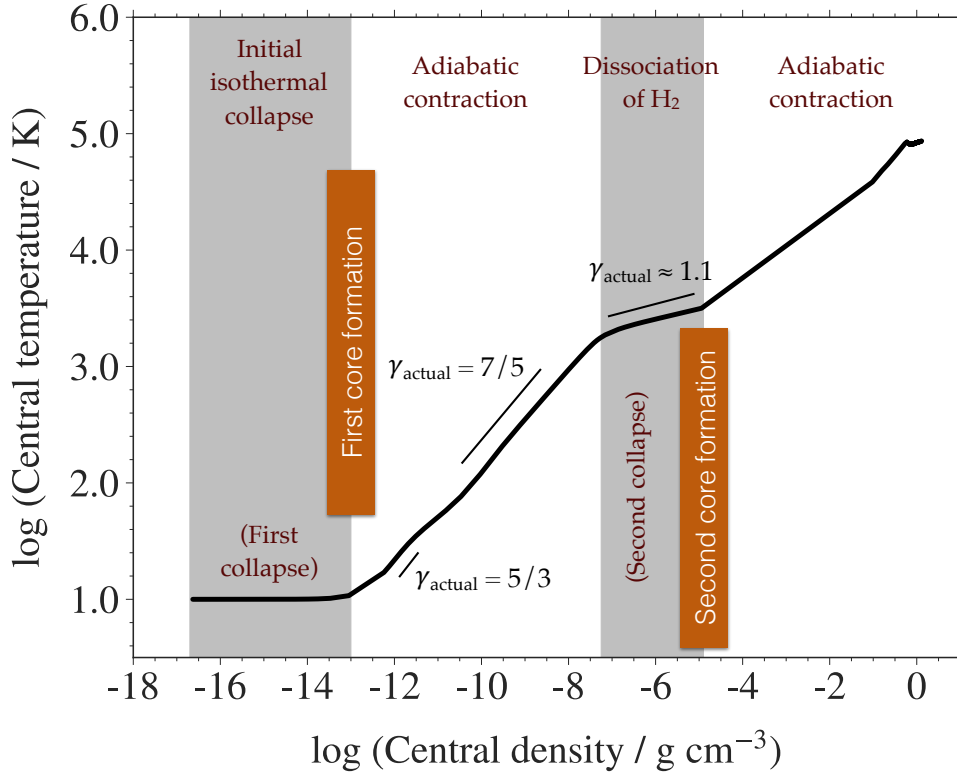
Figure 3.2: Thermal evolution showing the first and second collapse phase for a 1 $M_\odot$ cloud core. The change in adiabatic index γ_{actual} indicates the importance of using a realistic gas EOS.

absorption of radiation from the hot central region. Differences in the thermal evolution of the central region (black line) and the thermal structure at a time when ρ_c is approximately 10^{-1} g cm^{-3} (bluish purple line) can be seen in Fig. 3.1*i*.

- Finally (not simulated here), once the temperature inside the second core reaches ignition temperatures ($\geq 10^6$ K) for nuclear reactions, it eventually leads to the birth of a star.

Figure 3.2 summarises the different evolutionary stages that the molecular cloud core undergoes to form the first and second Larson cores and indicates the phase transition from monatomic to diatomic gas, seen as the change in the adiabatic index γ_{actual}.

3.2.2 Effect of different initial cloud core masses

This section highlights the core collapse scenario for different initial cloud core masses spanning a wide range from 0.5 $M_\odot$ to 100 $M_\odot$. As shown in Fig. 3.3, the cloud cores with different initial masses M_0 and central densities ρ_c at the same initial temperature of 10 K and an outer radius of 3000 au follow a similar evolution. Most significant differences are seen outwards from the first shock as a horizontal spread.

The thermal structure for cases with different initial cloud core masses (Fig. 3.3*f*) shows that the cloud cores begin with the same isothermal phase but eventually heat up at different densities. This difference in thermal evolution can have a significant effect on the properties of the first and second cores since for the intermediate- and high-mass cloud cores ($M_0 \geq 8\ M_\odot$) the dissociation temperature is reached earlier,
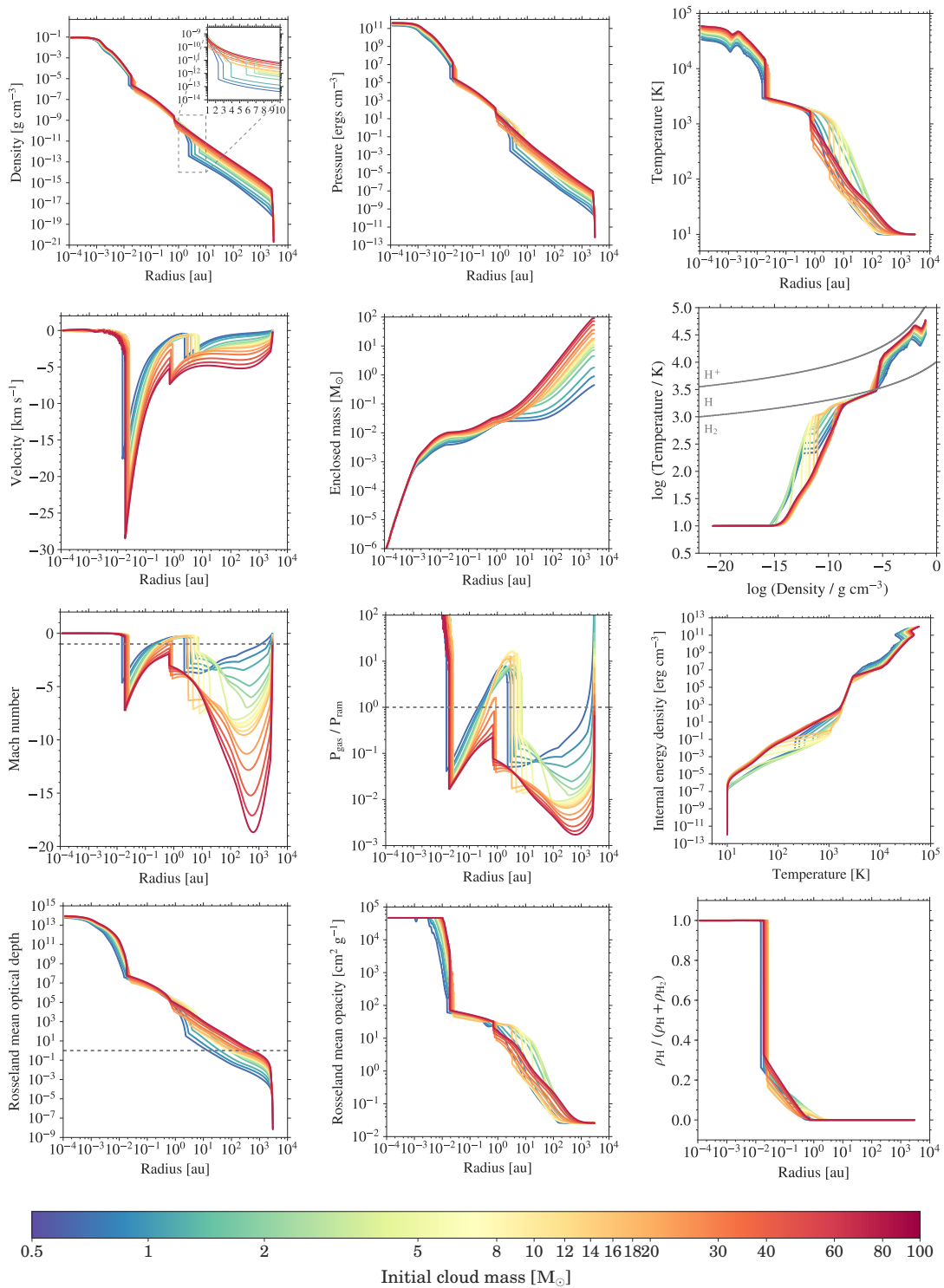
Figure 3.3: Shown above are the radial profiles (across and down) of **a)** density, **b)** pressure, **c)** gas temperature, **d)** velocity, and **e)** enclosed mass as well as the **f)** thermal structure, **g)** Mach number, **h)** ratio of gas to ram pressure, **i)** internal energy density as a function of temperature, **j)** optical depth, **k)** Rosseland mean opacity, and **l)** dissociation fraction at the time snapshot after second core formation. Different colours indicate cloud cores with different initial masses as seen in the colour bar. The grey lines in the thermal structure plot show the 50 % dissociation and ionisation curves according to Eq. (2.25) and Eq. (2.26).

Table 3.2: Properties of the first and second cores estimated at the snapshot after second core formation for different initial cloud core masses M_0 with a fixed outer radius of $R_{\text{cloud}} = 3000$ au and a constant initial temperature of $T_0 = 10$ K.

M_0 ($M_\odot$)	R_{fc} (au)	M_{fc} ($M_\odot$)	T_{fc} (K)	$\dot{M}_{\text{fc}}$ ($M_\odot$/yr)	R_{sc} (au)	M_{sc} ($M_\odot$)	T_{sc} (K)	$\dot{M}_{\text{sc}}$ ($M_\odot$/yr)
0.5	2.35	2.53e-02	2.13e+02	3.47e-05	1.46e-02	3.78e-03	6.12e+03	2.61e-02
1.0	2.96	3.18e-02	2.58e+02	6.32e-05	1.84e-02	4.68e-03	6.16e+03	3.02e-02
2.0	3.96	4.40e-02	3.30e+02	1.38e-04	2.00e-02	5.18e-03	6.14e+03	2.37e-02
5.0	5.76	7.20e-02	4.91e+02	6.63e-04	2.34e-02	6.32e-03	6.82e+03	2.70e-02
8.0	6.76	8.69e-02	6.03e+02	9.52e-04	2.33e-02	6.74e-03	6.87e+03	1.96e-02
10.0	7.24	9.24e-02	6.62e+02	1.34e-03	2.43e-02	7.29e-03	6.82e+03	2.31e-02
12.0	7.22	9.08e-02	7.59e+02	1.32e-03	2.42e-02	7.47e-03	7.51e+03	2.56e-02
14.0	6.54	8.10e-02	8.97e+02	1.19e-03	2.32e-02	7.55e-03	8.63e+03	2.98e-02
15.0	5.91	7.37e-02	9.71e+02	1.18e-03	2.48e-02	7.73e-03	7.90e+03	3.03e-02
16.0	5.16	6.58e-02	1.04e+03	1.16e-03	2.53e-02	7.91e-03	7.33e+03	2.25e-02
18.0	3.99	5.35e-02	1.11e+03	1.33e-03	2.55e-02	8.18e-03	8.01e+03	2.74e-02
20.0	3.04	4.27e-02	1.17e+03	1.49e-03	2.48e-02	8.26e-03	8.33e+03	2.63e-02
30.0	0.89	2.17e-02	1.46e+03	3.09e-03	2.45e-02	8.83e-03	9.28e+03	4.13e-02
40.0	0.74	2.23e-02	1.56e+03	7.79e-03	2.23e-02	9.20e-03	1.15e+04	4.83e-02
60.0	0.72	2.27e-02	1.65e+03	8.32e-03	2.00e-02	9.46e-03	1.32e+04	8.68e-02
80.0	0.70	3.01e-02	1.68e+03	1.98e-02	1.83e-02	1.03e-02	1.48e+04	8.73e-02
100.0	0.69	3.16e-02	1.67e+03	1.79e-02	1.79e-02	1.01e-02	1.50e+04	9.53e-02

Note: The properties listed are the first core radius R_{fc} (au), mass M_{fc} ($M_\odot$), temperature T_{fc} (K), and accretion rate $\dot{M}_{\text{fc}}$ ($M_\odot$/yr), and the second core radius R_{sc} (au), mass M_{sc} ($M_\odot$), temperature T_{sc} (K), and accretion rate $\dot{M}_{\text{sc}}$ ($M_\odot$/yr).

when the cloud core is at a comparatively lower density, which in turn affects the lifetime of the first and second cores. The change in optical depth shown in Fig. 3.3*j* as the cloud core evolves is mainly governed by the balance between radiative cooling and compressional heating. The sharp dissociation front seen in Fig. 3.3*l* indicates that most of the H_2 is dissociated at the second core accretion shock.

The first core radius R_{fc} is defined by the position of the outer discontinuity in the density profile or shock position in the velocity profile. The first core radius increases with an increase in the initial cloud core mass up to around $8 - 10 \ M_\odot$ after which there is a decrease in the first core radius with an increase in the cloud core mass (see inset in the radial density profile; Fig. 3.3*a*).

For the initial cloud cores of masses $40 \ M_\odot$, $60 \ M_\odot$, $80 \ M_\odot$, and $100 \ M_\odot$, the first core barely forms and the evolution proceeds rapidly to the second collapse phase. For these cases, since the ram pressure ($P_{\text{ram}} = \rho u^2$) is always higher than the thermal pressure P_{gas} both above and below the first core radius (see Fig. 3.3*h*), gravity acts as a dominant force that prevents a strong first accretion shock. These high-mass cloud cores also have the highest accretion rate and are the most unstable, which is why they evolve faster. In summary, in the high-mass regime, first cores do not exist. For comparison with the low- and intermediate-mass regimes, the shock-like velocity structure is still referred to as an "accretion shock" and the first core-like structure is referred to as a "first core" even in the high-mass regime.

The second core radius R_{sc} is defined by the position of the inner discontinuity in the density profile or inner shock position in the velocity profile. The main properties of the first and second cores for each of the different cases are listed in Table 3.2. The tabulated properties are the first core mass M_{fc}, temperature T_{fc}, and accretion rate $\dot{M}_{\text{fc}}$ calculated at the first core radius R_{fc} and the second core mass M_{sc}, temperature T_{sc}, and accretion rate $\dot{M}_{\text{sc}}$ calculated at the second core radius R_{sc}.

3.3 Properties of the first hydrostatic core

3.3.1 Dependence on initial cloud core mass

This section highlights the dependence of the first core properties on the initial cloud core mass. Our results indicate slight differences (within an order of magnitude) in the first core radius and mass for the collapse simulations with different initial cloud core masses. In our studies, because we span a wide range from 0.5 $M_\odot$ to 100 $M_\odot$, we are able to see a transition region around $8 - 10\ M_\odot$. Although the differences in the first core properties are within an order of magnitude, we would like to draw more attention to the diminishing first core lifetimes for higher initial cloud core masses. This in turn affects the size and mass of the first core.

The evolution of the first core radius from the onset of the first core formation until the second core formation is shown in the left panel in Fig. 3.4. The first core undergoes an initial contraction phase followed by a rapid expansion and a second contraction phase. As already noted, the first core radius increases with an increase in the cloud core mass until around $8 - 10\ M_\odot$ after which it decreases. The right panel in Fig. 3.4 shows the mean first core radius as a function of the initial cloud core mass, where the mean radius is calculated over time from the onset of the first core formation until the second core formation. The vertical lines span the minimum to maximum first core radius as the core evolves. The transition around $8 - 10\ M_\odot$ is also seen for the first core mass (see left panel in Fig. 3.5), whereas the first core temperature always increases with an increase in the initial cloud core mass (see right panel in Fig. 3.5).

The left panel of Fig. 3.6 shows the onset of the first core formation as a function of initial cloud core mass. In the low-mass range ($M_0 \leq 8\ M_\odot$), the cloud core undergoes a comparatively slower collapse, hence initiating the first core formation after 5000 – 18000 years. On the other hand, in the intermediate- and high-mass regimes, the collapse is much faster, with the first core forming after a few thousand years (≤ 5000 years) followed by an instantaneous second collapse phase that prevents the first core from growing.

The right panel of Fig. 3.6 shows the first core lifetime as a function of initial cloud core mass. The first core lifetime is defined as the time between the onset of formation of the first core until the onset of the second core formation. Since we stop our simulations a few years after the second core formation, the total simulation time minus the first core formation time is almost equivalent to the first core lifetime.

As seen in all the previous studies, we also note that in the low-mass regime ($\leq 8\ M_\odot$) the first core lifetime scales as $M^{-0.5}$ as seen in Fig. 3.6. In the intermediate- and high-mass regimes due to the vanishing thermal pressure support, this dependence changes to $M^{-2.5}$ (see Fig. 3.6), which can be analytically derived as follows. The accretion energy $\dot{E}$ is given as

$$\dot{E} = \frac{E_\mathrm{fc}}{\tau_\mathrm{fc}} \propto \frac{GM_\mathrm{fc}}{R_\mathrm{fc}}\dot{M}_\mathrm{fc}, \tag{3.1}$$

where M_fc is the mass enclosed within the first core, R_fc is the first core radius, τ_fc is the first core lifetime, and $\dot{M}_\mathrm{fc}$ is the accretion rate. The internal energy profiles seen in Fig. 3.3i look strikingly similar at the onset of the second collapse phase (i.e. at $T \approx 2000$ K) for all the different initial cloud core masses. This indicates that indeed the internal energy of the first core E_fc, at the onset of the second collapse phase is independent of the initial cloud core mass.
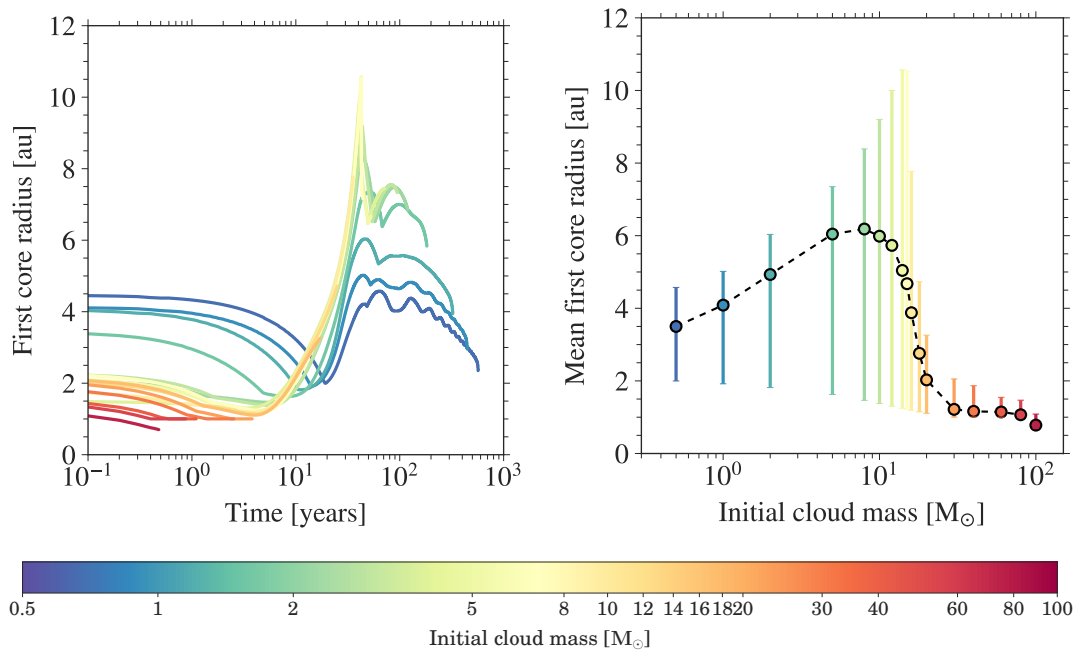
Figure 3.4: *Left:* Time evolution of the first core radius showing an initial contraction phase followed by a rapid expansion and a second contraction phase. The colours indicate the different initial cloud core masses ranging from 0.5 $M_\odot$ to 100 $M_\odot$ as shown in the colour bar. *Right:* Mean first core radius as a function of initial cloud core mass estimated at a time after the second core formation when the first core is stable and no longer evolves. The mean radius is calculated over the time from the onset of the first core formation until the second core formation. The vertical lines span the minimum to maximum first core radius as the core evolves. A transition region around $8-10\,M_\odot$ indicates the diminishing first core radius and mass towards the high-mass regime.
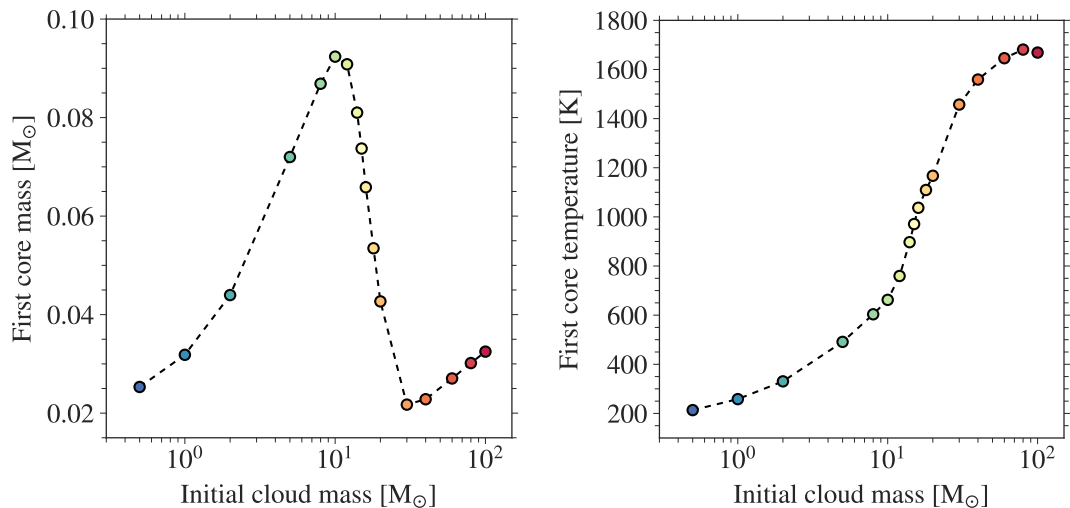
Figure 3.5: Dependence of the first core properties on initial cloud core mass. Shown on the left is the first core enclosed mass and on the right is the outer shock temperature as a function of initial cloud core mass, estimated at a time after the second core formation when the first core is stable and no longer evolves.
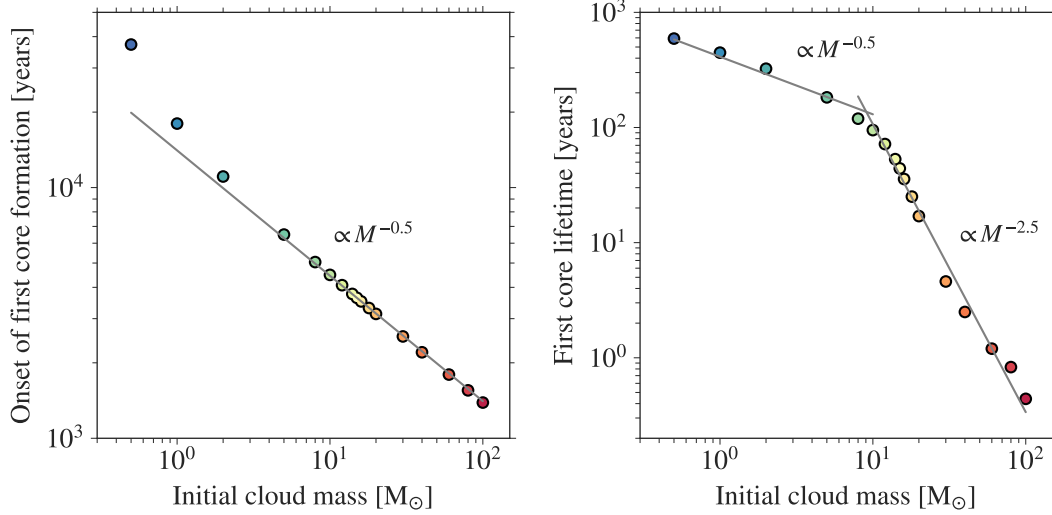
Figure 3.6: Shown on the left is the onset of formation of the first core for different initial cloud core masses. Shown on the right is the first core lifetime, estimated as the time between the onset of formation of the first and second cores for different initial cloud core masses. Cloud cores in the high-mass regime tend to collapse faster in comparison to the low-mass regime.

We consider the ratio M_{fc}/R_{fc} and multiply and divide by the velocity u_{fc} as follows:

$$\frac{M_{fc}}{R_{fc}} = \frac{4\pi}{3}\rho_{fc}R_{fc}^2 = \frac{4\pi\rho_{fc}R_{fc}^2 u_{fc}}{3 u_{fc}} = \frac{\dot{M}_{fc}}{3 u_{fc}}. \tag{3.2}$$

Inserting this into the expression for the accretion energy $\dot{E}$ yields

$$\dot{E} \propto \frac{GM_{fc}}{R_{fc}}\dot{M}_{fc} \propto \frac{G\dot{M}_{fc}^2}{3 u_{fc}}. \tag{3.3}$$

In the intermediate- and high-mass regimes, we assume the entire cloud core to be in free-fall and hence we can relate the local properties to the large scale properties. The accretion rate $\dot{M}_{fc}$ is then defined as

$$\dot{M}_{fc} = \frac{M_0}{t_{ff}}, \tag{3.4}$$

where t_{ff} is the free-fall time. We then assume that the accretion is constant in space (and time), which is valid only for a $\rho \propto R^{-2}$ profile, seen in the outer parts of a Bonnor–Ebert sphere like density profile. In this case, the mean velocity u_{fc} can be estimated as

$$u_{fc} = \frac{R_{cloud}}{t_{ff}}. \tag{3.5}$$

The free-fall time of a collapsing cloud core is given by

$$t_{ff} = \sqrt{\frac{3\pi}{32G\rho_c}} \propto \sqrt{\frac{R_{cloud}^3}{M_0}}. \tag{3.6}$$
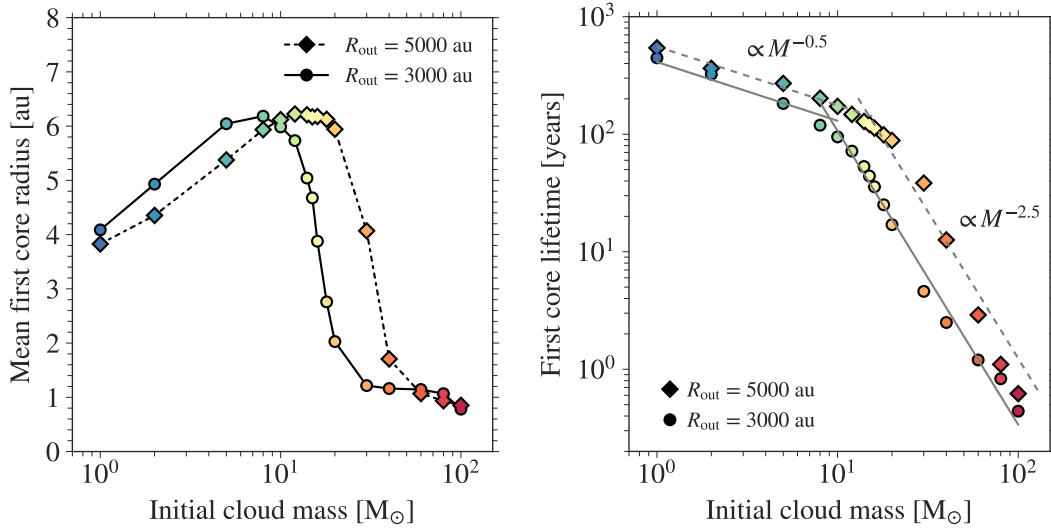
Figure 3.7: Shown on the left is the mean first core radius as a function of initial cloud core mass. The mean radius is calculated over the time from the onset of the first core formation until the second core formation. Shown on the right is the first core lifetime, estimated as the time between the onset of formation of the first and second cores for different initial cloud core masses. Both panels show comparisons between two different sets of simulations with outer cloud core radii of 3000 au (circles) and 5000 au (diamonds).

Using these relations in the expression for accretion energy $\dot{E}$, Eq. (3.3) yields

$$\dot{E} \propto \frac{\dot{M}_{\mathrm{fc}}^2}{u_{\mathrm{fc}}} \propto \left(\frac{M_0}{R_{\mathrm{cloud}}} \right)^{5/2}. \tag{3.7}$$

Furthermore, from Eq. (3.1)

$$\tau_{\mathrm{fc}} \propto \frac{1}{\dot{E}} \propto \left(\frac{R_{\mathrm{cloud}}}{M_0} \right)^{5/2}. \tag{3.8}$$

Thus in the intermediate- and high-mass regimes, the first core lifetime scales as $M^{-2.5}$ as seen in Fig. 3.6. The dependence on the cloud core radius is seen in Fig. 3.7 and discussed in Sect. 3.3.2.

3.3.2 Dependence on initial cloud core radius

In order to test the robustness of the transition region seen in the first core properties as described in our results, we perform an additional set of simulations spanning initial cloud core masses from $1 - 100\ M_\odot$ at a constant initial temperature of 10 K, but with a larger outer radius R_{cloud} of 5000 au, as listed in Table 3.3. The computational grid for these simulations comprises of 4568 cells. We use 320 uniformly spaced cells from 10^{-4} au to 10^{-2} au and 4248 logarithmically spaced cells from 10^{-2} au to 5000 au. We again make sure that the last uniform cell and the first logarithmic cell are identical in size as described previously in Sect. 2.5.1.

Figure 3.7 shows an increase in the mean first core radius until $12 - 14\ M_\odot$ beyond which it decreases towards the high-mass regime. Figure 3.7 indicates a shorter

Table 3.3: Initial cloud core properties

M_0 ($M_\odot$)	R_{cloud} (au)	T_0 (K)	M_{BE}/M_0	ρ_{c} (g cm^{-3})
1.0	5000	10.0	8.78e-01	5.04e-18
2.0	5000	10.0	4.39e-01	1.01e-17
5.0	5000	10.0	1.76e-01	2.52e-17
8.0	5000	10.0	1.01e-01	4.03e-17
10.0	5000	10.0	8.78e-02	5.04e-17
12.0	5000	10.0	7.32e-02	6.04e-17
14.0	5000	10.0	6.27e-02	7.05e-17
15.0	5000	10.0	5.85e-02	7.55e-17
16.0	5000	10.0	5.49e-02	8.06e-17
18.0	5000	10.0	4.88e-02	9.06e-17
20.0	5000	10.0	4.39e-02	1.01e-16
30.0	5000	10.0	2.93e-02	1.51e-16
40.0	5000	10.0	2.19e-02	2.01e-16
60.0	5000	10.0	1.46e-02	3.02e-16
80.0	5000	10.0	1.01e-02	4.03e-16
100.0	5000	10.0	8.78e-03	5.04e-16

Note: Listed above are the cloud core properties for runs with different initial cloud core mass M_0 ($M_\odot$), outer radius R_{cloud} (au), temperature T_0 (K), stability parameter M_{BE}/M_0, and central density ρ_{c} (g cm^{-3}).

first core lifetime towards intermediate- and high-mass regimes. In this figure, we compare the mean first core radius and first core lifetime from the runs with an outer radius of 3000 au (shown as circles) to those with an outer radius of 5000 au (shown as diamonds). We see that the lifetime scales as $M^{-2.5}$ in the intermediate- and high-mass regimes. In this case, the fit (dashed line) also incorporates the radial dependence of $R^{-2.5}$ as derived in Sect. 3.3. We thus confirm the presence of a transition region in the intermediate-mass regime seen in the first core radius and lifetime, which indicates that first cores are essentially non-existent in the high-mass regime. We find a linear dependence of the transition mass on the initial cloud core radius.

3.3.3 Dependence on initial cloud core temperature

In order to further assess the robustness of the transition region seen in properties of the first core, we perform three additional set of simulations using a different constant stability parameter M_{BE}/M_0 for the low-mass (0.5 $M_\odot$ to 10 $M_\odot$), intermediate-mass (8 $M_\odot$ to 20 $M_\odot$), and high-mass regimes (30 $M_\odot$ to 100 $M_\odot$), respectively, with some overlap between the low and intermediate masses. This implies a change in the initial temperature for the different cases, which now varies between 5 – 100 K. We use three different stability parameters to avoid extremely high initial cloud core temperatures in the intermediate- and high-mass regimes. The outer radius in all these simulations is fixed to 3000 au. The different runs with constant stability parameters are listed in Table 3.4.

We find a transition region in the intermediate-mass regime similar to that described in Sect. 3.3. The mean first core radius increases with an increase in the initial cloud core mass until around 5 $M_\odot$ to 8 $M_\odot$ and then decreases towards the

Table 3.4: Initial cloud core properties.

M_0 ($M_\odot$)	R_{cloud} (au)	T_0 (K)	M_{BE}/M_0	ρ_{c} (g cm^{-3})
0.5	3000	5.0	5.27e-01	1.16e-17
1.0	3000	10.0	5.27e-01	2.33e-17
2.0	3000	20.0	5.27e-01	4.66e-17
5.0	3000	50.0	5.27e-01	1.16e-16
8.0	3000	80.0	5.27e-01	1.86e-16
10.0	3000	100.0	5.27e-01	2.33e-16
8.0	3000	8.0	5.27e-02	1.86e-16
10.0	3000	10.0	5.27e-02	2.33e-16
12.0	3000	12.0	5.27e-02	2.80e-16
14.0	3000	14.0	5.27e-02	3.26e-16
15.0	3000	15.0	5.27e-02	3.50e-16
16.0	3000	16.0	5.27e-02	3.73e-16
18.0	3000	18.0	5.27e-02	4.20e-16
20.0	3000	20.0	5.27e-02	4.66e-16
30.0	3000	3.0	5.27e-03	6.99e-16
40.0	3000	4.0	5.27e-03	9.33e-16
60.0	3000	6.0	5.27e-03	1.40e-15
80.0	3000	8.0	5.27e-03	1.86e-15
100.0	3000	10.0	5.27e-03	2.33e-15

Note: Listed above are the cloud core properties for runs with different initial cloud core mass M_0 ($M_\odot$), outer radius R_{cloud} (au), temperature T_0 (K), stability parameter M_{BE}/M_0, and central density ρ_{c} (g cm^{-3}).

intermediate- and high-mass regimes. We compare this to the previously described runs with a fixed initial cloud core temperature of 10 K in the left panel of Fig. 3.8.

Figure 3.8 also shows the dependence of the first core lifetime on the initial cloud core mass. It is very similar to that previously seen in Fig. 3.6, thereby confirming that the first cores are essentially non-existent in the high-mass regime. These results also indicate that the first core properties do not have a very strong dependence on the initial cloud core properties.

3.3.4 Comparisons to a uniform density cloud core

There have been previous collapse studies using a uniform density cloud core as an initial setup instead of the Bonnor–Ebert sphere like profile considered in this work. However, the uniform density cloud core eventually evolves into a Bonnor–Ebert sphere like profile (Larson, 1969; Masunaga et al., 1998). We compare the effects of uniform density and Bonnor–Ebert sphere like density profiles on the properties of the hydrostatic cores. Figure 3.9 shows the radial profiles of the density, velocity, and ratio of gas to ram pressure for collapse of a 1 $M_\odot$ cloud core for three different cases, using an initial Bonnor–Ebert sphere like profile at 10 K (blue) and uniform density profiles at 10 K (dashed red) and 30 K (dashed yellow).

For the 30 K uniform density cloud core and the 10 K Bonnor–Ebert sphere like cloud core, we note that the initial density profile does not have a significant effect on
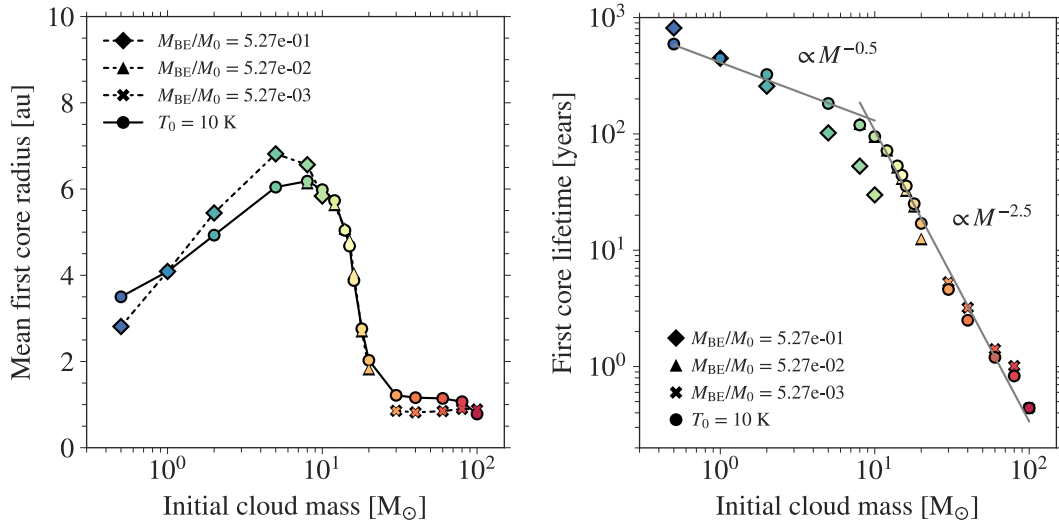
Figure 3.8: Shown on the left is the mean first core radius as a function of initial cloud core mass. The mean radius is calculated over the time from the onset of the first core formation until the second core formation. Shown on the right is the first core lifetime, estimated as the time between the onset of formation of the first and second cores for different initial cloud core masses. The circles indicate results from the simulation runs with a constant initial temperature of 10 K, whereas the diamonds, triangles, and crosses indicate results from the simulation runs with constant stability parameters M_{BE}/M_0 of 5.27e-01, 5.27e-02, and 5.27e-03 for the low-, intermediate-, and high-mass regimes, respectively.

evolution of the cloud core as also seen by Vaytet & Haugbølle (2017). However, in comparison to the Bonnor–Ebert sphere like set-up, the evolution of a uniform density cloud core is much slower ($\sim 3 \times 10^4$ years). In contrast, Masunaga & Inutsuka (2000) argued that the initial density profile does affect the protostellar evolution due to different dynamics. Since there are no significant differences between the two density profiles in our studies, we use a Bonnor–Ebert sphere like profile as the initial density profile. Vaytet & Haugbølle (2017) also suggested that a Bonnor–Ebert sphere is a better representation of the collapsing cloud core.

In case of a 10 K uniform density cloud core, we note a different behaviour. In this case, the strong ram pressure due to the high infall velocities is always higher than the gas pressure, as seen in Fig. 3.9. This may be because the cloud cores are highly unstable and gravity acts as the dominant force. Thus, there is little effect due to pressure forces, which prevents the formation of the first hydrostatic core. A similar case devoid of the first accretion shock is seen in Vaytet & Haugbølle (2017). They used an initial uniform density setup for a 4 $M_\odot$ cloud core collapse at an initial temperature of 5 K. This behaviour of the 10 K uniform density cloud core does not invalidate the previous studies that used initial uniform density, since the cloud cores were not unstable to skip the first core formation.
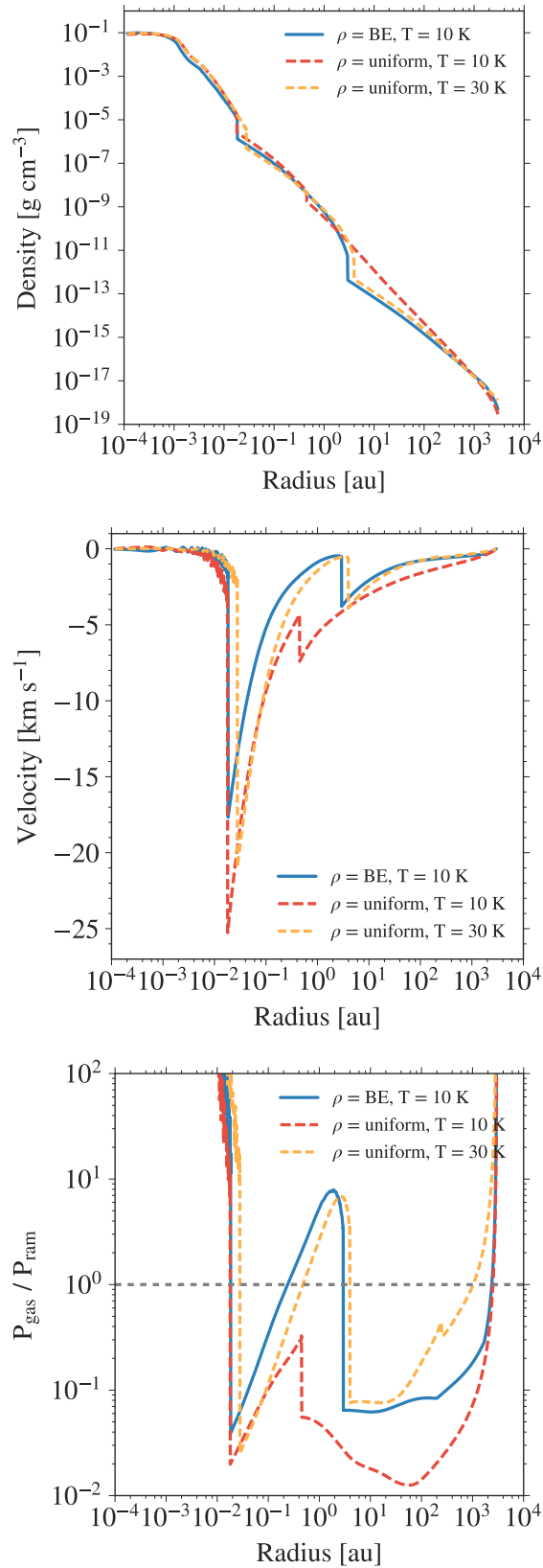
Figure 3.9: Radial profiles of the density, velocity, and the ratio of gas to ram pressure for collapse of a 1 $M_\odot$ cloud core for three different cases, using an initial Bonnor–Ebert sphere like density profile at 10 K (blue) and uniform density profiles at 10 K (dashed red) and 30 K (dashed yellow) are shown at a time snapshot after the second core formation.
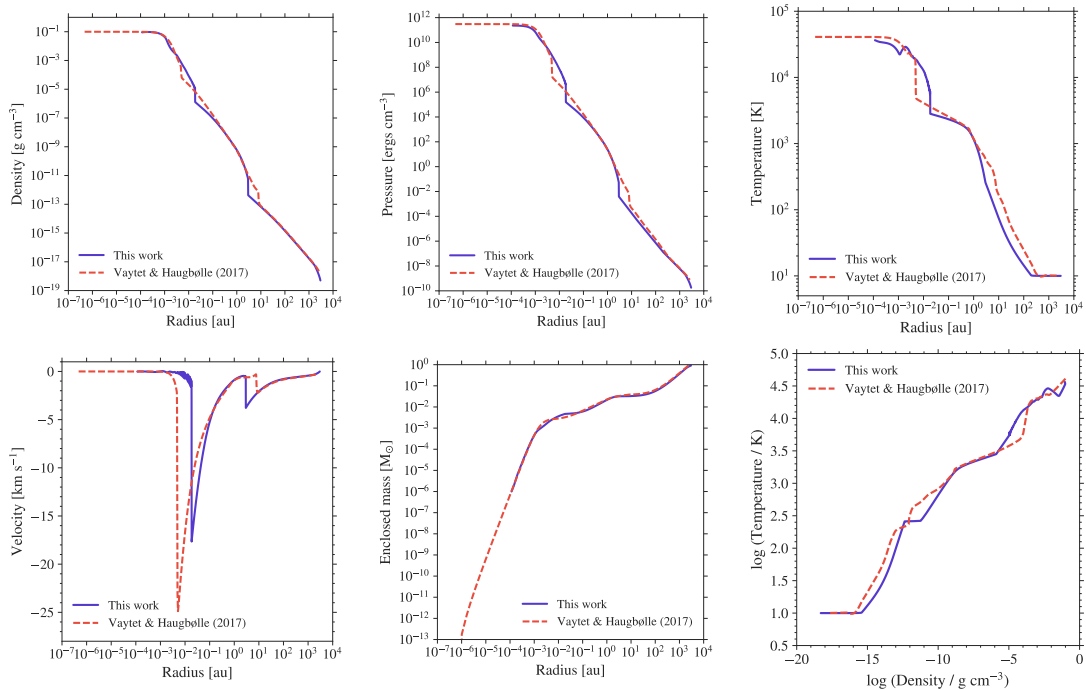
Figure 3.10: Comparisons of our results for an initial 1 $M_\odot$ cloud core indicated in bluish purple to those by Vaytet & Haugbølle (2017) shown using dashed red line. Radial profiles (across and down) of the **a)** density, **b)** pressure, **c)** gas temperature, **d)** velocity, **e)** enclosed mass, and **f)** thermal structure are shown at the time when the central density ρ_c in both simulations reaches roughly 10^{-1} g cm^{-3}.

3.4   Comparisons with previous work

In this work, we expand the parameter space of previous collapse simulations to cover a wide range of initial cloud core masses from 0.5 $M_\odot$ to 100 $M_\odot$. Figure 3.10 shows comparisons from our run for an initial 1 $M_\odot$ cloud core (bluish purple line) to those by Vaytet & Haugbølle (2017) (dashed red lines). Both the simulations use an initial Bonnor–Ebert density profile with an outer boundary $R_{\mathrm{cloud}} \approx 3000$ au, $\rho_c \approx 10^{-17}$ g cm^{-3}, and initial temperature of 10 K. We note that since the temporal evolution is slightly different in both our studies owing to the differences in the gas EOS (Saumon et al. 1995 used by Vaytet & Haugbølle 2017 versus D'Angelo & Bodenheimer 2013 used in this work), opacities, and gridding scheme (Lagrangian versus Eulerian), the comparisons are not made at the exact same time but when the central density ρ_c in both simulations reaches $\sim 10^{-1}$ g cm^{-3}.

Vaytet & Haugbølle (2017) reported a first core radius of roughly 2 au at the time of formation, which then expands to about 5 au and stays roughly constant for a few hundred years and undergoes a second expansion phase, which increases the core radius to ~ 8 au. In our simulations, the radius is also approximately 2 au at the time of formation, which then grows to about 5 au and gradually contracts back to ~ 3 au. Some earlier studies also estimate a first core radius of roughly 3 au, however the core is seen only to be contracting with time (Masunaga et al., 1998; Tomida et al., 2013). The first core lifetime is ~ 450 years in comparison to the ~ 415 years obtained by Vaytet & Haugbølle (2017) and ~ 650 years by Masunaga & Inutsuka (2000) and Tomida et al. (2013).

For an initial 1 $M_\odot$ cloud core, at the end of our simulation, the second core

radius is $\sim 3.95\ R_\odot$ in agreement with Masunaga & Inutsuka (2000, $\sim 4\ R_\odot$) and still expanding as seen by Tomida et al. (2013, $\sim 10\ R_\odot$). We note an initial contraction phase followed by an expansion due to heating or mass accumulation, as also seen by earlier studies (Larson, 1969; Masunaga & Inutsuka, 2000; Tomida et al., 2013). In comparison, Vaytet & Haugbølle (2017) obtained a much smaller second core of roughly $1\ R_\odot$ but they expect the core to expand to larger radii.

We note that Masunaga & Inutsuka (2000) assumed an initial uniform density profile with $\rho = 1.415 \times 10^{-19}$ g cm^{-3}, an outer boundary $R_{\mathrm{cloud}} = 10^4$ au, and initial temperature T_0 of 10 K, whereas Tomida et al. (2013) adopted an initial Bonnor–Ebert density profile with $\rho_c = 1.2 \times 10^{-18}$ g cm^{-3}, an outer boundary $R_{\mathrm{cloud}} \approx 8800$ au, and $T_0 = 10$ K.

Since the studies by Vaytet & Haugbølle (2017) are closest to our approach, we further investigate the differences between our results for the collapse of an initial $1\ M_\odot$ cloud core using the same temperature-dependent opacities instead of opacity tables (discussed in Sect. 3.4).

All of the previous spherically symmetric (i.e. 1D) RHD studies using frequency-dependent (Masunaga et al., 1998; Masunaga & Inutsuka, 2000) and grey FLD approximation (Vaytet & Haugbølle, 2017) and 3D RMHD simulations without rotation and magnetic fields (Tomida et al., 2013) were limited to the low-mass regime ($M_0 \leq 10\ M_\odot$). The thermal evolution and properties of the first and second cores from our low-mass runs are in good agreement with these previous works.

In their collapse calculations for the low-mass regime, Vaytet & Haugbølle (2017) showed comparisons for different initial cloud core masses ($M_0 \leq 8\ M_\odot$) at a time after the formation of the second core, which indicates that most significant differences in the radial profiles of different core properties are seen outwards from the first shock as a horizontal spread (see their Fig. 4) that is similar to our results presented in Sect. 3.2.2.

Baraffe et al. (2012), Vaytet et al. (2013), and Vaytet & Haugbølle (2017) found the first core radius and mass to be similar within an order of magnitude for their collapse simulations with different initial cloud core masses similar to the results presented herein for the low-mass regime (see Sect. 3.3). Masunaga et al. (1998) noted that the first core radius and mass are independent of the initial cloud core mass and density profile, but are weakly dependent on initial cloud core temperature and opacity. We also find this weak dependence on initial cloud core temperature as discussed in Sect. 3.3.3.

Tomida et al. (2010a) suggested that the thermal evolution may depend on the initial conditions such as cloud core mass, opacities, and temperature. In our studies, since we span a wide range of initial cloud core masses beyond $10\ M_\odot$, we find a transition region in the intermediate-mass regime, which indicates a dependence on the initial cloud core mass as discussed in the previous Sect. 3.3. We also find a linear dependence of this transition region on the initial cloud core radius (see Sect. 3.3.2).

Effect of opacities

We present comparison studies between our simulations and those kindly provided by N. Vaytet (2017, priv. comm.), mainly focussing on the effect of opacities.

As described in Sect. 3.4, since the studies by Vaytet & Haugbølle (2017) are closest to our approach we compare our results for the collapse of a $1\ M_\odot$ cloud core at an initial temperature of 10 K. We note the discrepancies due to the differences in the gas EOS (Saumon et al. (1995) used by Vaytet & Haugbølle (2017) versus
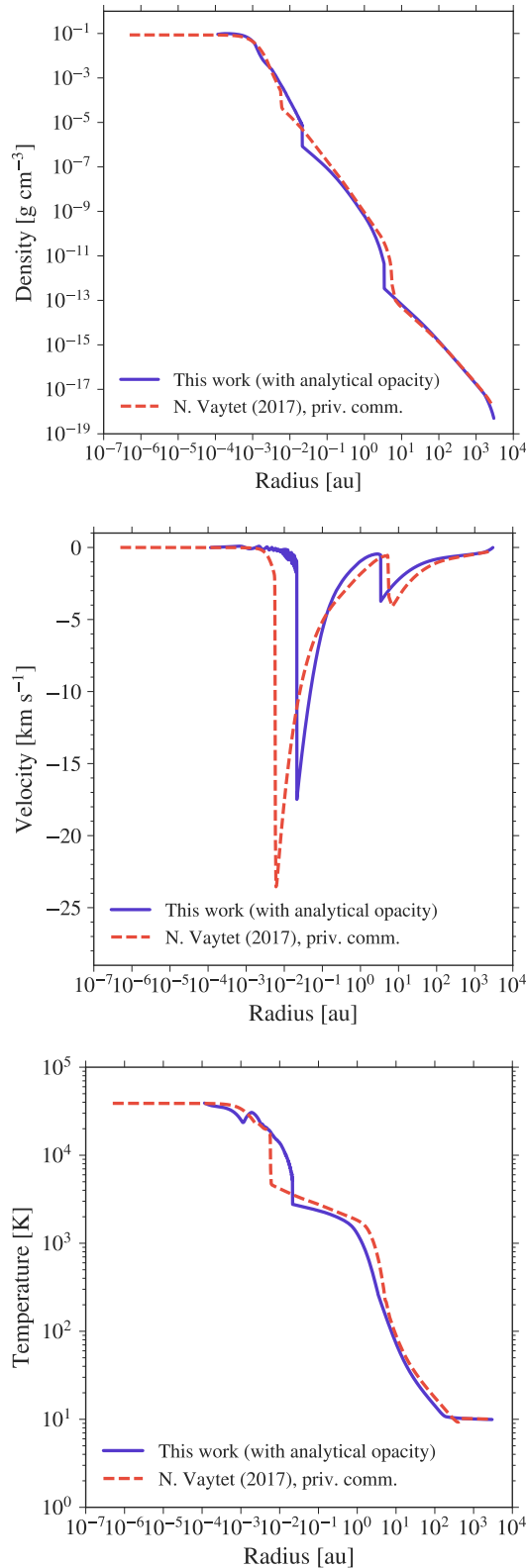
Figure 3.11: Radial profiles of the density, velocity, and gas temperature of an initial 1 $M_\odot$ cloud core at an initial temperature T_0 of 10 K are shown at the time when central density ρ_c in both simulations reaches roughly 10^{-1} g cm^{-3}. The bluish purple solid lines show results from our simulations, while the dashed red line represents results from simulations provided by N. Vaytet (2017, priv. comm.). We note that for this comparison both codes use the same temperature-dependent opacity $\kappa = 0.02\,(T/T_0)^2$ cm^2 g^{-1}.

D'Angelo & Bodenheimer (2013) used in this work), opacity tables, and gridding scheme (Lagrangian versus Eulerian) as seen in Fig. 3.10.

In order to investigate the effect of opacities, we compare our simulation for the collapse of a 1 $M_\odot$ cloud core using a temperature-dependent opacity $\kappa = 0.02 \, (T/T_0)^2$ cm^2 g^{-1} to the simulation provided by N. Vaytet (2017, priv. comm.) performed for an identical initial setup using the same temperature-dependent opacity. In both these runs, the initial temperature T_0 is 10 K. As seen in Fig. 3.11, although his simulations (dashed red line) still tend to produce a bigger first core radius, the difference is smaller compared to using different opacity tables (see Fig. 3.10). The second core does not contract as much in our simulations (bluish purple line), however as predicted the second core in his simulation may expand to obtain a value close to ours. These comparisons indicate that opacities play a role in determining the core properties but only provide some fine-tuning. Thus the main properties derived herein are still robust.

In addition, the different treatment of the gas EOS and gridding scheme may also contribute to the differences. We note that since the temporal evolution is slightly different in both our studies due to these differences, the comparisons are not made at the exact same time but when the central density ρ_c in both simulations reaches roughly 10^{-1} g cm^{-3}.

3.5 Limitations

In our studies, we use spherically symmetric models that neglect the effects of rotation and turbulence. It is however important to take into account effects due to non-negligible internal motions in molecular clouds. Rotation and magnetic fields are expected to have a significant effect on the evolution of the cloud core and properties of hydrostatic cores. In comparison to RHD simulations without rotation, depending on an ideal or resistive MHD model and how slow or fast the rotation is, Tomida et al. (2013) found significant differences mostly in the first core lifetime and second core radius (see their Table 2). Tomida et al. (2013) and Vaytet et al. (2013) suggested that the first core lifetime increases slightly in the presence of rotation since it would slow down the collapse. The lifetimes estimated in our studies can thus be considered as lower limits. Despite the absence of rotation and magnetic fields, our results can still be used as initial conditions in stellar evolution simulations.

3.6 Summary

We have performed 1D RHD simulations to model the gravitational collapse of a molecular cloud core through the formation of the first and second hydrostatic cores. As carried out by some previous studies, we emphasise on the importance of using a realistic gas EOS, which takes into account effects such as dissociation, ionisation, and rotational and vibrational degrees of freedom of H_2. This gas EOS plays a significant role in accounting for the phase transitions from the monatomic to diatomic gas.

Using an initial constant cloud core temperature ranging from 5 K to 100 K and outer radii of 3000 au and 5000 au, we model cloud cores with different initial masses spanning a range from 0.5 $M_\odot$ to 100 $M_\odot$. For each of these cases, we trace the evolution through an initial isothermal collapse phase, first core formation, adiabatic contraction, H_2 dissociation, second collapse phase, and the second core formation. The thermal evolution of the cloud core for the 1 $M_\odot$ case is summarised in Fig. 3.2.

We varied the initial cloud core mass, keeping a constant initial temperature of 10 K and an outer radius of 3000 au. We note the differences (within an order of magnitude) in the first core properties (listed in Table 3.2), although the cloud cores with different initial masses follow a similar evolution. We examine the dependence of the first core properties on the initial cloud core mass and find a transition region in the intermediate-mass regime. Our results indicate an increase in the first core radius with an increase in the initial cloud core mass until around $8 - 10 \, M_\odot$, after which the first core radius decreases towards the higher initial cloud core masses. This trend is also observed when comparing the first core mass for different initial cloud core masses.

We would like to draw more attention to the diminishing first core lifetimes for higher initial cloud core masses, which in turn affects the size and mass of the first core. It is also highly unlikely to observe first cores with such small lifetimes. Massive cloud cores have the highest accretion rate and are the most unstable, which is why they evolve faster. For these cases, since the ram pressure is higher than the gas pressure, gravity acts as a dominant force that prevents a strong accretion shock. Hence, we predict that *first cores are non-existent in the high-mass regime*.

We also investigated the influence of the outer cloud core radius on the first core properties by performing simulations with a cloud core radius of 5000 au for a constant initial temperature of 10 K. We found a similar transition region in the intermediate-mass regime. We confirmed the presence of the transition region in the intermediate-mass regime by performing an additional set of simulations. We used a different constant stability parameter M_{BE}/M_0 for the low-mass ($0.5 \, M_\odot$ to $10 \, M_\odot$), intermediate-mass ($8 \, M_\odot$ to $20 \, M_\odot$), and high-mass regimes ($30 \, M_\odot$ to $100 \, M_\odot$), respectively. This implies that the initial cloud core temperatures range from 5 K to 100 K. The outer cloud core radius for these runs was fixed to 3000 au. These results also indicate the weak dependence of the first core properties on the outer radius and initial cloud core temperature.

We note that the results for the first core lifetimes presented in this work should be treated as lower bounds on the core properties since we neglect the effects of rotation and magnetic fields, which could slow down the collapse and in turn affect the core properties. The influence of these effects on the collapsing cloud core is discussed in Chapter 5.

CHAPTER 4

Birth of a protostar

Stars form as an end product of the gravitational collapse of cold, dense gas in magnetized molecular clouds. This scenario spans a vast range of scales and occurs via the formation of two quasi-hydrostatic cores. Star formation involves complex physical processes, which require a robust, self-consistent numerical treatment as discussed in Chapter 3. Following the detailed analysis of the first core in the previous chapter, here, I first focus on the evolution and properties of the second hydrostatic core using our 1D models. Going beyond the 1D studies, we further investigate the collapse for cases of 1 $M_\odot$, 5 $M_\odot$, 10 $M_\odot$, and 20 $M_\odot$ initial non-rotating cloud cores using 2D RHD simulations with a resolution that has not been achieved before. We follow the evolution of the second hydrostatic core for ≥ 100 years after its formation, for each of these cases.

The primary aim of the work detailed in this chapter is to understand the formation and evolution of the second hydrostatic core and the dependence of its properties on the initial cloud core mass. We use the *PLUTO* code to perform high resolution 1D and 2D RHD collapse simulations. We include self-gravity and use a grey FLD approximation for the radiative transfer. Additionally, we use for the gas EOS density- and temperature-dependent thermodynamic quantities (heat capacity, mean molecular weight, etc.) to account for the effects of H_2 dissociation, ionisation of atomic hydrogen and helium, and molecular vibrations and rotations. The numerical scheme and setup is described in Chapter 2.

This chapter is structured as follows. Section 4.1 highlights the second core properties from our 1D collapse simulations for a wide range of initial cloud core masses spanning from 0.5 $M_\odot$ to 100 $M_\odot$. From Sect. 4.2 onward, the focus is on the results from our 2D simulations. In Sect. 4.2.1 the collapse scenario and resulting second core properties are discussed for the fiducial 1 $M_\odot$ molecular cloud core. The dependence of second core properties on the initial cloud core mass are presented in Sect. 4.2.2. The occurrence of the standing accretion shock instability (SASI) is discussed for each of these 2D cases in Sect. 4.2.3, which could describe the observed large-scale oscillations of the second accretion shock. Comparisons with previous studies are discussed in Sect. 4.3 and the limitations of our method are stated in Sect. 4.4. Lastly, Sect. 4.5 summarises the key findings from both our 1D and 2D collapse studies.

4.1 Second hydrostatic core in spherical symmetry

Chapter 3 highlights the outcome from our investigation of the collapse of a molecular cloud core through the phase of the first hydrostatic core formation and its evolution until the formation of the second core. In the studies presented here, we follow the

evolution of the second core for 150 – 500 years after its formation, depending on the initial cloud core mass.

The collapse of an initial isothermal molecular cloud core proceeds via a first phase of adiabatic compression and contraction, which forms the first hydrostatic core. This is followed by a second collapse, triggered due to dissociation of H_2 forming the second core, which undergoes another phase of adiabatic contraction. Figure 3.2 shows the different evolutionary stages during the collapse of a fiducial 1 $M_\odot$ cloud core in one of our simulation runs. The phase transitions at the different stages indicates the importance of using a realistic gas EOS as detailed in Sect. 2.3.

4.1.1 Dependence on initial cloud core mass

In order to investigate the dependence of the second core properties on the initial cloud core mass, we further span a wide range of cloud core masses from 0.5 $M_\odot$ to 100 $M_\odot$. Figure 4.1 shows the radial profiles of physical properties for all the different masses at a snapshot in time when the second core has evolved further and the first core no longer exists. Most of the material from the first core has been accreted on to the second core until this evolutionary stage. The accretion shock front in the radial velocity profile, which also coincides with the discontinuity in the density profile, defines the second core radius. This second shock is seen to be subcritical, that means the post-shock temperature is higher than the pre-shock temperature, suggesting that the accretion energy is transferred onto the second core and not radiated away (see discussions in Vaytet et al. 2013 and Bhandare et al. 2018, and compare to the planetary case in Marleau et al. 2017, 2019).

We compare the different cases at a point in time when the central densities are around 0.5 – 0.8 g cm^{-3} and the central temperatures are roughly 10^5 K. We note that the evolutionary timescales for the cloud cores with different initial masses are not the same, which indicates that high-mass cloud cores collapse faster than the low-mass ones. Most significant differences due to initial cloud core masses are visible outwards from the second core. The thermal structure indicates that the initially similar isothermal cloud cores eventually heat up at different densities. This has a significant effect on the formation timescale and the lifetime of the first and second cores.

The radial temperature profiles shows an off-centred peak. The location of this peak corresponds to the radial position of the plateau seen in the density profile. This off-centred peak is also seen in studies by Masunaga & Inutsuka (2000, see their Fig. 4) and Tomida et al. (2013, see their Fig. 2) (and also Winkler & Newman 1980a,b and Stahler et al. 1980a). Both these studies make use of the gas EOS by Saumon et al. (1995), which accounts for the effects of Fermi energy of the (partially) degenerate electrons. Masunaga & Inutsuka (2000) suggest that the off-centred peak seen in the temperature profile is due to partially degenerate electrons in the central region. In the off-centred region, the densities are not the highest and the thermal energy dominates the Fermi energy. There, the gas pressure is therefore more sensitive to the temperature. In the innermost regions, $P_{gas} \ll P_{deg}$ and hence there is no temperature rise. In other words, the off-centred temperature peak, for example in Masunaga & Inutsuka (2000) can be interpreted as a temperature depression in the centre. However, since the effects of Fermi energy are not included in the (ideal) gas EOS used in our models (D'Angelo & Bodenheimer, 2013), the reason for the off-centred peak in the temperature profile at the highest mass densities must be a different one in this case. The steady increase in density towards the centre of the second core due to the self-gravity of the core results in lower fraction of thermal
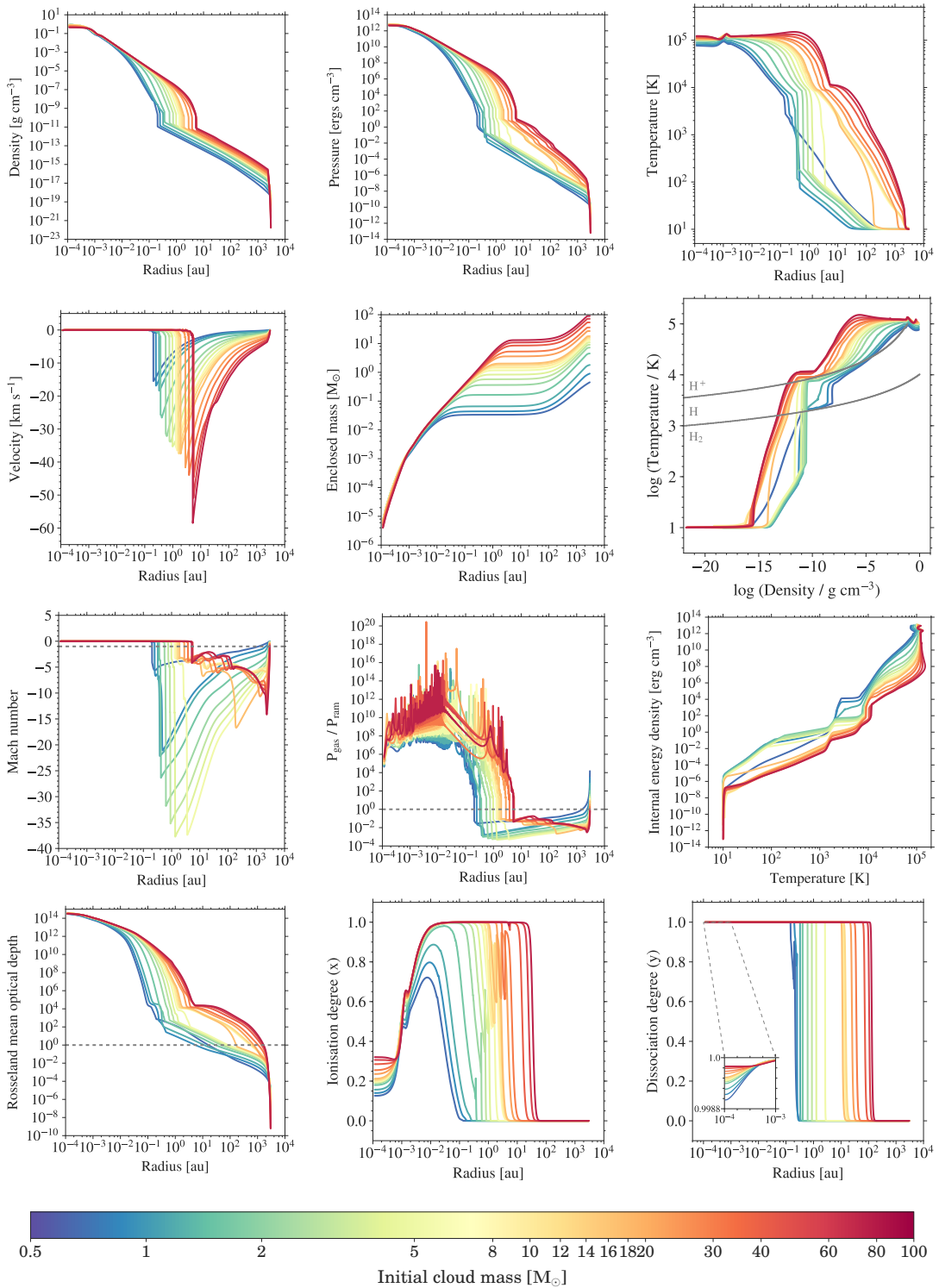
Figure 4.1: Radial profiles (across and down) of **a)** density, **b)** pressure, **c)** gas temperature (= radiation temperature), **d)** velocity, and **e)** enclosed mass as well as the **f)** thermal structure, **g)** Mach number, **h)** ratio of gas to ram pressure ($P_{\mathrm{ram}} = \rho u^2$), **i)** internal energy density as a function of temperature, **j)** optical depth, **k)** degree of ionisation (Bhandare et al., 2018, Eq. 16), and **l)** degree of dissociation (Bhandare et al., 2018, Eq. 17) for all the cases at the final simulation snapshot (final times for different cases indicated in Table 4.1) in our simulations when the central density is roughly $0.5 - 0.8\,\mathrm{g\,cm^{-3}}$. Different colours indicate cloud cores with different initial masses as seen in the colour bar. Grey lines in the thermal structure plot show the 50 % dissociation and ionisation curves.

Table 4.1: Properties of the second core estimated at the final simulation snapshot t_{final} (yr) when central density $\rho_{\text{c,final}}$ reaches $\approx 0.5 - 0.8$ g cm^{-3}, for different initial cloud core masses M_0 ($M_\odot$) with a fixed outer radius R_{cloud} of 3000 au and an initial temperature T_0 of 10 K.

M_0 ($M_\odot$)	$\rho_{\text{c,final}}$ (g cm^{-3})	t_{final} (yr)	R_{sc} (au)	M_{sc} ($M_\odot$)	T_{sc} (K)	$\dot{M}_{\text{sc}}$ ($M_\odot$ yr^{-1})	L_{acc} ($L_\odot$)
0.5	0.854	38039.76	0.203	3.36e-02	2.07e+03	3.23e-05	7.78e-01
1.0	0.851	18635.00	0.253	4.40e-02	1.79e+03	6.52e-05	1.65e+00
2.0	0.853	11543.76	0.329	6.58e-02	1.67e+03	1.52e-04	4.43e+00
5.0	0.849	6860.80	0.405	1.65e-01	1.54e+03	5.53e-04	3.27e+01
8.0	0.848	5433.00	0.613	3.62e-01	1.50e+03	1.18e-03	1.01e+02
10.0	0.853	4909.00	0.876	5.73e-01	1.56e+03	1.71e-03	1.64e+02
12.0	0.849	4530.70	0.987	8.31e-03	8.62e+03	2.32e-03	2.85e+02
14.0	0.848	4251.80	1.290	1.17e+00	8.89e+03	3.01e-03	3.97e+02
15.0	0.835	4138.62	1.359	1.36e+00	8.77e+03	3.26e-03	4.77e+02
16.0	0.825	4015.29	1.455	1.50e+00	8.77e+03	3.61e-03	5.41e+02
18.0	0.792	3799.47	1.656	1.77e+00	8.77e+03	4.34e-03	6.75e+02
20.0	0.761	3610.66	1.914	2.01e+00	8.99e+03	5.17e-03	7.93e+02
30.0	0.662	2996.06	2.829	3.57e+00	8.97e+03	9.64e-03	1.77e+03
40.0	0.596	2623.36	3.803	5.25e+00	8.96e+03	1.50e-02	3.02e+03
60.0	0.519	2160.45	5.605	8.48e+00	1.04e+04	2.77e-02	6.11e+03
80.0	0.474	1859.02	5.486	1.08e+01	1.11e+04	4.20e-02	1.21e+04
100.0	0.448	1655.55	5.206	1.31e+01	1.16e+04	5.78e-02	2.12e+04

Note: The properties listed are the second core radius R_{sc} (au), mass M_{sc} ($M_\odot$), temperature T_{sc} (K), accretion rate $\dot{M}_{\text{sc}}$ ($M_\odot$ yr^{-1}), and accretion luminosity L_{acc} ($L_\odot$).

ionisation (displayed in Fig. 4.1*k*). The associated release of energy leads to the peak in the radial temperature profile. Furthermore, in this density–temperature regime, the gas also departs from being fully thermally dissociated in hydrogen (see inset in Fig. 4.1*l*), which possibly plays a role in producing this peak.

Towards the high-mass regime, the temperature profiles of the second core becomes flat (i.e. isothermal) where the shock around $0.1 - 1$ au is hotter than in the core centre. In case this behaviour would hold as the core evolves further (in the high-mass case, accretion happens up to the ignition of hydrogen burning and longer), this will severely affect its internal evolution. The effect of the outer boundary conditions is visible in some of the profiles. For example, the sharp discontinuity seen in the temperature profiles for the high-mass cases is because the temperature at the outer boundary is set to a fixed value of 10 K. However, this does not have any significant effects on the evolution and properties of the hydrostatic cores on the smaller scales.

The bumps seen in the radial Mach number profiles for the high-mass cases are due to the behaviour of the adiabatic index Γ_1 during the dissociation and ionisation phase. In the high-mass regime, the temperature at the bump positions in the radial temperature profiles corresponds to the required temperatures for thermal hydrogen dissociation and ionisation.

The radial velocity in the inner core regions, which are in hydrostatic equilibrium, fluctuates around the zero value. This effect is visible as the noise or spikes in the radial profiles of the ratio of gas to ram pressure in Fig. 4.1*h*.

The radial profiles of the optical depth indicates that the second core is optically thick, which makes it extremely difficult to detect them observationally and trace this evolutionary stage.

The region of fully atomic hydrogen in the dissociation profile extends far beyond the second core radius. The underlying reason for this extension is that the infalling
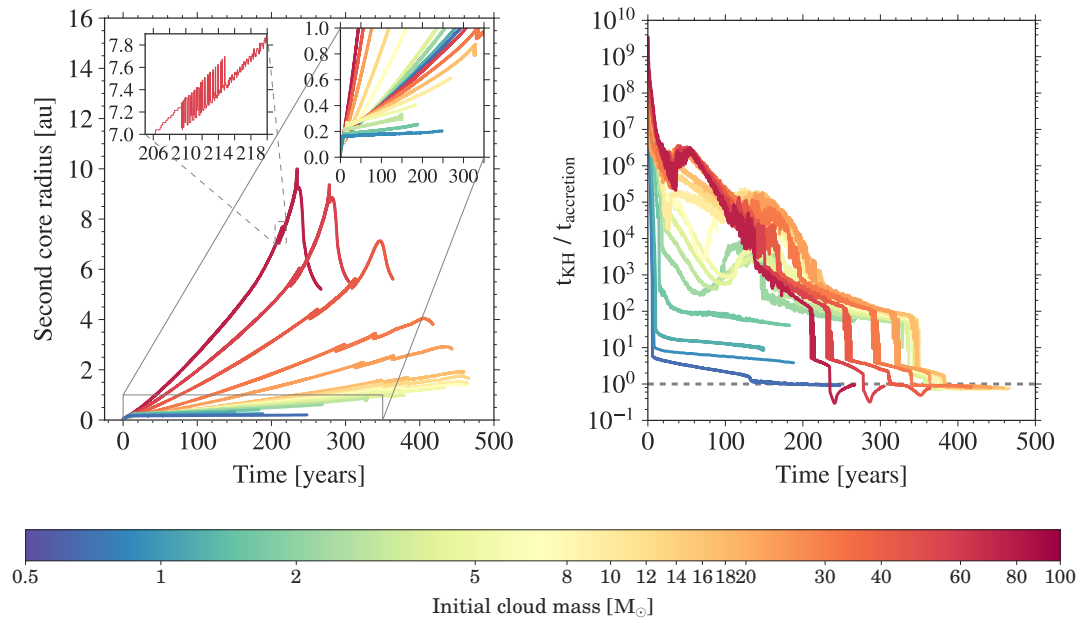
Figure 4.2: *Left panel:* Spatial evolution of the second core radius as a function of time for all the collapse scenarios with different initial cloud core masses ranging from 0.5 $M_\odot$ to 100 $M_\odot$ as indicated in the colour bar. The evolution is traced from the onset of the second core formation until the central density reaches $\approx 0.5 - 0.8$ g cm^{-3}. The inset in the upper left zooms in on the back and forth behaviour for one of the curves. This results from the jump between the two local minima in the velocity profile of the accretion shock, which is used to define the second core radius. *Right panel:* Comparison of the Kelvin–Helmholtz and accretion timescales. A large (small) ratio is associated with an expansion (contraction) phase of the second hydrostatic core (see left panel).

gas in front of the second core radius (indicated by the shock) is already heated to temperatures beyond the dissociation temperature. This effect becomes especially clear for cases of higher accretion rates (i.e. higher accretion energy).

4.1.2 Second core properties

In this section, the dependence of the second core properties on the initial cloud core mass are discussed. Figure 4.2 shows the spatial evolution of the second core radius over a period of time from the onset of the second core formation until the central density reaches $0.5 - 0.8$ g cm^{-3}. The second core radius is defined using the position of the accretion shock in the velocity profile, which is similar to the position of the discontinuity or sharp rise in the density profile. In this work, the onset of formation of the second core is defined as the time when a prominent second accretion shock is visible in the velocity profile. The central density is greater than 10^{-2} g cm^{-3} at this time snapshot in our simulations.

In the high-mass regime, we find that, initially, the second core gradually expands

with time, thus growing in size. This initial expansion occurs since the Kelvin–Helmholtz timescale[1] is much greater than the accretion timescale during this phase, as seen in the right panel in Fig. 4.2. After reaching a maximum radius, the second core undergoes a phase of contraction during which the accretion timescale dominates. We note a similar behaviour in the low-mass regime where the collapse proceeds relatively slowly.

There is a back and forth behaviour seen in the evolution of the second core radius for the intermediate- and high-mass cases (see left panel in Fig. 4.2). This effect results from the jump between the two close local minima in the velocity profile of the accretion shock, which is used to define the second core radius. Another contributing factor for this behaviour are the small-scale oscillations of the second accretion shock. Both these effects are resolved due to a high time resolution and do not affect the overall behaviour of the second core radius.

For a more quantitative comparison, Fig. 4.3 shows the second core radius, accretion rate, and accretion luminosity as a function of the enclosed mass for different initial cloud core masses. These second core properties are displayed over a period of time from the onset of the second core formation until the central density reaches $\approx 0.5 - 0.8$ g cm^{-3} as listed in Table 4.1. The accretion rate $\dot{M}_{\rm sc}$ is estimated as

$$\dot{M}_{\rm sc} = 4\pi \, R_{\rm sc}^2 \, \rho_{\rm sc} \, u_{\rm sc}, \tag{4.1}$$

where $\rho_{\rm sc}$ and $u_{\rm sc}$ are the density and velocity at the second core radius $R_{\rm sc}$, respectively. The accretion luminosity $L_{\rm acc}$ computed using the accretion rate and the enclosed mass $M_{\rm sc}$ within the second core radius is given as

$$L_{\rm acc} = \frac{GM_{\rm sc}\dot{M}_{\rm sc}}{R_{\rm sc}}. \tag{4.2}$$

The second core mass gradually increases as the core evolves through the expansion and contraction phases. As expected, higher initial cloud core masses lead to more massive second cores. Initially, material from the first core accretes onto the second core at a much faster rate of $\approx 10^{-2} \, M_\odot \, yr^{-1}$. The accretion rate slows down over time and can decrease to roughly a few times $10^{-5} \, M_\odot \, yr^{-1}$ in the low-mass end. The accretion luminosity in the high-mass regime is much higher than in the low-mass regime. Various properties of the second core are listed in Table 4.1.

---

[1]The Kelvin–Helmholtz and accretion timescales are computed using

$$t_{\rm KH} = \frac{GM_{\rm sc}^2}{L_{\rm sc} \, R_{\rm sc}} \quad \text{and} \quad t_{\rm accretion} = \frac{M_{\rm sc}}{\dot{M}_{\rm sc}},$$

respectively. Here, the luminosity $L_{\rm sc}$ is given as $L_{\rm sc} = 4\pi R_{\rm sc}^2 F_{\rm rad}$, where $F_{\rm rad}$ is the radiative flux just *outside* the second core radius, that means it includes the cooling flux from the second core as well as the accretion luminosity from the accretion shock.
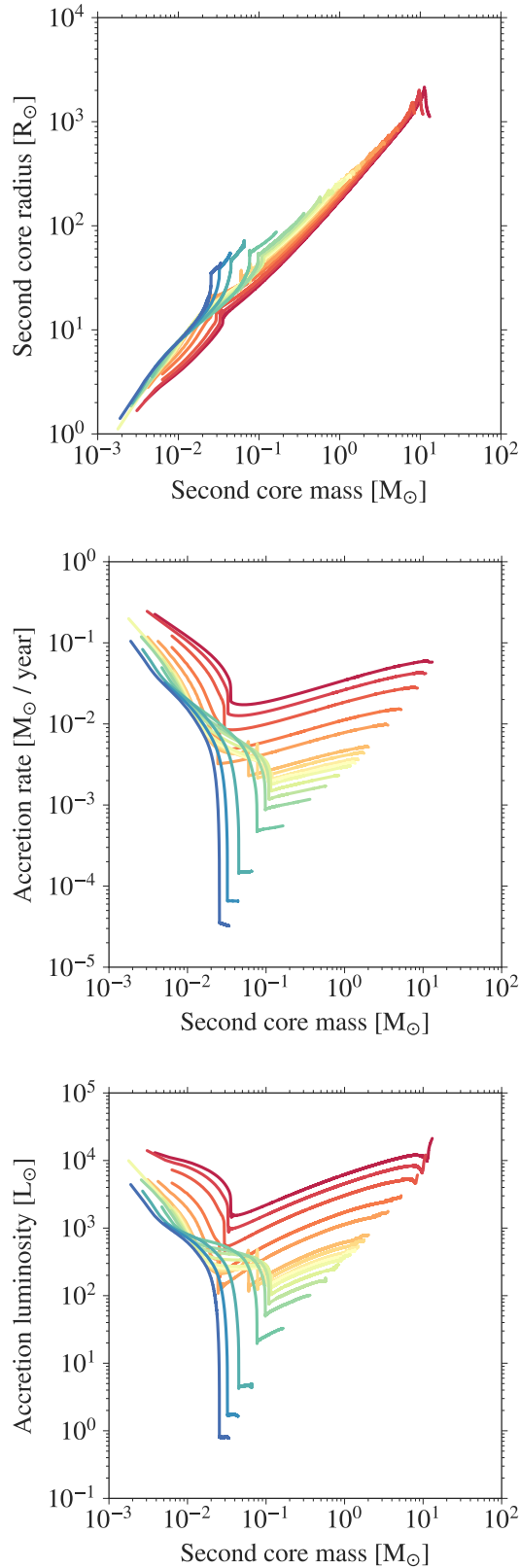
Figure 4.3: Second core radius (top), accretion rate (middle), and accretion luminosity (bottom) as a function of the enclosed mass for the collapse scenarios with different initial cloud core masses ranging from 0.5 $M_\odot$ (blue) to 100 $M_\odot$ (red). The evolution is traced from the onset of the second core formation until the central density reaches $\approx 0.5 - 0.8$ g cm^{-3}.

4.2   A two-dimensional view of the second hydrostatic core

In this section, we further expand our investigation to 2D collapse for selected initial cloud core masses of 1 $M_\odot$, 5 $M_\odot$, 10 $M_\odot$, and 20 $M_\odot$. The main aim of this study is to resolve the second core using a high resolution that has not been achieved before. The details of the computational grid and the resolution are discussed in Sect. 2.5.2.

The 2D simulations presented herein are a scaled-up version of the 1D runs; cloud core rotation is not included as the cloud core is initialised as being at rest. We use the same initial conditions as discussed in Sect. 2.5 with a fixed outer radius of 3000 au and a constant initial temperature of 10 K. We account for the effects of self-gravity, radiation, and phase transitions on the evolution of these pre-stellar cores.

4.2.1   Evolution of a fiducial 1 $M_\odot$ pre-stellar core

In this section, we first focus on the fiducial 1 $M_\odot$ case, which evolves through the two stages of the first and second collapse. Figure 4.4 shows temperature snapshots at different stages of the evolution zooming into a 3000 au cloud core down to 10^{-2} au (i.e. sub-au scales), thus covering five orders of magnitude in spatial scale.

We follow the evolution of the second core for 312 years after its formation where the onset $t = 0$ is defined when a prominent second accretion shock is seen in the velocity profile. The central temperature at this stage is around 40000 K. The gas and radiation temperatures are equal everywhere in our simulations.

Figure 4.5 shows the radial profiles of different properties of the cloud core at the final time snapshot (312 years after second core formation) of our simulation. The gradient from light to dark blue covers the polar angle range from the midplane ($\theta = 90°$) to the pole ($\theta = 0°$), respectively. We also compare this to the results from our 1D collapse studies of a 1 $M_\odot$ cloud core, which is indicated by the dashed red line in all the subplots in Fig. 4.5. The drop seen in the innermost part of the radial temperature profile is dependent on the inner radius and hence is affected by the inner boundary conditions. However, as discussed in Appendix A.1.2, this does not affect the second core properties nor violates energy conservation at the inner boundary.

As expected, the same initial conditions lead to similar evolution in 1D and 2D. In both cases, the cloud core has evolved through the two phases of the first and second collapse, until a stage where the first core is no longer present and only the second core is visible, as indicated by the accretion shock in the radial velocity profile.

The four panels in Fig. 4.6, showing the 2D view of the second hydrostatic core (zooming into the inner 0.5 au), indicate the Mach number, density, temperature, and entropy structure of the second core. The infalling gas flow and internal mixing are indicated by the black velocity streamlines. The white contour in Fig. 4.6 (panel *a*) indicates Mach number equal to 1.0. This sets a clear separation between the supersonic outer region and the subsonic second core. This transition is also seen as the strong jump in the radial Mach profile in Fig. 4.5 at the second core radius. The contour lines in the density panel are labelled with density values at the different radial positions, marking an increase towards the centre, which confirms the non-homologous behaviour of the collapsing cloud core. Similar behaviour is seen in the temperature panel with the core centre having the highest value.

We show the entropy panel again in Fig. 4.7 and plot it there with Line Integral Convolution to highlight the turbulent features within the second core. The entropy is calculated by the Sackur–Tetrode equation, which is consistent with the D'Angelo & Bodenheimer (2013) EOS used in our simulation and takes into account
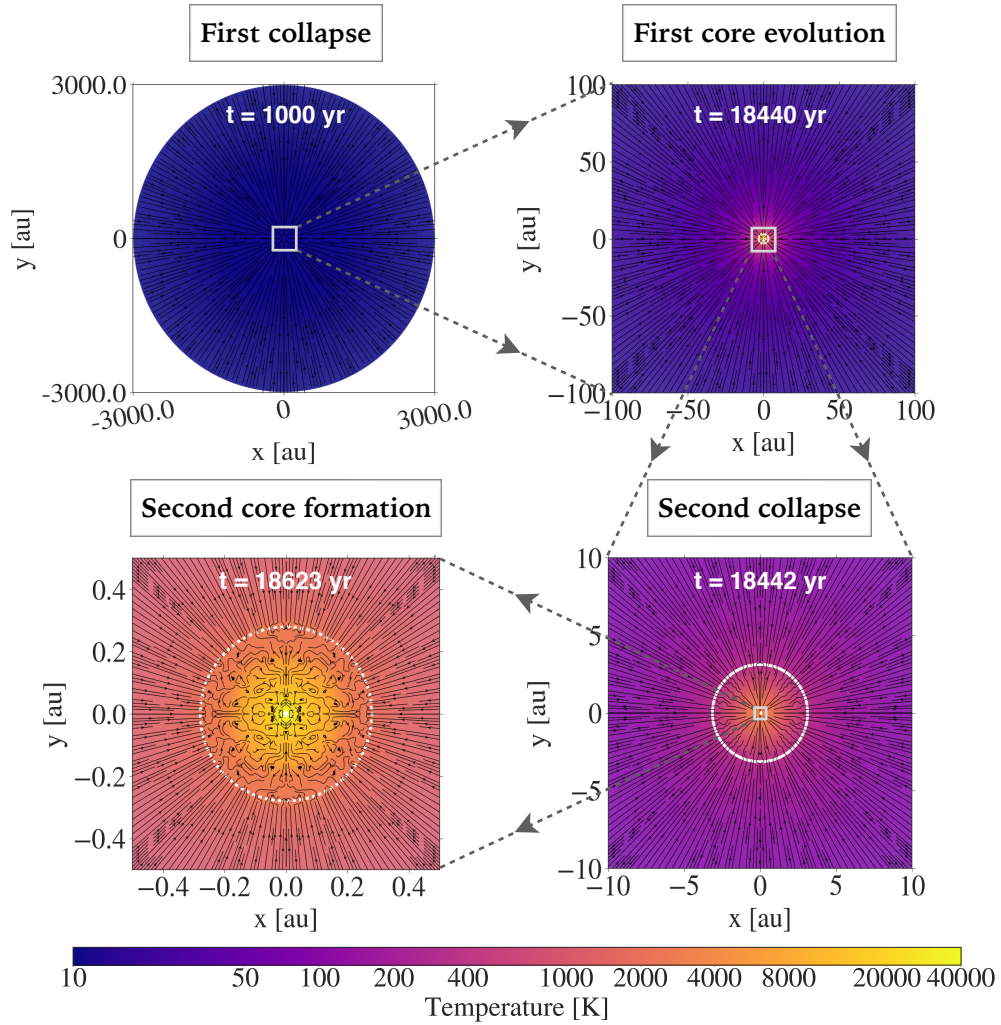
Figure 4.4: 2D temperature snapshots zooming into sub-au scales showing the evolution of a 1 $M_\odot$ cloud core with an initial temperature of 10 K and outer radius of 3000 au. The velocity streamlines (in black) indicate the infalling material and the mixing within the second core at the last time snapshot. The solid and dotted white contours indicate the first and second accretion shocks, respectively. Note the different spatial scales from top left to bottom left.

the molecular, atomic, and ionised hydrogen as well as the contribution from the electrons. It therefore represents a straightforward extension of the expressions in Berardo et al. (2017, Appendix A), the details of which will be provided in Marleau et al. (in prep.). We verified that the two agree well where ionisation (not included in Berardo et al. 2017) is not important.

The entropy gradient is also seen in the radial profile in Fig. 4.7, zoomed into the inner 1 au. A convective instability is known to occur when a lower-entropy fluid lies above a higher-entropy fluid as seen in the region below the second accretion shock at the second core radius in Figs. 4.6 and 4.7. We interpret our results to mean that the instability is generated by the shock and grows radially inwards as the second core evolves over time. The entropy is generated at the accretion shock and this yields a gradient from the high entropy at the shock towards the second core interior. Thus, convection is triggered in the outer layers of the second core at the accretion shock
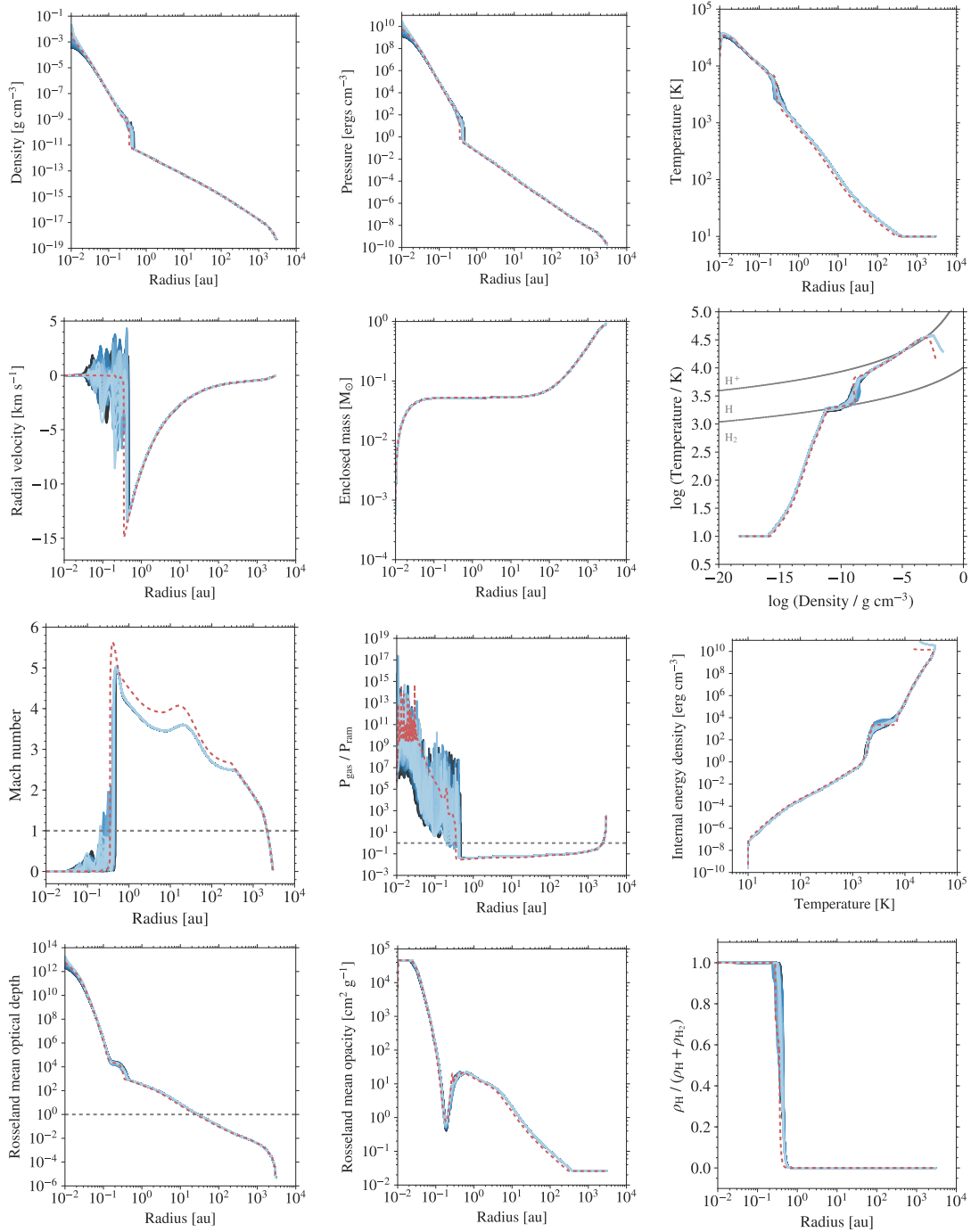
Figure 4.5: Radial profiles (across and down) at 312 years after formation of the second core, formed due to the collapse of a 1 $M_\odot$ cloud core with an outer radius of 3000 au and an initial temperature of 10 K. The different subplots show the radial profiles (across and down) of **a)** density, **b)** pressure, **c)** gas temperature, **d)** radial velocity, and **e)** enclosed mass as well as the **f)** thermal structure, **g)** Mach number, **h)** ratio of gas to ram pressure ($P_{ram} = \rho u^2$), **i)** internal energy density as a function of temperature, **j)** optical depth, **k)** Rosseland mean opacity, and **l)** dissociation fraction. The colour gradient from light to dark blue spans the polar angle from the midplane ($\theta = 90°$) to the pole ($\theta = 0°$). The grey lines in the thermal structure plot show the 50 % dissociation and ionisation curves. The radial profiles from the 1D collapse simulation for the same initial conditions and resolution are over-plotted as a dashed red line in all the subplots.
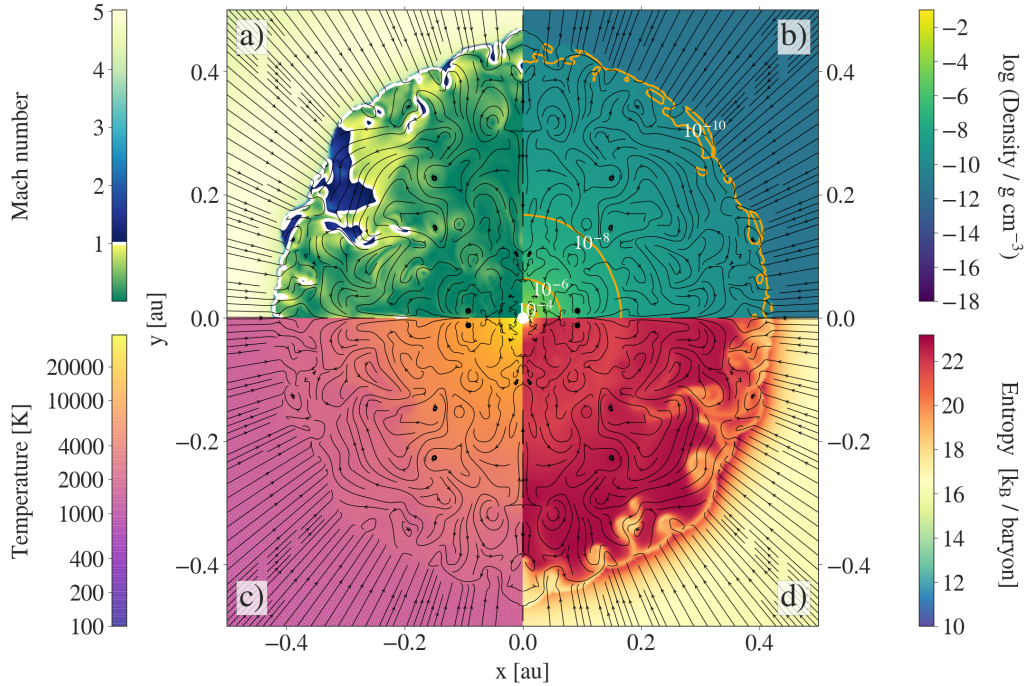
Figure 4.6: 2D view of the second hydrostatic core at 312 years after its formation as a result of the collapse of a 1 $M_\odot$ cloud core at an initial temperature of 10 K. The four panels show the **a)** Mach number, **b)** density, **c)** temperature, and **d)** entropy within the inner 0.5 au of a 3000 au collapsing cloud core. The velocity streamlines in black indicate the material falling onto the second core and the mixing inside the convective second core. The white contour in panel *a* indicates Mach = 1.0 and separates the sub- and supersonic regions. The different contour lines in panel *b* mark the increase in density towards the centre. When displayed in Adobe Acrobat, it is possible to switch to view the properties of the first core at the snapshot of the onset of the second core formation. A movie[2] of the entire collapse is available online.

and drives the eddies inwards (visualised in a movie[2] of the simulation results).

In Fig. 4.7, we also compare the radial entropy profile from our 1D (dashed red line) and 2D studies. Since there is no convection in 1D, entropy is generated and increases at the shock position. In comparison, since energy generated at the accretion shock is transported due to convection in the 2D case, the entropy profile flattens.

Figure 4.8 shows the spatial and temporal evolution of the polar-angle averaged radial entropy profile for a 1 $M_\odot$ collapsing cloud core with an initial temperature T_0 of 10 K and an outer radius of 3000 au. The two peaks in the entropy profile at earlier time snapshots (dashed red and yellow lines) are seen at the positions of the first and second accretion shocks. As the cloud core evolves further, material from the first core is accreted onto the second core and the first shock disappears.

In order to further investigate this behaviour within the second core, we compare in Fig. 4.9 the actual ratio of the temperature and pressure gradients ∇_{act} to the adiabatic gradient ∇_{ad}, which is the gradient at constant entropy. In a (quasi-)static
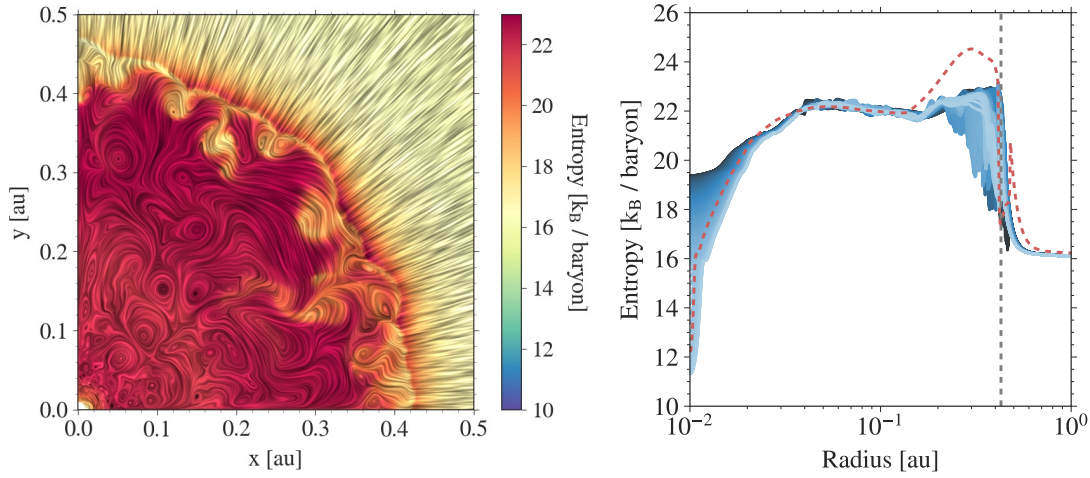
Figure 4.7: *Left:* Line integral convolution visualisation of the entropy behaviour indicating the presence of eddies within the second core. Shown here is the inner 0.5 au of the 3000 au collapsing 1 $M_\odot$ cloud core at 312 years after the formation of the second core. *Right:* Radial entropy profile for the 1 $M_\odot$ case, within the inner 1 au of the 3000 au collapsing cloud core at 312 years after the formation of the second core. The vertical grey dashed line indicates the radius of the second core. The colour gradient from light to dark blue spans the polar angle from the midplane ($\theta = 90°$) to the pole ($\theta = 0°$). The dashed red line shows the radial profile from the 1D collapse simulation for the same initial conditions and resolution, which by definition omits the effect of convection.
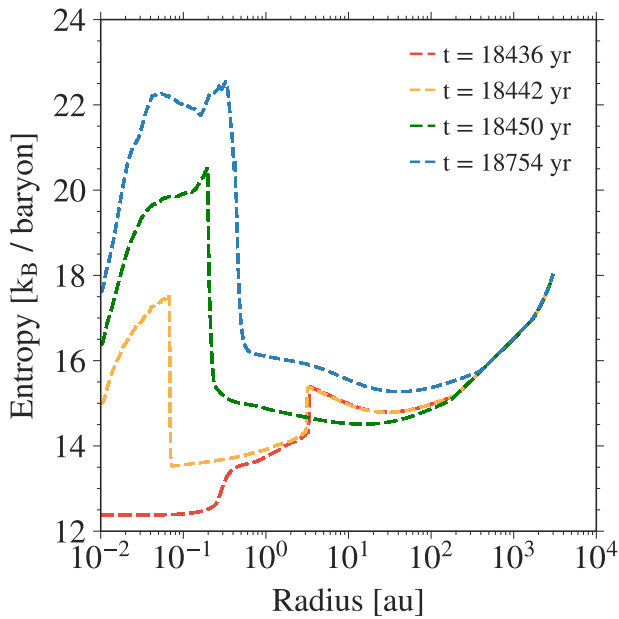
Figure 4.8: Polar-angle averaged radial entropy profiles are shown at four different time snapshots as a 1 $M_\odot$ cloud core transitions through the formation and evolution of the first and second hydrostatic cores.
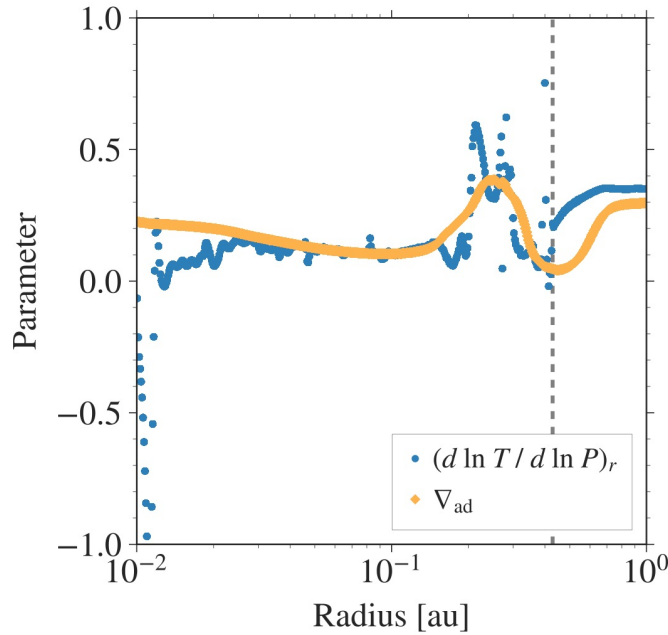
Figure 4.9: Polar-angle averaged actual temperature gradient $\nabla_{\rm act}(r)$ at 312 years after the formation of the second core in the 1 $M_\odot$ case compared to the polar-angle averaged adiabatic gradient $\nabla_{\rm ad}(\rho(r), T(r))$ (see Eq. 4.3). Classically, regions with $\nabla_{\rm act} > \nabla_{\rm ad}$ are convectively unstable. The vertical dashed line indicates the radius of the second core.

fluid, convective motions are expected if

$$\nabla_{\rm act} \equiv \left(\frac{d \ln T}{d \ln P} \right)_r > \left(\frac{d \ln T}{d \ln P} \right)_{\rm ad} \equiv \nabla_{\rm ad}. \tag{4.3}$$

We calculate $\nabla_{\rm ad}$ according to Hansen et al. (2004, Eq. 3.98) using simple differentiation of the $P(\rho, T)$ function provided by the Vaidya et al. (2015) implementation of the D'Angelo & Bodenheimer (2013) EOS.

The dashed grey line in Fig. 4.9 indicates the radius of the second core. The region interior to this radius is convectively unstable. Due to the high resolution, the grid cell size in our simulations is roughly an order of magnitude smaller than the pressure scale height, thus allowing us to resolve the convection. A comparison between different resolutions is shown in Appendix A.2, which indicates the need to use such high resolution in order to resolve the eddies.

Convection allows mixing within a star and contributes by being an efficient means of heat transport. We find that at this evolutionary stage, the energy flux is still dominated by radiation, however the convective flux can become stronger at later stages.

4.2.2   Dependence on initial cloud core mass

We further investigate the evolution of collapsing cloud cores with initial masses of 5 $M_\odot$, 10 $M_\odot$, and 20 $M_\odot$, thus covering a few cases in the intermediate- and high-mass regimes. The same initial temperature of 10 K and outer cloud core radius of 3000 au are used as in the 1 $M_\odot$ case. We study the effects of initial cloud core mass on the convective instability discussed in Sect. 4.2.1. Similar to the 1 $M_\odot$ case, for the 5 $M_\odot$, 10 $M_\odot$, and 20 $M_\odot$ runs, we find a turbulent pattern within the second core, indicated by the black velocity streamlines in Fig. 4.10 and seen as the eddies in Fig. 4.11. The plots are shown at 128 years, 91.4 years, and 86.4 years after the second core formation, for the 5 $M_\odot$, 10 $M_\odot$, and 20 $M_\odot$ cases, respectively.
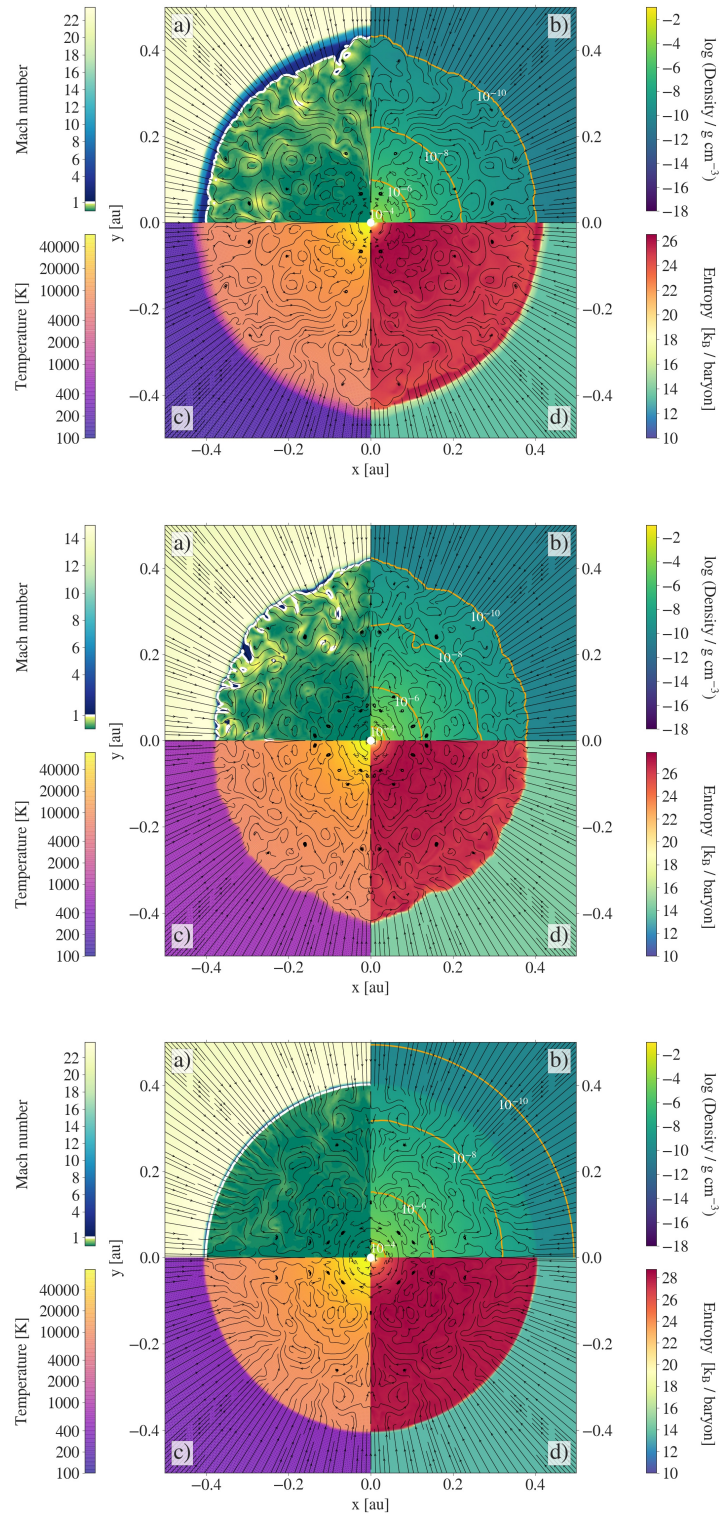
Figure 4.10: 2D view of the second hydrostatic core formed as a result of the collapse of a 5 $M_\odot$ (top), 10 $M_\odot$ (middle), and 20 $M_\odot$ (bottom) cloud core at an initial temperature of 10 K. The four panels in each of the subplots show the **a)** Mach number, **b)** density, **c)** temperature, and **d)** entropy within the inner 0.5 au of an initial 3000 au cloud core. The velocity streamlines in black indicate the material falling onto the second core and the mixing inside the core. The white contour in panel *a* indicates Mach = 1.0 and separates the sub- and supersonic regions. The different contour lines in panel *b* show the increase in density towards the centre. The plots are shown at 128 years, 91.4 years, and 86.4 years after the second core formation, for the 5 $M_\odot$, 10 $M_\odot$, and 20 $M_\odot$ cases, respectively.
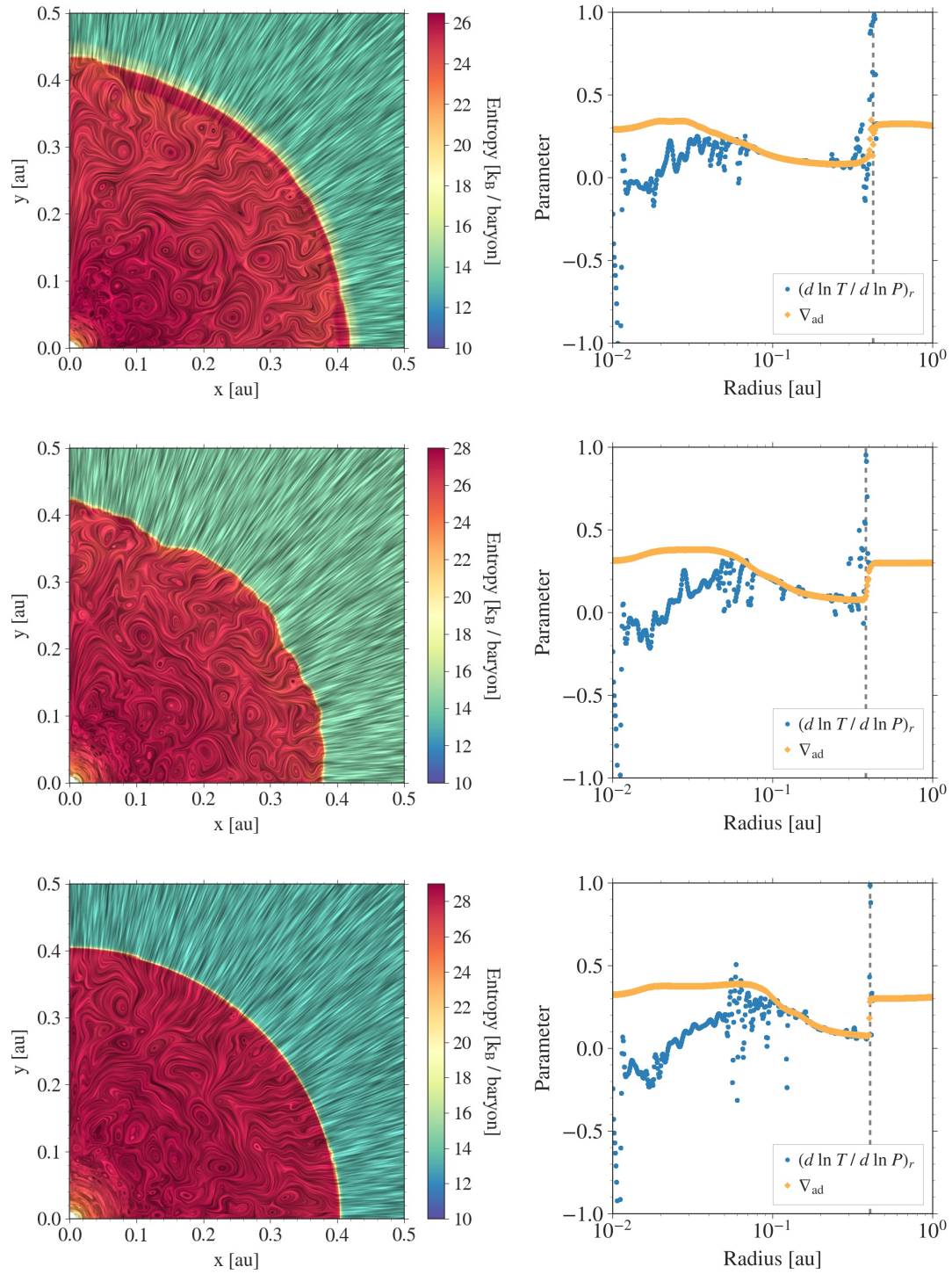
Figure 4.11: *Left column:* Line integral convolution visualisation of the entropy behaviour indicating the presence of eddies within the second core. Shown here are the inner 0.5 au of 3000 au collapsing cloud cores with different masses of 5 $M_\odot$ (top), 10 $M_\odot$ (middle), and 20 $M_\odot$ (bottom). *Right column:* Polar-angle averaged actual temperature gradient $\nabla_{\mathrm{act}}(r)$ compared to the polar-angle averaged adiabatic gradient $\nabla_{\mathrm{ad}}(\rho(r), T(r))$ (see Eq. 4.3) for the 5 $M_\odot$ (top), 10 $M_\odot$ (middle), and 20 $M_\odot$ (bottom) initial cloud core masses. The indication for convective instability is not as prominent as in the 1 $M_\odot$ case (see Fig. 4.9). The vertical grey dashed line indicates the radius of the second core. The plots are shown at 128 years, 91.4 years, and 86.4 years after the second core formation, for the 5 $M_\odot$, 10 $M_\odot$, and 20 $M_\odot$ cases, respectively.

Figure 4.11 shows the comparison between the adiabatic index and the ratio of temperature and pressure gradients. On testing the criterion for convective instability stated in Eq. (4.3), we do not find a strong indication as seen in the 1 $M_\odot$ case. However, this may change as the second core evolves further for these cases. We are currently unable to further follow the evolution of the second core due to high computational expenses and this remains to be tested as part of future studies.

Figure 4.12 shows the evolution of the second core radius, mass, and accretion rate for all the cases with different initial cloud core mass. The time $t = 0$ marks the onset of the second core formation, which is indicated by a prominent second accretion shock as per our definition. Higher initial cloud core mass leads to a faster collapse. Following the evolution, our results indicate that the 1 $M_\odot$ and 5 $M_\odot$ cloud cores will eventually form a protostar with a mass less than 0.5 $M_\odot$. Stars within this mass range are known to be fully convective throughout their life.

4.2.3   Standing accretion shock instability

In this section, we further investigate the source of the turbulence visible in the post-shock regions. The standing (or spherical) accretion shock instability, known to play a crucial role in the explosion mechanism of core collapse supernovae, induces large-scale non-spherical oscillations of the shock (Foglizzo & Tagger, 2000; Foglizzo, 2002; Blondin et al., 2003; Foglizzo et al., 2006; Guilet & Foglizzo, 2012). There are two proposed mechanisms that lead to the linear growth of this instability, one being the interplay between advected entropy–vorticity perturbations and acoustic waves (Foglizzo et al., 2007; Foglizzo, 2009), whereas the second is a purely acoustic mechanism, which assumes that the trapped acoustic waves can be amplified by the shock (Blondin & Mezzacappa, 2006).

During the evolution of the second core in our collapse simulations, we observed some non-spherical, large-scale oscillations of the accretion shock front in the 1 $M_\odot$, 5 $M_\odot$, and 10 $M_\odot$ cases and comparatively small-scale oscillations of the accretion shock front for the 20 $M_\odot$ case. In their study, Scheck et al. (2008) have reported that large-amplitude SASI oscillations produce strong variations in the entropy, which can drive convective instability in the supernova core.

We further investigate the presence of the SASI in the case of protostellar cores and its role to generate turbulence behind the shock for all the different collapse scenarios. Large-scale, non-spherical oscillations of the second accretion shock front are indicated by the black line in Fig. 4.13. For a quantitative analysis of the SASI, following Scheck et al. (2008), Fig. 4.13 shows the advected perturbations in terms of the amplitudes of the largest modes of the spherical harmonics of the quantity $A(t, r, \theta)$ given by

$$A(t, r, \theta) = \frac{1}{\sin\theta} \frac{\partial}{\partial\theta} (v_\theta(t, r, \theta) \sin\theta). \qquad (4.4)$$

The term $r^{-1}A$ is the divergence of the lateral velocity component.

Several works have shown that the SASI can be measured more easily by determining A even for lower amplitudes of the instability (Scheck et al., 2008; Blondin & Mezzacappa, 2006). For all the cases with different initial cloud core masses, we plot the amplitude for a small time interval since it helps to view the perturbations better. Although the amplitudes show more complex patterns than in Scheck et al. (2008, see their Fig. 12), there are some noticeable advected trajectories as well as some acoustic feedback. The characteristic acoustic feedback timescale is given by
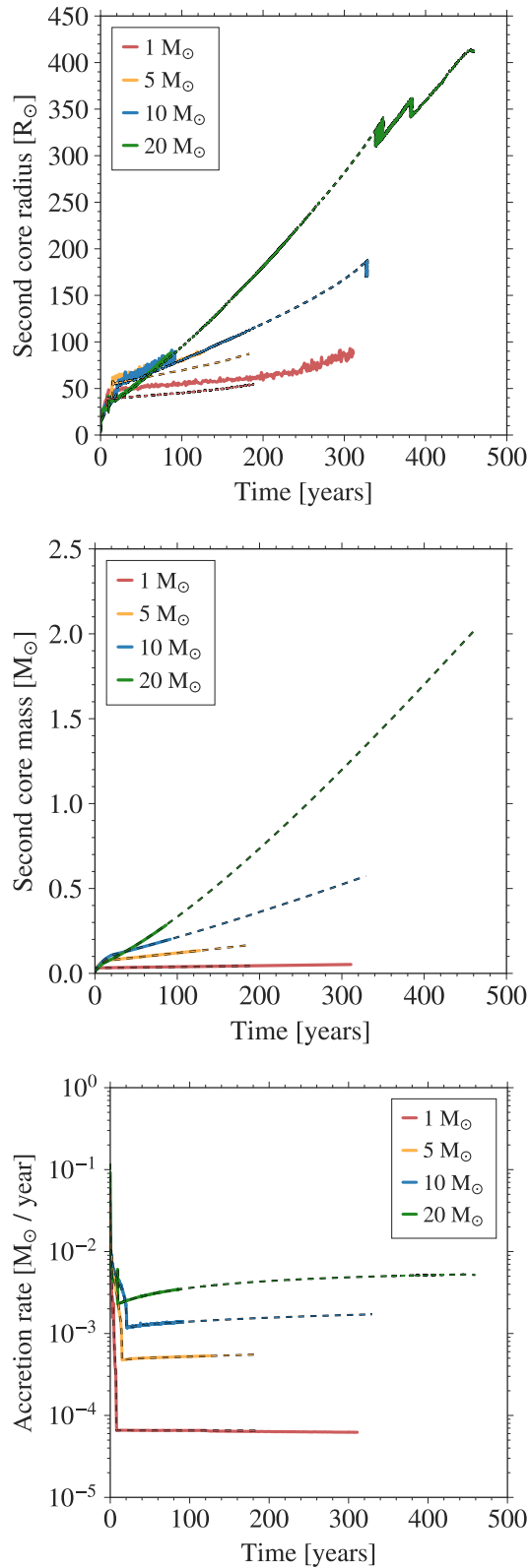
Figure 4.12: Time evolution of the second core radius (top), mass (middle), and accretion rate (bottom) for the different core collapse scenarios with initial cloud core masses of 1 $M_\odot$ (red), 5 $M_\odot$ (yellow), 10 $M_\odot$ (blue), and 20 $M_\odot$ (green). Time $t = 0$ marks the onset of the second core formation. The over-plotted dashed lines indicate the evolution from the high-resolution 1D simulations discussed in Sect. 4.1.2.
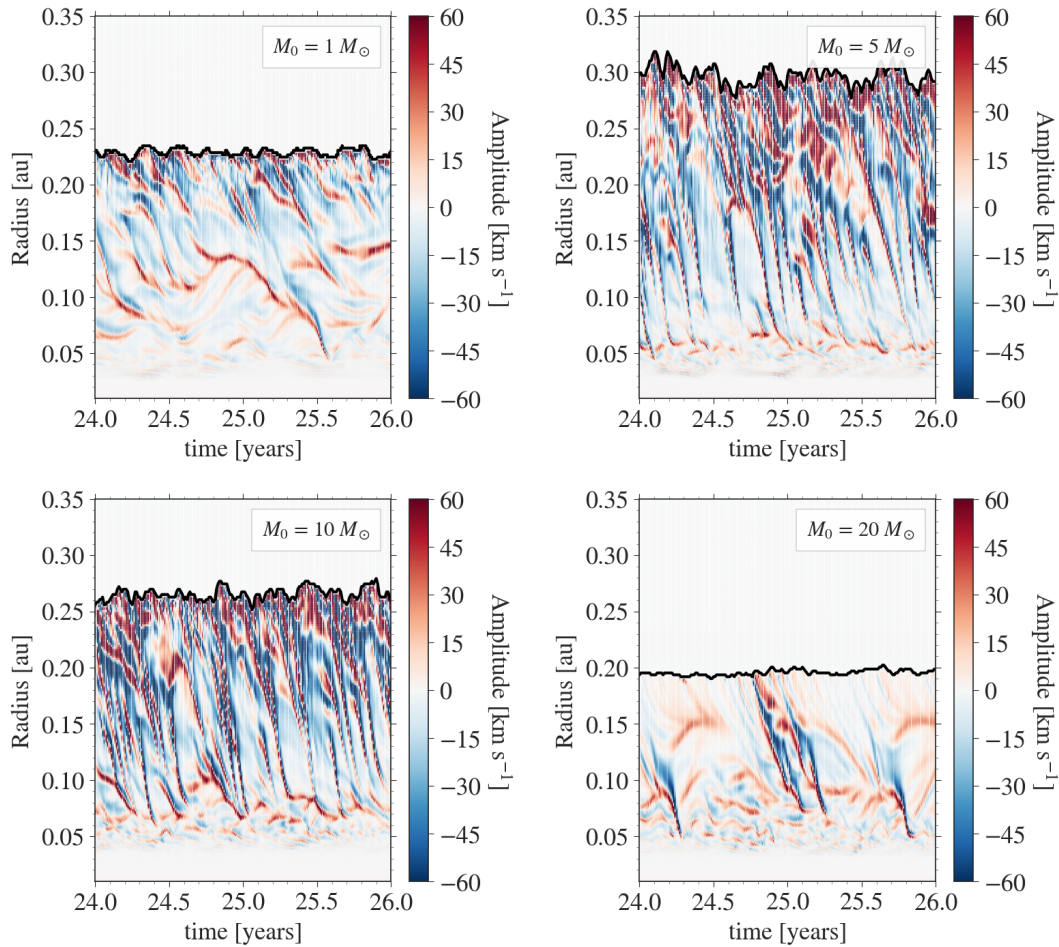
Figure 4.13: Time evolution of the amplitude of the dominant spherical harmonics mode of the quantity $A(t, r, \theta)$ from Eq. (4.4) as a function of radius. The second core radius is shown by the black line. Time $t = 0$ indicates the onset of the second core formation for the different collapse scenarios. Shown here is a small interval in time for the 1 $M_\odot$ (top left), 5 $M_\odot$ (top right), 10 $M_\odot$ (bottom left), and 20 $M_\odot$ (bottom right) cases.

the sound crossing time from the centre of the second core to the accretion shock and back.

We thus conclude that the SASI may not be operating as strongly as seen in the supernovae core-collapse studies and the convective instability seems to be the main source of the turbulent cells seen in the post-shock regions. However, the SASI could still be responsible for the large scale oscillations of the accretion shock front seen during the evolution of the second core. Nonetheless, it is interesting to note that the SASI can operate in different regimes.

4.3   Comparisons with previous work

In this section, we compare the second core properties from our 1D and 2D simulations to some of the previous studies for the case of a collapsing 1 $M_\odot$ cloud core.

In their study, Masunaga & Inutsuka (2000) use a uniform initial density profile with a density of 1.415×10^{-19} g cm^{-3} and an outer radius of 10^4 au. A few years[3] after the formation of the second core, when the central density reaches ≈ 1 g cm^{-3}, they find the second core radius to be ≈ 4 $R_\odot$ and the second core mass as 0.73 $M_\odot$. On the other hand, at central density greater than 10^{-1} g cm^{-3}, Tomida et al. (2013) report a bigger second core radius of ≈ 10 $R_\odot$ enclosing a mass of 2×10^{-2} $M_\odot$ within 0.7 years after its formation[4]. They suggest that the second core continues to expand during the main accretion phase. Their simulations are stopped once the central temperature reaches 10^5 K. In their work, they adopt a Bonnor–Ebert sphere like density profile with an initial central density of 1.2×10^{-18} g cm^{-3} and an outer radius of 8800 au.

In Fig. 4.14, we compare the behaviour of the density and temperature from our 1D simulations (bluish purple) to those by Vaytet & Haugbølle (2017, dashed red), since their method is closest to ours, at a snapshot when the central density is roughly 10^{-1} g cm^{-3}. Both studies use the same initial conditions for the collapse of a 1 $M_\odot$ cloud core with an initial temperature of 10 K, outer radius of 3000 au, and an initial Bonnor–Ebert sphere like density profile. We note some differences in the profiles which arise due to the different gas EOS (Saumon et al. (1995) used by Vaytet & Haugbølle (2017) versus D'Angelo & Bodenheimer (2013) used in this work), opacities, and grid schemes (Lagrangian versus Eulerian). Moreover, both simulations are not compared at the same time in evolution (see also discussion in Sect. 3.4). When comparing the studies, these differences in the numerical methods also lead to discrepancies in the second core properties, for example in the second core radius and enclosed mass. Vaytet & Haugbølle (2017) report a smaller second core radius of ≈ 1 $R_\odot$ with an enclosed mass of 2.62×10^{-3} $M_\odot$. They expect the second core to grow in size due to further heating and mass accretion from the infalling envelope. In this work, at a similar central density of 9.6×10^{-2} g cm^{-3}, we find the second core radius to be ≈ 4 $R_\odot$ with an enclosed mass of 5.12×10^{-3} $M_\odot$.

In our simulations, we follow the evolution of the second core for 188.2 years after the second core formation (see Fig. 4.2). At the final simulation time snapshot, our results indicate that as the central density reaches 0.85 g cm^{-3} the second core radius grows to be much bigger ≈ 54 $R_\odot$ with a mass of 4.40×10^{-2} $M_\odot$. As demonstrated in Fig. 4.2, the expansion and contraction of the evolving second Larson core is controlled by the timescale ratio of Kelvin–Helmholtz contraction versus accretion.

Figure 4.14 also shows the comparison of the radial entropy profile. The two peaks seen in the entropy correspond to the positions of the first and second accretion shocks in both 1D studies. In Appendix A.2, we discuss the dependence of entropy on the numerical resolution. In Sect. 4.2.1, we have already discussed the change in the entropy profile as the cloud core evolves beyond the formation of the second core in our 2D simulations.

Schönke & Tscharnuter (2011) followed the collapse of a 1 $M_\odot$ cloud core using grid-based 2D RHD simulations for up to 240 years after the formation of the second core. They included an initial uniform rotation of their cloud core and could hence also investigate the early phases of disc formation. In order to evolve the system for a longer duration, they replaced the physical domain within 0.7 au with a sink prescription once the second core reached a quasi-static state. Their main goal was to investigate the effect of hydrodynamically driven turbulence using a β-viscosity prescription. In their models with $\beta = 10^{-3}$ and $\beta = 10^{-2}$ they have described

---

[3]See Table 1 in Masunaga & Inutsuka (2000) for their simulation run-time.
[4]Tomida et al. (2013) define the onset of second core formation at the time when the central density exceeds 10^{-3} g cm^{-3} in their simulations.
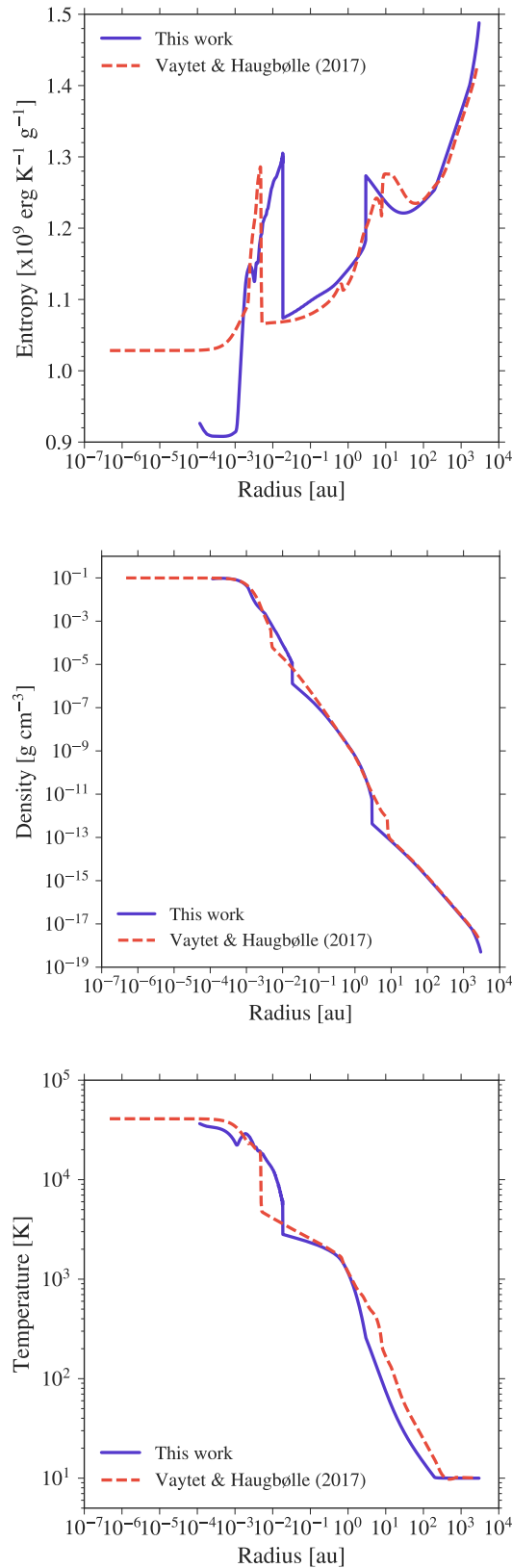
Figure 4.14: Comparisons of our results for an initial 1 $M_\odot$ cloud core indicated in bluish purple to those by Vaytet & Haugbølle (2017) shown using dashed red line (see also Fig. 3.10). Radial entropy (top), density (middle), and temperature (bottom) profiles are compared at the time when the central density ρ_c in both simulations reaches $\sim 10^{-1}$ g cm^{-3}.

dynamically unstable layers as a consequence of dust evaporation in the central regions within the inner 3 au. They also indicate the occurrence of convection seen via temperature gradients and the presence of a strong vortex in this innermost region.

In the 2D studies presented here, we observe some short-lived unstable regions within the first accretion shock during the evolution of the *first* core but without any prominent vortices or a convective instability. However, as discussed in Sect. 4.2.1, we observe convection in the outer layers of the *second* core, which eventually evolves to become the protostar. The ability to follow the evolution for 312 years after the formation of the second core allows us to trace the evolution of the eddies and we find that the convective instability grows radially inwards from the second shock as the second core evolves over time.

4.4 Limitations

The simulations discussed in this chapter include the effects of self-gravity, radiation transport, dissociation, and ionisation on the core properties. However, we do not include the effects of rotation. We discuss the effects of initial cloud core rotation and magnetic fields on the properties of the hydrostatic cores and young discs in Chapter 5. Magnetic fields are likely to affect the formation and evolution of the second core. However, convective instability within the second core, at least for the low-mass end, could still be generated during the core evolution.

The 2D simulations do not stay spherically symmetric. Hence, the evolution of the convective second core will also not stay axially symmetric. Unfortunately, a 3D model achieving the same resolution as in the axisymmetric and midplane symmetric 2D simulations presented here is unfeasible at the moment.

4.5 Summary

The collapse of a molecular cloud core proceeds through an initial isothermal phase, leading to the formation of the first hydrostatic core, which undergoes an adiabatic contraction phase. This is followed by the second collapse phase, triggered by the dissociation of H_2 once the central temperature rises above 2000 K. The second hydrostatic core is formed as a result of this process once most of the H_2 is dissociated.

This chapter highlights our results from the investigation of the gravitational collapse of molecular cloud cores using 1D and 2D RHD simulations. We include self-gravity and radiation transport. Additionally, the gas EOS takes into account rotational and vibrational degrees of freedom for the H_2 molecules, which start being excited as the cloud core transitions from being effectively monatomic to diatomic, as well as their dissociation and ionisation.

For the 1D studies, we model cloud cores with an initial constant temperature of 10 K, a fixed outer radius of 3000 au, and masses that span a wide range from 0.5 $M_\odot$ to 100 $M_\odot$. We further expand our collapse studies to 2D with an identical initial setup as in the 1D runs. We model 3000 au non-rotating cloud cores with masses of 1 $M_\odot$, 5 $M_\odot$, 10 $M_\odot$, and 20 $M_\odot$, thus covering a few cases in the low-, intermediate-, and high-mass regime.

Both the 1D and 2D studies focus on the formation and evolution of the second Larson core. The key findings of these simulation runs can be summarised as follows. Our 1D studies indicate that the cloud cores with an initial higher mass collapse faster and form bigger, more massive second cores. We describe the dependence

of the second core properties such as the radius, mass, accretion rate, and accretion luminosity on the initial cloud core mass. We discuss the expansion and contraction of the evolving second Larson core, which is controlled by the timescale ratio of Kelvin–Helmholtz contraction versus accretion. As expected, the accretion rate in the high-mass regime is much higher than in the low-mass end. Here we investigated cases in which the higher-mass molecular cloud cores are gravitationally more unstable than in the low-mass regime. A parameter study using different initial cloud core temperatures and outer radii for various initial cloud core masses is discussed in Chapter 3. The results presented herein are consistent with previous core collapse studies in the low-mass regime.

Circumstellar discs form as a consequence of the conservation of angular momentum around stars. Currently, evolving the disc until the Class 0 phase is often hindered due to time step restrictions and hence most studies replace the central (second) core with a sink particle. The influence of a sink particle on disc formation has been extensively discussed in Wurster & Li (2018). Data from the 1D studies presented herein can be used as a lookup-table to compute the evolution of the central object (i.e. protostar) for a longer duration, within a sink-cell paradigm.

Using our 2D setup for the four non-rotating collapse cases, we follow the evolution of the second core for ≥ 100 years after its formation. For the 1 $M_\odot$ case, we follow the evolution of the second core for 312 years after its formation. Our 2D studies show that the accretion shock leads to a convective instability in the outer layers of the second hydrostatic core, which grows radially inward over time. Due to the high resolution in our simulations (≈ 10 cells per pressure scale height below the shock), we can resolve the convective cells for the first time. *For the 1 $M_\odot$ case, we find convection being driven from the accretion shock towards the interior of the second Larson core.* In contrast to fully convective stars, here, the energy is not generated at the stellar centre, but is provided by the accretion energy from outside the core. Investigating the evolution from these early convective phases due to accretion up to fully convective low-mass stars due to hydrogen burning remains a challenging task for future research in stellar physics.

The origin of magnetic fields in low-mass stars is still a matter of debate. Several studies speculate that the fields are either dominated by primordial or fossil-fields or are replaced by dynamo-generated fields within the first 100 years of evolution. Since young low-mass stars are observed to have strong ($>$ kilogauss) magnetic field strengths, the likelihood of a fossil field could be excluded for cases where the magnetic field amplitude in the second core at birth is found to be less than a kilogauss. In this work, since we already observe convection in the outer layers of the second hydrostatic core, further evolution may enable the generation of a convective-dynamo (Chabrier & Küker, 2006). This would support the interesting possibility that dynamo-driven magnetic fields may be generated during this very early phase of low-mass star formation.

The simulations presented herein do not account for effects due to initial cloud core rotation and magnetic fields. Although both of these will affect the evolution of the second core and its properties, we predict that convection seen in our studies should still be generated during this collapse phase in the low-mass regime.

Protostellar discs and outflows

Magnetized molecular clouds provide the birth environment for stars, discs, and planets. The gravitational collapse of cold, dense, gaseous, and dusty cores within these clouds leads to the formation of stars. Several numerical studies, using both grid-based simulations (including Bhandare et al., 2018, 2020) and SPH methods, have deduced that star formation occurs via a two-step process of the formation of first and second quasi-hydrostatic Larson cores (Larson, 1969). During these collapse phases, the conservation of angular momentum can lead to the formation of a Keplerian disc around the second core (i.e. the forming protostar), which can eventually host planet(s). The combination of cloud rotation and magnetic fields can also drive outflows and jets from these quasi-hydrostatic cores, which act as mechanisms for angular momentum transport.

So far, in the previous chapters, we have detailed results from our numerical investigation of the gravitational collapse of isolated, non-rotating molecular cloud cores. However, observations suggest that molecular cloud cores have magnetic energy comparable to or less than the gravitational energy (Crutcher, 1999; Bourke et al., 2001; Troland & Crutcher, 2008) and have rotational energy in the range of $10^{-4} \leq E_{\rm rot}/E_{\rm grav} \leq 0.07$ (Arquilla & Goldsmith, 1986; Goodman et al., 1993; Caselli et al., 2002). Hence, in this chapter, we discuss the effects of initial cloud core rotation and magnetic fields during the different collapse phases.

In our studies, we make use of an axisymmetric and midplane symmetric 2D grid and account for the effects of self-gravity, radiation, rotation, and magnetic fields. This allows us to explore more initial cloud core properties compared to the non-axisymmetric (i.e. 3D) simulations that are computationally more expensive. To our knowledge, these are the first ever 2D collapse studies that account for the combined effects due to self-gravity, radiative transfer (FLD approximation), a realistic gas EOS, solid-body rotation as well as Ohmic resistivity. Table 1.1 provides a (non-exhaustive) list of some 2D and 3D simulations for star and disc formation studies.

We highlight the effects of ideal and non-ideal (resistive) MHD during the collapse. We explore the formation of protostellar discs and magnetically driven outflows from the first and second hydrostatic cores. The main aim of this work is to study the dependence of disc and outflow properties on the magnetic field strength (in terms of the mass-to-magnetic flux ratio), initial cloud core mass, and initial cloud core rotation.

This chapter is structured as follows. In Sect. 5.1 we discuss the initial setup, parameter space, and the numerical setup, including the computational grid and boundary conditions. In Sect. 5.2 we compare the effects of initial solid-body rotation as well as ideal and resistive MHD on the thermal evolution of the collapsing cloud core. Going from larger to smaller scales, in Sect. 5.3 we first discuss the launching of outflows from the first and second cores. In our simulations, we currently follow the evolution for ≤ 1 year after the formation of the second core. Hence, we mostly focus on outflows from the first core for quantitative comparisons and dependence on initial cloud core properties. In Sect. 5.3.1 we discuss the first core properties

resulting from our RHD simulation. In Sect. 5.3.2 we review the simulations with magnetic fields and compare the effects of ideal and resistive MHD on the outflow properties. In Sect. 5.3.3 we investigate the dependence of outflow properties on the initial magnetic field strength. We extend our simulations in Sect. 5.3.4 to investigate the collapse of 2 $M_\odot$, 5 $M_\odot$, and 10 $M_\odot$ cloud cores and the influence of initial cloud core mass on the launching of outflows.

Furthermore, zooming into the smallest scales, in Sect. 5.4 we study the onset of protostellar disc formation. In the context of disc formation, in Sects. 5.4.1 and 5.4.2 we compare our hydrodynamical models to those that include magnetic fields. In Sect. 5.4.3 we highlight the dependence of protostellar disc formation on the initial cloud core mass. In Sect. 5.5 we detail the limitations of our method and discuss the influence of our resistivity prescription. Section 5.6 provides a summary of our models investigating the launching of outflows from the hydrostatic cores and the onset of protostellar disc formation.

5.1 Initial and numerical setup

We perform 2D resistive MHD simulations of collapsing magnetized molecular cloud cores, using the *PLUTO* code. These simulations also include self-gravity and use a grey FLD approximation for the radiative transfer (Kuiper et al., 2010). The MHD equations that account for the mass, momentum, and energy conservation, the induction equation including the Ohmic dissipation term, and the time-dependent radiation transport equations are described in Sects. 2.1 and 2.2. The LTE approximation is used with a 2T approach for the gas and radiation. We use a gas EOS from D'Angelo & Bodenheimer (2013) to account for effects such as H_2 dissociation, ionisation of atomic hydrogen and helium, and molecular vibrations and rotations. This has been detailed in Sect. 2.3. Simulations discussed in this chapter as well use tabulated dust opacities from Ossenkopf & Henning (1994) and tabulated gas opacities from Malygin et al. (2014) as mentioned in Sect. 2.4. We updated the evaporation and sublimation module to consider a time-dependent evolution of the dust in order to account for the contribution from dust dominating at low temperatures as previously described in Sect. 2.4.

We employ a conservative finite volume approach based on second-order Godunov-type schemes, that means a shock capturing Riemann solver implemented in *PLUTO* to solve the MHD equations. We make use of the Harten-Lax-van Leer-Discontinuities (HLLD) approximate Riemann solver (Miyoshi & Kusano, 2005), a monotonised central difference flux limiter using piecewise linear interpolation, and integrate with a RK2 method. In order to preserve the solenoidality of the magnetic field naturally, we use *PLUTO*'s state-of-the-art constrained transport algorithm. The FLD equation is solved in an implicit way using a standard generalised minimal residual solver with approximations to the error from previous restart cycles with a relative convergence tolerance value of 10^{-10} in terms of temperature.

The initial and numerical setup is similar to that described in Sect. 2.5. We consider different initial cloud core masses of 1 $M_\odot$, 2 $M_\odot$, 5 $M_\odot$, and 10 $M_\odot$. For each case, we use a stable Bonnor–Ebert sphere like density profile as the initial density distribution. The initial temperature is fixed to 10 K and the outer radius is fixed to 3000 au. The core is set up with an initial solid-body rotation along the z-axis. For the 1 $M_\odot$ case, we perform simulations using two different values of the initial rotation rate of $\Omega_0 = 1.77 \times 10^{-13}$ rad s^{-1} and $\Omega_0 = 2.099 \times 10^{-13}$ rad s^{-1}. This results in a ratio of rotational to gravitational energies $E_{\rm rot}/E_{\rm grav}$ of 0.007 and 0.01 for the two rotation

Table 5.1: Initial cloud core properties.

M_0 ($M_\odot$)	μ_0	Ω_0 ($\times 10^{-13}$ rad s^{-1})	$E_{\rm rot}/E_{\rm grav}$	Resistive	Reference section
1	–	2.099	0.01	–	5.2
1	–	1.77	0.007	–	5.3.1 & 5.4.1
1	10	2.099	0.01	N	5.2 & 5.3.2
1	10	2.099	0.01	Y	5.2 & 5.3.2
1	5	1.77	0.007	Y	5.3.3
1	10	1.77	0.007	Y	5.3.3
1	20	1.77	0.007	Y	5.3.3 & 5.4.2
1	32	1.77	0.007	Y	5.3.3 & 5.4.2
2	20	2.48	0.007	Y	5.3.4 & 5.4.3
5	20	3.93	0.007	Y	5.3.4 & 5.4.3
10	20	5.55	0.007	Y	5.3.4 & 5.4.3

Note: Listed above are the cloud core properties for runs with different initial cloud core mass M_0, mass-to-magnetic flux ratio μ_0, initial rotation rate Ω_0, and ratio of rotational to gravitational energies $E_{\rm rot}/E_{\rm grav}$. It also states if resistivity is included in a given run and the sections which discuss the outcome of the simulation run. The common parameters are an initial cloud core temperature of 10 K and outer cloud core radius of 3000 au.

rates, respectively. The amount of rotation for the 2 $M_\odot$, 5 $M_\odot$, and 10 $M_\odot$ cases is parametrised using a fixed value of $E_{\rm rot}/E_{\rm grav}$ to be 0.007 as listed in Table 5.1. The ratio of rotational to gravitational energies is approximated as

$$\frac{E_{\rm rot}}{E_{\rm grav}} = \frac{R_{\rm cloud}^3 \, \Omega_0^2}{3 G M_0}. \tag{5.1}$$

We choose values of $E_{\rm rot}/E_{\rm grav} \leq 0.01$ in order to avoid the parameter regime of disc fragmentation (Matsumoto & Hanawa, 2003; Bate, 2011). As described in Sect. 2.1, we use a physical shear viscosity of the protostellar disc medium to mimic the effect of angular momentum transport.

The magnetic field is initially considered to be uniform and parallel to the rotation axis to satisfy the divergence-free condition. This eventually transforms into the well-known hour-glass shape as the cloud core evolves (see e.g. Fig. 2.1). We prescribe the magnetic field strength B_0 in terms of the mass-to-magnetic flux ratio (M/Φ) in units of the critical value for a uniform spherical cloud (Mestel, 1999; Mac Low & Klessen, 2004), which is given as

$$\mu_0 = \left(\frac{M}{\Phi}\right) \bigg/ \left(\frac{M}{\Phi}\right)_{\rm crit}, \tag{5.2}$$

where $\Phi = \pi R^2 B_0$ and $(M/\Phi)_{\rm crit} = (0.53/3\pi)(5/G)^{1/2}$. We adopt the critical mass-to-magnetic flux ratio from Mouschovias & Spitzer (1976). The gravitational force is in balance with the magnetic force at the critical value of $\mu_0 = 1$. The effect of magnetic fields is not as significant for large super-critical values of $\mu_0 \geq 20$ (e.g. Bate et al., 2014) whereas at sub-critical values of $\mu_0 < 1$, it can prevent a cloud core from
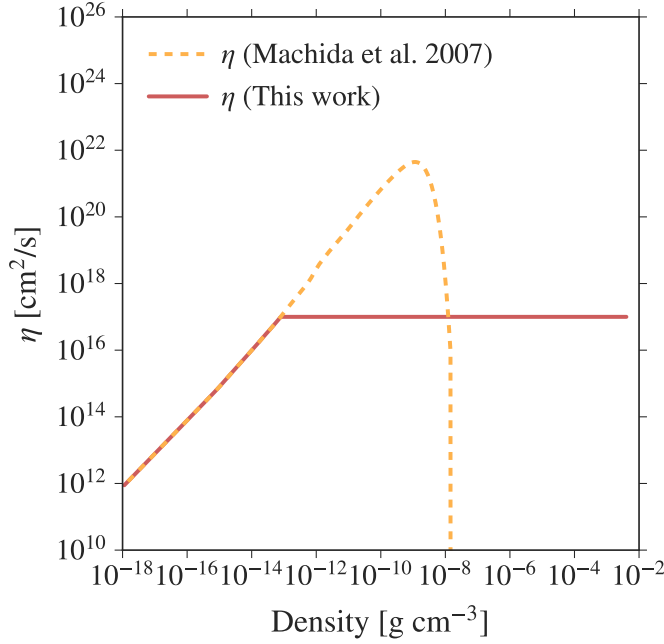
Figure 5.1: Resistivity η as a function of density. The dashed yellow line shows the resistivity used in Machida et al. (2007b). To avoid an extremely small diffusion time step, we implement the same equation but with a fixed upper limit of $\eta = 10^{17}$ cm^2 s^{-1}, as shown by the red line.

collapsing. It has been pointed out by Li et al. (2013) that observed mass-to-magnetic flux ratios in the range $\mu_0 \approx 2 - 10$ (e.g. Crutcher, 1999; Bourke et al., 2001; Heiles & Crutcher, 2005) could be smaller due to projection effects. In our studies, we perform simulations with different mass-to-magnetic flux ratios of $\mu_0 = 5$, 10, 20, and 32. Table 5.1 lists the different initial cloud core parameters that are explored in this work.

The simulations discussed here include Ohmic resistivity as the dissipation term, which yields a reduction of the magnetic braking and thereby enables the formation of protostellar discs and molecular outflows. The resistivity model is based on the numerical study by Nakano et al. (2002) who investigated different mechanisms of magnetic flux loss in molecular clouds due to the drift of dust grains. Machida et al. (2007b) used this model in their work with the resistivity equation given as

$$\eta = \frac{740}{X_e} \sqrt{\frac{T}{10 \text{ K}}} \left[1 - \tanh\left(\frac{n}{n_0}\right) \right] \text{cm}^2 \text{ s}^{-1}, \tag{5.3}$$

where T is the gas temperature, n is the number density with $n_0 = 10^{15}$ cm^{-3}, and the ionisation degree X_e of the gas is chosen to be

$$X_e = 5.7 \times 10^{-4} \left(\frac{n}{\text{cm}^{-3}} \right)^{-1}. \tag{5.4}$$

In our study, we also implement this resistivity formula. However, in order to avoid an extremely small diffusion time step we use a fixed upper limit of $\eta = 10^{17}$ cm^2 s^{-1} for the resistivity, as illustrated in Fig. 5.1. Additionally, we neglect the turn-over to the ideal MHD limit at the highest densities. Section 2.6 provides more details on the computational time of our simulations.

5.1.1 Grid

We adopt a 2D spherical Eulerian grid with axial and midplane symmetry for the RMHD simulations. The computational grid consists of 120 logarithmically spaced
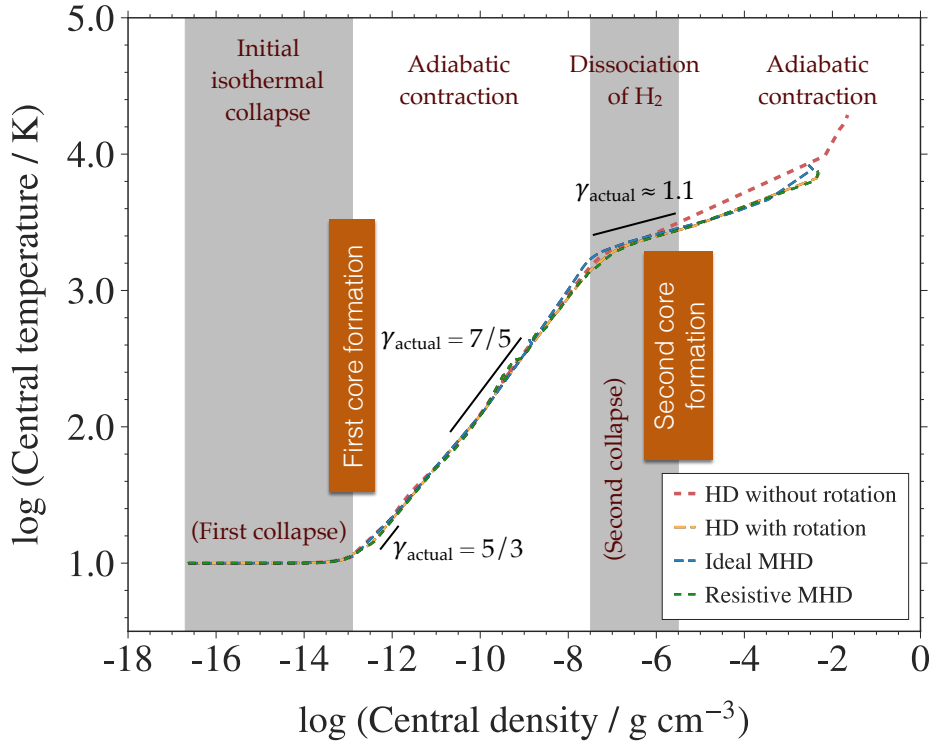
Figure 5.2: Thermal evolution showing the first and second collapse phase for a 1 $M_\odot$ cloud core. The change in adiabatic index γ_{actual} indicates the importance of using a realistic gas EOS. The different dashed lines indicate the thermal evolution for RHD simulation runs without rotation (red), with rotation (yellow), and RMHD runs accounting for ideal (blue) and resistive (green) effects. The initial mass-to-magnetic flux ratio is $\mu_0 = 10$ and the initial rotation rate is set to $\Omega_0 = 2.099 \times 10^{-13}$ rad s^{-1}.

cells in the radial direction extending from 10^{-2} au to 3000 au. This leads to a higher resolution in the central parts compared to the outer parts. The radial grid spans a dynamical range covering five orders of magnitude. We use 15 uniformly spaced cells in the polar direction stretching from the pole ($\theta = 0°$) to the midplane ($\theta = 90°$). The number of cells are chosen such that the spatial extent in the radial and polar direction is the same. The smallest cell size $\Delta x_{\mathrm{min}} = \Delta r = r\Delta\theta = 1.11 \times 10^{-3}$ au. This results in a minimum of 10 cells per Jeans length, which is estimated at the highest central density. Otherwise, we use 10 - 100 cells per Jeans length.

5.1.2 Boundary conditions

We use axisymmetric and mirror-symmetric boundaries at the pole and the equator, respectively. We adopt a reflective boundary condition at the inner radial edge for the hydrodynamics (i.e. density, thermal pressure, and radial velocity) and a zero gradient condition for the radiation energy (i.e. no radiative flux can cross the inner boundary interface) and the polar and azimuthal velocity components. We use a Dirichlet boundary condition on the radiation temperature with a constant boundary value of T_0 at the outer radial edge and an outflow–no-inflow condition for the hydrodynamics that includes a zero-gradient (i.e. no force) boundary condition for the thermal pressure as well as the polar and azimuthal velocity components. We set a zero gradient condition for the magnetic field components at both the inner and outer radial edges.

5.2 Effects of rotation and magnetic fields

In Fig. 5.2 we exhibit the thermal evolution of a 1 $M_\odot$ cloud core with an initial temperature of 10 K and outer radius of 3000 au. The different lines indicate results from 2D RHD simulation runs without rotation (red), with rotation (yellow), and RMHD runs accounting for ideal (blue) and resistive (green) effects. The prescribed initial mass-to-magnetic flux ratio is $\mu_0 = 10$ and the initial rotation rate is $\Omega_0 = 2.099 \times 10^{-13}$ rad s^{-1}. Interestingly, each of the simulations show a similar evolution of the cloud core through the phases of the formation of first and second hydrostatic cores. This is because in the central region the thermal energy is much larger than the magnetic energy and the dissipation of magnetic fields does not influence the thermal evolution at these scales. However, initial conditions such as rotation rate, temperature, opacities, gas EOS, and cloud core mass can lead to differences in the thermal evolution (Bate, 2011; Tomida et al., 2010a; Bhandare et al., 2018).

In the 2D simulation run without any rotation or magnetic fields, both first and the second cores are spherically symmetric, as seen in Chapter 4. On the other hand, in 2D simulation runs that include rotation and magnetic fields, the first core evolves into a more oblate shape whereas the second core is (nearly) spherically symmetric. This can be seen in the radial velocity profiles in Appendix B, as the spread of the accretion shock for different polar angles. In this work, we define the first core lifetime as the time between the onset of formation of the first and second cores. For the cases shown in Fig. 5.2, we find the lifetime of the first cores to be 442, 1514.7, 641.45, and 654.6 years for the non-rotating, rotating, ideal, and resistive MHD runs, respectively. This confirms that in the presence of rotation, the angular momentum slows down the collapse due to centrifugal forces. Properties of the first and second cores resulting from these simulations are listed in Table 5.2.

The conservation of angular momentum promotes disc formation around the second hydrostatic core (i.e. the forming protostar). Furthermore, during these initial phases, sufficient cloud rotation and magnetic field strength can lead to the launching of magnetic pressure and/or magneto-centrifugally driven outflows (and jets) from the first and second cores. The outflow and disc formation processes are discussed in the next sections.

5.3 Outflows

In this work, we focus on the outflows launched from the first and second hydrostatic cores. These are driven due to the interplay between gravitational energy and the Lorentz and centrifugal forces (Blandford & Payne, 1982; Pudritz & Norman, 1983; Pelletier & Pudritz, 1992; Shu et al., 1994; Lynden-Bell, 2003). This section highlights the dependence of magnetically driven outflows from the hydrostatic cores on the resistivity, magnetic field strength (in terms of mass-to-magnetic flux ratio), and the initial cloud core mass. Properties of the first and second cores as well as velocities of the outflows are listed in Table 5.2. We note that the hydrostatic core radii, enclosed mass, and outflow velocities for various simulation runs should not be directly compared since they are estimated at different "final" time snapshots after the formation of the second core (i.e. not at the exact same time in evolution).

5.3.1 First core evolution using radiation hydrodynamic simulations

Here we detail results from the 2D RHD simulation of a collapsing 1 $M_\odot$ molecular cloud core with an initial temperature of 10 K and an outer radius of 3000 au. We
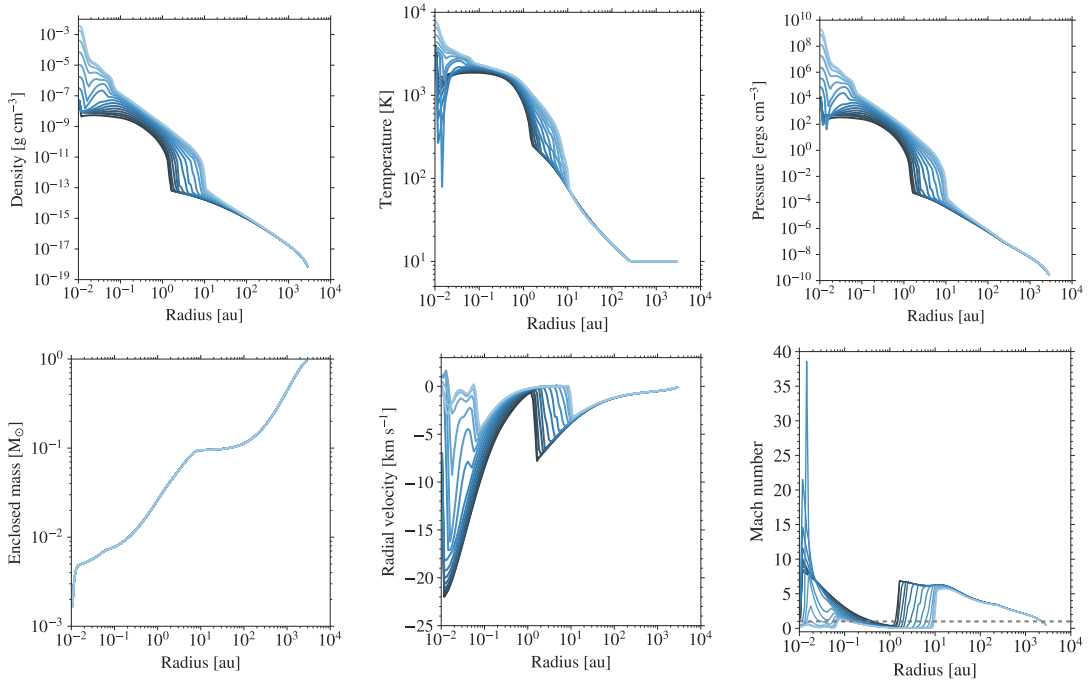
Figure 5.3: Radial profiles after formation of the second core, formed due to the collapse of a 1 $M_\odot$ cloud core with an outer radius of 3000 au and an initial temperature of 10 K. The initial rotation rate is set to $\Omega_0 = 1.77 \times 10^{-13}$ rad s^{-1}. The different subplots show the radial profiles (across and down) of **a)** density, **b)** gas temperature, **c)** thermal pressure, **d)** enclosed mass, **e)** radial velocity, and **f)** Mach number. The colour gradient from light to dark blue spans the polar angle from the midplane ($\theta = 90°$) to the pole ($\theta = 0°$).

use an initial solid-body rotation with a rate of $\Omega_0 = 1.77 \times 10^{-13}$ rad s^{-1}. We follow the evolution of the collapsing cloud core until 0.11 years after the formation of the second core. Figure 5.3 shows radial profiles of the density, temperature, thermal pressure, enclosed mass, radial velocity, and Mach number at the final simulation snapshot. Additionally, Fig. 5.4 shows the 2D behaviour of the Mach number, density, temperature, and ratio of centrifugal to gravitational force. The Mach number is computed using the ratio of poloidal flow velocity to the sound speed. The centrifugal and gravitational forces are computed along the cylindrical radius.

In this RHD simulation, the first core evolves into a more oblate shape during its evolution, compared to the non-rotating case. The estimated lifetime of the first core is 1246.3 years. At the final simulation snapshot the radius of the first core is 10.86 au and the enclosed mass is 0.095 $M_\odot$. Here, we estimate the first core radius using the position of the first accretion shock at the midplane (light blue line) as seen in the radial velocity profile in Fig. 5.3. This also corresponds to the discontinuity seen in the radial density profile. The first core is seen to be much bigger than in the non-rotating model (≈ 3 au). We do not see any (thermal pressure driven) outflow launched from either the first or second core in this RHD simulation.

5.3.2 Ideal versus resistive magneto-hydrodynamics

In this section, we focus on the effects of ideal and resistive RMHD on the properties of outflows launched from the first and second hydrostatic cores. In both cases, we investigate the collapse of a 1 $M_\odot$ cloud core with an outer radius of 3000 au and
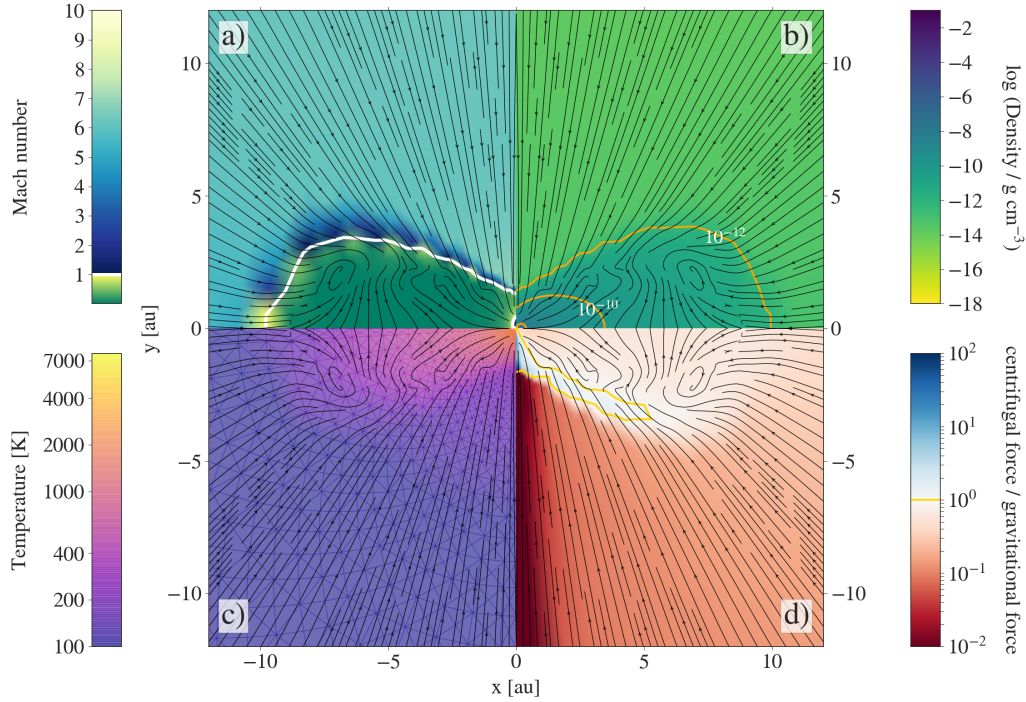
Figure 5.4: The four panels show the **a)** Mach number, **b)** density, **c)** temperature, and **d)** ratio of centrifugal to gravitational force at a simulation snapshot after the formation of the second core. Shown here is the outcome of the collapse of a 1 $M_\odot$ cloud core with an outer radius of 3000 au and an initial temperature of 10 K. The initial rotation rate is set to $\Omega_0 = 1.77 \times 10^{-13}$ rad s^{-1}. The black streamlines indicate the velocity field. The white contour in panel *a* shows the transition between sub- and supersonic regions (Mach = 1.0). The different contour lines in panel *b* highlight the increasing density towards the centre and the disc's midplane.

an initial temperature of 10 K. Both simulations use an initial mass-to-magnetic flux ratio of $\mu_0 = 10$ and an initial rotation rate of $\Omega_0 = 2.099 \times 10^{-13}$ rad s^{-1}.

We follow the evolution of the cloud core until 0.1 years (ideal run) and 0.4 years (resistive run) after the formation of the second core. We quantify several properties of the collapsing cloud core at these final simulation snapshots. In Fig. 5.5, we compare the behaviour of the Alfvén Mach number, density, temperature, and plasma beta ($\beta = 2P/\text{B}^2$) for the ideal and resistive RMHD models. The Alfvén Mach number is computed using the ratio of poloidal flow velocity (v_p) to the poloidal component of the Alfvén velocity ($v_\text{A} = \text{B} / \sqrt{4\pi\rho}$).

The Alfvén surface (indicated by the white line in panel *a*) is the region where the poloidal flow velocity is equal to the poloidal component of the Alfvén velocity. In the ideal MHD model, the outflow and surrounding region is seen to be sub-Alfvénic. On the other hand in the resistive model, the Alfvén surface shows the transition of sub- to super-Alfvénic Mach number in the outer regions of the outflow. Higher density (panel *b*) in the inner regions shows the non-homologous behaviour of the collapse. For both runs, the plasma beta (panel *d*) shows that the magnetic pressure dominates (or is comparable to the thermal pressure) everywhere in and around the first core. The first core is stabilised by contributions from both the thermal and magnetic pressure.

Additionally, in Fig. 5.6 we compare the behaviour of the ratios of centrifugal to gravitational force and toroidal to poloidal magnetic field components as well
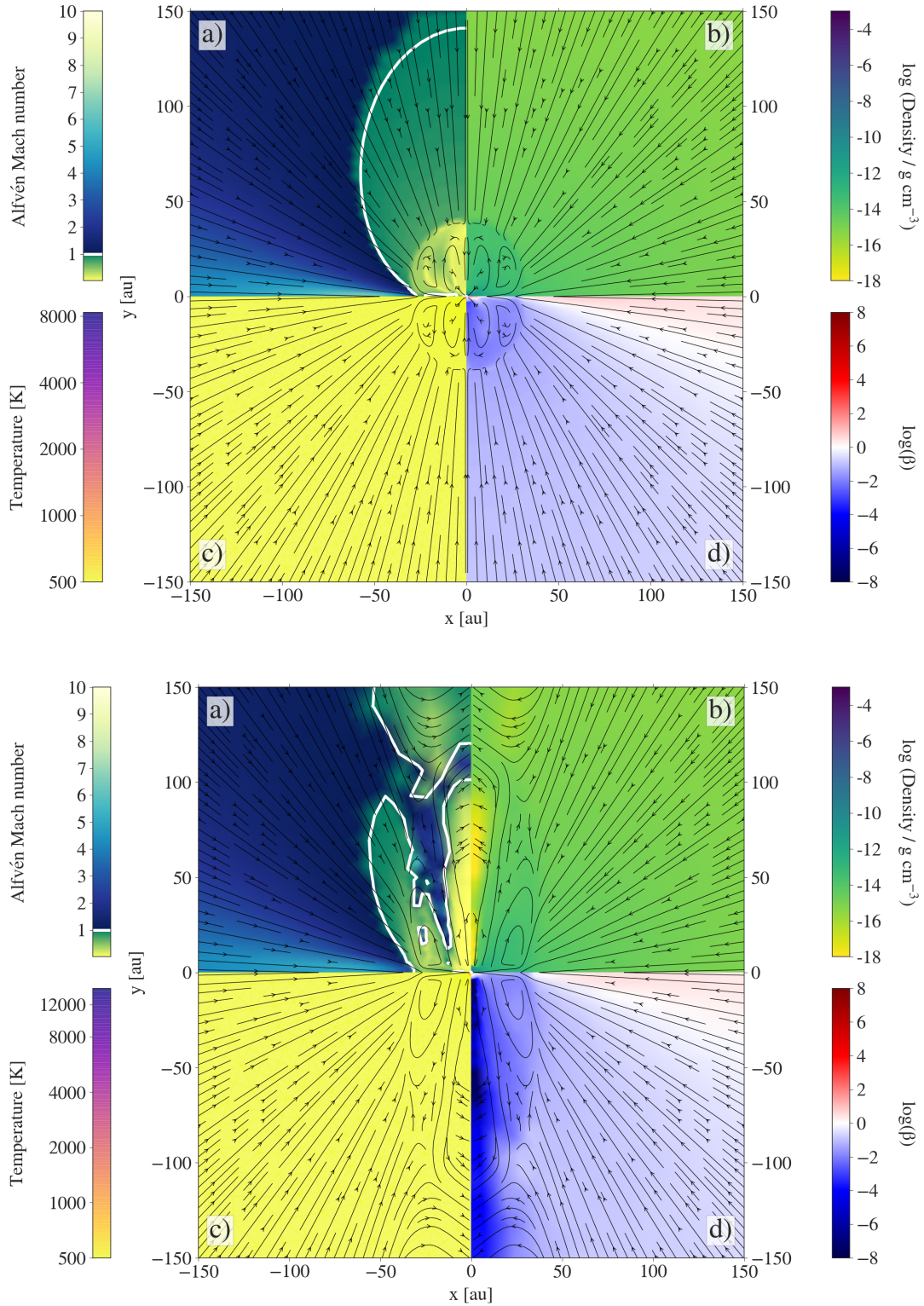
Figure 5.5: The top and bottom figures show a 2D view from simulation runs without and with resistivity, respectively. The four panels show the **a)** Alfvén Mach number, **b)** density, **c)** temperature, and **d)** plasma beta at a time snapshot after formation of the second core. The different properties are shown for the collapse of a 1 $M_\odot$ cloud core with an outer radius of 3000 au and an initial temperature of 10 K. The initial mass-to-magnetic flux ratio is $\mu_0 = 10$ and the initial rotation rate is set to $\Omega_0 = 2.099 \times 10^{-13}$ rad s^{-1}. The black streamlines indicate the velocity and the Alfvén surface is indicated by the white line in panel a.
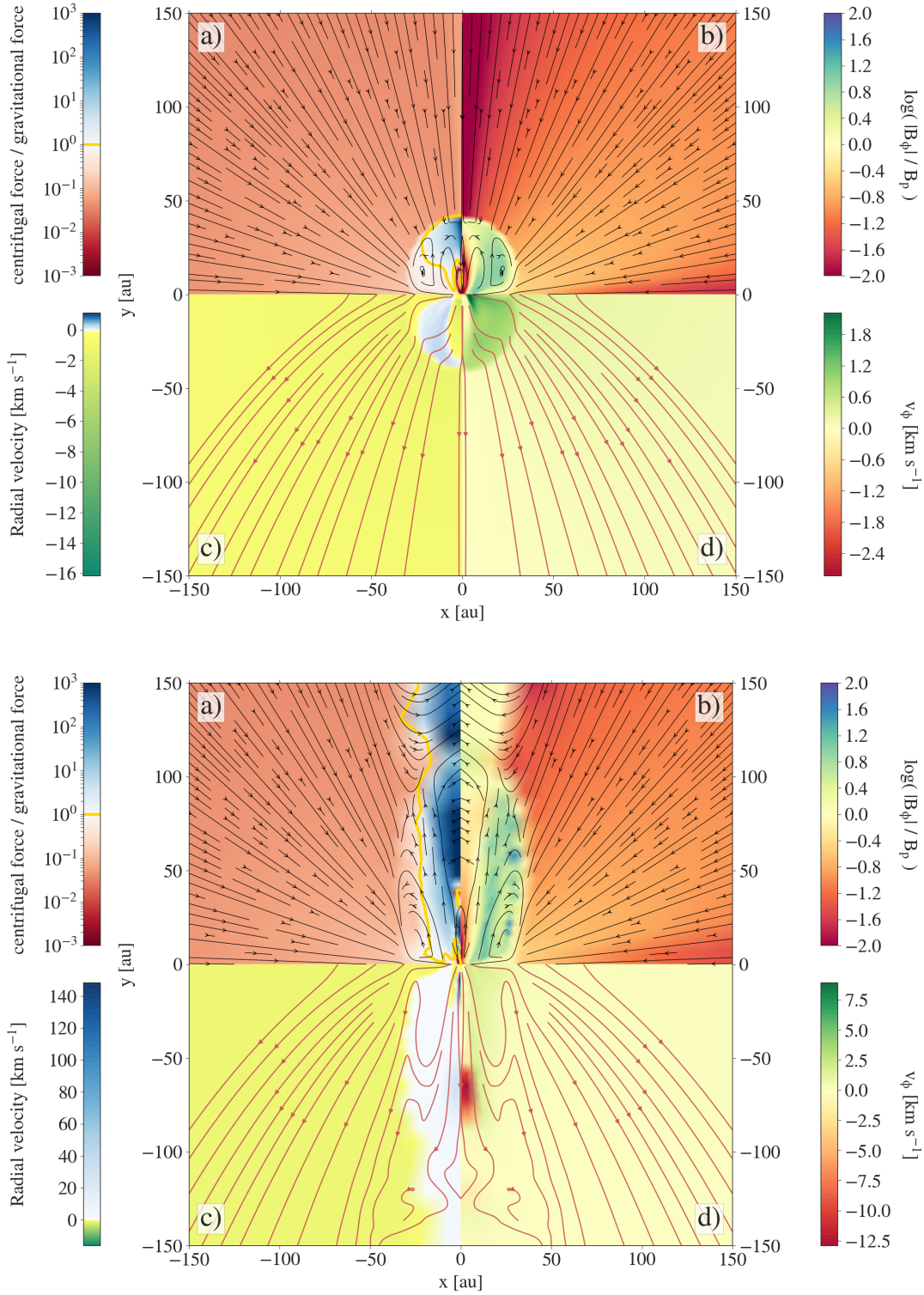
Figure 5.6: The top and bottom figures show a 2D view from simulation runs without and with resistivity, respectively. The four panels show the **a)** ratio of centrifugal to gravitational force, **b)** ratio of toroidal to poloidal magnetic field, **c)** radial velocity, and **d)** azimuthal velocity at a time snapshot after formation of the second core. The different properties are shown for the collapse of a 1 $M_\odot$ cloud core with an outer radius of 3000 au and an initial temperature of 10 K. The initial mass-to-magnetic flux ratio is $\mu_0 = 10$ and the initial rotation rate is set to $\Omega_0 = 2.099 \times 10^{-13}$ rad s^{-1}. The black streamlines in panels *a* and *b* represent the velocity whereas the poloidal field showing the pinching effect is indicated with red streamlines in panels *c* and *d*.

as the radial and azimuthal velocities for the ideal and resistive MHD runs. The centrifugal and gravitational forces are computed along the cylindrical radius. The toroidal field is the magnitude of the $|B_\phi|$ component, whereas the poloidal field is computed as $B_P = \sqrt{B_r^2 + B_\theta^2}$. The centrifugal force is stronger than (or comparable to) gravity in most parts of the outflow. In Fig. 5.6, both cases show that the toroidal field dominates over the poloidal field in the first core outflow regions. Although not well resolved in Fig. 5.6, we see that the toroidal field also dominates in the innermost sub-au regions, where the outflow from the second core is launched. Furthermore, Figs. B.1 and B.2 show the radial profiles of the density, temperature, enclosed mass, radial velocity, azimuthal velocity, angular momentum, total magnetic field strength, the ratio of toroidal to poloidal magnetic field, magnetic pressure, thermal pressure, Alfvén Mach number, and Alfvén velocity.

The behaviour of all these properties in Figs. 5.5 and 5.6 indicate that the outflows launched from both first and second cores are driven by magnetic pressure. Conventionally, the magneto-centrifugal launching mechanism is expected to play a role when the poloidal component dominates over the toroidal component, which is not the case here.

In the ideal MHD model, a slow outflow ($v_{r,\ max} \approx 1$ km s^{-1}) is launched from the first core. Efficient magnetic braking prevents an outflow (or a jet) from the second core in the ideal MHD model. However, an outflow (or a jet) could be launched at a later stage in evolution when the angular momentum transport is not that efficient. On the other hand, in the resistive MHD model, a fast outflow ($v_{r,\ max} \approx 148$ km s^{-1}) is launched from the first core whereas a (currently) slow outflow ($v_{r,\ max} \approx 4$ km s^{-1}) is launched from the second core. This can be seen in the radial velocity distribution in Fig. 5.6 (see panel *c*) and the radial velocity profile in Figs. B.1 and B.2 (see panel *d*). This comparison between ideal and resistive models is consistent with previous 3D RMHD studies by Tomida et al. (2013).

We define the first core radius using the position of the first accretion shock at the midplane. The estimated first core radius in the ideal MHD run is 30.81 au, while in the resistive MHD model it is 34.5 au. The larger first core in the resistive case is an effect of additional heating by Ohmic dissipation. The second core radius is defined using the position of the second accretion shock where the radial infall velocity is the highest.

5.3.3 Dependence of outflow properties on the mass-to-flux ratio

In this section, we discuss the effects of different magnetic field strengths (in terms of the mass-to-magnetic flux ratio) on the outflow properties. All the different simulation runs follow the collapse of a 1 $M_\odot$ cloud core with an outer radius of 3000 au and an initial temperature of 10 K. The initial rotation rate is set to $\Omega_0 = 1.77 \times 10^{-13}$ rad s^{-1}. We consider four different mass-to-magnetic flux ratios of $\mu_0 = 5, 10, 20,$ and 32, in decreasing order of magnetic field strength.

We follow the evolution of the molecular cloud core for each of these models until after the formation of the second core for 0.8 years (for $\mu_0 = 5$), 0.9 years (for $\mu_0 = 10$), 0.6 years (for $\mu_0 = 20$), and 1.3 years (for $\mu_0 = 32$). The lifetime of the first core is 601.7, 616.6, 927, and 1117.5 years and the first core radius is estimated to be 7.92, 31.06, 22.66, and 20.40 au for the models with $\mu_0 = 5, 10, 20,$ and 32, respectively. Here, as well, the position of the first accretion shock at the midplane defines the first core radius.
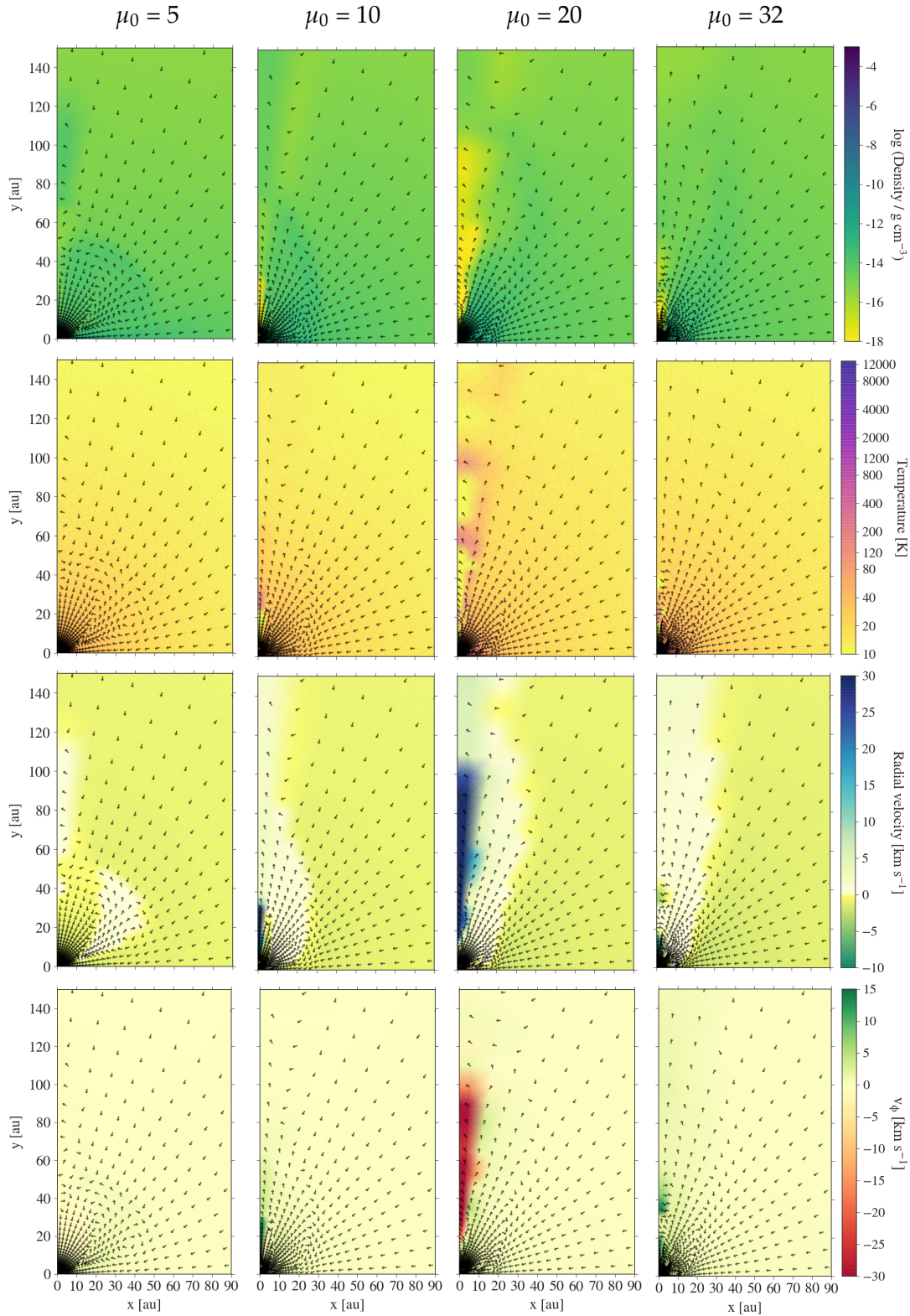
Figure 5.7: The four columns show a comparison of the density, temperature, radial velocity, and azimuthal velocity for four different simulations with mass-to-magnetic flux ratios of $\mu_0 = 5$, 10, 20, and 32, respectively. Each panel is shown at a time snapshot after the second core formation. This is an outcome of the collapse of a 1 $M_\odot$ cloud core with an outer radius of 3000 au, an initial temperature of 10 K, and an initial rotation rate of $\Omega_0 = 1.77 \times 10^{-13}$ rad s^{-1}. The velocity vectors are shown by the black arrows.
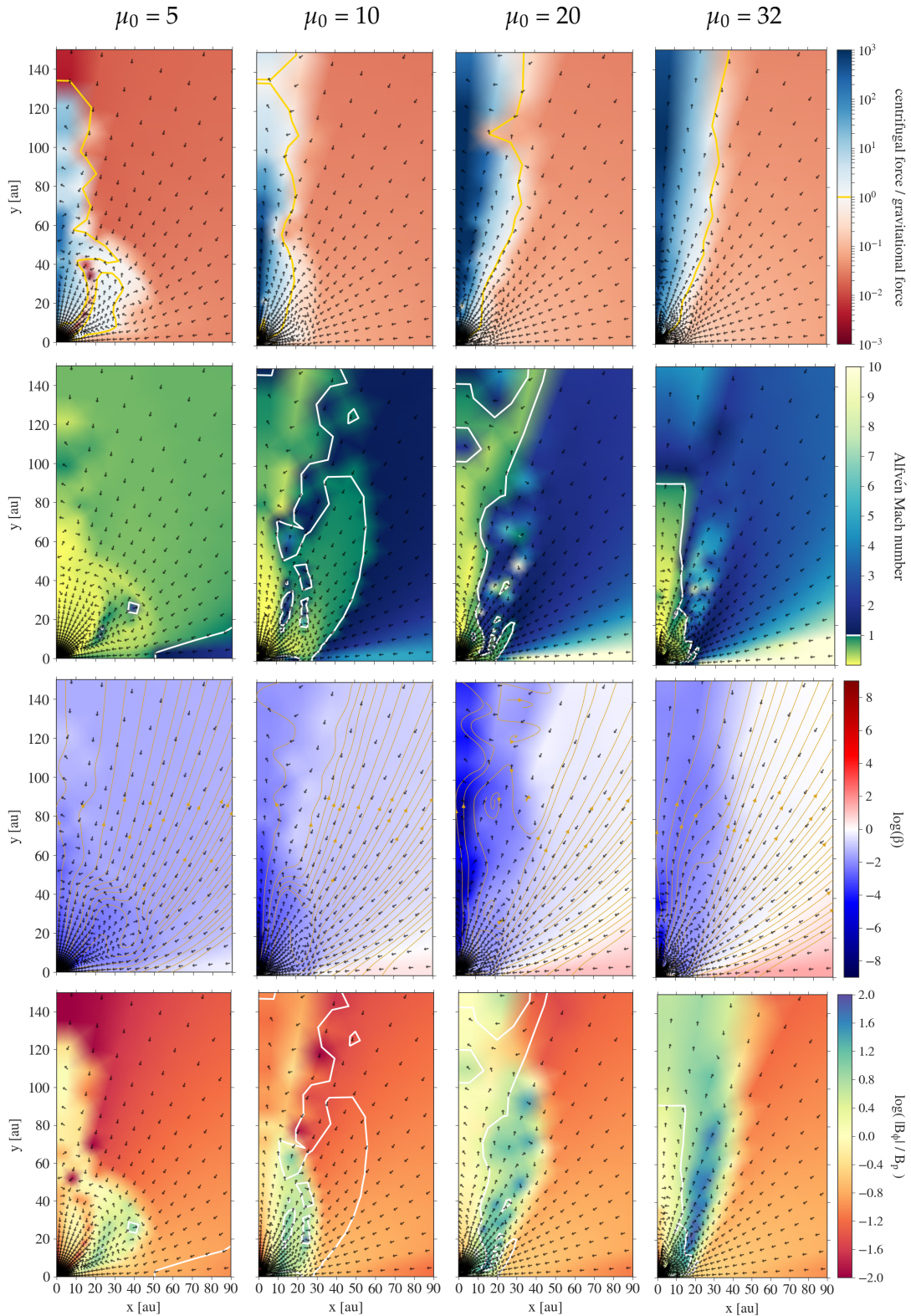
Figure 5.8: The four columns show a comparison of the ratio of centrifugal to gravitational forces, Alfvén Mach number, plasma beta, and ratio of toroidal to poloidal magnetic field for four different simulations with mass-to-magnetic flux ratios of μ_0 = 5, 10, 20, and 32, respectively. Each panel is shown at a time snapshot after the second core formation. This is an outcome of the collapse of a 1 $M_\odot$ cloud core with an outer radius of 3000 au, an initial temperature of 10 K, and an initial rotation rate of $\Omega_0 = 1.77 \times 10^{-13}$ rad s^{-1}. The velocity vectors are shown by the black arrows and the brown streamlines in the third row indicate the poloidal field. The white contour in rows 2 and 4 indicates the Alfvén surface.

In each model, we see outflows being launched from the vicinity of the first and second cores. Figure 5.7 shows the comparison of the density, gas temperature, radial and azimuthal velocities for the four different cases of μ_0. The density increases inwards except in the polar regions where the density is seen to be quite low for the runs with μ_0 = 10, 20, and 32. The temperature in the outflow regions and the surrounding envelope is well below the dissociation limit ($\ll$ 2000 K). The positive radial velocities indicate the material flowing outwards. The outflowing gas at the polar region appears to be counter-rotating as seen in the behaviour of the azimuthal velocity for the run with μ_0 = 20. The poloidal field lines are indicated by the brown streamlines on the plot for plasma beta in Fig. 5.8. For the case with μ_0 = 20, the poloidal field lines show vortex-like features with a change in the field direction. Thus, at a first glance, the Lorentz force could be responsible for the counter rotation. This possible explanation needs to be investigated further.

Additionally, Fig. 5.8 shows the ratio of centrifugal force to gravitational force, the Alfvén Mach number, plasma beta, and ratio of toroidal to poloidal field components. The centrifugal force is stronger than (or comparable to) the gravitational force in the outflow region. Similarly, as indicated by the plasma beta, the magnetic pressure dominates over the thermal pressure in the outflow region. The Alfvén surface (marked by the white contour) indicates the transition between sub- and super-Alfvénic regions. The Alfvén surface is also shown in the plots comparing the toroidal and poloidal field components. The toroidal field component becomes stronger with higher mass-to-magnetic flux ratio (i.e. weaker field strength). Interestingly, the toroidal component appears to be strongest in the super-Alfvénic outflow regions. In each case, the toroidal component dominates over the poloidal component in the outflow regions of the first and second core. This suggests that the outflows launched from both hydrostatic cores are driven by magnetic pressure. We only trace the onset of the outflow launched from the second core since we follow the evolution of the second core for less than a year after its formation. This outflow in the vicinity of the second core is expected to become stronger over time.

Figures B.3 – B.6 show the radial profiles of the velocity among other properties of different collapsing cloud core models. The first core outflow velocities are $v_{r,\,max} \approx 0.98$, 124.57, 83.86, and 3.15 km s^{-1} whereas the second core outflow velocities are $v_{r,\,max} \approx 2.51$, 3.81, 3.28, and 5.48 km s^{-1}, for the models with μ_0 = 5, 10, 20, and 32, respectively. The highest outflow velocities are found along the rotation axis. The model with the weakest mass-to-magnetic flux ratio (i.e. highest field strength) is most efficient in transporting angular momentum outwards and thus shows the weakest outflow. We find that the outflows get broader with weaker initial magnetic field strength (i.e. higher mass-to magnetic flux ratio). Similar broadening of the outflows is seen by Bate et al. (2014).

5.3.4 Dependence of outflow properties on initial cloud core mass

In this section, we extend our simulations to investigate the collapse for models with different initial cloud core masses of M_0 = 2 $M_\odot$, 5 $M_\odot$, and 10 $M_\odot$. All models use an initial temperature of 10 K and a fixed outer radius of 3000 au. The initial mass-to-magnetic flux ratio μ_0 is fixed to 20 times the critical value. We prescribe different initial rotation rates for these models, which is estimated using a fixed value of E_{rot}/E_{grav} = 0.007. All these initial parameters are listed in Table 5.1.

We follow the evolution of the cloud core for the different models until 0.6 years (for 1 $M_\odot$ run), 1.27 years (for 2 $M_\odot$ run), 0.24 years (for 5 $M_\odot$ run), and 0.16 years

(for 10 $M_\odot$ run) after the second core formation. In each model, we see outflows launched from the vicinity of the first and second cores.

Figure 5.9 shows a comparison of the density, gas temperature, radial and azimuthal velocities for the four different cases of M_0. The density increases inwards except in the polar regions where the density is low for the runs with $M_0 = 1\ M_\odot$ and 2 $M_\odot$. The temperature in the outflow regions and the surrounding envelope is well below the dissociation limit ($\ll$ 2000 K). The positive radial velocities indicate the material flowing outwards. The outflowing gas at the polar region appears to be counter-rotating as seen in the behaviour of the azimuthal velocity for the 1 $M_\odot$ run and in the innermost regions for the 2 $M_\odot$ case. This effect caused due to the Lorentz force has been discussed in Sect. 5.3.3.
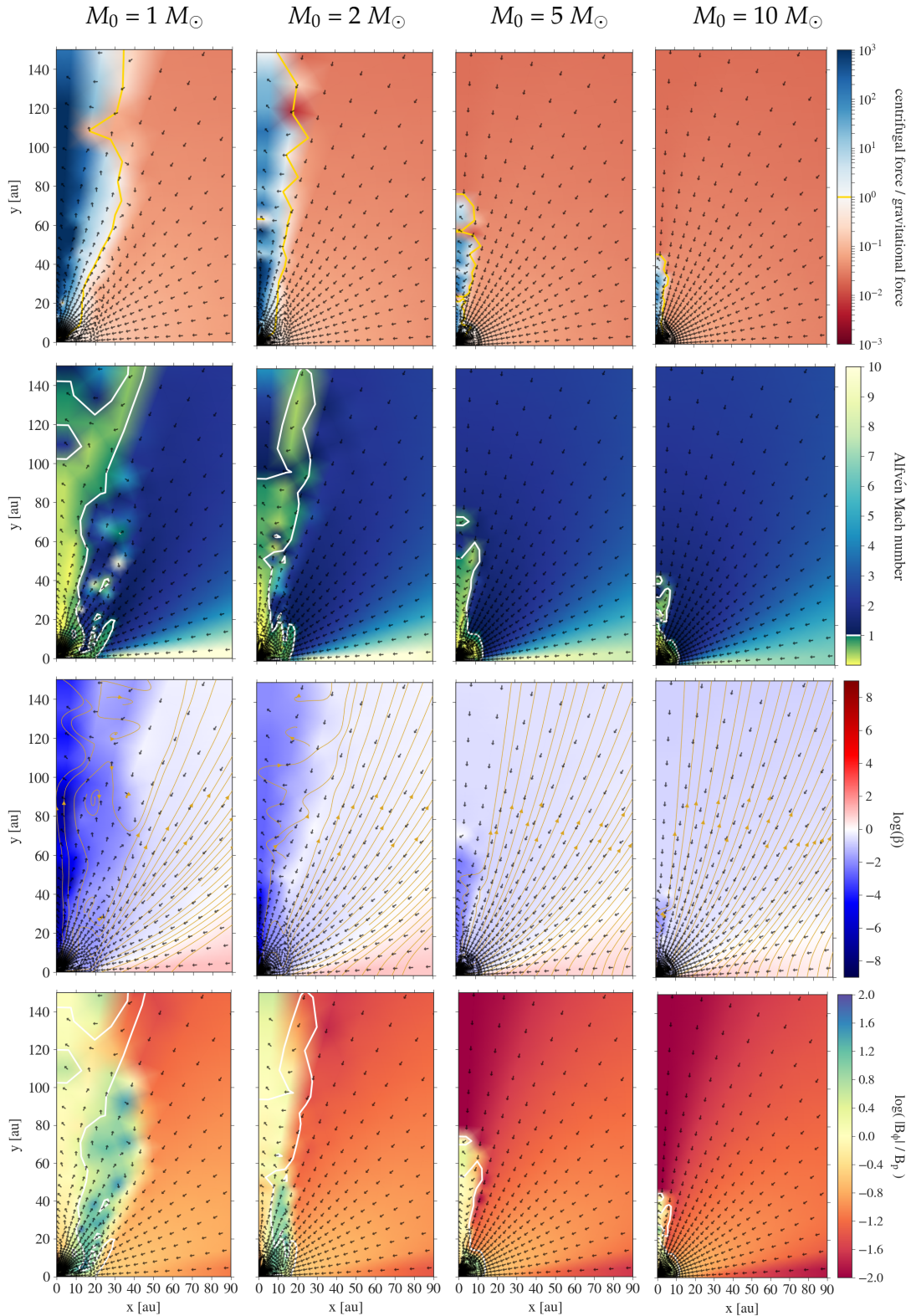
Furthermore, Fig. 5.10 shows the ratio of centrifugal force to gravitational force, Alfvén Mach number, plasma beta, and ratio of toroidal to poloidal field components. The centrifugal force is stronger than (or comparable to) the gravitational force in the outflow region. The gravitational force in the surrounding envelope is stronger for the higher-mass cases. As indicated by the plasma beta, the magnetic pressure dominates over the thermal pressure in the outflow region. The Alfvén surface (marked by the white contour) indicates the transition between sub- and super-Alfvénic regions. The Alfvén surface is also shown in the plots comparing the toroidal and poloidal field components. As also shown in the mass-to-magnetic flux ratio comparisons in Sect. 5.3.3, the toroidal component is the strongest in the super-Alfvénic outflow regions. This seems to be more prominent in the collapsing cases of 1 $M_\odot$ and 2 $M_\odot$ cloud cores.

In each case, the toroidal field component dominates over the poloidal component in the first and second core outflow regions. This suggests that the outflows launched from both hydrostatic cores are driven due to magnetic pressure. For the chosen set of initial cloud core properties, the strength and extent of the outflow launched from the first core decreases with increasing cloud core mass. For these simulation runs, we follow the evolution of the second core for ≤ 0.6 years after its formation. Hence we only trace the onset of outflow launching from the second core.

For each of the runs, Fig. B.5 and Figs. B.7 – B.9 show the radial profiles of various properties of the cloud core at the final simulation snapshot. In the following we state some of the first and second core properties for the different cases with initial mass of 1 $M_\odot$, 2 $M_\odot$, 5 $M_\odot$, and 10 $M_\odot$. The first core outflow velocities are $v_{\rm r,\ max} \approx$ 83.86, 91.75, 4.55, and 2.38 km s^{-1} whereas the second core outflow velocities are $v_{\rm r,\ max} \approx$ 3.28, 14.58, 8.87, and 6.76 km s^{-1}, respectively. The highest outflow velocities are along the rotation axis. For each of these cases, the first core lifetime is 927, 445.1, 130.6, and 98.1 years, respectively. This resembles the fact that the collapse is faster for more massive cloud cores. The first core radius, estimated using the position of the accretion shock at the midplane, is 22.66, 18.37, 14.89, and 13.4 au, respectively. At this final simulation snapshot, the second core radius is 0.04, 0.012, 0.063, and 0.045 au, respectively. The second core radius is defined as the position of the second accretion shock, where the infall velocity is highest. The second core accretion rate is 3.03×10^{-3}, 1.82×10^{-3}, 3.52×10^{-3}, and 4.89×10^{-3} $M_\odot$ yr^{-1}, respectively. As discussed in Chapter 4, more massive cloud cores accrete at a comparatively faster rate.
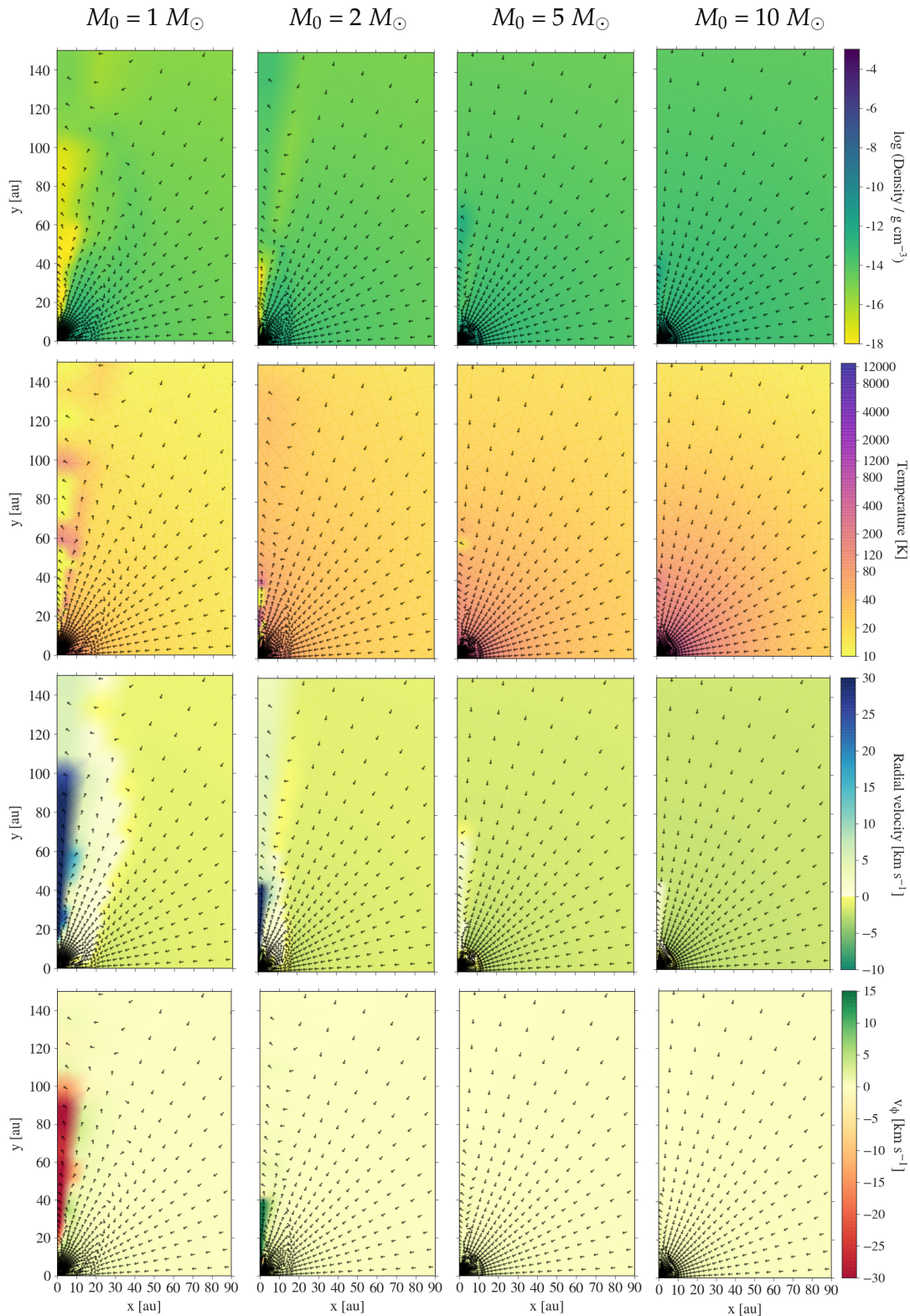
Figure 5.9: The four columns show a comparison of the density, temperature, radial velocity, and azimuthal velocity for four different simulations with cloud core masses of $M_0 = 1M_\odot$, $2M_\odot$, $5M_\odot$, and $10M_\odot$, respectively. Each panel is shown at a time snapshot after the second core formation. The common parameters are an outer radius of 3000 au, an initial temperature of 10 K, mass-to-magnetic flux ratio of $\mu_0 = 20$, and the ratio of rotational to gravitational energy of $E_{\mathrm{rot}}/E_{\mathrm{grav}} = 0.007$. The velocity vectors are shown by the black arrows.

Figure 5.10: The four columns show a comparison of the ratio of centrifugal to gravitational forces, Alfvén Mach number, plasma beta, and ratio of toroidal to poloidal magnetic field for four different simulations with cloud core masses of $M_0 = 1\,M_\odot$, $2\,M_\odot$, $5\,M_\odot$, and $10\,M_\odot$, respectively. Each panel is shown at a time snapshot after the second core formation. The common parameters are an outer radius of 3000 au, an initial temperature of 10 K, mass-to-magnetic flux ratio of $\mu_0 = 20$, and the ratio of rotational to gravitational energy of $E_{\rm rot}/E_{\rm grav} = 0.007$. The velocity vectors are shown by the black arrows and the brown streamlines in the third row indicate the poloidal field. The white contour in rows 2 and 4 indicates the Alfvén surface.

Figure 5.11: The four panels show the **a)** Mach number, **b)** density, **c)** temperature, and **d)** ratio of centrifugal to gravitational force at a simulation snapshot after the formation of the second core. Shown here is the outcome of the collapse of a 1 $M_\odot$ cloud core with an outer radius of 3000 au and an initial temperature of 10 K. The initial rotation rate is set to $\Omega_0 = 1.77 \times 10^{-13}$ rad s^{-1}. The black streamlines indicate the velocity field. The white contour (Mach = 1.0) in panel *a* separates the sub- and supersonic regions. The different contour lines in panel *b* highlight the increasing density towards the centre and the disc's midplane.

5.4 Onset of disc formation

In this section, we investigate the onset of disc formation during the very early stages of star formation. We compare models with and without magnetic fields and study the effects of resistivity on the formation of discs around the second hydrostatic core.

5.4.1 Disc formation using radiation hydrodynamic simulations

This section details results from our 2D non-magnetic RHD simulation of a collapsing 1 $M_\odot$ molecular cloud core with an initial temperature of 10 K and an outer radius of 3000 au. We use an initial solid-body rotation with a rate of $\Omega_0 = 1.77 \times 10^{-13}$ rad s^{-1}. We follow the evolution of the collapsing cloud core until 0.11 years after the formation of the second core. Figure 5.11 shows the 2D behaviour of the Mach number, density, temperature, and ratio of centrifugal to gravitational force within the disc and its surrounding envelope (i.e. the first core).

In this RHD simulation, the disc starts forming right after the onset of the second core formation and evolves simultaneously with the second core. In Fig. 5.12, we compare the radial (blue) and azimuthal (black) midplane velocities to the Keplerian velocities estimated with (yellow) and without (red) the contribution from the thermal
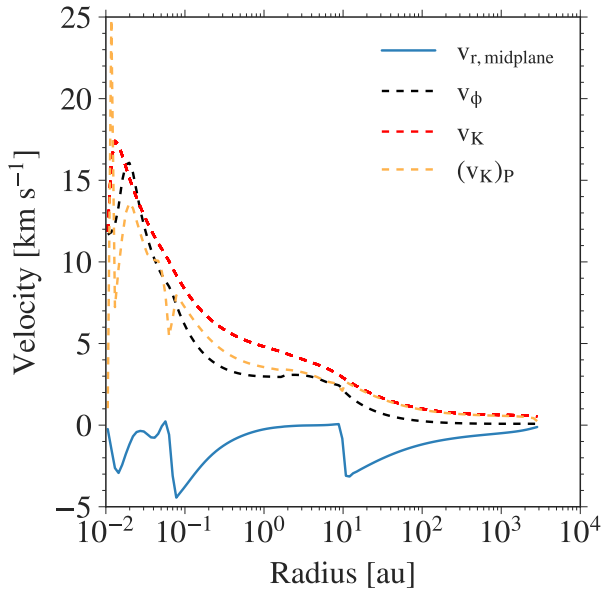
Figure 5.12: We follow the evolution of a collapsing 1 $M_\odot$ cloud core with an outer radius of 3000 au and an initial temperature of 10 K using an RHD simulation. The initial rotation rate is set to $\Omega_0 = 1.77 \times 10^{-13}$ rad s^{-1}. Shown here are the radial profiles comparing the radial (blue), azimuthal (dashed black), and Keplerian (dashed red) midplane velocities as well as the Keplerian midplane velocity including the thermal pressure force (dashed yellow), at a simulation snapshot after the formation of the second core. At this stage, the disc is in gravito-centrifugal-thermal pressure equilibrium.

pressure force[1]. As the thermal pressure increases with temperature, it is important to account for the pressure force in early discs that have a high temperature. At these early stages, the initial sub-Keplerian disc eventually evolves into a disc that is in gravito-centrifugal-thermal pressure equilibrium. The presence of this disc is indicated by the region where the azimuthal velocity is similar to the Keplerian velocity including the thermal pressure force.

At the final simulation snapshot the disc radius is ≈ 0.07 au and the enclosed mass is 7.4×10^{-3} $M_\odot$. Here, we estimate the disc radius using the position of the second accretion shock at the midplane (light blue line) as seen in the radial velocity profile in Fig. 5.3. This also corresponds to the discontinuity seen in the density profile. As the disc is still accreting material, we expect it to grow in size and mass as it transforms into a circumstellar disc.

5.4.2 Dependence of disc formation on the mass-to-flux ratio

This section highlights the effect of resistivity on the onset of disc formation as well as the dependence of the disc properties on the mass-to-magnetic flux ratio. We follow the evolution of a 1 $M_\odot$ cloud core with an outer radius of 3000 au and an initial temperature of 10 K. The initial rotation rate is set to $\Omega_0 = 1.77 \times 10^{-13}$ rad s^{-1}. Here, we focus on the previously discussed (see Sect. 5.3.3) simulation runs with the mass-to-magnetic flux ratio of $\mu_0 = 20$ and 32, since these are the only resistive models in our study that lead to the onset of disc formation.

---

[1]The orbital velocity for an equilibrium state of gravity, centrifugal force, and the thermal pressure force along the cylindrical radius, is given by

$$(\Omega_K)_P = \frac{(v_K)_P}{R} = \sqrt{\frac{GM_{encl}}{r^3} + \frac{\partial_R P}{\rho\, R}},$$

where R is the cylindrical radius and M_{encl} is the enclosed mass.

As stated above, we follow the evolution of the cloud core until 0.6 years for the model with $\mu_0 = 20$ and 1.3 years for the model with $\mu_0 = 32$ after the formation of the second core. In both these resistive models, the disc formation starts after the formation of the second core. The onset of disc formation is similar to that seen in the hydrodynamic case in Sect. 5.4.1. The disc and second core thus evolve simultaneously.

The two plots in Fig. 5.13 show a comparison of the properties of embedded discs for collapse simulations with $\mu_0 = 20$ and 32. The four panels show the behaviour of the Alfvén Mach number, density, temperature, and plasma beta. In both cases the innermost 0.5 au is mostly dominated by thermal pressure (see Fig. 5.13; panel *d*), as opposed to the first core outflow regions where the magnetic pressure dominates (see Fig. 5.8).

Figure 5.14 shows the behaviour of the ratio of centrifugal to gravitational forces, the ratio of the toroidal to poloidal magnetic field components, as well as the radial and azimuthal velocities for both collapse simulations with $\mu_0 = 20$ and 32. The toroidal component dominates in most parts of the disc and in the outflow region around the second core. Both plots in Fig. 5.15 indicate the equilibrium state of the gravitational, centrifugal, and thermal pressure forces within the disc. This is similar to the disc found in the non-magnetic RHD simulation, as detailed in Sect. 5.4.1. Here as well, the disc can be identified by the region where the azimuthal velocity is similar to the Keplerian velocity estimated by including the thermal pressure force.

In the simulation with $\mu_0 = 20$, within 0.6 years of formation, we find the disc size to be 0.18 au with an enclosed mass of $1.3 \times 10^{-2}\ M_\odot$. On the other hand, for the simulation with $\mu_0 = 32$, which is evolved for a bit longer (≈ 1.3 years), the disc size is 0.34 au with an enclosed mass of $1.8 \times 10^{-2}\ M_\odot$. Here as well, we estimate the disc radius using the second accretion shock position at the midplane (light blue line) as seen in the radial velocity profile in Fig. B.5 and Fig. B.6. This also corresponds to the discontinuity seen in the density profile.

Additionally, as seen in Fig. 5.13, the magnetic pressure dominates in the innermost regions, especially near the rotation axis. This is the location of the outflow from the second hydrostatic core, which currently lacks temporal and spatial resolution in our simulations. In Fig. 5.14, the positive radial velocity indicates the outflowing material in the innermost regions. This is comparatively more significant for the simulation run with $\mu_0 = 32$ (see panel *c*). We expect the outflow to become stronger as the second core and its surrounding disc evolve further over time. The launching of the outflow is previously discussed in Sect. 5.3.3 and is better visible in the radial velocity profile shown in Fig. B.5.

5.4.3 Dependence of disc formation on initial cloud core mass

In this section, we study the dependence of disc formation on the initial cloud core mass. We previously discussed the effect of initial mass on the outflow properties in Sect. 5.3.4. We presented results from the collapse of 2 $M_\odot$, 5 $M_\odot$, and 10 $M_\odot$ cloud cores with an initial temperature of 10 K and an outer radius of 3000 au. The initial mass-to-magnetic flux ratio μ_0 was fixed to 20 times the critical value. The initial rotation rate for each of the simulation runs were calculated using a fixed ratio of rotational to gravitational energies as $E_{\rm rot}/E_{\rm grav} = 0.007$.

We follow the evolution of the cloud core only for 1.27, 0.24, and 0.16 years after the second core formation, for the cases of $M_0 = 2\ M_\odot$, 5 $M_\odot$, and 10 $M_\odot$, respectively. Among these three runs, we currently only see the onset of disc formation in the simulation with an initial cloud core mass of 2 $M_\odot$. For this simulation run, we find a
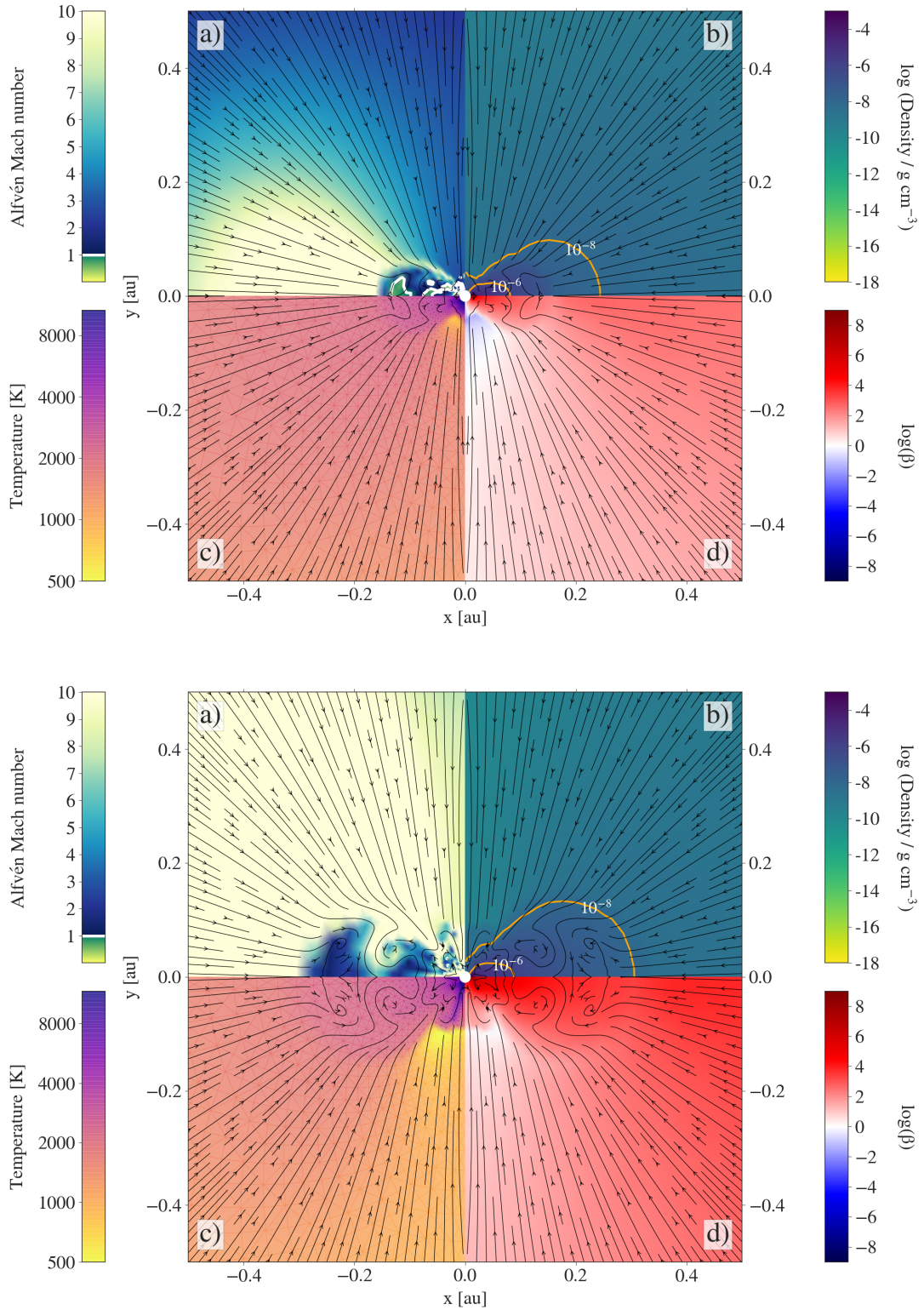
Figure 5.13: The four panels in both figures show the **a)** Alfvén Mach number, **b)** density, **c)** temperature, and **d)** plasma beta at a simulation snapshot after the formation of the second core. Shown here is the outcome of the collapse of a 1 $M_\odot$ cloud core with an outer radius of 3000 au and an initial temperature of 10 K. The initial rotation rate is set to $\Omega_0 = 1.77 \times 10^{-13}$ rad s^{-1}. The top figure shows the properties for a simulation run using the mass-to-magnetic flux ratio of $\mu_0 = 20$ whereas the bottom figure is for the case with $\mu_0 = 32$. The black streamlines indicate the velocity field. The different contour lines in panel *b* highlight the increasing density towards the centre and the disc's midplane.

Figure 5.14: The four panels in both figures show the **a)** ratio of centrifugal to gravitational force, **b)** ratio of toroidal to poloidal field components, **c)** radial velocity, and **d)** azimuthal velocity at a simulation snapshot after the formation of the second core. Shown here is the outcome of the collapse of a 1 $M_\odot$ cloud core with an outer radius of 3000 au and an initial temperature of 10 K. The initial rotation rate is set to $\Omega_0 = 1.77 \times 10^{-13}$ rad s^{-1}. The top figure shows the properties for a simulation run using the mass-to-magnetic flux ratio of $\mu_0 = 20$ whereas the bottom figure is for the case with $\mu_0 = 32$. The black streamlines in panels *a* and *b* indicate the velocity field. The red streamlines in panels *c* and *d* show the pinching effect of the poloidal field lines.

Figure 5.15: We follow the evolution of a collapsing 1 $M_\odot$ cloud core with an outer radius of 3000 au and an initial temperature of 10 K using RMHD simulations. The initial rotation rate is set to $\Omega_0 = 1.77 \times 10^{-13}$ rad s^{-1}. Shown here are the radial profiles comparing the radial (blue), azimuthal (dashed black), and Keplerian (dashed red) midplane velocities as well as the Keplerian midplane velocity including the thermal pressure force (dashed yellow), at a simulation snapshot after the formation of the second core. We compare the profiles from two different simulation runs with the mass-to-magnetic flux ratios of $\mu_0 = 20$ (left) and $\mu_0 = 32$ (right). In both models we find discs that are in gravito-centrifugal-thermal pressure equilibrium at this evolutionary stage.

disc with a size of 0.146 au and an enclosed mass of 2.21 $\times 10^{-2}$ $M_\odot$. Figure 5.16 shows the 2D behaviour of different properties within the forming disc and its surrounding envelope (i.e. the first core). The second core, disc, and outflow regions are sub-sonic in panel *a*. The density (panel *b*) of the second core will increase further since it is still accreting material via its surrounding disc. As seen in panel *d* the plasma beta indicates that the thermal pressure dominates over the magnetic pressure in the disc whereas the magnetic pressure dominates in the outflow region launched from the second core. The bottom plot (panel *a*) shows that the centrifugal force mostly dominates over gravity in the outflow regions, along the pole. The gravitational force dominates in the envelope surrounding the disc, where the material is still infalling. The toroidal field component dominates in the outflow region (panel *b*), indicating that magnetic pressure is the driving mechanism as discussed in Sect. 5.3.4. The positive velocities in the bottom plot (panel *c*) highlight the outflowing material. Figure 5.17 compares the midplane radial, azimuthal, and Keplerian velocities estimated with and without the thermal pressure force. Similar to the previous models, this disc is also found to be in gravito-centrifugal-thermal pressure equilibrium and is evolving further as it accretes material from its surrounding envelope.
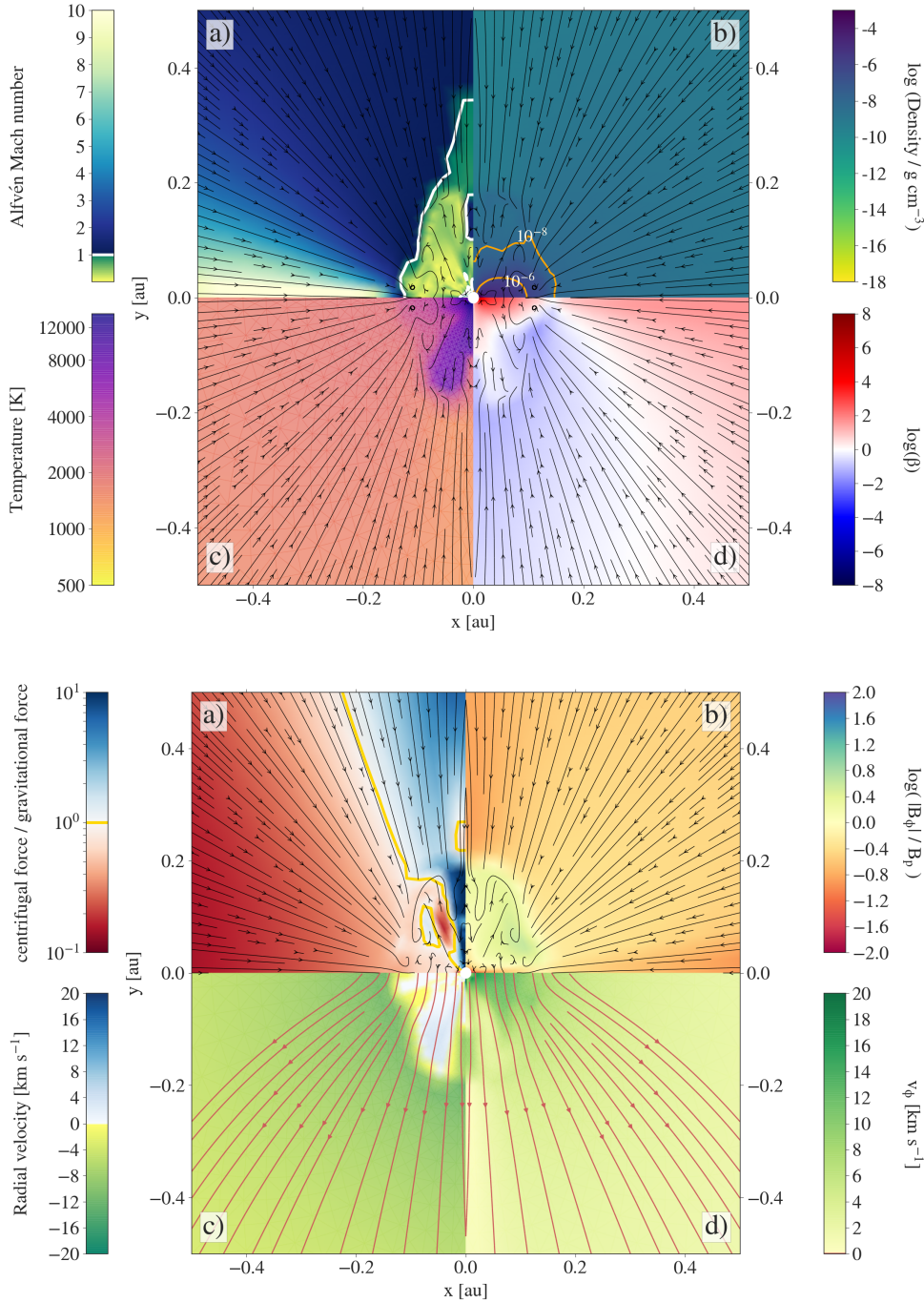
Figure 5.16: Shown here is the outcome of the collapse of a 2 $M_\odot$ cloud core with an outer radius of 3000 au and an initial temperature of 10 K. The initial rotation rate is set to $\Omega_0 = 2.48 \times 10^{-13}$ rad s^{-1} and the initial mass-to-magnetic flux ratio is $\mu_0 = 20$. *Top:* The four panels show the **a)** Alfvén Mach number, **b)** density, **c)** temperature, and **d)** plasma beta at a simulation snapshot after the formation of the second core. The black streamlines indicate the velocity field. The different contour lines in panel *b* highlight the increasing density towards the centre and the disc's midplane.
Bottom: The four panels show the **a)** ratio of centrifugal to gravitational force, **b)** ratio of toroidal to poloidal field components, **c)** radial velocity, and **d)** azimuthal velocity at a simulation snapshot after the formation of the second core. The black streamlines in panels *a* and *b* indicate the velocity field. The red streamlines in panels *c* and *d* show the pinching effect of the poloidal field lines.
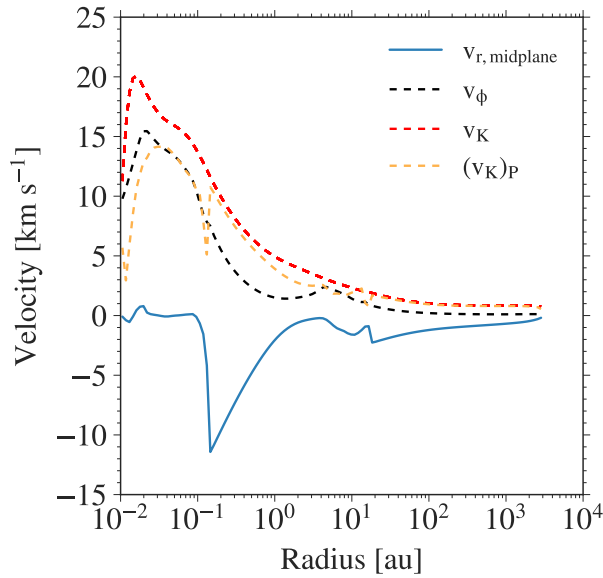
Figure 5.17: We follow the evolution of a collapsing 2 $M_\odot$ cloud core with an outer radius of 3000 au and an initial temperature of 10 K using an RMHD simulation. The initial rotation rate is set to $\Omega_0 = 2.48 \times 10^{-13}$ rad s^{-1} and the mass-to-magnetic flux ratio is $\mu_0 = 20$. Shown here are the radial profiles comparing the radial (blue), azimuthal (dashed black), and Keplerian (dashed red) midplane velocities, as well as the Keplerian midplane velocity including the thermal pressure force (dashed yellow), at a simulation snapshot after the formation of the second core. At this stage, the disc is in gravito-centrifugal-thermal pressure equilibrium.

5.5 Limitations

For the simulations discussed in this chapter, our resistive models currently only account for the effects of Ohmic resistivity. We do not include the other two non-ideal MHD terms in the induction equation, namely, the ambipolar diffusion and Hall terms (discussed in Sect. 2.2). The importance of each of these terms and their efficiency at different densities, temperatures, and radiation fields, that means at various stages of evolution, still remains widely debated. Additionally, the effects due to misalignment of the magnetic fields with the rotation axis, initial turbulence as well as grain chemistry, in terms of disc and outflow formation are still inconclusive. It remains numerically very challenging to include all these effects at the same time (see recent reviews by Wurster & Li, 2018; Teyssier & Commerçon, 2019).

For the simulations presented herein, a higher resolution than the one used is required to better resolve the outflow launched especially from the second core, as well as for convergence studies. Lastly, although the 2D axial and midplane symmetric setup of our computational grid gives us an advantage in terms of computation time, 3D studies have proven to be beneficial to explore the formation of spiral arms and effects due to fragmentation. Along these lines, some future ideas are presented in Chapter 7.

Effects of resistivity

As discussed in Sect. 5.1, in order to increase the diffusion time step we use a fixed upper limit for the resistivity as $\eta = 10^{17}$ cm^2 s^{-1} in all our models. This resistivity limit can have a significant impact on disc formation and the launching of outflows. Models with a lower resistivity behave similar to the one with ideal MHD and are extremely efficient in transporting angular momentum outwards thus hindering the formation of discs.

As a test, we re-ran the disc formation simulation for the 1 $M_\odot$ cloud core with a mass-to-magnetic flux ratio of $\mu_0 = 20$ and $E_{\mathrm{rot}}/E_{\mathrm{grav}} = 0.007$. Instead of the previously assigned upper limit for the resistivity ($\eta = 10^{17}$ cm^2 s^{-1}), we lowered the value to $\eta = 10^{15}$ cm^2 s^{-1}. For this simulation run with a weaker resistivity, we do not find a disc forming at the onset of the second core formation. The disc may form at a later time when the magnetic braking is not very efficient. This suggests that the absence of discs in some of our simulations could be an effect of prescribing a fixed upper limit for the resistivity. A thorough parameter scan in terms of different values for the upper limit of the resistivity with reasonable computation times will be explored as part of a follow-up study.

5.6   Summary

This chapter highlights our results from the investigation of magnetically driven outflows from the first and second hydrostatic cores as well as the onset of discs forming around the second core. In our collapse models, we include self-gravity, radiation, rotation, and a realistic gas EOS that includes effects due to rotational and vibrational degrees of freedom of H_2 molecules as well as dissociation and ionisation. Moreover, we account for the effects of ideal and non-ideal (including Ohmic resistivity) MHD. To our knowledge, these are the first ever 2D RMHD collapse simulations assuming axial and midplane symmetry to include the effects of self-gravity, radiation, rotation, a realistic gas EOS, and magnetic fields. A number of 3D RMHD studies with the same or even more physics have been performed (as listed in Table 5.1). However, the potential of 3D simulations to scan a broad parameter space is limited due to computational time restrictions. Here, using 2D RMHD, we explore different initial cloud core properties in terms of initial mass, rotation rate, and mass-to-magnetic flux ratio.

We study the dependence of disc formation and properties of magnetically launched outflows from the hydrostatic cores on the initial magnetic field strength (in terms of mass-to-magnetic flux ratio), cloud core mass, and cloud core rotation. All simulations adopt a fixed initial cloud temperature of 10 K and an outer radius of 3000 au. Since our simulations run for less than a year after the second core formation, we only trace the onset of the outflow from the second core. Hence, the focus is mainly on the outflows launched from the first core for quantitative comparisons and for understanding the dependence of outflow properties on various initial cloud core properties. Our key findings are summarised as follows.

- Thermal evolution of the molecular cloud core is similar in all the different simulation runs with and without rotation and magnetic fields. This is due to the thermal energy dominating over the magnetic energy at the centre of the cloud core.

- In our RHD simulations of rotating cloud cores, we find that the first core evolves into a "pseudo-disc" like oblate structure. We do not find any thermal pressure driven outflows from either the first or second core.

- Comparisons between ideal and resistive RMHD simulations indicate the presence of a magnetic pressure driven outflow from the first core in both cases. We only find a magnetic pressure driven outflow from the second core in our resistive RMHD model.

- We compare 1 $M_\odot$ RMHD collapse simulations with different initial mass-to-magnetic flux ratios of $\mu_0 =$ 5, 10, 20, and 32. We find magnetic pressure driven outflows emanating from the first and second cores. Our results indicate that the extent of the first core outflow increases with an increase in the mass-to-magnetic flux ratio μ_0. In other words, the first core outflow is more collimated for cases with lower μ_0 (i.e. higher magnetic field strength).

- We compare RMHD simulation runs with different initial cloud core masses of $M_0 =$ 1 $M_\odot$, 2 $M_\odot$, 5 $M_\odot$, and 10 $M_\odot$. We use a fixed mass-to-magnetic flux ratio of 20 times the critical value and the ratio of rotational to gravitational energy as $E_{\rm rot}/E_{\rm grav} = 0.007$. We find magnetic pressure driven outflows from both first and second cores. The strength and extent of the outflow from the first core decreases with increasing initial cloud core mass.

- We find a sub-au disc forming around the second core in our 1 $M_\odot$ rotating RHD simulation as well as for the 1 $M_\odot$ rotating RMHD runs with $\mu_0 = 20$ and 32. We also find a similar disc in our RMHD model for a 2 $M_\odot$ rotating cloud core. All these discs are in gravito-centrifugal-thermal pressure equilibrium.

- In both RHD as well as resistive RMHD cases where we do trace the onset of disc formation, we find that it begins after the formation of the second core. For all cases, the disc is still accreting material from the surrounding first core and is expected to grow in size as it evolves further.

Table 5.2 provides a summary of the different simulation runs including properties of the hydrostatic cores, outflows, and discs. For qualitative and quantitative comparisons, we need to follow the evolution of the disc and outflows, especially from the second core, for much longer times. This is also necessary for cases where we currently do not find a disc or outflows. Future work will include simulations for a wider parameter space as well as longer time evolution, including the effects of resistivity cut-offs that have not yet been explored extensively.

Table 5.2: Properties of the hydrostatic cores, outflows, and discs.

M_0 ($M_\odot$)	μ_0	E_{rot}/E_{grav}	Resistive	R_{fc} (au)	$M_{fc} \times 10^{-2}$ ($M_\odot$)	t_{fc} (yr)	$v_{(r,max)fc}$ (km s^{-1})	$R_{sc} \times 10^{-2}$ (au)	$M_{sc} \times 10^{-2}$ ($M_\odot$)	$v_{(r,max)sc}$ (km s^{-1})	R_{disc} (au)	$M_{disc} \times 10^{-2}$ ($M_\odot$)
1	–	0.01	N	14.88	11	1514.7	–	1.3	0.42	–	0.02	0.48
1	–	0.007	N	10.86	9.5	1246.3	–	1.4	0.48	–	0.07	0.74
1	10	0.01	N	30.81	0.87	641.45	1.0	1.48	0.0013	–	–	–
1	10	0.01	Y	34.5	4.85	654.6	148	4.1	0.89	4	–	–
1	5	0.007	Y	7.92	3.79	601.7	0.98	7.77	1.19	2.51	–	–
1	10	0.007	Y	31.06	4.66	616.6	124.57	6.99	1.36	3.81	–	–
1	20	0.007	Y	22.66	6.29	927	83.86	4.13	0.82	3.28	0.18	1.3
1	32	0.007	Y	20.40	8.03	1117.5	3.15	9.59	1.21	5.48	0.34	1.8
2	20	0.007	Y	18.37	7.33	445.1	91.75	11.83	2.18	14.58	0.146	2.21
5	20	0.007	Y	14.89	10.5	130.6	4.55	6.30	1.15	8.87	–	–
10	20	0.007	Y	13.4	11.8	98.1	2.38	4.59	0.98	6.76	–	–

Note: Listed above are the first and second hydrostatic core properties as well as the fastest outflow velocities and disc properties for runs with different initial cloud core mass M_0, mass-to-magnetic flux ratio μ_0, and ratio of rotational to gravitational energy E_{rot}/E_{grav}. It is also stated if resistivity is included. The common cloud core properties are an initial temperature of 10 K and an outer radius of 3000 au. We note that the hydrostatic core and disc properties for various simulations should not be directly compared since they are estimated at different "final" time snapshots after the formation of the second core.

Summary

Magnetized molecular clouds serve as the cradle for nascent stars. The gravitational collapse of cold and dense gas within these clouds initiates the process of star formation. A collapsing molecular cloud core forms two hydrostatic cores, the so-called first and second Larson cores. An optically thin cloud core undergoes an initial isothermal first collapse phase. Gradually, the collapsing cloud core becomes optically thick due to an increase in central density. At this stage, thermal pressure acts as the dominant force to counteract gravity, which leads to the formation of the first hydrostatic core. As the central temperature reaches ≈ 2000 K, the onset of H_2 dissociation triggers the second collapse phase. The second hydrostatic core is formed at the end of this phase, once most of the H_2 is dissociated. The central temperature continues to increase as this second core grows within the first core. The second core eventually transforms into a protostar, once the temperature in the core rises to $\sim 10^6$ K and initiates deuterium burning. During these initial stages, conservation of angular momentum leads to the formation of a protostellar disc. Magnetic fields also contribute towards the outward transport of angular momentum and drive outflows (and jets). The complex physical processes involved during these evolutionary stages require a robust, self-consistent numerical treatment.

Richard Larson pioneered the use of numerical simulations to further our understanding of how star formation proceeds in his seminal work more than 60 years ago (Larson, 1969), which has ever since been an active area of research. However, the comprehensive characterisation of the gravitational collapse still remains unanswered (as highlighted in the reviews by Larson, 2003; McKee & Ostriker, 2007; Inutsuka, 2012; Teyssier & Commerçon, 2019; Hull & Zhang, 2019; Pudritz & Ray, 2019).

In this thesis, we probe the initial stages of star and disc formation via robust numerical simulations, including the effects of self-gravity, radiation, cloud rotation, and magnetic fields. In this chapter, I briefly summarise our key findings from the 1D and 2D collapse simulations. Using the RMHD code *PLUTO*, we follow the evolution of a molecular cloud core along two main routes:

⋆ Protostellar collapse: We study the gravitational collapse of an isolated gas sphere using detailed thermodynamical modelling in terms of radiation transport and phase transitions. The main goal is to understand the entire collapse scenario through the stages of first and second core formation by incorporating a more complex gas EOS with a variable adiabatic index (depending on density and temperature) to model the phase transitions.

◎ Disc formation: We investigate protostellar disc formation and the launching of magnetically driven outflows from the first and second cores. We incorporate an initial cloud rotation and resistive MHD in our simulations to explore their effects on disc and outflow formation.

In Chapter 2, we detail the gas thermodynamics and microphysics including the gas EOS and opacity tables used in our simulations. We also provide details of the

initial setup, numerics, computational grid, and the boundary conditions for both our 1D and 2D simulations. We include self-gravity, a grey FLD approximation for the radiative transfer, and appropriate dust and gas opacity tables. Additionally, we make use of the gas EOS from D'Angelo & Bodenheimer (2013), which was implemented in the *PLUTO* code by Vaidya et al. (2015). For this work, we updated the radiation transport module to account for this realistic gas EOS that accounts for the rotational and vibrational degrees of freedom for the H_2 molecules, which start being excited as the cloud transitions from being effectively monatomic to diatomic, as well as their dissociation and ionisation.

In Chapter 3, we present results from our spherically symmetric RHD collapse simulations, which span seven orders of magnitude in spatial scale. These collapse studies, for the first time, involve a parameter scan across initial low- to high-mass ($0.5 - 100 \, M_\odot$) molecular cloud cores. The thermal evolution and structure of the cloud cores from our low-mass runs are consistent with previous 1D RHD collapse simulations, which were limited to the low-mass regime ($\leq 10 \, M_\odot$). This work explores the dependence of the first and second core properties on initial cloud core properties, such as mass, temperature, and outer radius. We mainly highlight the properties of the first hydrostatic core. The key results indicate that *in the high-mass regime, first cores do not have time to form because of high accretion rates* (published in Bhandare et al., 2018). This also provides a useful observational constraint for ongoing efforts involving detections of first hydrostatic core candidates.

In Chapter 4, we follow the evolution of the second hydrostatic core and study its dependence on the initial cloud core properties. In the first part, we describe results from our 1D RHD simulations. Compared to the previous chapter, here, we follow the evolution of the second core for ≥ 100 years after its formation, for all the different cases. These studies indicate that the cloud cores with a higher initial mass collapse faster and form bigger, more massive second cores. We discuss the expansion and contraction of the evolving second core, governed by the timescale ratio of Kelvin–Helmholtz contraction versus accretion. We expand our studies to 2D RHD simulations and follow the collapse of $1 \, M_\odot$, $5 \, M_\odot$, $10 \, M_\odot$, and $20 \, M_\odot$ initial non-rotating cloud cores with an unprecedented resolution. The most important result of this investigation is that for the $1 \, M_\odot$ case, we find *convection being driven in the outer layers of the second hydrostatic core* (Bhandare et al., 2020, accepted). This supports the intriguing possibility that dynamo-driven magnetic fields may be generated during the very early phases of star formation. The results also show large-scale oscillations of the second accretion shock front resulting from the SASI, which has so far not been seen in simulations of the early evolutionary stages of star formation.

Finally, in Chapter 5, we discuss the effects of solid-body rotation and magnetic fields (including Ohmic resistivity) during the early stages of star and disc formation. We detail results from the first ever 2D RMHD simulations assuming axial and midplane symmetry, which include the combined effects of self-gravity, radiation, a realistic gas EOS, solid-body rotation, and Ohmic resistivity. Over the past years, there have been various 3D RMHD studies that include the same or more physics but explore only a limited parameter space due to computational time restrictions. The main aim of these simulations was to study the formation of centrifugally supported Keplerian discs and to investigate the onset of magnetically launched outflows from the hydrostatic cores, for collapse scenarios spanning a wide range of initial properties. We study the dependence of the disc and outflow properties on different initial cloud core properties such as mass, rotation rate, and magnetic field strength. We explore mass-to-magnetic flux ratios of 5, 10, 20, and 32 and initial cloud core masses of $1 \, M_\odot$, $2 \, M_\odot$, $5 \, M_\odot$, and $10 \, M_\odot$. We consider two different ratios of rotational to

gravitational energy of 0.007 and 0.01, both below the fragmentation limit (> 0.01). This parameter space will be extended in our future work, which will also include the less explored effects of resistivity cut-offs.

Our results indicate the presence of magnetic pressure driven outflows launched from first and second hydrostatic cores formed during collapse simulations that include non-ideal MHD effects (via Ohmic resistivity). We find a strong dependence of the extent of the outflow on the magnetic field strength and on the initial cloud core mass. Furthermore, we find that disc formation begins after the formation of the second core in the RHD and resistive RMHD runs. The second hydrostatic core and its surrounding disc thus evolve simultaneously. In less than a year after its formation, the disc is found to be in gravito-centrifugal-thermal pressure equilibrium. Disc formation not only has a strong dependence on the initial cloud core properties but also on the prescribed numerics (e.g. resistivity, included physics, resolution etc.). Our disc formation studies indicate that discs can start forming at sub-au scales during the early stages of star formation.

In conclusion, we use state-of-the-art numerical simulations to quantify the properties of the hydrostatic cores, outflows, and discs for gravitational collapse scenarios spanning a wide range of initial cloud core properties. By sequentially investigating each evolutionary stage during the global collapse process, this work yields a valuable contribution to our understanding of the intimate connection between the formation of stars and discs.

CHAPTER 7

Outlook

In this thesis, we used self-consistent numerical simulations to gain insights into various physical mechanisms involved during the transition of a molecular cloud core (i.e. pre-stellar core) to the second hydrostatic core (i.e. the forming protostar) and its surrounding disc. In recent years, astronomers have gathered a wealth of high-resolution observations of young discs (e.g. Tobin et al., 2012; Murillo et al., 2013; Codella et al., 2014; Lee et al., 2017; Tychoniec et al., 2018). However, there still remain several open questions, which can be answered using newly developed theoretical and numerical models to explore our understanding of the formation and evolution of disc substructures.

Keeping this in mind, the next steps will involve linking star and planet formation by further tracing the evolution of the circumstellar disc (the birthplace of planets), down to disc fragmentation. Future studies will proceed along two main ideas, with a focus on understanding the dust dynamics (necessary for the core accretion scenario of planet formation theory) during the early formation stages. The first will be to provide better constraints on circumstellar disc properties to investigate the hypothesis of gas giant planet formation via gravitational instabilities. In the second, the focus will be on bridging the gap between the theoretical understanding and observational signatures of these systems using synthetic observations. This will enable us to address some of the fundamental questions regarding the formation and evolution of circumstellar discs and provide a useful link between star and protoplanet formation.

Zooming in on star and disc formation

Zooming in on the smallest scales in order to understand the influence of complex physical processes such as hydrodynamics, radiative transfer, phase transition, chemistry, and magnetic fields has been challenging both theoretically and observationally. Several fundamental questions, for example, the values of initial magnetic field strengths and orientation, angular momenta, and turbulence of the cloud cores from which stars and discs form still remain unanswered. This in turn introduces various caveats in understanding the initial conditions for planet formation and the final outcome of star-planet systems. The main aim of my current and future work is to unravel the role of various physical mechanisms using a robust, self-consistent numerical treatment in order to investigate this multi-scale transition of a molecular cloud core to a star-disc system harbouring planet(s).

So far, most cloud collapse studies have considered dust and gas to be strongly coupled and use the dust-to-gas mass ratio as the standard interstellar medium value of 1:100. However, recent studies have pointed out the possible decoupling of micrometre dust grains in molecular clouds (Hopkins & Lee, 2016; Tricco et al., 2017) as well as millimetre sized grains in collapsing cloud cores (Bate & Lorén-Aguilar, 2017) and hence the influence on the dust-to-gas mass ratio. In this regard, my aim is to use a dust size distribution in the initial molecular cloud core and investigate the

influence of dust dynamics on the local dust-to-gas mass ratio and its role during the early evolutionary stages of disc formation. I expect that the dust size distribution will have a significant influence on the cooling efficiency, opacities, and resistivity calculations.

Recently, a new particle module, which accounts for the drag forces between the different sized dust grains and gas, has been implemented in *PLUTO* (Mignone et al., 2019). The first step will be to incorporate this module in the current working setup for the 2D R(M)HD collapse simulations from Bhandare et al. (2020). The results from this project will provide significant insights into the role of dust dynamics in collapsing clouds with a wide range of initial conditions, such as different values for cloud core mass, angular momentum, magnetic field strength, and orientation, which has not been extensively studied so far.

Furthermore, the onset of disc formation still remains widely debated (as discussed in the detailed review by Wurster & Li, 2018). Some studies have found that the first hydrostatic core evolves into a disc even before the onset of the second core formation. On the contrary, other studies have found that the disc is formed only much later, after the formation of the second hydrostatic core. This discrepancy has a strong dependence on the initial conditions and evolution of the collapsing cloud, and has a consequence on disc lifetimes. It is thus essential to investigate the effect of initial conditions on the onset of disc formation, while tracing the evolution of dust and gas separately.

Currently, evolving the disc for a longer time, i.e. until the Class 0 phase, is often hindered due to time step restrictions and hence most studies replace the central (second) core with a sink particle. The influence of a sink particle on disc formation has been extensively discussed in Wurster & Li (2018). Towards this end, the next steps will include developing a robust sub-grid model for the sink particle treatment. As presented in this thesis, we have studied the evolution of the first and second Larson cores (discussed in Bhandare et al., 2018, 2020). These data will be used as a lookup-table to compute the evolution of the central object, i.e. protostar within a sink-cell paradigm. This will enable following the disc evolution until the Class 0/I phase, during which several circumstellar discs have been observed to show local enhancements of dust-to-gas mass ratios (e.g. Boneberg et al., 2016). Therefore, results from these future models will be compared with observations of young discs from recent ALMA surveys (e.g. Andrews et al., 2018). Disc properties from this proposed parameter study will also be used as initial conditions for future studies involving the modelling of dust growth, which will allow for a more self-consistent picture of the disc structure.

The main drawback of this project would be that 2D models fail to capture the formation of 3D structures such as spiral arms. However, evolving the star-disc system using 3D RMHD simulations entails several numerical challenges, one of the most important being computational time restrictions. Thus a parameter scan for 3D RMHD studies proves to be very expensive. Nonetheless, to compare my results with the state-of-the-art research focused on disc studies, the future steps will be to perform 3D RMHD simulations, for a few interesting cases from the 2D runs, with a focus on deriving the parameter space of disc (and molecular cloud core) configurations in which giant planet formation is enabled via gravitational instabilities (detailed in the next section).

Impact of disc evolution on giant planet core formation

Numerical investigations focusing on disc formation have emphasised the importance of considering effects due to (non-ideal) MHD, radiative transfer, cosmic-ray ionisation, turbulence, and chemistry (detailed in the recent review by Wurster & Li, 2018). Despite a plethora of theoretical work, several aspects of disc formation and evolution such as its onset, lifetime, fragmentation probability, and the effect of misalignment still remain debated, mostly due to numerical and computational constraints.

Recent collapse studies (Matsumoto et al., 2017; Lewis & Bate, 2018; Lam et al., 2019) investigated the combined effects of initial turbulence and (non-ideal) MHD on disc formation. They found a strong dependence of the disc properties, lifetime, and fragmentation probability on the strength of the magnetic field and the initial turbulence. These studies show contradicting results, which suggest that initial turbulence can either hinder or promote disc formation and fragmentation.

So far, none of these studies include the effects of radiation transport or a realistic gas EOS (to account for H_2 dissociation, ionisation, molecular vibrations, and rotations), in combination with resistivity and both turbulence- and rotation-induced angular momentum transport. These initial conditions can have a significant influence on triggering or preventing gravitational instabilities in early discs. The dynamical feedback from magnetically driven jets, outflows, and disc winds, known to arise from MHD processes during the very early phases, might also impact the angular momentum transport in circumstellar discs, which will influence their evolution and their potential to form planets. The effects due to this feedback can have strong implications on forming the initial seeds (for example, clumps formed due to gravitational instabilities) for giant planet formation, embedded in the disc.

Recent observational evidence of substructures such as rings and gaps, and spiral arms in young discs (e.g. the recent DSHARP survey described in Andrews et al., 2018) suggest, among other things, ongoing (giant) planet formation or the presence of already formed planets carving gaps in these discs. This provides a strong motivation to derive better constraints on the initial conditions leading to the formation of circumstellar discs and to further investigate the hypothesis of forming gas giant planets rapidly via gravitational instability during the very early stages. This study will aim at connecting the stages of star-disc formation to early signatures of giant protoplanet formation.

The outlook in this direction will be to investigate gravitational instabilities in early discs, while accounting for dust dynamics via 3D RMHD simulations. These runs will also include decaying turbulence and a sink particle treatment for the central protostar. Using the dust opacity resulting from a proper dust treatment will help to accurately determine the cooling of the disc, which will have an impact on gravitational instability within the disc and hence its fragmentation probability. Additionally, modelling disc evolution through the episodic accretion phase can help to investigate the origin of FU Orionis and EX Orionis outbursts that have been widely observed in low-mass star-disc systems (e.g. Cieza et al., 2018).

In an effort to paint a complete picture of star-disc-planet systems by connecting numerical models with the observational evidence, my aim is to follow up these studies with synthetic observations. This can be achieved by deriving dust continuum maps using the open source software *RADMC-3D* (Dullemond et al., 2012), for snapshots from the simulations which resemble observed discs and compare them with (ALMA) observations. A working pipeline from *PLUTO* (version 4.1) to *RADMC-3D* and *CASA* (Common Astronomy Software Applications) has already

been established. Similar comparisons have been successfully carried out in previous works, for example, Tomida et al. (2017). Multi-scale observations in the current ALMA-era and future capabilities of the James Webb Space Telescope and the European Extremely Large Telescope, will allow for many more comparisons with new and resolved discs.

Numerical convergence

A.1 Convergence tests for one-dimensional simulations

A.1.1 Resolution tests

Resolution plays an important role especially when treating regions near accretion shocks. For an initial 1 $M_\odot$ cloud core, we performed core collapse simulations with the same initial conditions but using different resolutions. We investigate the case of a molecular cloud core extending from 10^{-4} – 3000 au at an initial temperature of 10 K. The simulations using different resolutions have no significant effects on the evolution seen in Fig. A.1, which indicates the numerical convergence of our studies. As expected for the lowest resolution, for which there are fewer grid cells in the inner region, we see slight differences at the second shock position. These differences probably increase for even lower resolutions. There seems to be a convergence around 4400 cells and above. This indicates a minimum resolution of around 4400 cells required for our 1D simulations.

We use an inner radius R_{in} of 10^{-2} au for the 2D simulations discussed in Chapter 4 with 1445 grid cells in the radial direction. Due to the high computational expenses, we currently cannot perform simulations with an even higher resolution in 2D. However, since there are no significant differences in the properties of the first and second hydrostatic cores between the 1D and 2D simulations, we perform convergence tests in 1D for the 1 $M_\odot$ case. We use a 1D grid extending from 10^{-2} – 3000 au. In Fig. A.1 we compare, for two different resolutions, the radial density, temperature, and entropy profiles from these 1D simulations. The peak in the entropy profile corresponds to the position of the second accretion shock. The two runs show convergence with no significant differences in their behaviour. This suggests that a radial resolution of 1445 cells is sufficient for the 2D simulations with R_{in} of 10^{-2} au.

A.1.2 Comparisons for different inner radii

In order to ensure that the inner radius does not affect the second shock position, we perform further tests with different inner radii. As seen in Fig. A.2, all of the runs evolve in a similar manner. We note the differences for the simulations with $R_{in} = 3 \times 10^{-4}$ au and $R_{in} = 10^{-3}$ au. However, there seems to be a convergence for an inner radius around 10^{-4} au. For our studies, we chose an inner radius of 10^{-4} au to avoid the boundary being too close to the second shock.

We used an inner radius R_{in} of 10^{-2} au for the simulations discussed in Chapter 4. We note the decrease in temperature at the inner boundary seen in Fig. 4.5 for both the 1D and 2D studies. Due to the high computational expenses, we currently cannot perform tests with an inner radius less than 10^{-2} au in 2D. However, given that there are no significant differences in the second core properties between the 1D and 2D simulations with the same initial setup, we compare the 1D results for runs with two
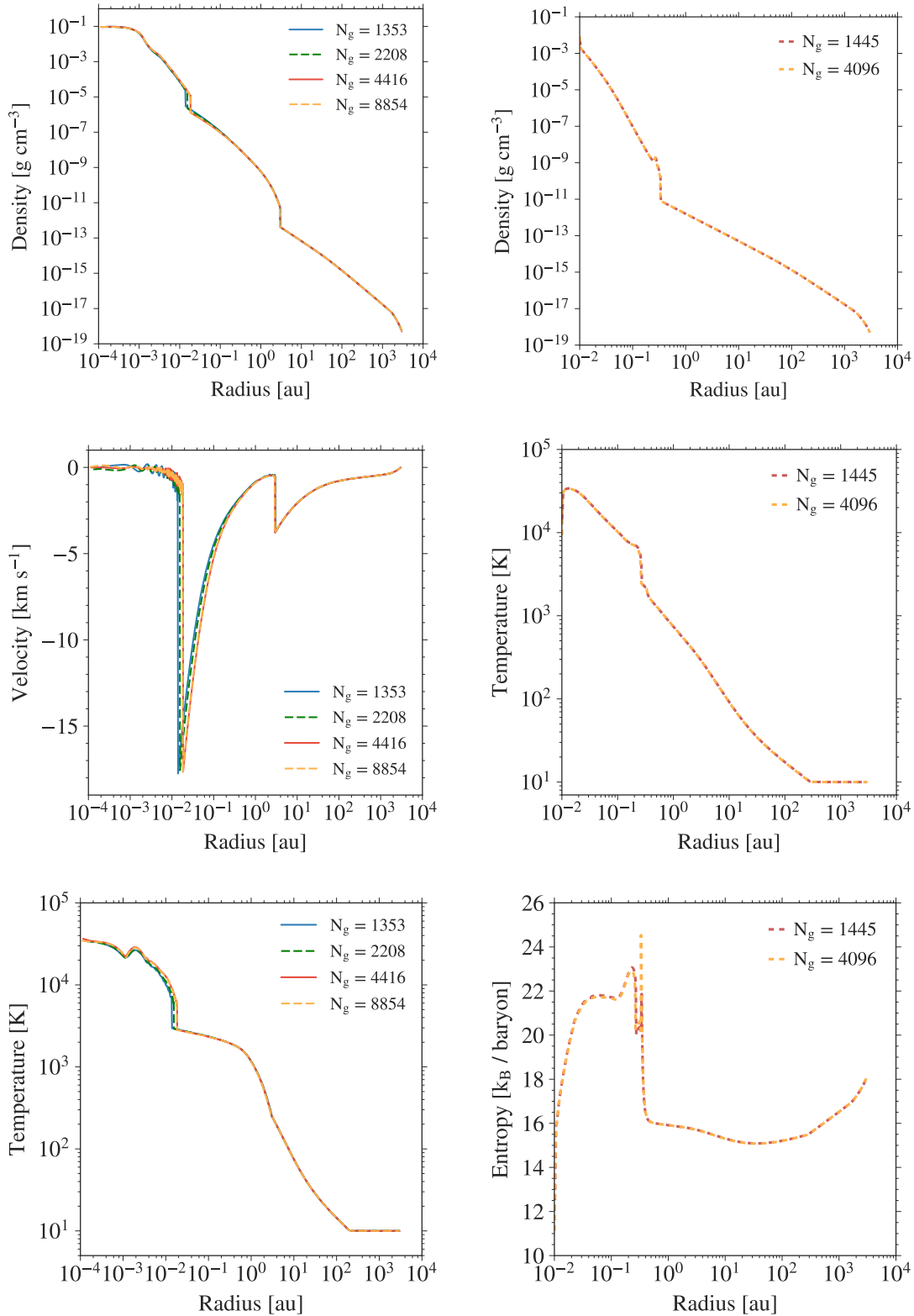
Figure A.1: *Left column:* Radial profiles of the density (top), velocity (middle), and gas temperature (bottom) for an initial 1 $M_\odot$ cloud core at an initial temperature T_0 of 10 K are shown at a time step after the second core formation. The different lines indicate the results using various 1D grid resolutions for a grid extending from 10^{-4} – 3000 au. *Right column:* Radial profiles of the density (top), gas temperature (middle), and entropy (bottom) for an initial 1 $M_\odot$ collapsing cloud core at an initial temperature T_0 of 10 K. The yellow and red lines indicate the results using two different 1D grid resolutions for a grid extending from 10^{-2} – 3000 au.
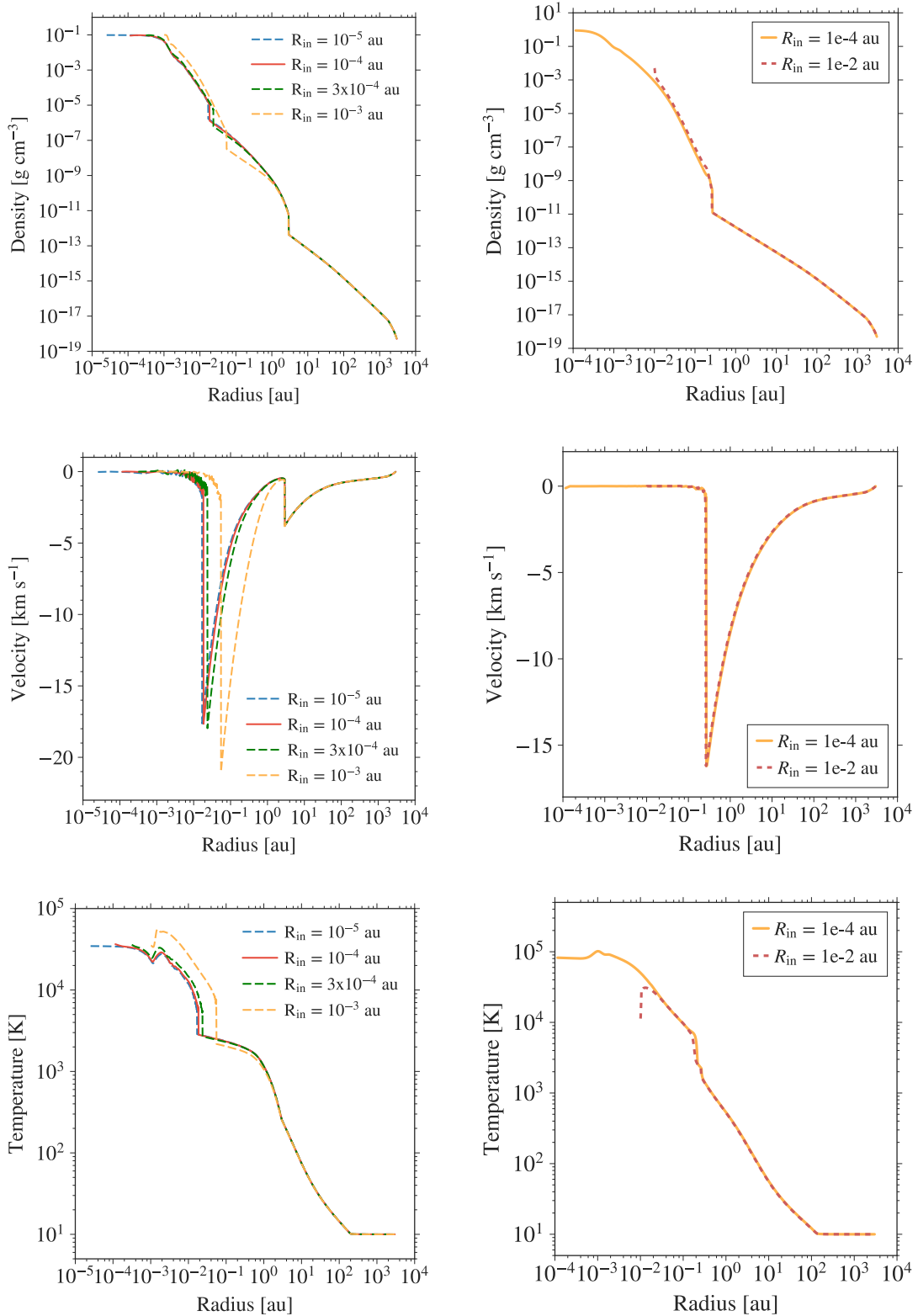
Figure A.2: Radial profiles of the density (top), velocity (middle), and gas temperature (bottom) for an initial 1 $M_\odot$ collapsing cloud core from the 1D simulations are shown at a time step after the second core formation. *Left column:* The different lines indicate the results each using a different inner radius of the cloud core. The dashed blue line indicates 10^{-5} au, the red line indicates 10^{-4} au, the dashed green line indicates 3×10^{-4} au, and the dashed yellow line indicates 10^{-3} au. *Right column:* The yellow line indicates an inner radius of 10^{-4} au and the dashed red line indicates an inner radius of 10^{-2} au.

different inner radii of 10^{-4} au and 10^{-2} au. Both these runs employ a total of 4096 logarithmically spaced grid cells from 10^{-2} au to 3000 au.

We do not see a drop in the innermost regions for the collapse case with $R_{\text{in}} = 10^{-4}$ au. We therefore conclude that the decrease seen in case of $R_{\text{in}} = 10^{-2}$ au could be a numerical artefact due to the inner boundary being much closer to the second accretion shock. Besides the temperature decrease in the innermost central region, we do not find any significant differences in the second core properties when comparing both R_{in} cases. We also confirm that energy conservation is not violated at the inner boundary.

A.2 Resolution tests for two-dimensional simulations

For an initial 1 $M_\odot$ cloud core, we perform collapse simulations using three different resolutions shown in Fig. A.3. In both the figures, we indicate the results at a snapshot in time where the central densities are roughly similar. Polar-angle averaged radial density, velocity, and temperature profiles for the three different resolution runs in Fig. A.3 do not show any significant differences in the second core properties.

The main aim of this resolution test was to highlight the importance of using a higher resolution in order to better resolve the eddies indicating a convective instability as discussed in Sect. 4.2.1. Resolution differences within the second core are more prominent in the 2D entropy plots seen in Fig. A.3. Computational time restrictions prevent us from using an even higher resolution to test the convergence.
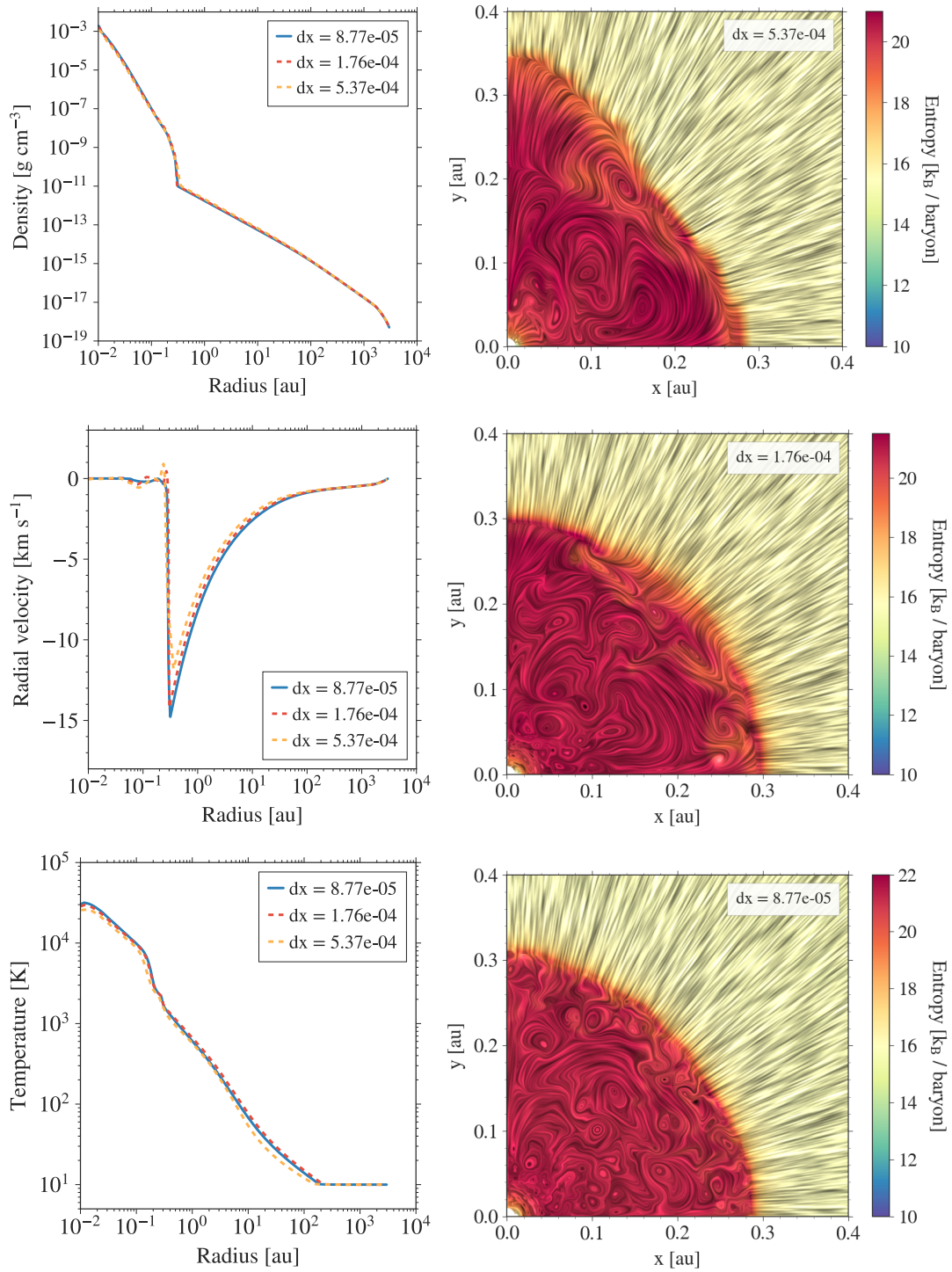
Figure A.3: *Left column:* Polar-angle averaged radial profiles of the density (top), velocity (middle), and gas temperature (bottom) for an initial 1 $M_\odot$ collapsing cloud core at an initial temperature T_0 of 10 K are shown at a time step after the second core formation. The different lines indicate the results using various grid resolutions in the 2D simulations. *Right column:* Line integral convolution visualisation of the second core formed from the collapse of a 1 $M_\odot$ cloud core at an initial temperature T_0 of 10 K and an outer radius of 3000 au. The panels (top to bottom) show results from runs using different resolutions in an increasing order as indicated in the legends. The entropy behaviour is shown at a time snapshot when the central densities are roughly similar. For the results presented in this thesis, we use the highest resolution, which allows us to resolve the convective eddies within the second core.

Supplemental material for Chapter 5

In this Appendix we provide some additional material for Chapter 5. Shown in each of the figures are the radial profiles of the density, temperature, enclosed mass, radial velocity, azimuthal velocity, angular momentum, total magnetic field strength, the ratio of toroidal to poloidal magnetic field components, magnetic pressure, thermal pressure, Alfvén Mach number, and Alfvén velocity. The different quantities are shown at a time snapshot after the formation of the second hydrostatic core. The initial cloud core properties for the corresponding simulations are stated in each figure caption.
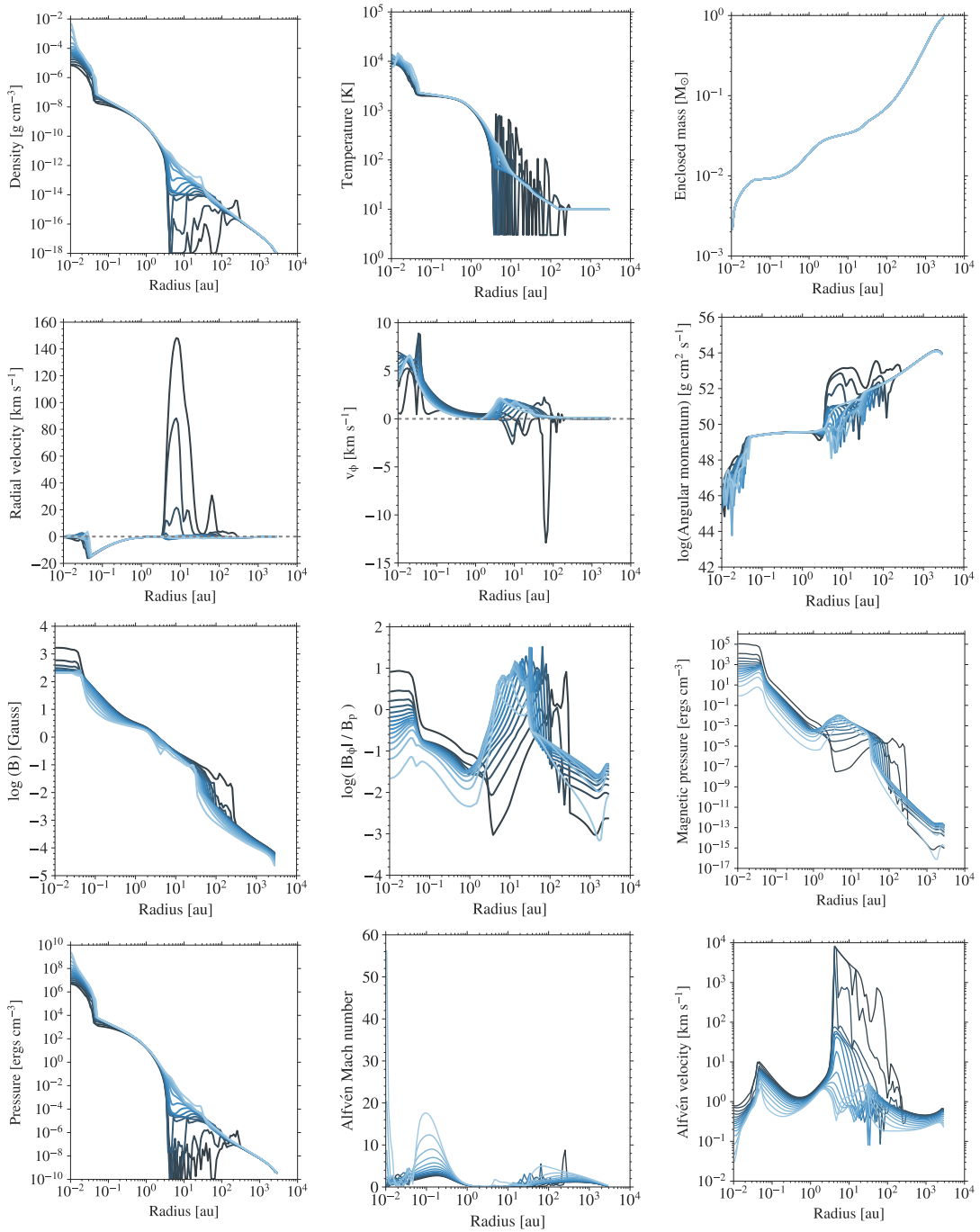
Figures B.1 and B.2 provide cloud core properties for a comparison between an ideal and resistive MHD runs that are discussed in Sect. 5.3.2. Both these runs simulate the collapse of a 1 $M_\odot$ cloud core with an initial temperature of 10 K and an outer radius of 3000 au. The initial mass-to-magnetic flux ratio is $\mu_0 = 20$ and the rotation rate is set to $\Omega_0 = 2.099 \times 10^{-13}$ rad s^{-1}.

Figures B.3 – B.6 display the radial profiles for the simulation runs with different mass-to-magnetic flux ratios of $\mu_0 = 5, 10, 20,$ and 32. The common properties are an initial mass of 1 $M_\odot$, a temperature of 10 K, an outer radius of 3000 au, and a rotation rate of $\Omega_0 = 1.77 \times 10^{-13}$ rad s^{-1}. The effect of varying the initial mass-to-magnetic flux ratio μ_0 is discussed in Sects. 5.3.3 and 5.4.2.

Figures B.7 – B.9 show the radial profiles for simulation runs with different initial cloud core masses of $M_0 = 2\ M_\odot, 5\ M_\odot,$ and 10 $M_\odot$. The common properties are an initial temperature of 10 K, an outer radius of 3000 au, and the mass-to-magnetic flux ratio μ_0 of 20. The initial rotation rate is computed using a fixed ratio of rotational to gravitational energy $E_{\mathrm{rot}}/E_{\mathrm{grav}}$ as 0.007. The dependence of the hydrostatic core, outflow, and disc properties on the initial cloud core mass is detailed in Sects. 5.3.4 and 5.4.3.
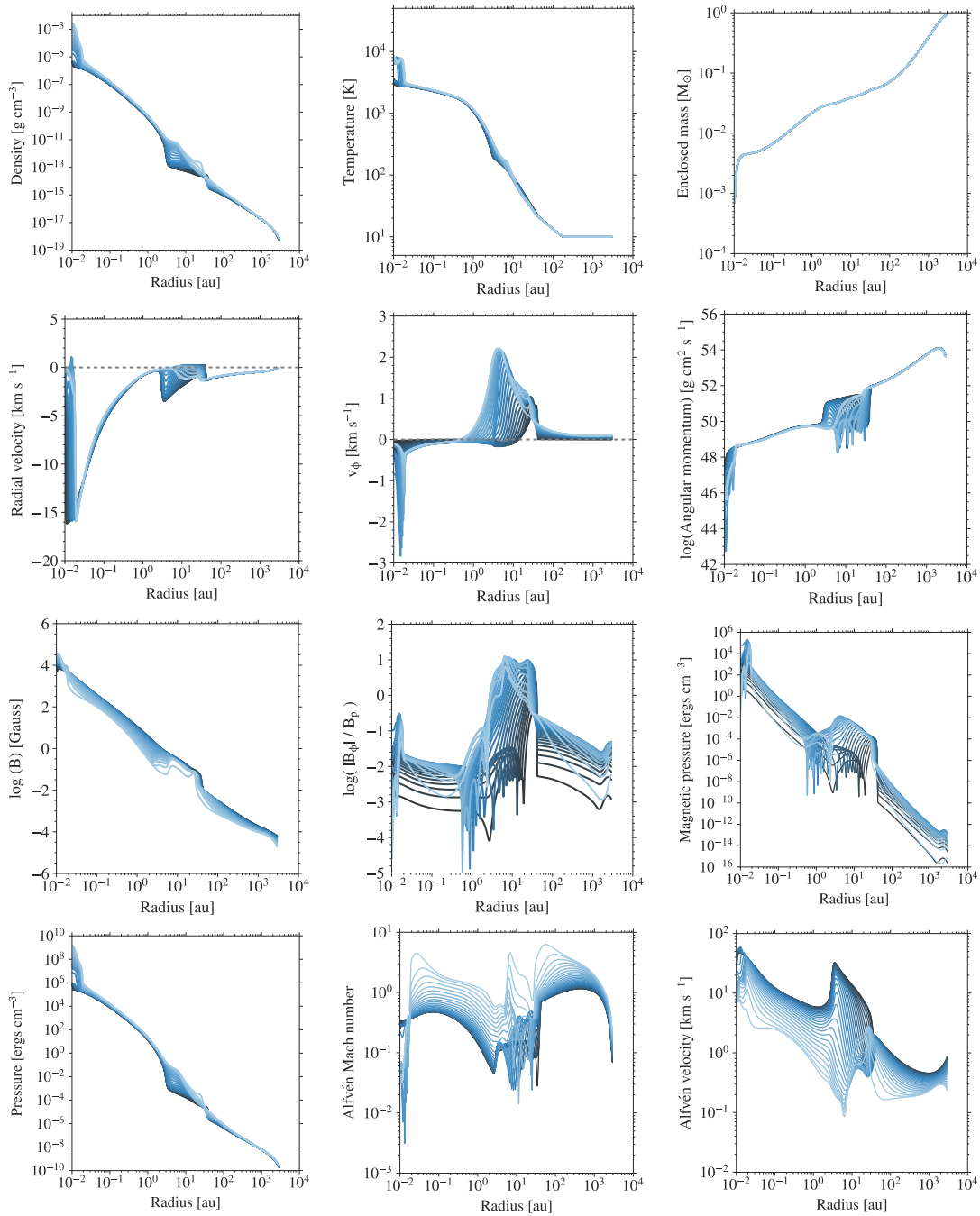
Figure B.1: *Ideal MHD run:* Radial profiles (across and down) after formation of the second core, formed due to the collapse of a 1 $M_\odot$ cloud core with an outer radius of 3000 au and an initial temperature of 10 K. The initial mass-to-magnetic flux ratio is $\mu_0 = 10$ and the initial rotation rate is set to $\Omega_0 = 2.099 \times 10^{-13}$ rad s^{-1}. Different subplots show the radial profiles (across and down) of **a)** density, **b)** gas temperature, **c)** enclosed mass, **d)** radial velocity, **e)** azimuthal velocity, **f)** angular momentum, **g)** magnetic field strength, **h)** ratio of toroidal to poloidal field, **i)** magnetic pressure, **j)** thermal pressure, **k)** Alfvén Mach number, and **l)** Alfvén velocity. The colour gradient from light to dark blue spans the polar angle from the midplane ($\theta = 90°$) to the pole ($\theta = 0°$).

Figure B.2: *Resistive MHD run:* Radial profiles (across and down) after formation of the second core, formed due to the collapse of a 1 $M_\odot$ cloud core with an outer radius of 3000 au and an initial temperature of 10 K. The initial mass-to-magnetic flux ratio is $\mu_0 = 10$ and the initial rotation rate is set to $\Omega_0 = 2.099 \times 10^{-13}$ rad s^{-1}. Different subplots show the radial profiles (across and down) of **a)** density, **b)** gas temperature, **c)** enclosed mass, **d)** radial velocity, **e)** azimuthal velocity, **f)** angular momentum, **g)** magnetic field strength, **h)** ratio of toroidal to poloidal field, **i)** magnetic pressure, **j)** thermal pressure, **k)** Alfvén Mach number, and **l)** Alfvén velocity. The colour gradient from light to dark blue spans the polar angle from the midplane ($\theta = 90°$) to the pole ($\theta = 0°$).

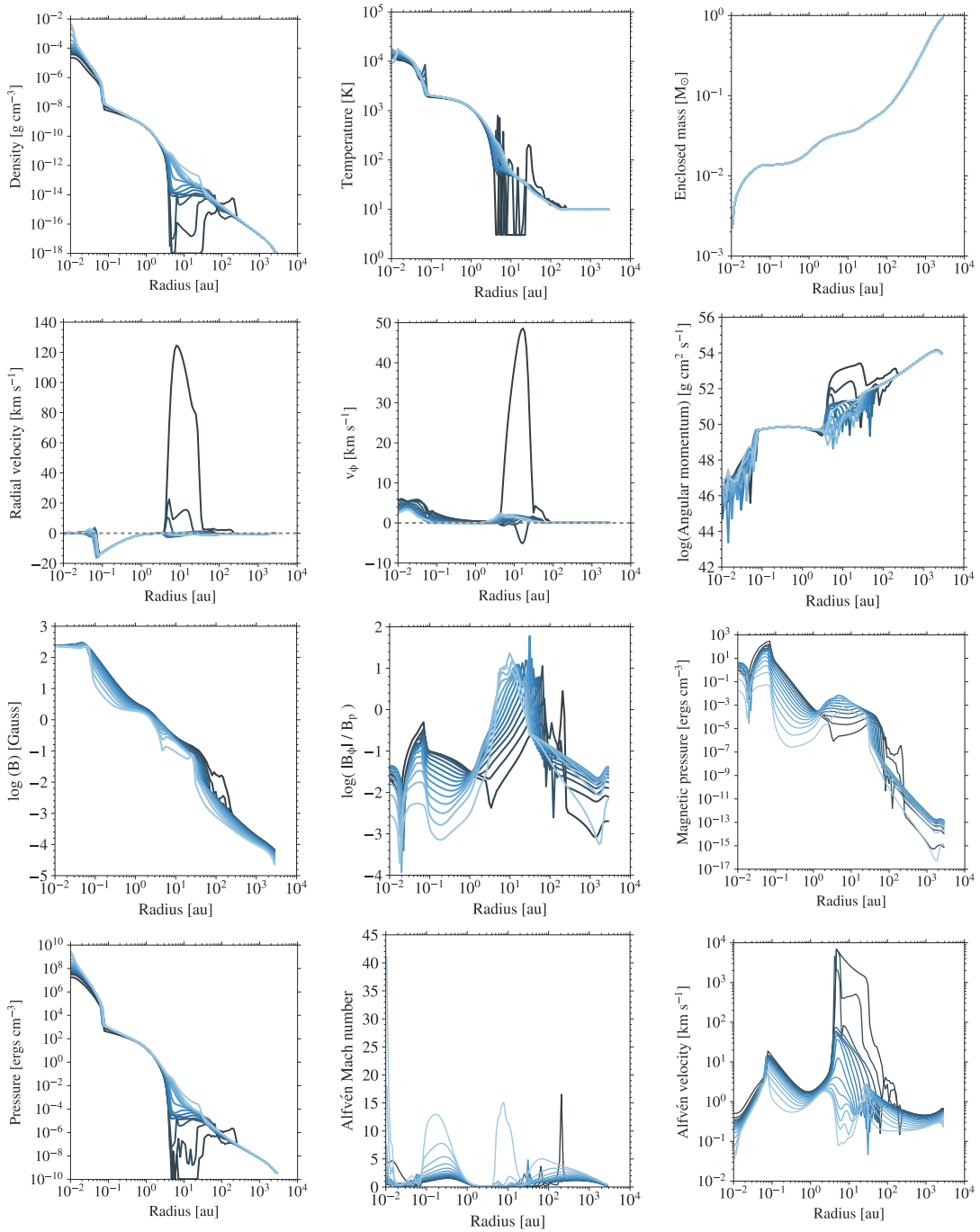**Figure B.3:** Radial profiles (across and down) after formation of the second core, formed due to the collapse of a 1 $M_\odot$ cloud core with an outer radius of 3000 au and an initial temperature of 10 K. The initial mass-to-magnetic flux ratio is $\mu_0 = 5$ and the initial rotation rate is set to $\Omega_0 = 1.77 \times 10^{-13}$ rad s^{-1}. The different subplots show the radial profiles (across and down) of **a)** density, **b)** gas temperature, **c)** enclosed mass, **d)** radial velocity, **e)** azimuthal velocity, **f)** angular momentum, **g)** magnetic field strength, **h)** ratio of toroidal to poloidal field, **i)** magnetic pressure, **j)** thermal pressure, **k)** Alfvén Mach number, and **l)** Alfvén velocity. The colour gradient from light to dark blue spans the polar angle from the midplane ($\theta = 90°$) to the pole ($\theta = 0°$).

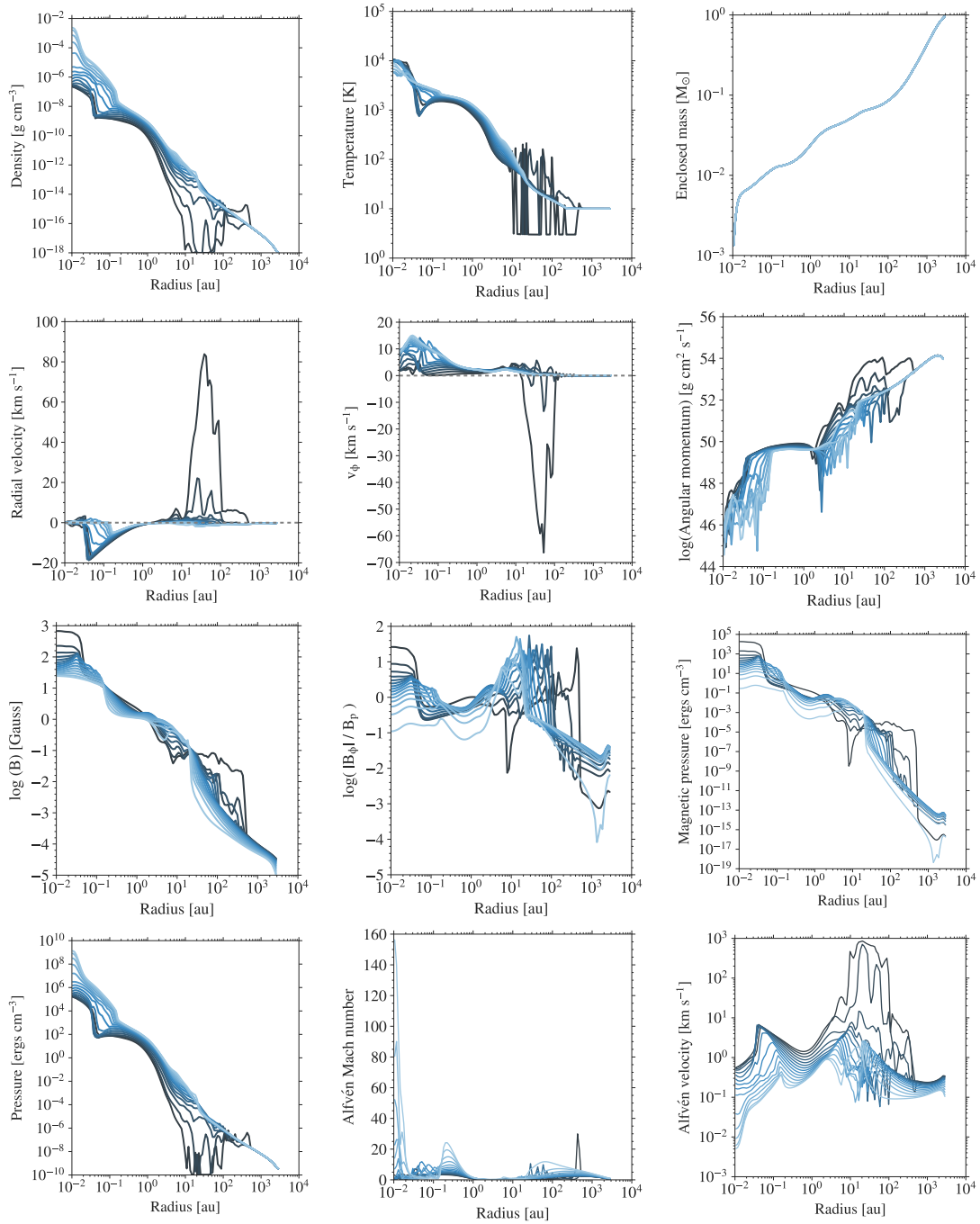**Figure B.4:** Radial profiles (across and down) after formation of the second core, formed due to the collapse of a 1 $M_\odot$ cloud core with an outer radius of 3000 au and an initial temperature of 10 K. The initial mass-to-magnetic flux ratio is $\mu_0 = 10$ and the initial rotation rate is set to $\Omega_0 = 1.77 \times 10^{-13}$ rad s^{-1}. Different subplots show the radial profiles (across and down) of **a)** density, **b)** gas temperature, **c)** enclosed mass, **d)** radial velocity, **e)** azimuthal velocity, **f)** angular momentum, **g)** magnetic field strength, **h)** ratio of toroidal to poloidal field, **i)** magnetic pressure, **j)** thermal pressure, **k)** Alfvén Mach number, and **l)** Alfvén velocity. The colour gradient from light to dark blue spans the polar angle from the midplane ($\theta = 90°$) to the pole ($\theta = 0°$).
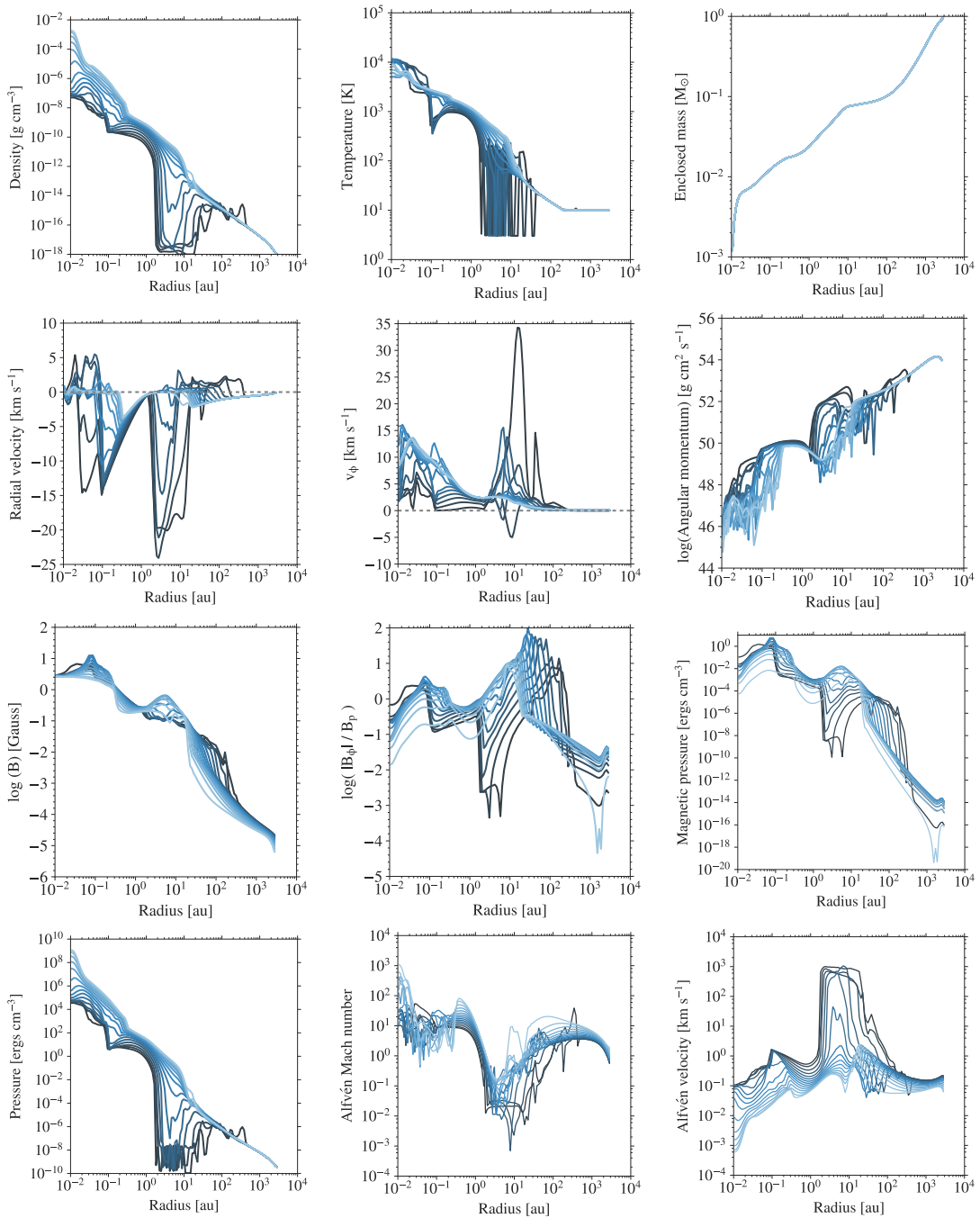
Figure B.5: Radial profiles (across and down) after formation of the second core, formed due to the collapse of a 1 $M_\odot$ cloud core with an outer radius of 3000 au and an initial temperature of 10 K. The initial mass-to-magnetic flux ratio is $\mu_0 = 20$ and the initial rotation rate is set to $\Omega_0 = 1.77 \times 10^{-13}$ rad s^{-1}. Different subplots show the radial profiles (across and down) of **a)** density, **b)** gas temperature, **c)** enclosed mass, **d)** radial velocity, **e)** azimuthal velocity, **f)** angular momentum, **g)** magnetic field strength, **h)** ratio of toroidal to poloidal field, **i)** magnetic pressure, **j)** thermal pressure, **k)** Alfvén Mach number, and **l)** Alfvén velocity. The colour gradient from light to dark blue spans the polar angle from the midplane ($\theta = 90°$) to the pole ($\theta = 0°$).
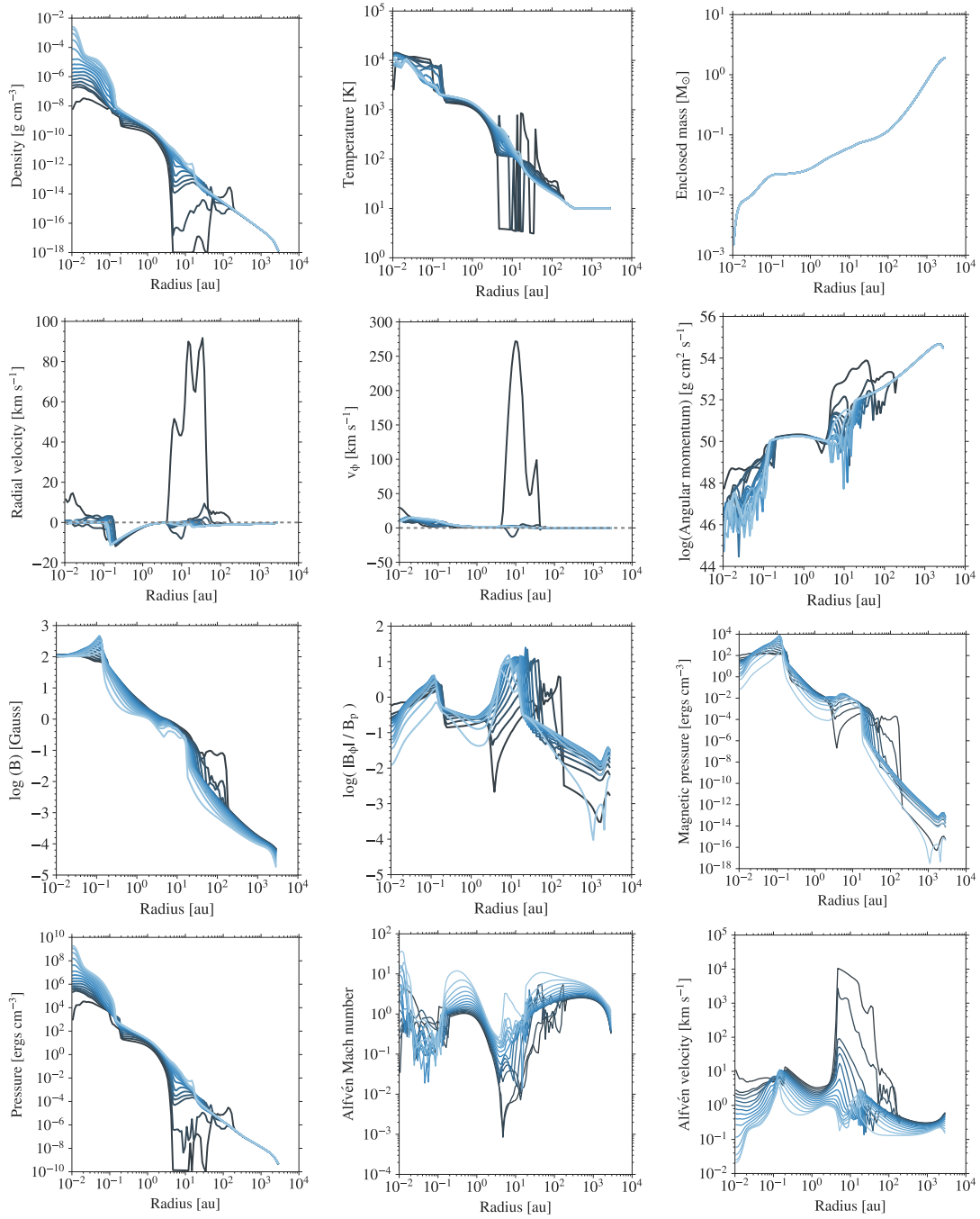
Figure B.6: Radial profiles (across and down) after formation of the second core, formed due to the collapse of a 1 $M_\odot$ cloud core with an outer radius of 3000 au and an initial temperature of 10 K. The initial mass-to-magnetic flux ratio is $\mu_0 = 32$ and the initial rotation rate is set to $\Omega_0 = 1.77 \times 10^{-13}$ rad s^{-1}. Different subplots show the radial profiles (across and down) of **a)** density, **b)** gas temperature, **c)** enclosed mass, **d)** radial velocity, **e)** azimuthal velocity, **f)** angular momentum, **g)** magnetic field strength, **h)** ratio of toroidal to poloidal field, **i)** magnetic pressure, **j)** thermal pressure, **k)** Alfvén Mach number, and **l)** Alfvén velocity. The colour gradient from light to dark blue spans the polar angle from the midplane ($\theta = 90°$) to the pole ($\theta = 0°$).
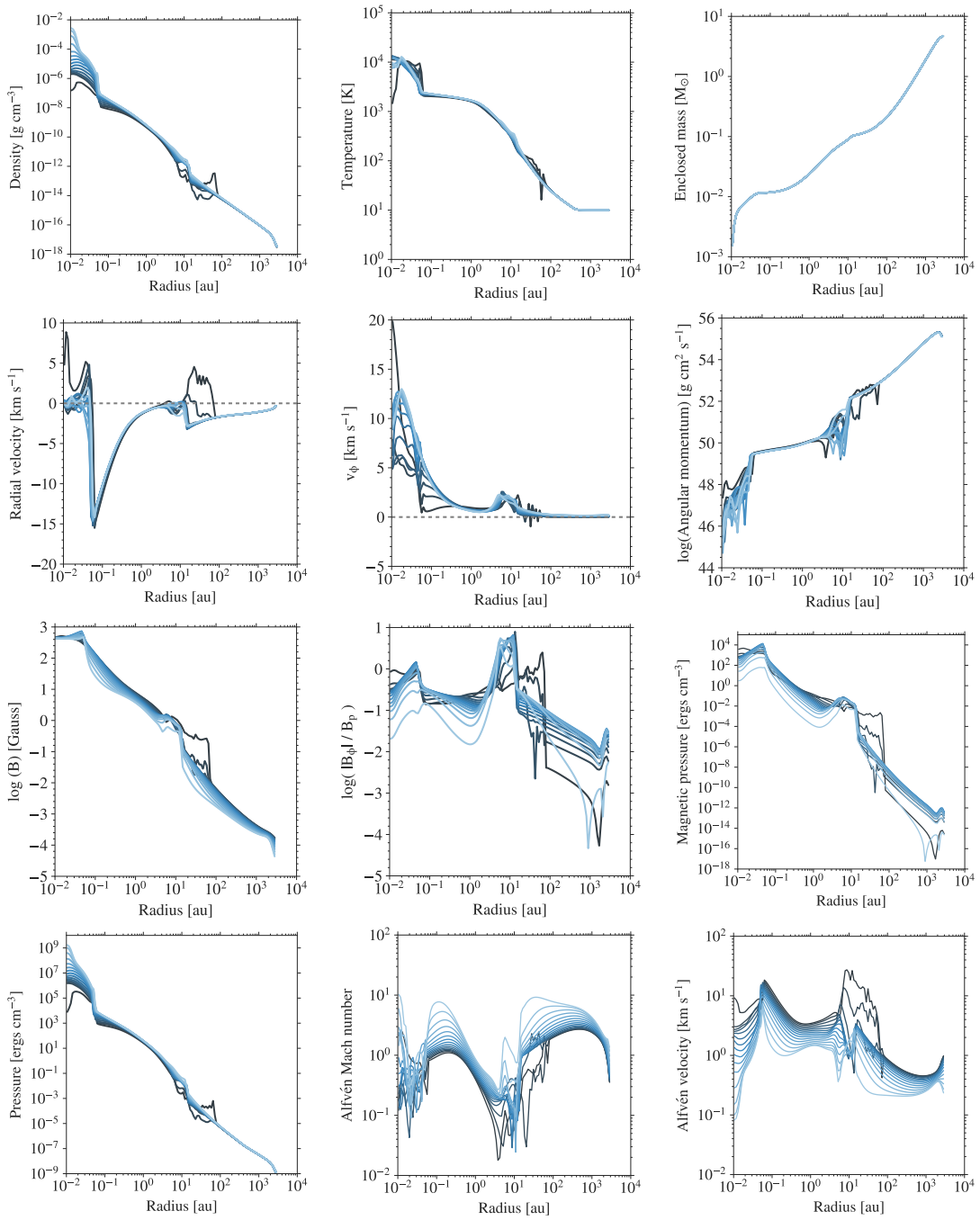
Figure B.7: Radial profiles (across and down) after formation of the second core, formed due to the collapse of a 2 $M_\odot$ cloud core with an outer radius of 3000 au and an initial temperature of 10 K. The initial mass-to-magnetic flux ratio is $\mu_0 = 20$ and the initial rotation rate is set to $\Omega_0 = 2.48 \times 10^{-13}$ rad s^{-1}. Different subplots show the radial profiles (across and down) of **a)** density, **b)** gas temperature, **c)** enclosed mass, **d)** radial velocity, **e)** azimuthal velocity, **f)** angular momentum, **g)** magnetic field strength, **h)** ratio of toroidal to poloidal field, **i)** magnetic pressure, **j)** thermal pressure, **k)** Alfvén Mach number, and **l)** Alfvén velocity. The colour gradient from light to dark blue spans the polar angle from the midplane ($\theta = 90°$) to the pole ($\theta = 0°$).
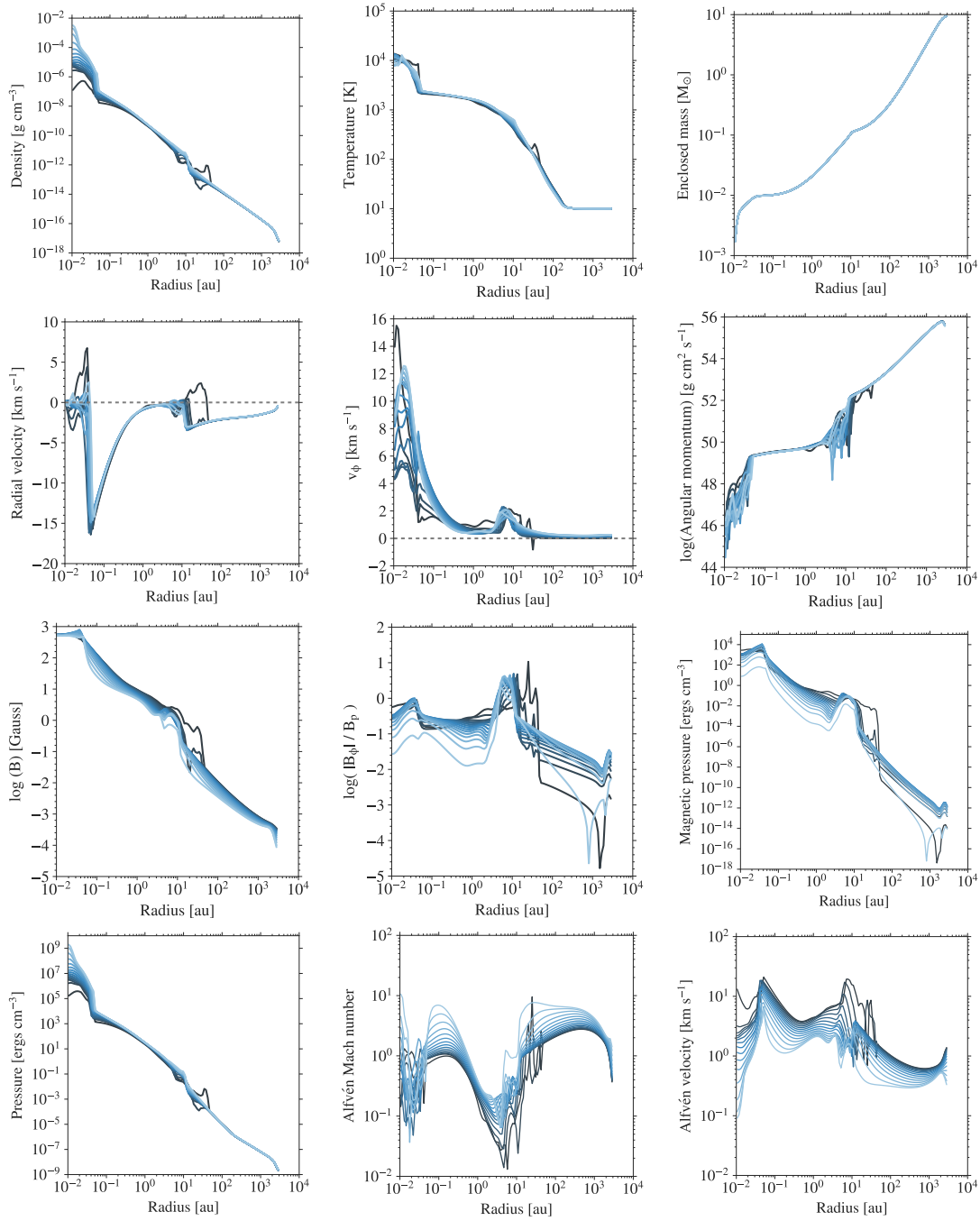
Figure B.8: Radial profiles (across and down) after formation of the second core, formed due to the collapse of a 5 $M_\odot$ cloud core with an outer radius of 3000 au and an initial temperature of 10 K. The initial mass-to-magnetic flux ratio is $\mu_0 = 20$ and the initial rotation rate is set to $\Omega_0 = 3.93 \times 10^{-13}$ rad s^{-1}. Different subplots show the radial profiles (across and down) of **a)** density, **b)** gas temperature, **c)** enclosed mass, **d)** radial velocity, **e)** azimuthal velocity, **f)** angular momentum, **g)** magnetic field strength, **h)** ratio of toroidal to poloidal field, **i)** magnetic pressure, **j)** thermal pressure, **k)** Alfvén Mach number, and **l)** Alfvén velocity. The colour gradient from light to dark blue spans the polar angle from the midplane ($\theta = 90°$) to the pole ($\theta = 0°$).

Figure B.9: Radial profiles (across and down) after formation of the second core, formed due to the collapse of a 10 $M_\odot$ cloud core with an outer radius of 3000 au and an initial temperature of 10 K. The initial mass-to-magnetic flux ratio is $\mu_0 = 20$ and the initial rotation rate is set to $\Omega_0 = 5.55 \times 10^{-13}$ rad s^{-1}. Different subplots show the radial profiles (across and down) of **a)** density, **b)** gas temperature, **c)** enclosed mass, **d)** radial velocity, **e)** azimuthal velocity, **f)** angular momentum, **g)** magnetic field strength, **h)** ratio of toroidal to poloidal field, **i)** magnetic pressure, **j)** thermal pressure, **k)** Alfvén Mach number, and **l)** Alfvén velocity. The colour gradient from light to dark blue spans the polar angle from the midplane ($\theta = 90°$) to the pole ($\theta = 0°$).

Physical Constants

Radiation constant	$a = 7.5657 \times 10^{-15}\,\mathrm{erg\,cm^{-3}\,K^{-4}}$
Astronomical unit	$\mathrm{au} = 1.495\,978\,706\,91 \times 10^{13}\,\mathrm{cm}$
Speed of light	$c = 2.997\,924\,58 \times 10^{10}\,\mathrm{cm\,s^{-1}}$
Electron volt	$\mathrm{eV} = 1.602\,176\,5 \times 10^{-12}\,\mathrm{erg}$
Gravitational constant	$G = 6.674\,28 \times 10^{-8}\,\mathrm{cm^3\,g^{-1}\,s^{-2}}$
Hydrogen mass	$m_\mathrm{H} = 1.6737 \times 10^{-24}\,\mathrm{g}$
Planck constant	$h = 6.626\,068\,96 \times 10^{-27}\,\mathrm{erg\,s}$
Boltzmann constant	$k_\mathrm{B} = 1.3807 \times 10^{-16}\,\mathrm{erg\,K^{-1}}$
Solar luminosity	$L_\odot = 3.839 \times 10^{33}\,\mathrm{erg\,s^{-1}}$
Solar mass	$M_\odot = 1.9891 \times 10^{33}\,\mathrm{g}$
Electron mass	$m_\mathrm{e} = 9.1094 \times 10^{-28}\,\mathrm{g}$
Atomic mass unit	$m_\mathrm{u} = 1.660\,538\,9 \times 10^{-24}\,\mathrm{g}$
Parsec	$\mathrm{pc} = 3.0857 \times 10^{18}\,\mathrm{cm}$
Universal gas constant	$\mathfrak{R} = 8.314\,472 \times 10^{7}\,\mathrm{g\,cm^2\,s^{-2}\,mol^{-1}\,K^{-1}}$
Solar radius	$R_\odot = 6.955 \times 10^{10}\,\mathrm{cm}$
Year	$\mathrm{yr} = 31\,557\,600\,\mathrm{s}$

List of Symbols

Variable	Name
a	acceleration source term due to self-gravity
α	alpha viscosity parameter
B_0, B	initial and total magnetic field strength
B_{rad}	integral of the black-body Planck spectrum
B_{p}	poloidal magnetic field strength
B_ϕ	toroidal magnetic field strength
β	plasma beta
χ_{abs}	coefficient of absorption
χ_{T}	temperature exponent
χ_ρ	density exponent
c_{s}	sound speed
c_{s0}	initial sound speed
C_P	specific heat at constant pressure
C_V	specific heat at constant volume
$\mathrm{dx}, \Delta r$	radial grid cell size
D_{rad}	radiative diffusion coefficient
∇_{act}	actual temperature gradient
∇_{ad}	adiabatic temperature gradient
E, E_{tot}	total energy
E_{int}, e	internal energy density
E_{kin}	kinetic energy density
E_{rad}	radiation energy density
$\dot{E}$	accretion energy
ϵ_{H}	translational energy for hydrogen
$\epsilon_{\mathrm{H+H}}$	dissociation energy for molecular hydrogen
$\epsilon_{\mathrm{H^+}}$	ionisation energy for atomic hydrogen
$\epsilon_{\mathrm{H_2}}$	internal energy for molecular hydrogen
ϵ_{He}	translational energy for helium
$\epsilon_{\mathrm{He^+}}$	ionisation energy for helium
η	resistivity
F_{rad}	radiation energy flux
γ	adiabatic index
Γ_1	first adiabatic index
H	local pressure scale height
κ	opacity
κ_{R}	Rosseland mean opacity
λ	diffuse radiation flux limiter

Variable	Name
L_{acc}	accretion luminosity
M_{dust}/M_{gas}	dust-to-gas mass ratio
M_0	initial cloud core mass
M_A	Alfvén Mach number
M_{BE}	mass of a Bonnor–Ebert sphere
M_{fc}, M_{sc}	first and second core mass
$\dot{M}$	accretion rate
μ	mean molecular weight
μ_0	mass-to-magnetic flux ratio
N_g	number of grid cells
Ω_0	initial rotation frequency
Ω_K	Keplerian angular velocity
P, P_{gas}	thermal gas pressure
P_{deg}	degenerate gas pressure
P_{ram}	ram pressure
ϕ	azimuthal angle
Φ_{sg}	gravitational potential of gas mass
r	spherical radius
$r\Delta\theta$	cell size in polar direction
ρ	gas density
ρ_c	central gas density
ρ_{fc}, ρ_{sc}	first and second core density
ρ_o	initial outer density
R	cylindrical radius
R_{fc}, R_{sc}	first and second core radius
R_{in}, R_{cloud}	inner and outer cloud core radius
T	gas temperature
T_0	fixed lower gas temperature
$t_{accretion}$	accretion timescale
T_{BE}	temperature of a Bonnor–Ebert sphere
T_{dust}	radiation temperature
T_{evap}	local dust evaporation temperature
T_{fc}, T_{sc}	first and second core temperature
t_{ff}	free-fall time
t_{final}	final simulation time
τ_{fc}	first core lifetime
t_{KH}	Kelvin–Helmholtz timescale
T_{rad}	radiation temperature
θ	polar angle
u	dynamical velocity
u_{fc}, u_{sc}	first and second core velocity
$v_r, v_\theta, v_\phi, v_K, v_A$	radial, polar, azimuthal, Keplerian, and Alfvén velocities
x	degree of ionisation of atomic hydrogen
ξ	dimensionless radius
X	hydrogen mass fraction
X_e	ionisation degree
y	degree of dissociation of molecular hydrogen
Y	helium mass fraction
z_1, z_2	degree of single and double ionisation of helium
ζ	partition function

Bibliography

Allen, A., Li, Z.-Y., & Shu, F. H. 2003, ApJ, 599, 363

Alves, J. F., Lada, C. J., & Lada, E. A. 2001, Nature, 409, 159

Andersen, B. C., Stephens, I. W., Dunham, M. M., et al. 2019, ApJ, 873, 54

André, P. 2002, in EAS Publications Series, Vol. 3, EAS Publications Series, ed. J. Bouvier & J.-P. Zahn, 1

André, P., Di Francesco, J., Ward-Thompson, D., et al. 2014, in Protostars and Planets VI, ed. H. Beuther, R. S. Klessen, C. P. Dullemond, & T. Henning, 27

Andrews, S. M., Huang, J., Pérez, L. M., et al. 2018, ApJ, 869, L41

Arce, H. G., & Sargent, A. I. 2006, ApJ, 646, 1070

Arquilla, R., & Goldsmith, P. F. 1986, ApJ, 303, 356

Arzoumanian, D., André, P., Didelon, P., et al. 2011, A&A, 529, L6

Arzoumanian, D., André, P., Könyves, V., et al. 2019, A&A, 621, A42

Balay, S., Gropp, W. D., McInnes, L. C., et al. 1997, in Modern Software Tools in Scientific Computing, ed. E. Arge, A. M. Bruaset, & H. P. Langtangen (Birkhäuser Press), 163

Balay, S., Abhyankar, S., Adams, M. F., et al. 2019a, PETSc Users Manual, Tech. Rep. ANL-95/11 - Revision 3.11, Argonne National Laboratory

Balay, S., Abhyankar, S., Adams, M. F., et al. 2019b, PETSc Web page, https://www.mcs.anl.gov/petsc

Banerjee, R., & Pudritz, R. E. 2006, ApJ, 641, 949

Baraffe, I., Vorobyov, E., & Chabrier, G. 2012, ApJ, 756, 118

Barnard, E. E. 1907, ApJ, 25, 218

Basu, S., & Mouschovias, T. C. 1994, ApJ, 432, 720

Basu, S., & Mouschovias, T. C. 1995a, ApJ, 452, 386

Basu, S., & Mouschovias, T. C. 1995b, ApJ, 453, 271

Bate, M. R. 1998, ApJ, 508, L95

Bate, M. R. 2010, MNRAS, 404, L79

Bate, M. R. 2011, MNRAS, 417, 2036

Bate, M. R., & Lorén-Aguilar, P. 2017, MNRAS, 465, 1089

Bate, M. R., Tricco, T. S., & Price, D. J. 2014, MNRAS, 437, 77–95

Berardo, D., Cumming, A., & Marleau, G.-D. 2017, ApJ, 834, 149

Bergin, E. A., & Tafalla, M. 2007, ARA&A, 45, 339

Beuther, H., Churchwell, E. B., McKee, C. F., et al. 2007, in Protostars and Planets V, ed. B. Reipurth, D. Jewitt, & K. Keil, 165

Bhandare, A., Kuiper, R., Henning, T., et al. 2020, A&A, accepted

Bhandare, A., Kuiper, R., Henning, T., et al. 2018, A&A, 618, A95

Bjerkeli, P., Ramsey, J. P., Harsono, D., et al. 2019, A&A, 631, A64

Black, D. C., & Bodenheimer, P. 1975, ApJ, 199, 619

Blandford, R. D., & Payne, D. G. 1982, MNRAS, 199, 883

Blondin, J. M., & Mezzacappa, A. 2006, ApJ, 642, 401

Blondin, J. M., Mezzacappa, A., & DeMarino, C. 2003, ApJ, 584, 971

Bodenheimer, P., & Sweigart, A. 1968, ApJ, 152, 515

Bok, B. J., & Reilly, E. F. 1947, ApJ, 105, 255

Boneberg, D. M., Panić, O., Haworth, T. J., et al. 2016, MNRAS, 461, 385

Bonnor, W. B. 1956, MNRAS, 116, 351

Boss, A. P. 1984, ApJ, 277, 768

Bourke, T. L., Myers, P. C., Robinson, G., et al. 2001, ApJ, 554, 916

Caratti o Garatti, A., Stecklum, B., Garcia Lopez, R., et al. 2017, Nature Physics, 13, 276

Caselli, P., Benson, P. J., Myers, P. C., et al. 2002, ApJ, 572, 238

Chabrier, G., & Küker, M. 2006, A&A, 446, 1027

Chen, X., Arce, H. G., Zhang, Q., et al. 2010, The Astrophysical Journal, 715, 1344

Cieza, L. A., Ruíz-Rodríguez, D., Perez, S., et al. 2018, MNRAS, 474, 4347

Codella, C., Cabrit, S., Gueth, F., et al. 2014, A&A, 568, L5

Commerçon, B., Hennebelle, P., Audit, E., et al. 2010, A&A, 510, L3

Commerçon, B., Audit, E., Chabrier, G., et al. 2011a, A&A, 530, A13

Commerçon, B., Teyssier, R., Audit, E., et al. 2011b, A&A, 529, A35

Courant, R., Friedrichs, K., & Lewy, H. 1928, Mathematische Annalen, 100, 32

Crutcher, R. M. 1999, ApJ, 520, 706

D'Angelo, G., & Bodenheimer, P. 2013, ApJ, 778, 77

Dapp, W. B., & Basu, S. 2010, A&A, 521, L56

Dapp, W. B., Basu, S., & Kunz, M. W. 2012, A&A, 541, A35

di Francesco, J., Evans, N. J., I., Caselli, P., et al. 2007, in Protostars and Planets V, ed. B. Reipurth, D. Jewitt, & K. Keil, 17

Dobbs, C. L., Krumholz, M. R., Ballesteros-Paredes, J., et al. 2014, in Protostars and Planets VI, ed. H. Beuther, R. S. Klessen, C. P. Dullemond, & T. Henning, 3

Dullemond, C. P., Juhasz, A., Pohl, A., et al. 2012, RADMC-3D: A multi-purpose radiative transfer tool

Dunham, M. M., Chen, X., Arce, H. G., et al. 2011, The Astrophysical Journal, 742, 1

Dunham, M. M., Stutz, A. M., Allen, L. E., et al. 2014, Protostars and Planets VI, 195–218

Duschl, W. J., Strittmatter, P. A., & Biermann, P. L. 2000, A&A, 357, 1123

Ebert, R. 1955, Z. Astrophys., 37, 217

Foglizzo, T. 2002, A&A, 392, 353

Foglizzo, T. 2009, ApJ, 694, 820

Foglizzo, T., Galletti, P., Scheck, L., et al. 2007, ApJ, 654, 1006

Foglizzo, T., Scheck, L., & Janka, H. T. 2006, ApJ, 652, 1436

Foglizzo, T., & Tagger, M. 2000, A&A, 363, 174

Galli, D., Lizano, S., Shu, F. H., et al. 2006, ApJ, 647, 374

Gerin, M., Pety, J., Fuente, A., et al. 2015, A&A, 577, L2

Gerin, M., Pety, J., Commerçon, B., et al. 2017, A&A, 606, A35

Girart, J. M., Rao, R., & Marrone, D. P. 2006, Science, 313, 812

Goodman, A. A., Benson, P. J., Fuller, G. A., et al. 1993, ApJ, 406, 528

Guilet, J., & Foglizzo, T. 2012, MNRAS, 421, 546

Hansen, C. J., Kawaler, S. D., & Trimble, V. 2004, Stellar interiors: physical principles, structure, and evolution, 2nd ed. (New York: Springer-Verlag)

Heiles, C., & Crutcher, R. 2005, Magnetic Fields in Diffuse HI and Molecular Clouds, ed. R. Wielebinski & R. Beck, Vol. 664, 137

Hennebelle, P., & Falgarone, E. 2012, A&A Rev., 20, 55

Herbig, G. H. 1960, ApJS, 4, 337

Heyer, M., & Dame, T. M. 2015, ARA&A, 53, 583

Hirano, S., & Machida, M. N. 2019, MNRAS, 485, 4667

Hopkins, P. F., & Lee, H. 2016, MNRAS, 456, 4174

Hull, C. L. H., & Zhang, Q. 2019, Frontiers in Astronomy and Space Sciences, 6, 3

Hull, C. L. H., Plambeck, R. L., Kwon, W., et al. 2014, ApJS, 213, 13

Hull, C. L. H., Girart, J. M., Tychoniec, Ł., et al. 2017a, ApJ, 847, 92

Hull, C. L. H., Mocz, P., Burkhart, B., et al. 2017b, ApJ, 842, L9

Inutsuka, S.-i. 2012, Progress of Theoretical and Experimental Physics, 2012, 01A307

Isella, A., & Natta, A. 2005, A&A, 438, 899

Isella, A., Huang, J., Andrews, S. M., et al. 2018, ApJ, 869, L49

Jeans, J. H. 1902, Philosophical Transactions of the Royal Society of London Series A, 199, 1

Jeans, J. H. 1928, Astronomy and cosmogony

Joos, M., Hennebelle, P., & Ciardi, A. 2012, A&A, 543, A128

Karnath, N., Megeath, S. T., Tobin, J. J., et al. 2020, ApJ, 890, 129

Kirk, J. M., Ward-Thompson, D., & André, P. 2005, MNRAS, 360, 1506

Koyamatsu, S., Takakuwa, S., Hayashi, M., et al. 2014, ApJ, 789, 95

Krasnopolsky, R., Li, Z.-Y., & Shang, H. 2011, ApJ, 733, 54

Kuiper, R., & Hosokawa, T. 2018, A&A, 616, A101

Kuiper, R., Klahr, H., Beuther, H., et al. 2010, The Astrophysical Journal, 722, 1556

Kuiper, R., Klahr, H., Beuther, H., et al. 2011, ApJ, 732, 20

Kuiper, R., Klahr, H., Dullemond, C., et al. 2010, A&A, 511, A81

Kuiper, R., Turner, N. J., & Yorke, H. W. 2016, ApJ, 832, 40

Kuiper, R., & Yorke, H. W. 2013, ApJ, 772, 61

Kuiper, R., Yorke, H. W., & Turner, N. J. 2015, ApJ, 800, 86

Kunz, M. W., & Mouschovias, T. C. 2010, MNRAS, 408, 322

Lada, C. J. 1987, in IAU Symposium, Vol. 115, Star Forming Regions, ed. M. Peimbert & J. Jugaku, 1

Lam, K. H., Li, Z.-Y., Chen, C.-Y., et al. 2019, MNRAS, 489, 5326

Larson, R. B. 1969, MNRAS, 145, 271

Larson, R. B. 2003, Reports on Progress in Physics, 66, 1651

Launhardt, R., Stutz, A. M., Schmiedeke, A., et al. 2013, A&A, 551, A98

Lee, C.-F., Li, Z.-Y., Ho, P. T. P., et al. 2017, Science Advances, 3, e1602935

Lee, Y.-N., & Hennebelle, P. 2018, A&A, 611, A89

Levermore, C. D., & Pomraning, G. C. 1981, ApJ, 248, 321–334

Lewis, B. T., & Bate, M. R. 2018, MNRAS, 477, 4241

Li, H.-b., Fang, M., Henning, T., et al. 2013, MNRAS, 436, 3707

Li, Z.-Y., Krasnopolsky, R., & Shang, H. 2011, ApJ, 738, 180

Li, Z.-Y., Krasnopolsky, R., Shang, H., et al. 2014, ApJ, 793, 130

Lilley, A. E. 1955, ApJ, 121, 559

Lynden-Bell, D. 2003, MNRAS, 341, 1360

Mac Low, M.-M., & Klessen, R. S. 2004, Reviews of Modern Physics, 76, 125

Machida, M. N., & Basu, S. 2019, ApJ, 876, 149

Machida, M. N., Inutsuka, S.-i., & Matsumoto, T. 2006a, ApJ, 647, L151

Machida, M. N., Inutsuka, S.-i., & Matsumoto, T. 2007a, arXiv e-prints, arXiv:0705.2073

Machida, M. N., Inutsuka, S.-i., & Matsumoto, T. 2007b, ApJ, 670, 1198

Machida, M. N., Inutsuka, S.-i., & Matsumoto, T. 2008, ApJ, 676, 1088

Machida, M. N., Inutsuka, S.-i., & Matsumoto, T. 2010, ApJ, 724, 1006

Machida, M. N., Inutsuka, S.-I., & Matsumoto, T. 2011, PASJ, 63, 555

Machida, M. N., Inutsuka, S.-i., & Matsumoto, T. 2014, MNRAS, 438, 2278

Machida, M. N., & Matsumoto, T. 2011, MNRAS, 413, 2767

Machida, M. N., Matsumoto, T., Hanawa, T., et al. 2006b, ApJ, 645, 1227

Malygin, M. G., Kuiper, R., Klahr, H., et al. 2014, A&A, 568, A91

Marleau, G.-D., Klahr, H., Kuiper, R., et al. 2017, ApJ, 836, 221

Marleau, G.-D., Mordasini, C., & Kuiper, R. 2019, ApJ, 881, 144

Masson, J., Chabrier, G., Hennebelle, P., et al. 2016, A&A, 587, A32

Masunaga, H., & Inutsuka, S.-i. 1999, ApJ, 510, 822

Masunaga, H., & Inutsuka, S.-i. 2000, ApJ, 531, 350–365

Masunaga, H., Miyama, S. M., & Inutsuka, S.-i. 1998, ApJ, 495, 346–369

Matsumoto, T., & Hanawa, T. 2003, ApJ, 595, 913

Matsumoto, T., Machida, M. N., & Inutsuka, S.-i. 2017, ApJ, 839, 69

Maureira, M. J., Arce, H. G., Dunham, M. M., et al. 2017, ApJ, 838, 60

Maury, A. J., Girart, J. M., Zhang, Q., et al. 2018, MNRAS, 477, 2760

McKee, C. F., & Ostriker, E. C. 2007, ARA&A, 45, 565

McLeod, A. F., Reiter, M., Kuiper, R., et al. 2018, Nature, 554, 334

Mellon, R. R., & Li, Z.-Y. 2008, ApJ, 681, 1356

Mellon, R. R., & Li, Z.-Y. 2009, ApJ, 698, 922

Mestel, L. 1999, Stellar magnetism

Mestel, L., & Spitzer, L., J. 1956, MNRAS, 116, 503

Mignone, A., Bodo, G., Massaglia, S., et al. 2007, ApJS, 170, 228

Mignone, A., Flock, M., & Vaidya, B. 2019, ApJS, 244, 38

Mignone, A., Zanni, C., Tzeferacos, P., et al. 2012, The Astrophysical Journal Supplement Series, 198, 7

Miyoshi, T., & Kusano, K. 2005, Journal of Computational Physics, 208, 315

Mouschovias, T. C. 1991, ApJ, 373, 169

Mouschovias, T. C., & Paleologou, E. V. 1979, ApJ, 230, 204

Mouschovias, T. C., & Paleologou, E. V. 1980, ApJ, 237, 877

Mouschovias, T. C., & Spitzer, L., J. 1976, ApJ, 210, 326

Murillo, N. M., Lai, S.-P., Bruderer, S., et al. 2013, A&A, 560, A103

Nakano, T. 1998, ApJ, 494, 587

Nakano, T., Nishi, R., & Umebayashi, T. 2002, ApJ, 573, 199

Nielbock, M., Launhardt, R., Steinacker, J., et al. 2012, A&A, 547, A11

Ossenkopf, V., & Henning, T. 1994, A&A, 291, 943

Pattle, K., Ward-Thompson, D., Berry, D., et al. 2017, ApJ, 846, 122

Pelletier, G., & Pudritz, R. E. 1992, ApJ, 394, 117

Pezzuto, S., Elia, D., Schisano, E., et al. 2012, A&A, 547, A54

Pineda, J. E., Arce, H. G., Schnee, S., et al. 2011, ApJ, 743, 201

Planck Collaboration, Ade, P. A. R., Aghanim, N., et al. 2015, A&A, 576, A104

Planck Collaboration, Ade, P. A. R., Aghanim, N., et al. 2016, A&A, 586, A138

Pokhrel, R., Myers, P. C., Dunham, M. M., et al. 2018, ApJ, 853, 5

Pollack, J. B., Hollenbach, D., Beckwith, S., et al. 1994, ApJ, 421, 615

Pudritz, R. E., & Norman, C. A. 1983, ApJ, 274, 677

Pudritz, R. E., & Ray, T. P. 2019, Frontiers in Astronomy and Space Sciences, 6, 54

Sadavoy, S. I., Stephens, I. W., Myers, P. C., et al. 2019, ApJS, 245, 2

Saigo, K., & Tomisaka, K. 2006, ApJ, 645, 381

Saigo, K., Tomisaka, K., & Matsumoto, T. 2008, ApJ, 674, 997

Santos, F. P., Chuss, D. T., Dowell, C. D., et al. 2019, ApJ, 882, 113

Saumon, D., Chabrier, G., & van Horn, H. M. 1995, ApJS, 99, 713

Scheck, L., Janka, H. T., Foglizzo, T., et al. 2008, A&A, 477, 931

Schneider, N., Csengeri, T., Hennemann, M., et al. 2012, A&A, 540, L11

Schönke, J., & Tscharnuter, W. M. 2011, A&A, 526, A139

Schwartz, R. D. 1977, ApJ, 212, L25

Shakura, N. I., & Sunyaev, R. A. 1973, A&A, 500, 33

Shu, F., Najita, J., Ostriker, E., et al. 1994, ApJ, 429, 781

Shu, F. H., Adams, F. C., & Lizano, S. 1987, ARA&A, 25, 23

Snell, R. L., Loren, R. B., & Plambeck, R. L. 1980, ApJ, 239, L17

Soler, J. D. 2019, A&A, 629, A96

Soler, J. D., Alves, F., Boulanger, F., et al. 2016, A&A, 596, A93

Spitzer, Lyman, J., & Tomasko, M. G. 1968, ApJ, 152, 971

Stahler, S. W., & Palla, F. 2005, The Formation of Stars

Stahler, S. W., Shu, F. H., & Taam, R. E. 1980a, ApJ, 241, 637

Stahler, S. W., Shu, F. H., & Taam, R. E. 1980b, ApJ, 242, 226

Stahler, S. W., Shu, F. H., & Taam, R. E. 1981, ApJ, 248, 727

Stamatellos, D., & Whitworth, A. P. 2009, MNRAS, 400, 1563

Stamatellos, D., Whitworth, A. P., Bisbas, T., et al. 2007, A&A, 475, 37

Stephens, I. W., Looney, L. W., Kwon, W., et al. 2013, ApJ, 769, L15

Strom, S. E. 1972, PASP, 84, 745

Tassis, K., & Mouschovias, T. C. 2005, ApJ, 618, 783

Tassis, K., & Mouschovias, T. C. 2007a, ApJ, 660, 388

Tassis, K., & Mouschovias, T. C. 2007b, ApJ, 660, 402

Teyssier, R., & Commerçon, B. 2019, Front. Astron. Space Sci., 6, 51

Tielens, A. G. G. M. 2005, The Physics and Chemistry of the Interstellar Medium

Tobin, J. J., Hartmann, L., Chiang, H.-F., et al. 2012, Nature, 492, 83

Tobin, J. J., Sheehan, P. D., Megeath, S. T., et al. 2020, ApJ, 890, 130

Tomida, K. 2014, ApJ, 786, 98

Tomida, K., Machida, M. N., Hosokawa, T., et al. 2017, ApJ, 835, L11

Tomida, K., Machida, M. N., Saigo, K., et al. 2010a, ApJ, 725, L239–L244

Tomida, K., Okuzumi, S., & Machida, M. N. 2015, ApJ, 801, 117

Tomida, K., Tomisaka, K., Matsumoto, T., et al. 2013, ApJ, 763, 6

Tomida, K., Tomisaka, K., Matsumoto, T., et al. 2010b, ApJ, 714, L58

Tomisaka, K. 1998, ApJ, 502, L163

Tomisaka, K. 2000, ApJ, 528, L41

Tomisaka, K. 2002, ApJ, 575, 306

Tricco, T. S., Price, D. J., & Laibe, G. 2017, MNRAS, 471, L52

Troland, T. H., & Crutcher, R. M. 2008, ApJ, 680, 457

Tscharnuter, W. M. 1987, A&A, 188, 55

Tscharnuter, W. M., Schönke, J., Gail, H. P., et al. 2009, A&A, 504, 109

Tsukamoto, Y., Iwasaki, K., Okuzumi, S., et al. 2015, MNRAS, 452, 278

Tsukamoto, Y., Okuzumi, S., Iwasaki, K., et al. 2018, ApJ, 868, 22

Tsukamoto, Y., Okuzumi, S., Iwasaki, K., et al. 2017, PASJ, 69, 95

Tychoniec, Ł., Tobin, J. J., Karska, A., et al. 2018, ApJ, 852, 18

Umebayashi, T., & Nakano, T. 1981, PASJ, 33, 617

Urquhart, J. S., König, C., Giannetti, A., et al. 2018, MNRAS, 473, 1059

Vaidya, B., Mignone, A., Bodo, G., et al. 2015, A&A, 580, A110

Vaytet, N., Audit, E., Chabrier, G., et al. 2012, A&A, 543, A60

Vaytet, N., Chabrier, G., Audit, E., et al. 2013, A&A, 557, A90

Vaytet, N., Commerçon, B., Masson, J., et al. 2018, A&A, 615, A5

Vaytet, N., & Haugbølle, T. 2017, A&A, 598, A116

Vaytet, N., Tomida, K., & Chabrier, G. 2014, A&A, 563, A85

Whelan, E. T., Ray, T. P., Bacciotti, F., et al. 2005, Nature, 435, 652

Whitehouse, S. C., & Bate, M. R. 2006, MNRAS, 367, 32

Williams, J. P., Blitz, L., & McKee, C. F. 2000, in Protostars and Planets IV, ed. V. Mannings, A. P. Boss, & S. S. Russell, 97

Winkler, K.-H. A., & Newman, M. J. 1980a, ApJ, 236, 201

Winkler, K.-H. A., & Newman, M. J. 1980b, ApJ, 238, 311

Wurster, J., & Bate, M. R. 2019, MNRAS, 486, 2587

Wurster, J., Bate, M. R., & Price, D. J. 2018a, MNRAS, 480, 4434

Wurster, J., Bate, M. R., & Price, D. J. 2018b, MNRAS, 475, 1859

Wurster, J., Bate, M. R., & Price, D. J. 2018c, MNRAS, 476, 2063

Wurster, J., & Li, Z.-Y. 2018, Frontiers in Astronomy and Space Sciences, 5, 39

Wurster, J., Price, D. J., & Bate, M. R. 2016, MNRAS, 457, 1037

Yen, H.-W., Takakuwa, S., Koch, P. M., et al. 2015, ApJ, 812, 129

Acknowledgements

Success and happiness over the last four years would not have been possible without the constant guidance, encouragement, and support from several people.

First and foremost, I would like to express my deepest gratitude to all my supervisors, Thomas Henning, Rolf Kuiper, and Christian Fendt. Thomas, thank you for always making sure that I see the bigger picture, for your timely advice and inputs on all my projects, for encouraging me to have interesting science discussions with several experts in the field, and for refereeing this thesis. Rolf, thank you for making distant supervision work so well, for sharing your expertise, for always being extremely patient with me, and for always providing helpful answers to all my questions, no matter how basic they were. I always hope to learn from your extremely efficient time management and organisational skills. Christian, thank you for always being around for discussing even the smallest results, for sharing ideas and suggestions that helped me throughout this period, and for being excited about my results, especially when I was not, it really helped to keep me motivated. A big thank you to you and Huong for always making sure that all the students are being listened to and are taken care of. IMPRS-HD is a big success thanks to your constant efforts. I am very grateful to Gabriel-Dominique Marleau for being a part of all my projects. Your curiosity and enthusiasm to understand every tiny detail is very inspiring. Thank you for always being helpful, responsive, patient, and kind.

I would like to express my sincere thanks to Kees Dullemond for refereeing this thesis and for being on my thesis committee. The yearly discussions with you have been very helpful. MPIA is a unique place with many in-house experts. A big thank you to Mario Flock for sharing his *PLUTO*/python expertise and for always being open to discussions. I am grateful to Hubert Klahr for making numerical hydrodynamics sound so much fun. I would also like to thank everyone on my PAC for making sure I was on track and was enjoying the process. A special thank you to Paola Pinilla for helping me with my postdoc applications. I am grateful to Henrik Beuther for his valuable advice on several occasions. I would also like to thank everyone in the MPIA administration, especially the travel office for helping me organise all my frequent trips to Tübingen. A big thank you to Thomas Müller from the HdA for creating beautiful visualisations for my publication.

It has been a pleasure to spend my PhD time at the MPIA as well as the institute in Tübingen. I really appreciate everyone who supported a comfortable and healthy working environment. My go-to people, Christos and Hans, a big thank you for always answering all my questions related to numerics, coding, and the cluster. For these reasons and many more, I have benefited greatly from each one of you throughout my time in Heidelberg. I really appreciate the time and effort by Rolf, Melanie, Manuel, and Jacob for proofreading my thesis.

A very strong motivation for me to go to work everyday has been my office mates from 216B and E115. Christos, you were the best person to share an office with. I am immensely grateful to you for always being there for me and for your friendship. Mikhail, your knowledge about so many different topics is quite impressive. Camille, you have been a great addition to the office. Keep enjoying your time, your kindness is much appreciated. Jonas (old), thank you for always giving me the space. Jonas (new), it was great to have you sitting next to me. I hope you enjoy this new phase of your life. I will always miss the background soundtracks, all the random discussions,

and of course the office itself. Melanie and Neige, although I did not spend as much time in my new office, it was a pleasure sharing it with you two. Your determination and dedication towards science and health has been motivating.

I could not have asked for a better group of friends to share this journey. Arianna, your energy and enthusiasm about everything is contagious. Josha, all I want to say is high-five and also thank you for those delicious pancakes. Johanna, muchas gracias for always being so supportive and a great friend. Felipe, thank you for sharing the love for boardgames and for making yummy cinnamon rolls, and Ivana, thank you for sticking with me through the tough times. I had such a great time during all the boardgame evenings, potlucks, and movie nights. Thank you for being my support system in Heidelberg. A big shout-out to Paula, Miriam, Martin, Matthias, Sepideh, Sara, Christina, Aida, Micah, Alex, Jacob, and Vince. I will always cherish the wonderful time we have spent together in Heidelberg and during our travels. I truly value our friendship.

A big thank you to my landlords, Robert and Julia, for making me feel at home. I could not have asked for a better house to live in. Thank you for the thoughtful stick notes that have always managed to brighten my day. You are an inspiration to keep a healthy work-life balance. To the most adorable kids, Olivia and Fabio, I have enjoyed all the fun times playing and drawing with you two. Thank you for bringing a smile on my face.

To my backbone, Sayali. I am so lucky to have moved continents at the same time as you. You are my person. Thank you for always being a phone call away and for everything. To my support system and cheer leaders, Aparna, Sudeshna and Kanchan. Thank you for encouraging me ever since high-school and for always making sure that some things never change. Thanks to a bunch of my friends who always make things better, Biplob, Manasi, Vrinda, and Chandra. Thank you, Deepu, for being there so I never had to worry about being away from home. Thank you, Sathe Kaka and Kaku, for shaping my life the way you did. I probably would not have studied Astronomy, had it not been for your guidance.

To the most important people in my life. Mummy and Papa, this one is for you! None of this would have been possible without your constant support, motivation, and encouragement. Thank you for believing in my abilities, more than I do and for letting me follow my dreams. Papa, your curiosity and excitement to learn new things and to travel has always been inspiring. Mummy, I have always admired your patience, hard work, and kindness. Anita, khupach aabhar for being my strongest supporter, for always keeping me entertained, and for always teaching me, in the most authentic way, to enjoy what I do. Anupam, thank you for joining the team and teaching me to stay calm. Finally, to the person who has been the most positive influence in my life over the last two years. Manuel, I cannot thank you enough for always making sure that I smile. Thank you for holding my hand and lifting my spirits, especially during the last year. You have kept me sane, motivated, and made sure that I take enough time off work. I have enjoyed spending all the fun times bonding over the love for food and boardgames. I cannot wait for all the exciting adventures over the next years.

On a final note, the seed for my interest to learn about this universe was planted during my frequent visits to the Inter-University Centre for Astronomy and Astrophysics and the different outreach groups in Pune. Because outreach has been such a big part of my decision to pursue Astronomy, I find it apt to close this chapter of my life with the Astronomy version of one of the most famous poems for kids. A stanza of this poem also includes the process that defines my PhD project. I hope this inspires the young and entertains the adults.

Twinkle Twinkle Little Star
I know exactly what you are

Opaque ball of hot dense gas
Million times our planet's mass
Looking small because you're far
I know exactly what you are

Atmospheric turbulence
Causes rays of light to bend
Blurry light gives views subpar
Causing twinkling little star

We see you as if in the past
Light's not infinitely fast
Lookback time delays our view
I know exactly what you do

Fusing atoms in your core
Hydrogen, helium, carbon and more
With such power you shine far
Twinkle twinkle little star

Classed by their spectroscopy
Types named O, B, A, F, G…
Bright when close and faint when far
I know exactly what you are

Smallest ones burn cool and slow
Still too hot to visit, though
Red stars dominate by far
Twinkle twinkle little star

Largest ones are hot and blue
Supernova when they're through
Then black hole or neutron star
I know exactly what you are

Gravity holds on too tight
Nothing gets out, mass or light
Black holes are the most bizarre
Remnants of a twinkling star

Neutron stars spin really fast
When their beams of light sweep past
Then we call you a pulsar
I know exactly what you are

Our Sun's average as stars go
Formed 5 billion years ago
Halfway through its life so far
Twinkle mid-size yellow star

Sunspots look dark but they're bright
Slightly cooler so less light
Temporary surface scar
I know exactly what you are

Swelling up before it's dead
Cooling off and growing red
Then its end is not so far
Twinkle big red giant star

Outer layers float away
Planetary nebulae
Wispy gas is gossamer
I know exactly what you were

White dwarf is the core you get
matter is degenerate
When small stars say au revoir
Twinkle very little star

Interstellar medium
Recycled ad nauseam
Gas and dust are spread afar
I know exactly what you are

Forming from collapsing clouds
Cold and dusty gas enshrouds
Spinning, heating protostar
Twinkle twinkle little star

Often forming multiply
Clusters bound by gravity
Open type or globular
I know exactly how you purr

Two stars make a binary
Or a triple if there's three
Some are solo just like ours
Twinkle twinkle little stars

Two hundred billion stars all stay
Bound up in the Milky Way
Dusty spiral with a bar
I know exactly what you are

Stars have planets orbiting
Rocky or gassy, moons or rings
Earth's unique with life so far
Twinkle twinkle little star!

(*by Julia Kregenow* & *Jason Wright,
2011, 2012, 2015*)